Convection and Dynamo Action in Rapidly Rotating Suns

by

B. P. Brown

B.S., Harvey Mudd College, 2003

A thesis submitted to the

Faculty of the Graduate School of the

University of Colorado in partial fulfillment

of the requirements for the degree of

Doctor of Philosophy

Department of Astrophysical and Planetary Sciences

2009

This thesis entitled:
Convection and Dynamo Action in Rapidly Rotating Suns
written by B. P. Brown
has been approved for the Department of Astrophysical and Planetary Sciences

Juri Toomre

John Bally

Allan Sacha Brun

Keith Julien

Mark Miesch

Mark Rast

Date

The final copy of this thesis has been examined by the signatories, and we find that both the content and the form meet acceptable presentation standards of scholarly work in the above mentioned discipline.

Brown, B. P. (Ph.D., Astrophysical and Planetary Sciences)

Convection and Dynamo Action in Rapidly Rotating Suns

Thesis directed by Prof. Juri Toomre

When our Sun was young it rotated much more rapidly than it does now. Observations of young, rapidly rotating stars indicate that many possess substantial magnetic activity and strong axisymmetric magnetic fields. There is furthermore an observed correlation between the stellar rotation rate and surface magnetism. Yet the origins of the magnetic activity or the correlation with rotation remain unclear. We conduct simulations of dynamo action in rapidly rotating suns with the 3-D MHD anelastic spherical harmonic (ASH) code to explore the complex coupling between rotation, convection and magnetism. Here we study global-scale flows of differential rotation and meridional circulation as well as dynamo action realized in the bulk of the convection zone for stars rotating from one to fifteen times the current solar rate.

We find that more rapidly rotating stars generally have stronger flows of differential rotation but weaker meridional circulations that break into multiple cells in both radius and latitude. Surprising localized states arise in the rapidly rotating simulations, with convection modulated in longitude. In the most rapid rotators convection can be entirely confined to narrow active nests which persist for thousands of days and propagate through the shearing flow of differential rotation at their own distinct velocity.

We find that substantial organized global-scale magnetic fields are achieved by dynamo action in these rapidly rotating suns. Striking wreaths of magnetism are built in the midst of the convection zone, coexisting with the turbulent convection. This is a great surprise, for many solar dynamo theories have suggested that a tachocline of penetration and shear at the base of the convection zone is a crucial ingredient for organized dynamo action, whereas these simulations generally do not include such

tachoclines. Some dynamos achieved in these rapidly rotating states build persistent global-scale fields which maintain amplitude and polarity for thousands of days. Other dynamos can undergo cycles of activity, with fields varying in strength and even changing in global-scale polarity. As the magnetic fields wax and wane in strength, the primary response in the convective flows involves the axisymmetric differential rotation, which begins to vary on similar time scales. Bands of relatively fast and slow fluid propagate toward the poles on time scales of roughly 500 days. In the Sun, similar patterns are observed in the poleward branch of the torsional oscillations, and these may represent a response to poleward propagating magnetic field deep below the solar surface.

In one simulation, rotating at three times the solar rate, we explore how the wreaths of magnetism are built and maintained by the differential rotation and the turbulent correlations. We further explore whether a simple mean-field theory can reproduce our 3-D results and find several discrepancies. We generally find that wreath-building dynamos are present in every region of parameter space we have sampled, including simulations of the solar dynamo. We find that previous simulations had bottom boundary conditions which make wreath formation difficult if not impossible, but that new simulations of the solar dynamo can produce strong magnetic wreaths. Lastly, we show that wreaths of magnetism survive in the presence of a tachocline of penetration and shear at the base of the convection zone. These wreaths fill the convection zone and undergo quasi-regular reversals of global-scale polarity.

Dedication

To my mother and father who have encouraged every step along this path of discovery, and to Mindy who has made the journey one of joy.

Acknowledgements

This journey has only been possible with the help of many friends. First and foremost, I thank my advisor Juri Toomre for his support, friendship, generosity and wise advice. Juri has provided me with opportunities beyond compare. I cherish the many evenings I have spent with Juri and his wife Linda, and look forward to the many wonderful meals and celebrations to be shared together in the years to come.

My collaborators and co-authors have become close friends over the years. Sacha Brun has provided constant and good advice, and reflections on scientific careers and life, even as he has undertaken his own journeys on these paths. His European perspective is always refreshing. I have always looked forward with pleasure to my visits with Mark Miesch at HAO. His positive outlook and deep insights have contributed greatly to my own growth, and his excitement about the discoveries contained herein has kept my own alive. His thesis has been at my side for many years, and it became particularly helpful in the past months; I hope to one day write as well he does regularly. And Mark, you're right: the high mountains do soothe the soul. My thanks also go to Matt Browning, who walked these steps before me, and is now helping me to find my own way. Over the years Mark Rast has been a sage source of advice, helping me remember what really matters in the pursuit of scientific discovery, and reminding me that the standard path to success is not the only one, and that it is perhaps not always the the best. Gwen Dickinson has been a friend and a constant eye of calm in the whirling storm that can be our research. She has remained unflappably calm in the face of looming deadlines, and has saved us all from disaster (myself in particular) many, many times.

My office mates over the years, Jason Lisle, Geoff Vasil and Nick Nelson, have each helped shape this continuing adventure. Jason reminded me early on of the importance of balancing life and science, and the value of time. Geoff has become a dear friend, and many evenings have been spent together thinking on science and life, in our tower office or over good food and good beer. We both venture forth now to postdocs in colder climes. Nick has helped me realize that I really have finally learned a few things of use. Good luck sir, on your own path to discoveries! Kyle Augustson and Nick Featherstone are part of our cohort as well; I would not be here now with out their aid. I look forward to seeing where each of us ventures in the future. Along my path, I've had the pleasure of meeting and working with John Clyne and Alan Norton at NCAR, and Carter Emmart at the American Museum of Natural History. These three have helped me realize how beautiful our science can be, and how enthusiastically it can be received when shown in the right light. With them, I look forward to many fruitful years ahead.

My close friends and housemates, Brennan Gantner and Than Putzig, have joined me in many wonderful adventures during our years in Boulder. To them and Licia Ray, I owe my sanity. Ben Mates and Dave Schneider held the final watch at the Greenbriar estate, through the craziness of moving, writing and planning a wedding; during these times, they reminded me that this too would pass.

These adventures in science began at a young age when my father told me "there are four fundamental forces of nature. You should learn about them, how they work, what they are." This fueled a love for physics and then astronomy. My mother and father have supported me with love on every step of this adventure. In recent days my path has been made clearer by the presence of my beloved, Mindy Wilkinson, who has been my companion and guide. During dark days she reminds me that what we do is fundamentally really, really neat. That it matters. That people care. And to me, that has value beyond words. On the journeys ahead, we will tread our paths together, which brings me incomparable joy.

I thank Juri Toomre, Mark Rast, Mark Miesch, Keith Julien, Sacha Brun, and John Bally for serving on my thesis committee. Over the years, they each have acted to kindle my scientific enthusiasm, to provide perspective on life, and to help me find my way. It was an honor to have them present at the close of this chapter of life.

This research has been supported by NASA through Heliophysics Theory Program grants NNG05G124G and NNX08AI57G. I have additionally been supported through the NASA GSRP program by award number NNG05GN08H. The simulations in this thesis were carried out with NSF PACI support of SDSC, PSC, TACC and NICS. In particular, these simulations ran variously on Blue Horizon, Datastar and Bluegene at SDSC, on Lemieux and Bigben at PSC, on Ranger at TACC and on Kraken at NICS. Volume renderings used in the analysis and the field line tracings shown were produced using VAPOR (Clyne et al. 2007). None of this analysis would have been possible without the resources at Laboratory for Computational Dynamics (LCD) here at the University of Colorado.

Contents

Chapter

Tables

Table

Figures

Figure

Chapter 1

Convection, Rotation and Magnetism

We live near a magnetic star and our Earth is embedded within its magnetized wind. The surface of the Sun is covered in magnetism on all scales, with global-scale structures including prominences that reach high into the solar atmosphere (Fig. 1.1*a*) as well as smaller concentrated magnetic structures like sunspots, where the magnetism becomes strong enough to largely halt the turbulent convection leaving dark regions at the surface (Fig. 1.1*b*). On the smallest scales visible at the surface, magnetic fields are swept aside by vigorous granulation which are convective cells that overturn every 10-15 minutes and have flows that are near the speed of sound. The magnetism collects in the surrounding network of downflow lanes, where it is swept out by the slower flows of supergranulation, whose characteristic timescales are closer to a day. There the magnetism traces out the supergranular network, and expands outwards into the solar chromosphere and corona.

Solar magnetism is far from being static, and it evolves on many timescales, with a prominent and regular eleven-year cycle of sunspots and global-scale polarity reversals. We stand at the start of a new cycle now (called cycle 24); few sunspots are present on the solar disk and eruptive events and space storms are rare. Over the next eleven years we will likely see spots emerging at the surface, initially at higher latitudes (near $\pm 30^{\circ}$) and then at lower and lower latitudes until, near the end of the cycle, they appear almost at the solar equator. Time-latitude maps of spot emergence form characteristic

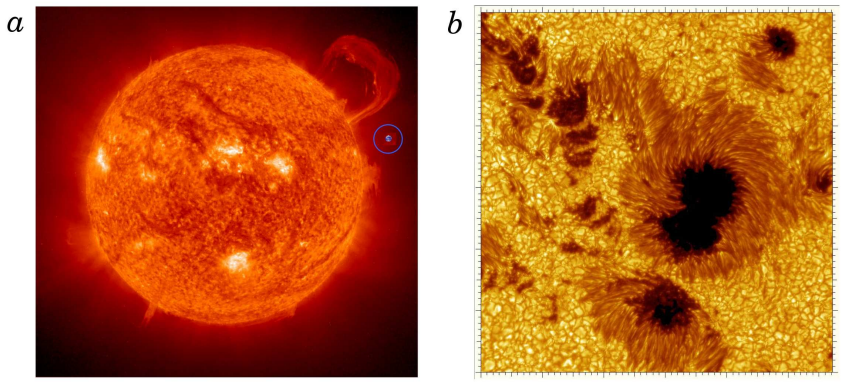

FIGURE 1.1 — Solar magnetism at many scales. (*a*) On global-scales, a large prominence lifting off the limb of the Sun is revealed in this SOHO EIT image. A scaled-image of the Earth (inside blue circle) is provided for comparison. (*b*) On finer scales, as seen in this image from the SSVT, sunspots at the surface are regions of strong magnetism. Tick marks indicate 1Mm spacings. Individual sunspots are roughly the size of the Earth.

"butterfly" patterns and these diagrams illustrate the migration of the active latitudes as the cycle progresses (Fig.1.2*a*). When sunspots emerge at the solar surface, they generally have characteristic polarities and orientations. Spots can be large or small, with most as large as the Earth or larger.

Within the sunspots, the magnetism can evolve on very short timescales. In some active regions the strong magnetic fields reconnect, leading to explosive releases of energy in the form of high-energy photon flares and eruptive plasma coronal mass ejections. As these photons and magnetized plasma storms strike the Earth's magnetosphere, they can profoundly affect our modern society, imperiling astronauts and satellites in space and scrambling communications and navigation systems on the ground. The largest solar storms can threaten the very infrastructure of national power grids and can disrupt or destroy computational systems.

As the cycle progresses, the sunspots will become more numerous, peaking in number roughly midway through (Fig. 1.2*b*). Generally, the number of sunspots present on the solar disk increases rapidly at the start of a new solar cycle and then declines more gradually. It is during the later half of the cycle that the largest storms and

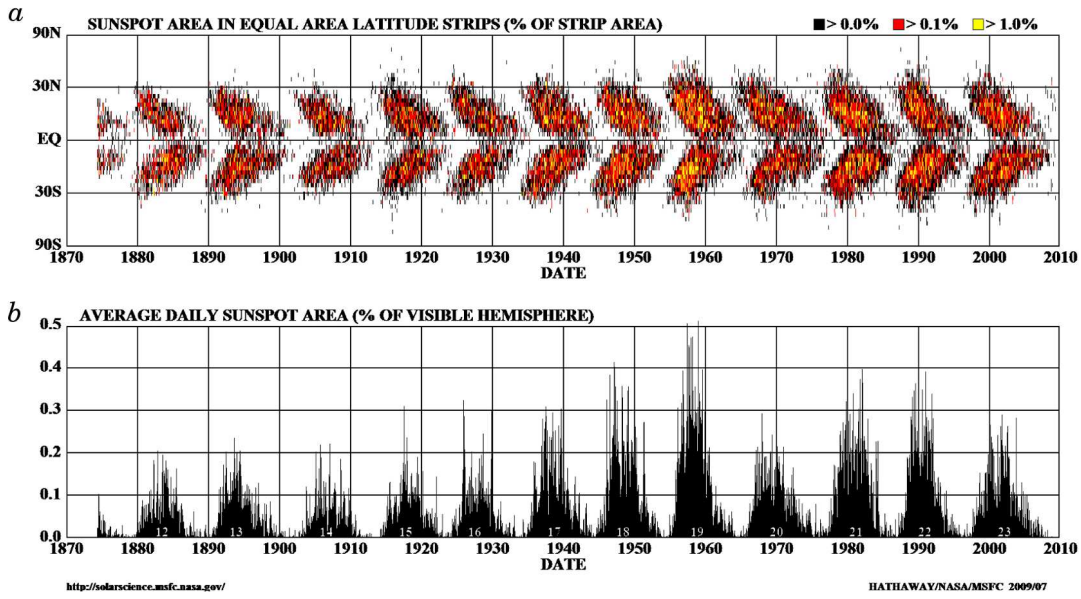

FIGURE 1.2 — Temporal variation of global-scale solar magnetism. (*a*) Butterfly diagram, or time-latitude map, showing emergence of sunspots at the surface. When a new cycle begins, sunspots emerge first at high latitudes. As time passes, they become more numerous and appear at lower latitudes. When their number is near maximum, the global-scale polarities reverse. As their number declines and the sunspots approach the equator, a cycle begins anew with opposite polarity sunspots. (*b*) Percentage of the visible solar disk that is covered by sunspots. These figures adapted from Hathaway (2009).

eruptive events tend to occur, though major flares and eruptions can occur at any time. Near the middle of the roughly eleven-year solar cycle, when the number of sunspots is near maximum, the magnetic poles of the Sun flip in polarity. As the number of sunspots declines and the active latitudes approach the equator, a cycle begins anew with sunspots of opposite polarity emerging at high latitudes. Though the timing of the solar cycle is fairly regular, the magnetic activity shows modulation on longer timescales as well. Some cycles are strong, with many spots, while some cycles are weak. At times,as during the Maunder Minimum, the surface of the Sun has remained barren of sunspots for decades.

1.1 Operation of the Solar Dynamo

Solar magnetism and the cycles of magnetic activity must arise from organized dynamo action in the Sun's interior. This dynamo action is achieved by turbulent plasma motions in the solar convection zone, which spans the outer 29% of the Sun in radius. Here vigorous convective motions and rotation couple to drive the differential rotation and meridional circulation. These flows are important ingredients in stellar dynamo theory, and in many theories the differential rotation plays an important role in building and organizing the global-scale fields. The meridional circulations may be important for returning flux to the base of the convection zone and advecting it equatorward, enabling cycles of magnetic activity.

The manner in which the Sun achieves global-scale dynamo action is gradually being sorted out. The seat of this dynamo is generally thought to be located in the tachocline, an interface of shear between the differentially rotating convection zone and the radiative interior which is in solid body rotation (e.g., Parker 1993; Charbonneau & MacGregor 1997; Ossendrijver 2003). Helioseismology, which uses acoustic oscillations to probe the radial structure of the Sun as well as convective flows beneath the surface, has revealed that the solar differential rotation profile observed at the surface prints throughout the bulk of the convection zone with two important regions of shear (Fig. 1.3*a*). The near-surface shear layer occupies the outer 5% of the Sun while the tachocline is at the base of the convection zone and separates the strong differential rotation of that region from the uniform rotation of the deeper radiative interior (e.g., Thompson et al. 2003; Thompson 2009).

The stably stratified tachocline may also provide a region for storing and amplifying coherent tubes of magnetic field which may eventually rise to the surface of the Sun as sunspots. It has generally been believed that magnetic buoyancy instabilities may prevent fields from being strongly amplified within the bulk of the convection zone

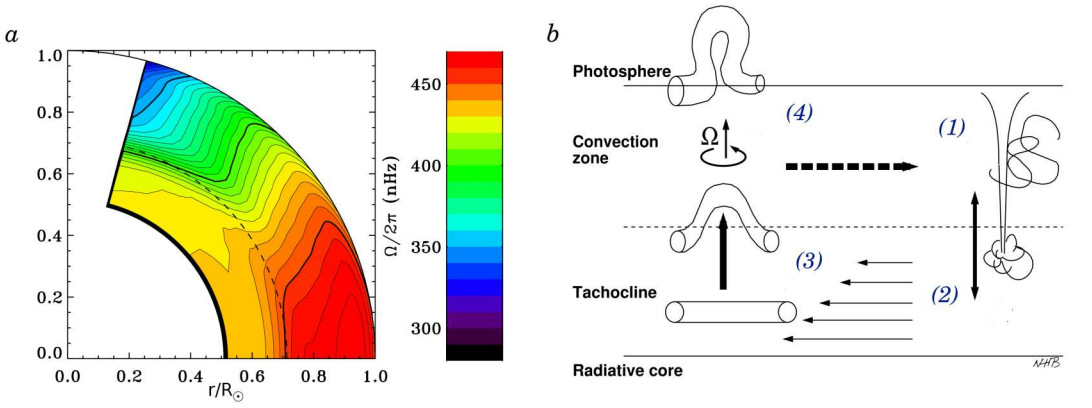

FIGURE 1.3 — Differential rotation and the solar dynamo. (*a*) Helioseismically determined differential rotation profile for the Sun, showing the best determination to date of the internal angular velocity Ω profile (Thompson 2009), with fast (red) equator and slow (blue) poles. Two layers of radial shear are prominently visible, one near the surface and one at the interface between the convection zone and the radiative interior. This deeper layer, the tachocline, may be the seat of the global solar dynamo. (*b*) Sketch of processes likely at work in the solar dynamo. In interface dynamo models, magnetic fields in the convection zone are wound up by helical convective flows (1) and pumped downwards into the tachocline by the compressible convection (2). There the field is organized and stretched into global-scale structures (3) which may become buoyantly unstable and rise to emerge at the surface as sunspots (4). As they transit the convection zone, the magnetic tubes are influenced by rotation and some of the field is shredded by convection, closing the loop back to (1). Meridional circulations may additionally contribute to the transport of field down to the tachocline.

itself (Parker 1975). In the now prevalent "interface dynamo" model, solar magnetic fields are partly generated in the convection zone by helical convection, then transported downward into the tachocline where they are organized and amplified by the shear. Ultimately the fields may become unstable and rise to the surface. This model is illustrated in Figure 1.3*b*.

In the interface dynamo model, magnetic fields are amplified by turbulent flows throughout the convection zone. This "magnetic chaff" is pumped downwards into the tachocline by asymmetries in the compressible convection, which generally has fast and narrow downflows and slower and broader upflows. In the tachocline, the fluctuating magnetic fields are stored and gradually stretched out by the differential rotation into global-scale coherent sheets of magnetism. These magnetic sheets become strong enough

to undergo magnetic buoyancy instabilities, and this may break up the sheet into rising magnetic tubes of predominantly toroidal magnetic field. If these tubes survive their transit of the convection zone, they emerge at the surface as sunspots. Coriolis forces cause the rising tubes to twist, which leads to the observed tilt angle of emerging sunspots and may contribute to the global-scale poloidal field.

Though some tubes of magnetism may survive, many more are likely to be shredded by the intense turbulence in the convection zone. Generally, to emerge at the surface, the average magnetic energy density of the tube must exceed the kinetic energy density of the strongest downflows that the tube encounters during its rise (e.g., Cline 2003; Fan et al. 2003; Abbett et al. 2004; Jouve & Brun 2009). This strong criteria may be difficult to satisfy in the solar tachocline (Vasil & Brummell 2008, 2009). As the magnetic structures are shredded, helical convection twists the toroidal field into poloidal field. This poloidal field is amplified in the convection zone before being caught in the vigorous downflows and pumped into the tachocline closing the loop on the dynamo circuit, though some may also be transported by the global-scale meridional circulations. This dynamo model and the cartoon sketch shown in Figure 1.3*b* summarize the fundamental features found in most modern solar dynamo theories (e.g., Charbonneau 2005; Miesch 2005).

1.2 Theoretical Treatments of Stellar Convection

The elements of the solar dynamo are often interpreted in a mean-field framework, where the complex turbulent correlations in the induction equation are linearized in terms of the global-scale magnetic fields. In these approaches, the magnetism and plasma flows of the interior are separated into mean components and fluctuations about those means. These means are usually taken over large spatial scales and long temporal epochs, and are often assumed to be much larger in amplitude than the fluctuating magnetic and velocity fields.

The language of mean-field theory has become the language of dynamo theory. In this terminology, the production of mean poloidal field through the winding up of toroidal field by helical convection is called an α-effect (e.g., Moffatt 1978; Steenbeck et al. 1966). The stretching of mean poloidal field into mean toroidal field by the shearing flows of differential rotation is called an Ω-effect.

In the solar dynamo, the tachocline of shear at the base of the convection zone is thought to play a key role by providing a region where the Ω-effect can operate without turbulent convection shredding and disrupting the global-scale toroidal fields. The fields there are thought to grow in strength until magnetic buoyancy carries them upwards into the convection zone. There, some of this toroidal field is shredded and turned into poloidal field by the α-effect from the convection and by Coriolis forces on the rising tube. Some flux survives to erupt at the solar surface, creating sunspots, active regions and, eventually, explosive solar magnetic activity. Some of the poloidal field generated by this process is pumped downward by convection into the tachocline where it is amplified into toroidal field, thus completing the dynamo cycle. Conceptual models similar to this are called "$\alpha - \Omega$" dynamos, with the α-effect dominating the production of poloidal field and the Ω-effect largely responsible for the production of the toroidal fields. These models and variants incorporating the global-scale flow of meridional circulations have shaped our current views on solar and stellar magnetism. Other variants including α^2 and $\alpha^2\Omega$ dynamos are also proposed for the Sun and particularly for other stars (e.g., Küker & Rüdiger 1999, 2005b; Chabrier & Küker 2006).

Though instructive, these theories fall short in describing the fully nonlinear dynamo processes occurring in real stars. A fundamental assumption of mean-field theories is that the large-scale fields can be separated from the small-scale fluctuations, and in these theories the fluctuations are often assumed to scale in strength with the mean fields. In the turbulent environment of stellar convection, fields of all scales interact and are of similar magnitude, with strong local fluctuations that are not dependent on

the weaker large-scale fields. Major 3-D simulations (e.g., Brun et al. 2004; Browning et al. 2006) and observations suggest that, at least in the bulk of the convection zone, magnetism occurs over a broad range of scales with little separation between "mean" scales and fluctuations, and that the mean fields are not the dominant players in the overall magnetism. The impact of this lack of scale separation in both the magnetic and velocity fields is unclear and a subject of active research in both the dynamo and turbulence communities. As an additional concern, mean-field theory is fundamentally a linear theory, and while it can describe the initial growth of magnetic fields it cannot address their ultimate saturation as the fields strengthen and react back on the flows that create them. Some attempts have been made to include such nonlinear effects, with "α-quenching" and "Ω-quenching" terms added to the mean-field equations, but such treatments are fairly ad-hoc and the subject of substantial debate.

1.3 Exploring Magnetism in Other Stars

Our Sun is not the only magnetic star. Indeed, magnetism appears to be a ubiquitous feature in stars across the Hertzsprung-Russell (H-R) diagram. When our Sun was younger, it must have rotated much more rapidly, as is suggested both by the solar wind which continually removes angular momentum from the Sun and by many observations of rapidly rotating solar-like stars. Some of these young suns are observed to rotate as much as 50 times faster than the current solar rate. In more rapidly rotating suns the coupling between rotation and convection is strong and must continue to drive global scales of flow. These young solar-type stars, which rotate much more rapidly than the sun's current rate, possess much stronger magnetic activity.

Rotation appears to be inextricably linked to stellar magnetic activity. Observations indicate that in stars with extensive convective envelopes, chromospheric and coronal activity – which partly trace magnetic heating of stellar atmospheres – first rise with increasing rotation rate, then eventually level off at a constant value for ro-

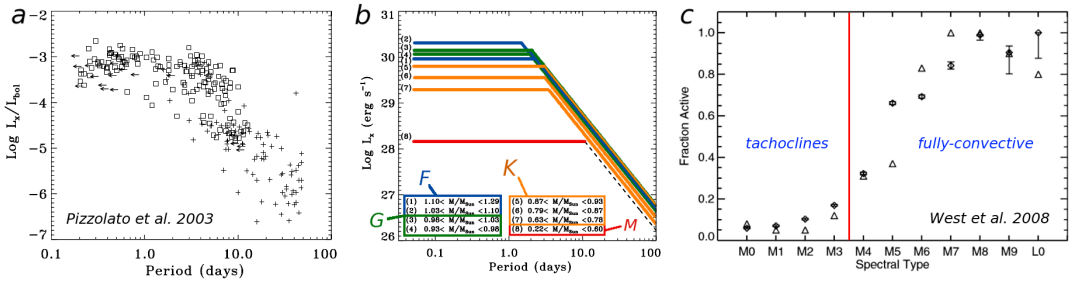

FIGURE 1.4 — Observational rotation-activity correlations in main-sequence stars. (a) X-ray activity measured by its luminosity L_x as a function of rotation period, showing growth and saturation phases of the relationship across broad populations of stars. (b) Different stellar types (approximately indicated) saturate at various levels of activity L_x and reach saturation at rotation rates dependent on spectral type. The growth of activity with more rapid rotation is similar in all G-, K- and M-type stars (adapted from Pizzolato et al. 2003). (c) Despite their lack of tachoclines, most fully-convective stars (types M3.5-M9) show signs of magnetic activity, here measured by Hα emission. Indeed, the fraction of active stars increases with decreasing mass (adapted from West et al. 2008).

tation rates above a mass-dependent threshold velocity (e.g., Noyes et al. 1984; Patten & Simon 1996; Delfosse et al. 1998; Pizzolato et al. 2003). Activity may even decline somewhat in the most rapid rotators (e.g., James et al. 2000). This rotation-activity correlation is shown in Figure 1.4a, b for a variety of solar-like stars. Similar correspondence is observed between rotation rate and estimates of the unsigned surface magnetic flux (Saar 1996, 2001; Reiners et al. 2009).

Global-scale magnetic activity has also been observed in the lower-mass main-sequence (dwarf) K- and M-type stars. Their convection zones occupy an increasingly large fraction of the interior and their tachoclines must play a diminishing role in the overall dynamics, being located in ever deeper regions of the star. Even fully convective stars, such as M-dwarfs with masses below 0.35 solar masses, show strong surface magnetism through observations of Hα emission (e.g., Hawley et al. 1996; Mohanty & Basri 2003; West et al. 2004, 2006, 2008) and magnetically sensitive FeH line ratios (Reiners & Basri 2007, 2008). Though these stars possess no tachoclines and should have distinctly different stellar dynamos than the sun, there is no observed break in magnetic activ-

ity with stellar type. Indeed, the fraction of magnetically active stars increases as the stellar mass decreases (Fig. 1.4*c*). These stars also show rotation-activity correlations.

Recent observations of magnetic fields in a fully convective M-dwarf by Donati et al. (2006) are raising further questions for stellar dynamo theory. There, Zeeman Doppler imaging is used to map the surface of the rapidly rotating and fully convective star v374 Peg. These observations indicate strong, organized axisymmetric fields that have strengths of a few kilo-Gauss but no surface differential rotation. The global-scale fields appear to be stable on one-year timescales (Morin et al. 2008). The stable axisymmetric nature of these fields is in striking contrast to theoretical predictions for fully convective stars (e.g., Küker & Rüdiger 1999, 2005b; Chabrier & Küker 2006). Observations of stellar magnetism are indirectly raising serious questions about the current paradigm of solar dynamo theory, where the tachocline is thought to play a crucial role in amplifying and organizing the global-scale fields and the radial velocity shear of differential rotation is a necessary ingredient for dynamo action.

The rotation-activity relationship is tightened across the full range of solar-like stars when stellar rotation is given in terms of the Rossby number $\mathrm{Ro} \sim P/\tau_c$, with P the rotation period and τ_c an estimate of the convective overturning time (e.g., Noyes et al. 1984). Expressed in this fashion, a common rotation-activity correlation appears to span spectral types ranging from late F to late M (e.g., Patten & Simon 1996; Mohanty & Basri 2003; Pizzolato et al. 2003; Reiners & Basri 2007). These stellar magnetic fields must be generated by dynamo action in the stellar convection zones. At present, the rotational dependence of this dynamo action is unknown. In mean-field theory, both generation terms are sensitive to rotation – the α-effect because it is proportional to the kinetic helicity of the convective flows, which sense the overall rotation rate, and the Ω-effect because more rapidly rotating stars are generally expected to have stronger differential rotation. But the detailed nature of these effects in the solar dynamo and the appropriate scaling with rotation has been very difficult to elucidate.

Rotation and stellar magnetism are inextricably linked, as the stronger magnetic fields in rapidly rotating stars are thought to produce a larger outward transport of angular momentum by the magnetized stellar winds, which slowly spin down the stars. (e.g., Weber & Davis 1967; Skumanich 1972; MacGregor & Brenner 1991; Matt & Pudritz 2008). The time needed for significant spindown appears to be a strong function of stellar mass (e.g., Barnes 2003; West et al. 2004). Solar-mass stars slow less rapidly than somewhat less massive G and K-type stars, but still appear to lose much of their angular momentum by the age of the Hyades (about 1 Gyr). They spin more slowly yet when they are as old as the Sun. Present day observations of the solar wind likewise indicate that the current angular momentum flux from the Sun is a few times 10^{30} dyne cm (e.g., Pizzo et al. 1983), suggesting a time-scale for substantial angular momentum loss of a few billion years. Analyses of stellar spindown as a function of age and mass have thus provided further constraints on stellar magnetism and its connections to rotation.

In addition, recent observations of solar-type stars suggest that the topology of the global-scale fields changes with rotation rate, with the rapid rotators having substantial global-scale toroidal magnetic fields at their surfaces (Petit et al. 2008). The overall picture that emerges from these observations is that rapid rotation, as realized in the younger Sun and in a host of other stars, can aid in the generation of strong magnetic fields, and that young stars tend to be rapidly rotating and magnetically active, whereas older ones are slower and less active (e.g., Barnes 2003; West et al. 2004, 2008).

A full theoretical understanding of the rotation-activity relationship, and likewise of stellar spindown, has remained elusive. Some aspects of these phenomena probably depend upon the details of magnetic flux emergence, chromospheric and coronal heating, and mass loss mechanisms – but the basic existence of a rotation-activity relationship is widely thought to reflect some underlying rotational dependence of the dynamo process itself (e.g., Knobloch et al. 1981; Noyes et al. 1984; Baliunas et al. 1996).

Research into the stellar magnetism of solar-like stars is timely. These lower-mass stars are the primary targets of the NASA Kepler mission and the ESA CoRoT satellite, which both seek to find the signatures of Earth-like planets orbiting other stars and to perform asteroseismology on some of these stars. These solar-like stars have large habitable zones and are the closest analogues to our own Sun and solar system. In the search for their possible life-bearing worlds, we will learn much more about their host stars. Kepler will observe about 10^5 stars over the course of the mission, searching for other Earths by the transit method. While searching for the slight dips in stellar light from these eclipses, the satellite will make detailed measurements of surface magnetic activity and differential rotation through high-precision photometry. For several hundred low-mass stars, Kepler will also carry out asteroseismology, which will yield new insights into the masses, sizes and ages of these stars, possibly along with measurements of their convection zone depths and internal rotation. Such observations are likely to lead to a renaissance in stellar physics, challenging our views on stellar structure, aging processes and stellar magnetism. A much better understanding of stellar magnetism and activity may well shed new light on the solar dynamo and may be crucial for reliably detecting distant Earths.

Probing the nature of these dynamos and the impact of faster rotation on the internal stellar dynamics requires both accurate observations and detailed dynamical models of the stellar interiors. The faster flows of differential rotation are much easier to detect than the relatively slow motions associated with meridional circulations; observations across the HR diagram indicate that differential rotation is a common feature in many stars. Asteroseismic observations with the Kepler and CoRoT missions may soon begin to constrain the internal rotation structure. At present only measurements of surface differential rotation are available, as assessed with a variety of techniques including photometric variability (Donahue et al. 1996; Walker et al. 2007), Doppler imaging (Donati et al. 2003) and Fourier transform methods (Reiners & Schmitt 2003).

At our current state of knowledge, stellar magnetism raises three fundamental questions, which missions like Kepler and CoRoT will begin to address in great observational detail

(1) Where are global-scale magnetic fields built and organized within the interiors of stars like our sun?

(2) Why is there a correlation between rotation rate and magnetic activity, and why is this behavior similar in stars with very different convection zone depths?

(3) What role do tachoclines play in stellar dynamos?

To probe these questions more deeply, we can now turn to simulations of magnetohydrodynamic (MHD) convection and dynamo action. These large computations must be carried out on supercomputers, and these theoretical tools are helping to sort out the mysteries of stellar magnetism.

1.4 Global Models of Stellar Dynamos

Advances in supercomputing have enabled three-dimensional (3-D) simulations that are beginning to capture many of the dynamical elements of the solar convection zone. Early global-scale simulations of solar convection by Gilman (1975, 1977, 1979) under the Boussinesq approximation were extended by the pioneering work of Gilman & Glatzmaier (1981). Such global-scale simulations of solar convection conducted in full spherical shells sought to capture the largest scales of convective flows and began to study how they can establish differential rotation and meridional circulations. However, the range of spatial and temporal scales present in solar convection are vast and thus the computational resources required by the modeling are daunting.

Through recent advances in massively parallel computer architectures, 3-D solar convection simulations are now beginning to make detailed contact with the observational constraints provided by helioseismology (e.g., Brun & Toomre 2002; Miesch et al.

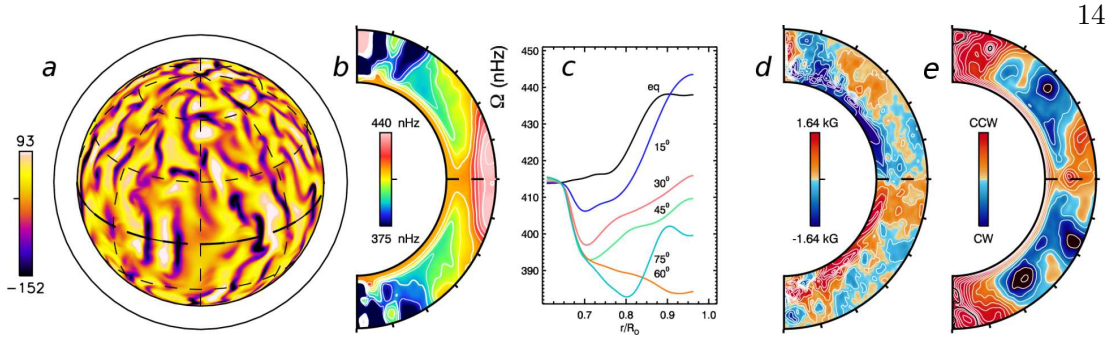

FIGURE 1.5 — Snapshot of 3-D ASH solar dynamo simulation which includes a tachocline. This layer of shear and penetration is located at the base of the convection zone. (*a*) Radial velocity in orthographic projection at 0.88 $R_\odot$, showing the north pole and equatorial regions with upflows in light tones and downflows in dark tones (scale in m/s). (*b*) Its mean profile of angular velocity $\Omega(r, \theta)$, with a solar-like differential rotation profile in the bulk of the convection zone and near uniform rotation in the deeper interior. (*c*) Radial cuts of Ω at selected latitudes. These simulations are beginning to capture in a self-consistent fashion the key ingredients of latitudinal and radial shear. (*d*) Profile of temporally- and azimuthally-averaged longitudinal magnetic field $\langle B_\phi \rangle$, with substantial mean field present in the tachocline and little in the convection zone above. (*e*) Accompanying mean poloidal field lines, with polarity indicated by color. These snapshots are from a model based on the simulation of Browning et al. (2006).

2006, 2008). Other efforts have focused on the vigorous turbulence and the dynamo action achieved in the bulk of the solar convection zone (Brun et al. 2004), with recent studies beginning to include the tachocline as a region of penetrative overshoot, shear, and magnetic field amplification (Browning et al. 2006). Facilitated by these computational advances, models of convection and dynamo action within the cores of A-type stars have also begun to be investigated (Browning et al. 2004; Brun et al. 2005; Featherstone et al. 2007, 2009), as have models of fully-convective M-dwarf stars (Browning 2008) and red giant branch stars (Palacios & Brun 2007; Brun & Palacios 2009).

To date, most models of stellar differential rotation and dynamo action in stars like our Sun that rotate more rapidly have been carried out in 2-D under the simplifying assumptions of mean-field theory (e.g., Rüdiger et al. 1998; Küker & Stix 2001; Küker & Rüdiger 2005a,b). The time is ripe to pursue the question with fully 3-D simulations of global-scale stellar convection.

Simulations of the global-scale solar dynamo have generally affirmed the view that the tachocline may play a central role in building the globally-ordered magnetism in the Sun. Early 3-D simulations of solar convection without a tachocline at the base of the convection zone achieved dynamo action and produced magnetic fields which were strongly dominated by fluctuating components with little global-scale order (Brun et al. 2004). When a tachocline of penetration and shear was included, remarkable global-scale structures were realized in the tachocline region, while the convection zone remained dominated by fluctuating fields (Browning et al. 2006). These results are illustrated in Figure 1.5.

These simulations are making good progress toward clarifying the elements at work in the operation of the solar global-scale dynamo, but for other stars many questions remain. In particular, observations of large-scale magnetism in fully convective M-stars (Donati et al. 2006), along with the persistence of a rotation-activity correlation in such low-mass stars, hint that perhaps tachoclines may not be essential for the generation of global-scale magnetic fields. This view is partly borne out by 3-D simulations of M-dwarfs under strong rotational constraints (Browning 2008), where strong longitudinal mean fields were realized despite the lack of either substantial differential rotation or a stable interior and thus no classical tachocline. Major puzzles remain in the quest to understand stellar magnetism and its scaling with stellar rotation.

With growing computational resources available, the time has come to extend these solar simulations to broader classes of stars. Such studies will enhance our understanding of stellar dynamo action, by making detailed contact with the evolving observations of stellar magnetism in stars like our sun. Studying dynamo action in other stars is likely to shine new light on the uncertain physical processes at work within the solar dynamo.

1.5 Convection and Dynamo Action in Rapidly Rotating Suns

Encouraged by the success of the solar simulations, we have begun exploring convection and dynamo action in younger and more rapidly rotating suns in this thesis. We have found that younger suns likely possess a much stronger differential rotation and that the flows of meridional circulation become weaker with more rapid rotation. At high rotation rates, the convection becomes strongly modulated in strength with longitude. Striking localized patterns of convection emerge at the equator, and these active nests of convection dominate the transport of heat and angular momentum in that region. At the highest rotation rates, the convection can be entirely confined to narrow intervals (or active nests) in longitude.

Modulated convection has persisted under more turbulent conditions and the active nests of convection appear in some dynamo simulations as well. When present, these nests of localized convection persist for long intervals of time and despite their small filling factor maintain a strong differential rotation. The emergence of spatially localized convective states has been observed in other systems, particularly in theoretical studies of doubly-diffusive systems such as thermosolutal convection (e.g., Spina et al. 1998; Batiste et al. 2006), in laboratory studies of convection in binary fluids (e.g., Surko et al. 1991), and in simulations of magnetoconvection where isolated "convectons" have been observed (Blanchflower 1999). In shells of rapidly rotating fluid, temporally intermittent patches of localized convection emerged in Boussinesq simulations of the geodynamo (Grote & Busse 2000) and in anelastic simulations of convection in young suns with much deeper convection zones (Ballot et al. 2006, 2007). In many of these systems, spatial modulation occurs in the weakly nonlinear regime close to the onset of convection. In contrast, our simulations of stellar convection in younger suns are in a regime of fully developed turbulent convection.

We have begun preliminary simulations of the dynamo action possible in these stars and have found several surprises. These MHD simulations span the convection zone alone, as the nature of tachoclines in more rapidly rotating suns is at present unclear. We find that a variety of dynamos can be excited, including steady and oscillating states, and that dynamo action is substantially easier to achieve at these faster rotation rates than in the solar simulations. Some of the oscillating simulations undergo quasi-regular global-scale polarity reversals, with the mean toroidal and poloidal fields exchanging polarities.

In these rapidly rotating solar-type stars, substantial global-scale organization of magnetic fields can occur in the middle of the convection zone. These wreaths of magnetism fill the convection zone and appear to be a general feature of our dynamos, appearing now in our solar dynamos as well. Generally, we find that the dynamos operating in the rapidly rotating suns may not require the presence of a tachocline, being able to instead organize global-scale fields in the bulk of their convection zones.

We describe briefly in Chapter 2 the 3-D magnetohydrodynamic anelastic spherical harmonic simulation code called ASH and the parameter space explored by our simulations that are carried out in spherical shells. In Chapter 3, we discuss the nature of convection realized in more rapidly rotating stars and the emergence of spatially-localized patterns of convection. Here we also examine the global-scale flows realized in our simulations, including differential rotation and meridional circulation, and their scaling with more rapid rotation. A more detailed exploration of the active nests of convection is presented in Chapter 4.

We then turn to dynamo simulations, examining in Chapter 5 the persistent wreaths of magnetism achieved in a rapidly rotating dynamo rotating at three times the current solar rate. In Chapter 6 we examine time-dependent behavior and organized global-scale polarity reversals in a dynamo rotating five times faster than the Sun. We return in Chapter 7 to the three solar dynamo with persistent magnetic wreaths and

examine how those global-scale structures are created and maintained. In Chapter 8 we explore the broad parameter space sampled by rapidly rotating dynamos spinning at up to fifteen times the solar rate. We find that magnetic wreaths are a nearly ubiquitous feature in all of these simulations. Here we also return to the Sun itself and find wreaths of magnetism as well. We further briefly consider convective and dynamo processes at work in older, more slowly spinning suns. In Chapter 9 we show preliminary results for wreath-building dynamos that include tachoclines of shear and penetration. We find that magnetic wreaths continue to fill the convection zone and undergo cycles of polarity reversal. Here we summarize our explorations of rapidly rotating dynamos and look to projects of the future.

Chapter 2

Elements in Modeling 3-D Stellar Convection and Dynamo Action

To study the coupling between rotation, magnetism and the large-scale flows achieved in stellar convection zones, we must employ a global model which simultaneously captures the spherical shell geometry and admits the possibility of zonal jets and large eddy vortices, and of convective plumes that may span the depth of the convection zone. The solar convection zone is intensely turbulent and microscopic values of viscosity and magnetic and thermal diffusivities in the Sun are estimated to be very small. Numerical simulations cannot hope to resolve all scales of motion present in real stellar convection and must instead strike a compromise between resolving dynamics on small scales and capturing the connectivity and geometry of the global scales. Here we focus on the latter by studying a full spherical shell of convection.

2.1 Anelastic MHD Formulation

Our tool for exploring MHD stellar convection is the anelastic spherical harmonic (ASH) code, which is described in detail in Clune et al. (1999). The implementation of magnetism is discussed in Brun et al. (2004). ASH solves the 3-D MHD anelastic equations of motion in a rotating spherical shell using the pseudo-spectral method and runs efficiently on massively parallel architectures. We use the anelastic approximation to capture the effects of density stratification without having to resolve sound waves which have short periods (about 5 minutes) relative to the dynamical time scales of the

global scale convection (weeks to months) or possible cycles of stellar activity (years to decades). This criteria effectively filters out the fast magneto-acoustic modes while retaining the slow modes and Alfvén waves. Under the anelastic approximation the thermodynamic fluctuating variables are linearized about their spherically symmetric and evolving mean state, with radially varying density $\bar{\rho}$, pressure $\bar{P}$, temperature $\bar{T}$ and specific entropy $\bar{S}$. The fluctuations about this mean state are denoted as ρ, P, T and S. In the reference frame of the star, rotating at average rotation rate Ω_0, the resulting MHD equations are:

$$\boldsymbol{\nabla} \cdot (\bar{\rho}\boldsymbol{v}) = 0\,, \tag{2.1}$$

$$\boldsymbol{\nabla} \cdot \boldsymbol{B} = 0\,, \tag{2.2}$$

$$\begin{aligned} \bar{\rho}\left[\frac{\partial \boldsymbol{v}}{\partial t} + (\boldsymbol{v}\cdot\boldsymbol{\nabla})\boldsymbol{v} + 2\boldsymbol{\Omega}_0 \times \boldsymbol{v}\right] = \\ -\boldsymbol{\nabla}(\bar{P}+P) + (\bar{\rho}+\rho)\boldsymbol{g} + \frac{1}{4\pi}(\boldsymbol{\nabla}\times\boldsymbol{B})\times\boldsymbol{B} - \boldsymbol{\nabla}\cdot\mathcal{D}, \end{aligned} \tag{2.3}$$

$$\frac{\partial \boldsymbol{B}}{\partial t} = \boldsymbol{\nabla}\times(\boldsymbol{v}\times\boldsymbol{B}) - \boldsymbol{\nabla}\times(\eta\boldsymbol{\nabla}\times\boldsymbol{B}), \tag{2.4}$$

$$\begin{aligned} \bar{\rho}\bar{T}\left[\frac{\partial S}{\partial t} + \boldsymbol{v}\cdot\boldsymbol{\nabla}(\bar{S}+S)\right] = \\ \boldsymbol{\nabla}\cdot\left[\kappa_r\bar{\rho}c_p\boldsymbol{\nabla}(\bar{T}+T) + \kappa_0\bar{\rho}\bar{T}\boldsymbol{\nabla}\bar{S} + \kappa\bar{\rho}\bar{T}\boldsymbol{\nabla}S\right] \\ +\frac{4\pi\eta}{c^2}\boldsymbol{j}^2 + 2\bar{\rho}\nu\left[e_{ij}e_{ij} - \frac{1}{3}(\boldsymbol{\nabla}\cdot\boldsymbol{v})^2\right], \end{aligned} \tag{2.5}$$

where $\boldsymbol{v} = (v_r, v_\theta, v_\phi)$ is the local velocity in the stellar reference frame, $\boldsymbol{B} = (B_r, B_\theta, B_\phi)$ is the magnetic field, $\boldsymbol{j}$ is the vector current density, $\boldsymbol{g}$ is the gravitational acceleration, c_p is the specific heat at constant pressure, κ_r is the radiative diffusivity and $\mathcal{D}$ is the viscous stress tensor, given by

$$\mathcal{D}_{ij} = -2\bar{\rho}\nu\left[e_{ij} - \frac{1}{3}(\boldsymbol{\nabla}\cdot\boldsymbol{v})\delta_{ij}\right], \tag{2.6}$$

where e_{ij} is the strain rate tensor. Here ν, κ and η are the diffusivities for vorticity, entropy and magnetic field. We assume an ideal gas law

$$\bar{P} = \mathcal{R}\bar{\rho}\bar{T}, \tag{2.7}$$

where $\mathcal{R}$ is the gas constant, and close this set of equations using the linearized relations for the thermodynamic fluctuations of

$$\frac{\rho}{\bar{\rho}} = \frac{P}{\bar{P}} - \frac{T}{\bar{T}} = \frac{P}{\gamma\bar{P}} - \frac{S}{c_p}. \tag{2.8}$$

The mean state thermodynamic variables that vary with radius are evolved with the fluctuations, thus allowing the convection to modify the entropy gradients which drive it.

The mass flux and the magnetic field are represented with a toroidal-poloidal decomposition as

$$\bar{\rho}\boldsymbol{v} = \quad \boldsymbol{\nabla} \times \boldsymbol{\nabla} \times (W\hat{r}) + \boldsymbol{\nabla} \times (Z\hat{r}), \tag{2.9}$$

$$\boldsymbol{B} = \quad \boldsymbol{\nabla} \times \boldsymbol{\nabla} \times (\beta\hat{r}) + \boldsymbol{\nabla} \times (\zeta\hat{r}), \tag{2.10}$$

with streamfunctions W and Z and magnetic potentials β and ζ. This approach ensures that both quantities remain divergence-free to machine precision throughout the simulation. The velocity, magnetic and thermodynamic variables are all expanded in spherical harmonics for their horizontal structure and in Chebyshev polynomials for their radial structure. The solution is time evolved with a second-order Adams-Bashforth/Crank-Nicolson technique.

ASH is a large-eddy simulation (LES) code, with subgrid-scale (SGS) treatments for scales of motion which fall below the spatial resolution in our simulations. We treat these scales with effective eddy diffusivities, ν, κ and η, which represent the transport of momentum, entropy and magnetic field by unresolved motions in the simulations. In these simulations ν, κ and η are taken for simplicity as functions of radius alone and are

proportional to $\bar{\rho}^{-1/2}$. This adopted SGS variation, as in Brun et al. (2004), Browning et al. (2006) and Ballot et al. (2007) yields lower diffusivities near the bottom of the layer and thus higher Reynolds numbers. In their stellar structure, our simulations here are similar to case AB as reported in Brun & Toomre (2002) though with a different SGS functional form (there $\nu, \kappa \propto \bar{\rho}^{-1}$), and here we shall consider the effects of faster Ω_0 (there $\Omega_0 = \Omega_\odot$). Acting on the mean entropy gradient is the eddy thermal diffusion κ_0 which is treated separately and occupies a narrow region in the upper convection zone. Its purpose is to transport entropy through the outer surface where radial convective motions vanish.

Our simulations are still separated by many orders of magnitude from the intensely turbulent conditions present within the solar convection zone. They are likely to capture many aspects of the dynamics of solar convection, and we are encouraged by the success that similar simulations (e.g., Miesch et al. 2000; Brun & Toomre 2002; Miesch et al. 2006, 2008) have had in beginning to match the detailed observational constraints for differential rotation within the solar convection zone provided by helioseismology (c.f. Thompson et al. 2003).

2.2 Boundary Conditions and Their Impacts

In this thesis we will explore how patterns of convection and dynamo-generated magnetism change in more rapidly rotating suns. In models of the solar dynamo, the magnetic fields observed at the surface are thought to be in the convection zone, with the tachocline of penetration and shear at the base of the convection zone possibly allowing field to be stored and organized on global-scales. The tachocline is a complex internal boundary layer. Below the tachocline lies the radiative zone, a region of stable stratification. Above it is the intensely turbulent and highly magnetized convection zone. Plunging downflows originating there splash into the tachocline, carrying magnetic field downwards and likely driving gravity waves and large-scale circulations. In the Sun, the

origin and maintenance of the tachocline remains unclear, but it seems likely that slow meridional circulations in that layer are crucial to its long term evolution. These flows likely have turnover times of millions of years while the fast downflows in the convection zone evolve on timescales of a few days.

In nearly all of the simulations contained in this thesis, we will explore dynamics within the convection zone only. Simulations which include model tachoclines are now being conducted in ASH, with the first simulations of the solar dynamo coupled to a tachocline reported on in Browning et al. (2006). Explorations that include a tachocline will be extended to the rapidly rotating suns in the future, and preliminary results for such a system will be shown in Chapter 9. However, the majority of our simulations here consist of spherical shells of convectively unstable fluid which capture the bulk of the solar convection zone in radius. We adopt boundary conditions appropriate to this region, and for now we neglect the region of penetration, shear and stable stratification at the base of the convection zone.

One area of focus in this thesis is the differential rotation which is naturally established within a shell of fluid that experiences no external torques. In these systems, convection and magnetism built by dynamo action act to redistribute angular momentum within the convection zone and establish gradients of angular velocity in both radius and latitude. Our velocity boundary conditions that are implemented in ASH are fairly straight forward and are chosen to eliminate external torques. The velocity boundary conditions imposed at the top and bottom of the convectively unstable shell are:

(1) Impenetrable top and bottom: $v_r = 0\,,$

(2) Stress-free top and bottom:

$$(\partial/\partial r)(v_\theta/r) = (\partial/\partial r)(v_\phi/r) = 0\,, \tag{2.11}$$

In recent solar simulations (Miesch et al. 2006, 2008) a latitudinal gradient of entropy has been imposed to mimic the balance likely achieved within the sub-adiabatic

tachocline. This modified boundary condition (with $S|_{\mathrm{r=r_{bot}}} = F(\theta)$ constant in time) slightly modifies the thermal wind balance achieved throughout the convection zone and can modify the profiles of differential rotation. The overall angular velocity contrast in latitude remains similar. Ballot et al. (2007) explored the consequences of such a boundary condition in one of their young, rapidly rotating suns with deep convection zones and found that the results were similar to those of Miesch et al. (2006). In these simulations of rapidly rotating suns however, we do not employ such a treatment. Instead, a latitudinal contrast in entropy is naturally established throughout the convection zone and at the bottom boundary by the convection itself. We make this choice because of our uncertainties about the structure of stellar tachoclines. In the case of the Sun, bounds can be placed on this thermal gradient from helioseismic observations of the tachocline.

In other stars we have no such asteroseismic observations of their tachoclines. In the more rapidly rotating suns, we thus do not yet know how the tachoclines scale with rotation rate, magnetic activity or stellar age. As such, the possible thermal structure of those tachoclines is poorly constrained. With these observational uncertainties in mind we choose constant flux thermal boundary conditions and allow the convection to establish its own gradients of entropy in latitude within the convection zone. The thermal boundary conditions at the top and bottom of the shell are thus

(3) Constant entropy gradient at top and bottom:

$$\partial(S + \bar{S})/\partial r = \text{const} . \tag{2.12}$$

2.3 Magnetic Boundary Conditions

The most natural choice for the magnetic boundary conditions is somewhat less clear, and thus deserves some detailed discussion. Typically in ASH we employ one of three treatments for magnetism at the boundaries. Those conditions are:

(4) Match to external potential field at top:

$$\boldsymbol{B} = \boldsymbol{\nabla}\Phi \quad \text{and} \quad \nabla^2\Phi = 0\big|_{r=r_{\rm top}}\,,$$

(5) Perfect conductor at bottom:

$$E_\theta = E_\phi = 0$$

$$B_r = (\partial/\partial r)(rB_\theta) = (\partial/\partial r)(rB_\phi) = 0\,, \tag{2.13}$$

(6) Radial field only at the boundary:

$$\boldsymbol{B} = B_r\,.$$

In our later discussions, it will be helpful to understand the impact of these different boundary conditions on the transport of angular momentum and energy through the boundary. We examine those properties for each boundary condition in turn.

2.3.1 Potential Field Boundaries

A potential field boundary condition is most appropriate when the region outside the boundary mimics a vacuum or other extremely good insulator. Under the potential field approach, no currents can cross the boundary, nor can currents be supported in the external volume. Magnetic fields can however extend out of the simulation, in a fashion the preserves $\boldsymbol{\nabla}\cdot\boldsymbol{B} = 0$. This boundary condition is most appropriate near the surface of the star, though it entirely neglects the dynamics present in the photosphere, as well as the complex balances achieved in the chromosphere of the star and the likely force-free corona. The dynamo simulations in this thesis use this as their upper boundary condition.

Our boundaries are impenetrable to the fluid motions, and thus the transport of energy by magnetism is from the Poynting flux. This flux is

$$F_{\rm Poynting} = S = \frac{c}{4\pi}\left(\boldsymbol{E}\times\boldsymbol{B}\right) = \frac{c}{4\pi}\Big(\left(-\boldsymbol{v}\times\boldsymbol{B} + \eta\boldsymbol{\nabla}\times\boldsymbol{B}\right)\times\boldsymbol{B}\Big)\,, \tag{2.14}$$

where we have used Ohm's law to replace the electric field. We are most interested in the flux of energy entering or leaving the volume, which is given by the radial flux at the boundary. This is

$$S_r = -\frac{c}{4\pi}\left(B_r \left(\boldsymbol{B}\cdot\boldsymbol{v}\right) + v_r \left(B^2\right) + \eta\Big(\left[\boldsymbol{\nabla}\times\boldsymbol{B}\right]\times\boldsymbol{B}\Big)_r \right), \tag{2.15}$$

where we use a vector identity to expand the first term in the electromotive force. Our impenetrable boundary conditions ensure that $v_r = 0$. Using this, and expanding the diffusion term we obtain

$$S_r = -\frac{c}{4\pi}\left(B_r \left(\boldsymbol{B}\cdot\boldsymbol{v}\right) + \eta\left(\left[\boldsymbol{\nabla}\times\boldsymbol{B}\right]_\theta B_\phi - \left[\boldsymbol{\nabla}\times\boldsymbol{B}\right]_\phi B_\theta \right) \right). \tag{2.16}$$

With a potential field boundary condition, $\boldsymbol{B} = \boldsymbol{\nabla}\Phi$ and $\boldsymbol{\nabla}\times\boldsymbol{B} = 0$, and thus the diffusive terms vanish. There is however radial field that can cross the boundary, and thus an overall energy flux of

$$S_r = -\frac{c}{4\pi} B_r \left(\boldsymbol{B}\cdot\boldsymbol{v}\right). \tag{2.17}$$

In these simulations, both the mean and fluctuating magnetic fields contribute to a Poynting flux through the boundary. The radial fields enter only through the B_r factor, as $v_r = 0$ at the upper surface. With stress-free boundary conditions, v_θ and v_ϕ are non-zero. The horizontal magnetic fields B_θ and B_ϕ can also be non-zero, though the azimuthally averaged longitudinal field is zero. This can be seen from

$$\langle B_\phi \rangle = \frac{1}{r\sin\theta}\frac{\partial}{\partial\phi}\langle\Phi\rangle = 0\,, \tag{2.18}$$

where angle brackets denote an average in longitude. This quantity is zero because there are no longitudinal gradients in the azimuthally averaged quantities by definition of the average.

There is clearly a fluctuating Poynting flux through a potential field boundary. Indeed, the horizontal fields can contribute to a mean Poynting flux through their correlation with the horizontal flows, and the colatitudinal field B_θ can contribute on both

mean and fluctuating scales, while the longitudinal field B_ϕ contributes only through correlations between the fluctuating fields and fluctuating velocities. This mean flux is given by

$$\langle S_r \rangle = -\frac{c}{4\pi}\Big(\langle B_r \rangle \Big(\langle B_\theta \rangle \langle v_\theta \rangle + \langle B'_\theta v'_\theta \rangle + \langle B'_\phi v'_\phi \rangle \Big) + \langle B'_r B'_\theta v'_\theta \rangle + \langle B'_r B'_\phi v'_\phi \rangle \Big) , \quad (2.19)$$

with fluctuating fields $\boldsymbol{B'} = \boldsymbol{B} - \langle \boldsymbol{B} \rangle$ and flows $\boldsymbol{v'} = \boldsymbol{v} - \langle \boldsymbol{v} \rangle$, with again $\langle \boldsymbol{B'} \rangle = \langle \boldsymbol{v'} \rangle = 0$ by definition. Generally, the total Poynting flux across a shell is very small, as local regions of inward and outward directed flux tend to cancel one another when an average is taken across both the northern and southern hemispheres.

The transport of angular momentum in the hydrodynamic simulations will be discussed later in detail in §3.4. In the dynamo simulations, the magnetic contribution to the radial angular momentum flux through a boundary is given by

$$F_r^{MS} = -\frac{r \sin\theta}{4\pi} \langle B'_r B'_\phi \rangle , \quad (2.20)$$

$$F_r^{MT} = -\frac{r \sin\theta}{4\pi} \langle B_r \rangle \langle B_\phi \rangle , \quad (2.21)$$

with F^{MS} the angular momentum transport from fluctuating Maxwell stresses and F^{MT} the transport by large-scale magnetic torques (Brun et al. 2004, 2005). At a potential field boundary, $\langle B_\phi \rangle = 0$, thus F^{MT} vanishes. In principle there could be a remaining flux from the fluctuating terms; in practice there is not. Locally there is a flux, but when integrated over a full shell F_r^{MS} is near zero. This is likely related to the nature of the external potential field. With no currents and no external forces, the external region is entirely connected to the simulation and there is no ability to remove angular momentum entirely from the coupled system.

2.3.2 Perfect Conductor Boundaries

A perfect conductor boundary condition is more appropriate when the external volume is filled with a plasma that is very highly conductive. This boundary condition prevents magnetic field from crossing the boundary, though currents can flow through. This boundary condition seems most appropriate at the bottom of the convection zone, and it appears that such a boundary condition is more in keeping with the internal boundary layer that forms when we capture a mock tachocline within our simulations (see §9.2). The dynamo simulations generally have perfectly conducting bottom boundaries.

Perfect conductor boundaries have no radial Poynting flux. To show this, we recall that the horizontal electric fields E_θ and E_ϕ vanish at the boundary, as does the radial magnetic field. Thus the radial Poynting flux is

$$S_r = \frac{c}{4\pi}\Big(E_\theta B_\phi - E_\phi B_\theta\Big) = 0\,. \tag{2.22}$$

We can see how this feeds into our magnetic boundary conditions by examining equation (2.16). At a perfect conducting boundary, that equation becomes

$$\begin{aligned} S_r &= -\frac{c}{4\pi}B_r\left(\boldsymbol{B}\cdot\boldsymbol{v}\right) + \frac{c}{4\pi}\frac{\eta}{r}\left(\left[\frac{1}{\sin\theta}\frac{\partial}{\partial\phi}B_r - \frac{\partial}{\partial r}(rB_\phi)\right]B_\phi - \left[\frac{\partial}{\partial r}(rB_\theta) - \frac{\partial}{\partial\theta}B_r\right]B_\theta\right) \\ &= -\,0 + \frac{c}{4\pi}\frac{\eta}{r}\left(\left[\,0 - \frac{\partial}{\partial r}(rB_\phi)\right]B_\phi - \left[\frac{\partial}{\partial r}(rB_\theta) - 0\,\right]B_\theta\right) = 0\,, \end{aligned} \tag{2.23}$$

and thus our requirement that $\partial/\partial r(rB_\theta) = \partial/\partial r(rB_\phi) = 0$ at a perfect conductor.

Perfect conducting boundaries also do not support a radial flux of angular momentum. This is guaranteed by the radial field vanishing at the boundary, which causes both F_r^{MS} and F_r^{MT} to vanish as well.

2.3.3 Radial Field Boundaries

The last boundary condition, that of a radial field only, is not used in these dynamo simulations, but has often been important in magnetoconvection studies where an external field is imposed. This boundary condition is numerically simple to implement and corresponds to a system where the external volume is a region of high magnetic permeability (e.g., Jackson 1998, pg. 194).

Radial field boundaries have no Poynting flux. The impenetrable condition for velocities ($v_r = 0$) eliminates the contribution from $B_r v_r$, and the lack of horizontal magnetic fields eliminates the radial component of $(\boldsymbol{\nabla} \times \boldsymbol{B}) \times \boldsymbol{B}$. Likewise, there is no angular momentum flux across this type of boundary. This results again from $\langle B_\phi \rangle = 0$ and $B'_\phi = 0$ at the boundary.

2.3.4 Magnetic Boundary Conditions and Effects on CFL Limits

The properties of our three possible boundary conditions are summarized in Table 2.1. To summarize, the perfectly conducting and radial field only boundary conditions do not permit a flux of energy or angular momentum across the boundary and thus in or out of the system. Potential field boundary conditions do permit a flux of energy and angular momentum, though the azimuthally-averaged magnetic fields do not contribute to the transport of angular momentum through the boundary. Generally, we find that the total flux of energy or angular momentum through a potential field boundary is small, as the contributions from the northern and southern hemispheres largely cancel each other. Horizontal magnetic fields are permitted near potential field boundaries and perfectly conducting boundaries, but are not permitted at a radial field only boundary. Likewise, radial magnetic fields can thread through the potential field boundaries and radial field only boundaries, but are not present at a perfectly conducting boundary.

Table 2.1. Properties of Magnetic Boundary Conditions

	Energy	Angular Momentum		Radial Alfvén CFL limited
Type	S_r	F_r^{MS}	F_r^{MT}	$v_a = \frac{B_r}{\sqrt{4\pi\bar{\rho}}}$
Potential Field	$-\frac{c}{4\pi}B_r(\boldsymbol{B}\cdot\boldsymbol{v})$	$-\frac{r\sin\theta}{4\pi}\langle B_r' B_\phi'\rangle$	0	yes
Perfect Conductor	0	0	0	no
Radial Field	0	0	0	yes

Note. — Boundary conditions affect the flux of energy and angular momentum in and out of the system. With some boundary choices the simulation may be CFL limited by Alfvén waves near the boundary.

The choice of magnetic boundary conditions can also have direct effect on the typical timesteps achieved by a simulation. Our simulations will become numerically unstable and diverge if we exceed the Courant-Friedrichs-Lewy (CFL) criteria by taking timesteps which are too large. Thus our our timesteps must be shorter than the the fastest flow of information between individual grid points. In dynamo simulations, this becomes an issue with boundary conditions that permit a radial magnetic field. Here, Alfvén waves traveling radially encounter the fine grid-spacing inherent to our Chebyshev expansion. The CFL timestep limit in the dynamo modeling is dominated by these relatively rapid waves and becomes

$$\tau = \alpha_0\,\tau_{\mathrm{CFL},\boldsymbol{B}} = \alpha_0\left(\frac{v_{A,r}}{\Delta r}\right) = \alpha_0\left(\frac{B_r}{\sqrt{4\pi\bar{\rho}}}\frac{1}{\Delta r}\right)\,, \tag{2.24}$$

with α_0 a safety factor which is slightly less than unity.

The limitation arises because we are able in these dynamo simulations to admit waves which propagate through the narrow grid near the boundaries. In contrast, our hydrodynamic simulations of stellar convection zones do not encounter a similar limitation, as v_r smoothly tends to zero as the boundary is approached, and typically decreases sufficiently quickly that the narrow grid spacing is not felt. Hydrodynamic simulations that include penetration into a stable layer may of course encounter similar

limitations when stacked Chebyshev domains are used to resolve the internal interface and where the radial motions are non-zero. In our dynamo simulations, the Alfvén wave CFL timestep, set by waves at the upper potential field boundary, can be one or two orders of magnitude more stringent than the limits set by either the convection or the Alfvén waves propagating in the rest of the domain. In a practical sense, this stringent CFL limit increases the computational cost of dynamo simulations with radial field or potential field boundaries by well over an order of magnitude compared to comparable hydrodynamic cases or dynamo cases with perfect conducting boundaries at top and bottom.

2.4 Approach to Hydrodynamic Simulations

Our numerical model is a relatively simple description of the solar convection zone that captures the essential spherical geometry and global connectivity of that domain. Solar values are taken for heat flux, mass and radius and a perfect gas is assumed. Near the solar surface the H and He ionization zones, coupled with radiative losses, drive intense convective motions on very small scales which appear at the surface as granulation. Capturing granulation in a global simulation would require spherical harmonic degrees of order 4000 and this is currently too demanding. We therefore position the top of our domain slightly below these ionization layers. In these simulations our lower boundary is positioned near the base of the convection zone, thus omitting the stably stratified radiative interior and the shear layer at the base of the convection zone known as the tachocline. We make this choice both because the nature of tachoclines in rapidly rotating stars is quite uncertain at present and because simulations that include penetration into a stable region are quite challenging in terms of computational resources.

Table 2.2. Parameters for Primary Hydrodynamic Simulations

Case	N_r, N_θ, N_ϕ	Ra	Ta	Re	Re$'$	Ro	Roc	ν	κ	$\Omega_0/\Omega_\odot$
G1	$96 \times 256 \times 512$	3.22×10^4	3.14×10^5	84	63	0.92	0.61	2.75	11.0	1
G2	$96 \times 256 \times 512$	1.75×10^5	3.21×10^6	205	85	0.55	0.45	1.72	6.87	2
G3	$96 \times 256 \times 512$	4.22×10^5	1.22×10^7	326	103	0.41	0.36	1.32	5.28	3
G4	$96 \times 256 \times 512$	7.89×10^5	3.18×10^7	433	119	0.33	0.31	1.09	4.36	4
G5	$96 \times 256 \times 512$	1.29×10^6	6.70×10^7	543	133	0.28	0.27	0.94	3.76	5
G7	$192 \times 512 \times 1024$	2.63×10^6	2.06×10^8	763	154	0.22	0.22	0.75	3.01	7
G10	$192 \times 512 \times 1024$	5.58×10^6	6.74×10^8	1051	188	0.17	0.18	0.59	2.37	10
G3a	$96 \times 256 \times 512$	7.83×10^5	2.41×10^7	528	158	0.50	0.34	0.94	3.76	3
G3b	$192 \times 256 \times 512$	2.26×10^6	8.02×10^7	1121	324	0.70	0.32	0.52	2.06	3
G5b	$192 \times 512 \times 1024$	4.03×10^6	2.23×10^8	1347	274	0.41	0.26	0.52	2.06	5

Note. — All simulations have inner radius $r_{\rm bot} = 5.0 \times 10^{10}$cm and outer radius of $r_{\rm top} = 6.72 \times 10^{10}$cm, with $L = (r_{\rm top} - r_{\rm bot}) = 1.72 \times 10^{10}$cm the thickness of the spherical shell. Evaluated at mid-depth are the Rayleigh number ${\rm Ra} = (-\partial\rho/\partial S)({\rm d}\bar{S}/{\rm d}r)gL^4/\rho\nu\kappa$, the Taylor number ${\rm Ta} = 4\Omega_0^2 L^4/\nu^2$, the rms Reynolds number ${\rm Re} = v_{\rm rms}L/\nu$ and fluctuating Reynolds number ${\rm Re}' = v'_{\rm rms}L/\nu$, the Rossby number ${\rm Ro} = \omega/2\Omega_0$, and the convective Rossby number ${\rm Roc} = ({\rm Ra/TaPr})^{1/2}$. Here the fluctuating velocity v' has the differential rotation removed: $v' = v - \langle v \rangle$, with angle brackets denoting an average in longitude. The Prandtl number ${\rm Pr} = \nu/\kappa$ is 0.25 for all simulations. The viscous and thermal diffusivity, ν and κ, are quoted at mid-depth (in units of 10^{12} cm^{2}s^{-1}). The rotation rate of each reference frame Ω_0 is in multiples of $\Omega_\odot = 2.6 \times 10^{-6}$ rad s^{-1} or 414 nHz. The viscous time scale at mid-depth $\tau_\nu = L^2/\nu$ is 1250 days for case G1 and is 3640 days for case G5. Additional cases considered other rotation rates at $1.25, 1.5, 1.75$ and 6 $\Omega_\odot$.

We focus here on the bulk of the convection zone, with our computational domain extending from $0.72R_\odot$ to $0.965R_\odot$, thus spanning 172 Mm in radius. The total density contrast across the shell is about 25. The reference or mean state of our thermodynamic variables is derived from a one-dimensional solar structure model (Brun et al. 2002) and is continuously updated with the spherically symmetric components of the thermodynamic fluctuations as the simulations proceed. These values are illustrated in Figure 2.1 after convection has readjusted the stratification.

Our hydrodynamic studies here explore a variety of solar-like stars rotating from 1 to 10 $\Omega_\odot$ (cases G1-G10). All cases use the same initial stellar structure. We seek to explore the general effects of rotation on stellar convection rather than the evolution of a particular star, which would require modifications to the stellar structure as the star aged. In surveying the effects of more rapid rotation on global-scale convection, we seek to achieve reasonably high levels of turbulence in the resulting flows. Thus our trajectory through the parameter space of Ω_0, ν, and κ attempts to maintain strong nonlinearity without having the increasing Ω_0 serve to laminarize the convection. As we increase the rotation rate, we simultaneously decrease the effective eddy diffusivities ν and κ to maintain the supercriticality of the simulated turbulent convection. We note that the critical Rayleigh number for the onset of convection scales with rotation as $\mathrm{Ra}_c \propto \mathrm{Ta}^{2/3} \propto \Omega_0^{4/3}\nu^{-4/3}$ for Boussinesq convection (e.g., Chandrasekhar 1961; Dormy et al. 2004). Lower diffusivities lead to both longer viscous and thermal diffusion time scales and to flows possessing finer spatial scales. Achieving equilibrated states in these systems requires high resolution simulations carried out over extended periods. We have taken a middle ground between attempting to maintain constant supercriticality (which may require scaling $\nu, \kappa \propto \Omega_0^{-2}$) and keeping resolution requirements reasonable by scaling our diffusivities as $\nu, \kappa \propto \Omega_0^{-2/3}$. All of our cases studied are highly supercritical, noting that the critical Rayleigh number for these simulations at 1 $\Omega_\odot$ is $\mathrm{Ra}_c \sim 1000$ (Gilman & Glatzmaier 1981; Miesch 1998). We have also maintained a constant Prandtl

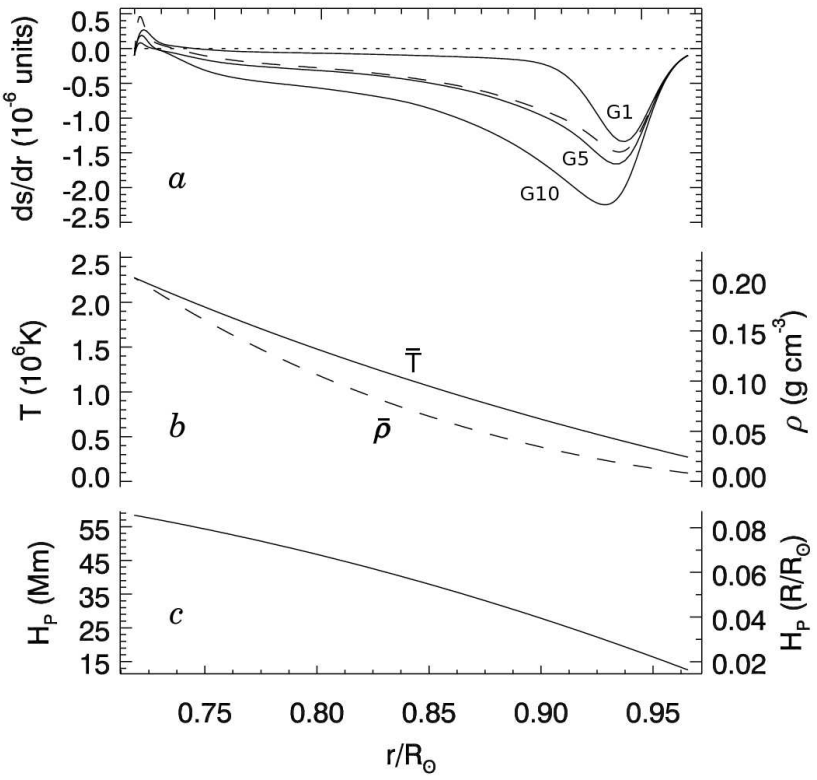

FIGURE 2.1 — Radial variation of mean stellar structure in the ASH models. (a) Entropy gradient ($\mathrm{d}\bar{S}/\mathrm{d}r$) for cases G1, G5 and G10 (as labeled). At higher rotation rates the entropy gradient becomes steeper throughout the convection zone, even for our most turbulent cases (case G5b, long dashes). (b) Temperature and density (latter ranging from 0.203 to 0.008 $\mathrm{g\,cm^{-3}}$ in the region simulated) for case G1. (c) Pressure scale height H_P (in Mm and fractional solar radii), for case G1, with cases G2-G10 similar in their mean stratification.

number $\mathrm{Pr} = \nu/\kappa = 0.25$ in all of our simulations. The parameters of our models are detailed in Table 2.2. Our choice of scalings for the eddy diffusivities with rotation rate may have some influence on the nature of the convective patterns and mean flows we achieve. To assess some of the sensitivity the choice of our path through parameter space, we have also sampled a limited range of more turbulent simulations at a few rotation rates (cases G3a, G3b and G5b).

Some of our simulations are initialized by perturbing a quiescent state in solid body rotation. The growth of convection leads to velocity correlations that serve to redistribute angular momentum within the shell, building a differential rotation and meridional circulation. We evolve the simulation for long periods compared variously to convective overturning times, rotation periods or typical diffusive times. Other simulations were started from these evolved states and then run for long intervals after all adjustments have been made to the frame rotation rate Ω_0 and to the viscous and thermal diffusivities.

All of the hydrodynamic simulations discussed in this thesis are at approximately the same level of maturity in their evolution. Case G1 was the progenitor case at 1 $\Omega_\odot$ and was evolved for some 3000 days after branching away from case AB from Brun & Toomre (2002), which itself has seen about 10000 days of total simulated life. Starting with this case, each subsequent simulation was spun up from the next fastest case (i.e., G3 was spun up from G2) and evolved for over 4000 days, or many hundreds of rotation periods.

The time evolution of case G5, which was started from an evolved state, is shown in Figure 2.2. At day zero the rotation rate Ω_0 and eddy diffusivities ν and κ are set to appropriate values for case G5. The convection responds and equilibrates to these changes on a timescale of a few hundred days but the mean flows of differential rotation and meridional circulation take significantly longer to fully equilibrate. As shown in Figure 2.2*b* the differential rotation can take nearly 4000 days to equilibrate. During

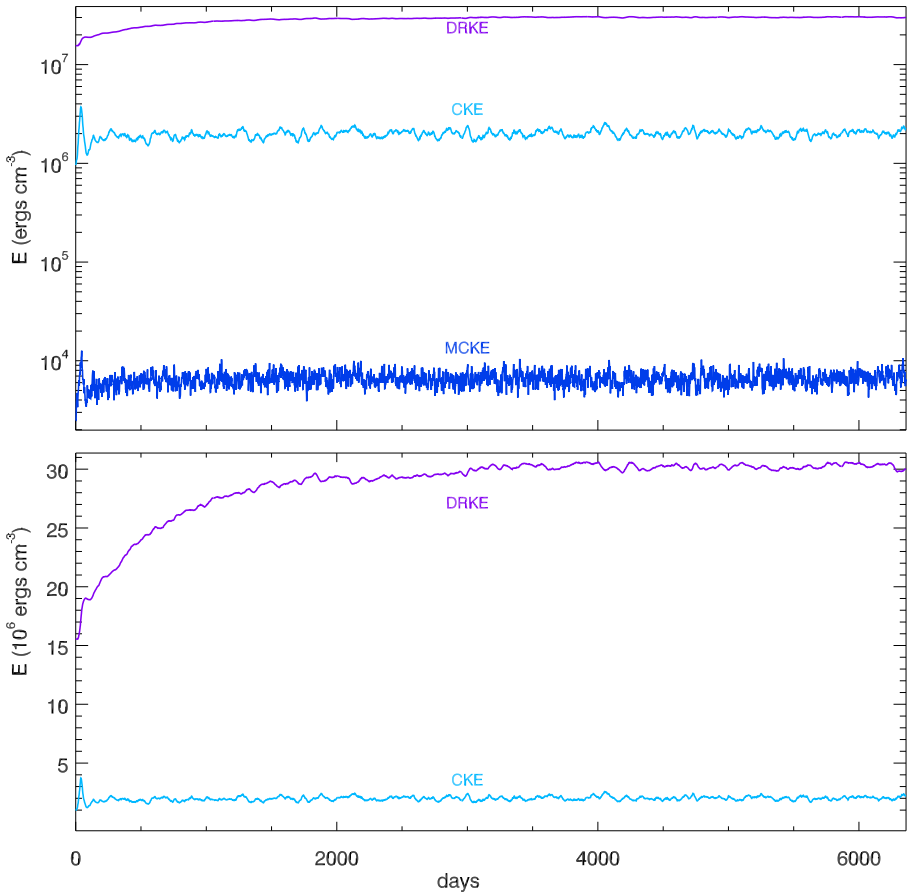

FIGURE 2.2 — Evolution of kinetic energies in hydrodynamic case G5. (*a*) Volume-averaged kinetic energy densities of differential rotation (DRKE), convection (CKE) and meridional circulations (MCKE) shown in logarithmic plot for the first 6500 days of the simulation. Convective kinetic energies adjust very quickly, but the energy of the mean circulations take longer to equilibrate. After approximately 4000 days all three energies have reached a stationary state. (*b*) Linear plot of evolving DRKE and CKE.

this interval the convection and meridional circulations are redistributing angular momentum and heat, building a latitudinal contrast of angular velocity and of temperature with hot poles, cool mid-latitudes and a warm equator (see Chapter 3). After 4000 days the profile of differential rotation remains nearly steady and we are able to explore the time evolution of the patterns of convection.

After similar intervals of evolution, all cases appear to be statistically stationary in terms of the angular momentum fluxes and the kinetic energies. We believe that the differential rotation profiles presented are effectively stationary, though there are small fluctuations as determined from short averages over a few rotation periods. Certain cases (including G5) were evolved for much longer intervals (over 10000 days and more than 2000 rotation periods) to explore the long-term behavior of convective patterns in these rapidly rotating systems. To test that our results are not unduly subject to hysteresis in the system, we explored a branch of cases which were successively spun down from 5 $\Omega_\odot$ to 1 $\Omega_\odot$. No significant hysteresis was found.

We shall discuss the properties of cases G1-G10 in Chapters 3 and 4, and there explore the nature of the convective patterns realized, as well as the differential rotation and meridional circulation that are achieved for a range of rotation rates.

2.5 Hydrodynamic Progenitors to Dynamo Simulations

The hydrodynamic progenitors used in our dynamo solutions are slightly different from the solutions presented as cases G1-G10. In conducting those hydrodynamic studies, we learned that at the highest rotation rates the unresolved flux carried out the top of the domain by κ_0 was beginning to imprint deeper into the convection zone. This occurs because $\mathrm{d}\bar{S}/\mathrm{d}r$ generally increases in amplitude in the more rapidly rotating simulations.

In most of the hydrodynamic simulations, the κ_0 diffusion term has the form

$$\kappa_0 = \kappa_{0,\mathrm{top}} \left(\frac{\bar{\rho}_{\mathrm{top}}}{\bar{\rho}} \right)^{\alpha} + \kappa_{0,\mathrm{C}} \tag{2.25}$$

with $\kappa_{0,\mathrm{top}}$ the diffusivity at the top boundary, and $\kappa_{0,\mathrm{C}}$ a small constant (of order $10^{10}\,\mathrm{cm}^2\,\mathrm{s}^{-1}$) added to smooth out potential spikes in $\mathrm{d}\bar{S}/\mathrm{d}r$ near the bottom of the convection zone, and α controlling the tapering of the unresolved flux in radius. The value of $\kappa_{0,\mathrm{top}}$ is chosen to transport a solar luminosity through the upper boundary, with

$$L_u\big|_{r=r_{\mathrm{top}}} = \left(4\pi r^2 \kappa_0 \bar{\rho} \bar{T} \boldsymbol{\nabla} \bar{S}\right)\big|_{r=r_{\mathrm{top}}} = L_\odot. \tag{2.26}$$

In all of these rapidly rotating simulations $\kappa_{0,\mathrm{top}} = 2.979 \times 10^{14}$, based on the self-consistently determined profiles of entropy, temperature and density within ASH.

In cases G1-G10, we chose $\alpha = 4$. Larger values of α lead to stronger confinement of the unresolved flux to the top of the convection zone, but also lead to heating within the entropy equation and modification of the entropy gradients. Thus, in cases H3 and H5, we chose $\alpha = 7$ to better confine the unresolved flux in a narrow upper boundary layer. As a result, this flux is largely confined within the upper 10% of the convection zone and shows only small variations with rotation rate.

In these cases the profile of $\mathrm{d}\bar{S}/\mathrm{d}r$ is somewhat steeper near the top of the convection zone. This effect is visible in Figure 2.3, where the stellar structure of cases H3 and H5 are compared with that in cases G3 and G5. The profiles of $\mathrm{d}\bar{S}/\mathrm{d}r$ come into good agreement at depths below $0.87R_\odot$ for both branches of simulations, but are deeper for cases H3 and H5 near the top of the convection zone. This leads to somewhat stronger driving of the convection as the Rayleigh numbers are also higher near the top of the domain. This partially explains why cases H3 and H5 have higher Reynolds numbers and higher Rossby numbers (Table 2.3) than cases G3 and G10 (Table 2.2). The effects of this are subtle, resulting primarily in slightly stronger latitudinal gradients of differential rotation and temperature in the uppermost regions of the shell.

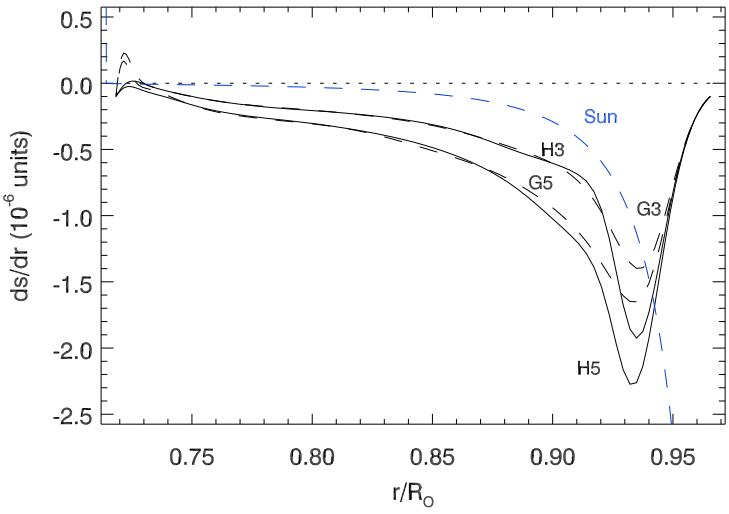

FIGURE 2.3 — Radial structure of dynamo progenitor simulations. Shown is the entropy gradient ($\mathrm{d}\bar{S}/\mathrm{d}r$) for dynamo progenitor cases H3 and H5 (solid lines) compared with hydrodynamical cases G3 and G5 (dashed lines). The entropy gradient in the dynamo progenitor cases is somewhat steeper throughout the convection zone, and the minimum is deeper. This leads to higher Rayleigh numbers in these simulations and stronger driving. Though the convection is driven more strongly, the temperature, density and pressure profiles are nearly identical to those shown in Figure 2.1. Overlain with a blue, dashed line is a 1-D solar structure model computed with the CESAM code by Brun et al. (2002).

The entropy gradient from a 1-D, helioseismically-constrained solar structure model is also shown in Figure 2.3. The equilibrated profiles of $\mathrm{d}\bar{S}/\mathrm{d}r$ in ASH tend to be somewhat steeper than the solar model at depths below $0.95\,R_\odot$ and significantly shallower in the upper convection zone. The large change in $\mathrm{d}\bar{S}/\mathrm{d}r$ between about $0.93\,R_\odot$ and the surface appears to result from heating in that layer by our adopted unresolved flux. New simulations are now being explored in ASH, with different treatments of the unresolved flux, and these models appear able to better match the structure of $\mathrm{d}\bar{S}/\mathrm{d}r$ from the solar model. Here however, all of our simulations have $\mathrm{d}\bar{S}/\mathrm{d}r$ profiles akin to those illustrated in Figure 2.3.

Convective structures in these hydrodynamic progenitor cases are similar to those realized in cases G1-G10, though the patterns tend to be slightly more complex near the top of the shell. The patterns of convection for cases G5 and H5 are shown in Figure 2.4. Shown in global Mollweide projection are radial velocities at a radius of $0.95\,R_\odot$ and near the upper boundary. These cases were well evolved and possess intricate convective patterns and solar-like differential rotation profiles, with fast zonal flow at the equator and slower flows at the poles. The prominent modulation visible in case G5 (Fig. 2.4*a*) is less visible in case H5. Here in case H5 fine-scaled convection has filled in the regions between the patches and obscures the modulation. These modulated convective states, called active nests of convection, will be explored in detail in Chapter 4 for case G5 and G10. Time-longitude maps indicate that these structures are still present in case H5 and remain comparable in amplitude to those seen in case G5.

Ultimately, these changes in stratification are modest compared to the overall structure of the star. As such, the profiles of density, temperature and pressure are nearly unaffected by the changes in the entropy gradient.

2.6 Studies of Dynamo Action in Rapidly Rotating Suns

We have explored a number of dynamo scenarios in our rapidly rotating suns. Two solutions, one rotating at three times the current solar rate ($3\,\Omega_\odot$) and one rotating five times the solar rate ($5\,\Omega_\odot$), will be the primary focus of our discussion of dynamo action in Chapters 5, 6 and 7. We begin here by discussing the basic formulation of the dynamo studies. The parameter space explored by our broader family of dynamos will be discussed in turn in Chapter 8.

The dynamo simulations were initiated from mature hydrodynamic progenitor cases which had been evolved for at least 5000 days at each rotation rate and were well equilibrated. Our simulations at three and five times the solar rate $\Omega_\odot$ lie again on a path where the SGS diffusivities ν, κ and η decrease as $\Omega_0^{-2/3}$, in order to maintain vigorous

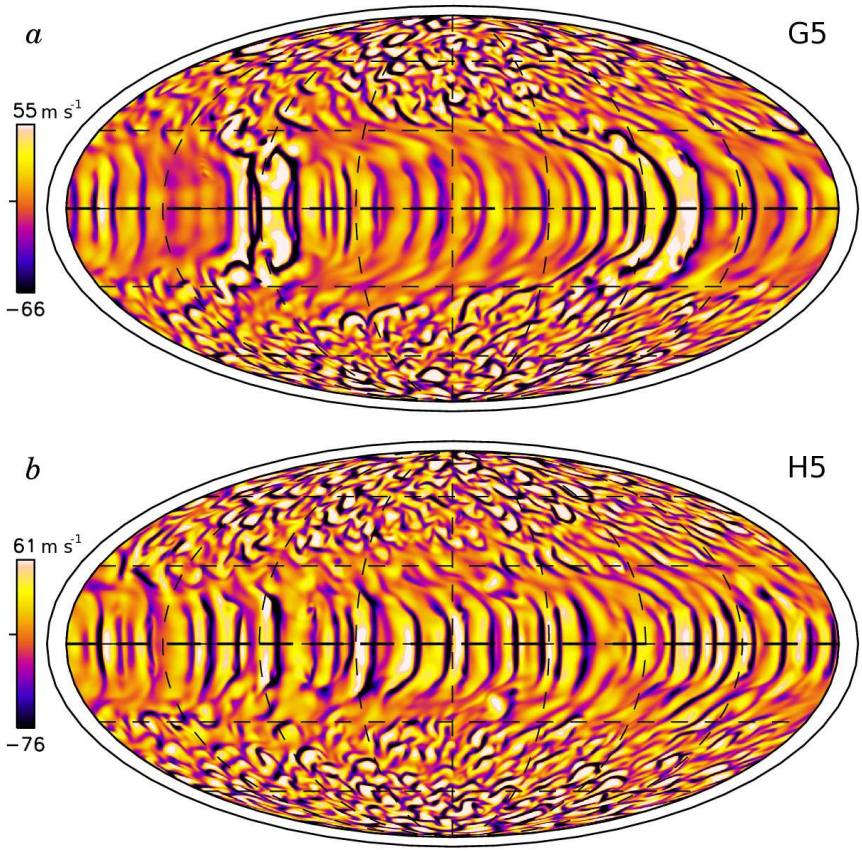

FIGURE 2.4 — Patterns of convection in cases G5 and H5. (*a*) Snapshot of radial velocity v_r in global Mollweide projection for case G5 near the upper boundary ($0.95\,R_\odot$) with scale indicated. Downflows are dark and narrow, while upflows are broad and indicated by light tones. A prominent modulation in longitude is visible near the equator. These active nests of convection persist for thousands of days. (*b*) Radial velocities in case H5 at same depth, showing somewhat more vigorous convection. Here the active nests are obscured by the finer-scale convection but are still visible over long intervals of time.

convection as rotation attempts to constrain and quench the motions. The fundamental characteristics of our primary dynamo simulations and their hydrodynamic progenitors are summarized in Table 2.3; other cases will be defined in Chapter 8.

To initiate our dynamo cases, a small seed dipole magnetic field was introduced and evolved via the induction equation. The time evolution of magnetic and kinetic energies is presented for case D3 in Figure 2.5. Here and throughout the thesis, day 0 refers to the last adjustments made to the simulation (generally to the rotation rate Ω_0 and eddy diffusivities ν, κ and η). This time-trace shows about 7000 days of simulated time throughout the history of the dynamo. As shown, the energy in the magnetic fields is initially many orders of magnitude smaller than the energy contained in the convective motions. These fields are amplified by shear and grow to become comparable in energy to the convective motions. Generally the dynamos spend about 2000 days reaching fully equilibrated states.

These dynamo simulations are computationally intensive, requiring both high spatial resolution to correctly represent the velocity fields and long time evolution to capture the equilibrated dynamo behavior, which may include cyclic variations on time scales of hundreds to thousands of days. The strong magnetic fields can produce rapidly moving Alfvén waves which seriously restrict the Courant-Friedrichs-Lewy (CFL) timestep limits in the upper portions of the convection zone. Case D3, rotating three times faster than the current Sun, has been evolved for over 7000 days (or over 2 million timesteps with typical timesteps of 300 seconds), and case D5, rotating five times faster than the Sun, has seen more than 17000 days of evolution (representing more than 10 million timesteps, with typically 140 seconds of evolution per timestep).

These two cases were conducted at magnetic Prandtl number $\mathrm{Pm} = \nu/\eta = 0.5$, a value significantly lower than employed in our previous solar simulations. In particular, Brun et al. (2004) explored $\mathrm{Pm} = 2, 2.5$ and 4, and Browning et al. (2006) studied $\mathrm{Pm} = 8$. The high magnetic Prandtl numbers were required in the solar simulations to

Table 2.3. Parameters for Primary Dynamo Simulations

Case	N_r, N_θ, N_ϕ	Ra	Ta	Re	Re′	Rm	Rm′	Ro	Roc	ν	η	$\Omega_0/\Omega_\odot$
D3	$96 \times 256 \times 512$	3.22×10^5	1.22×10^7	173	105	86	52	0.378	0.311	1.32	2.64	3
D5	$96 \times 256 \times 512$	1.05×10^6	6.70×10^7	273	133	136	66	0.273	0.241	0.940	1.88	5
H3	$96 \times 256 \times 512$	4.10×10^5	1.22×10^7	335	105	—	—	0.427	0.353	1.32	—	3
H5	$96 \times 256 \times 512$	1.27×10^6	6.70×10^7	576	141	—	—	0.303	0.268	0.940	—	5

Note. — Dynamo simulations at three and five times the solar rotation rate are cases D3 and D5, and their hydrodynamic (non-magnetic) companions are H3 and H5. All simulations have inner radius $r_{\rm bot} = 5.0 \times 10^{10}$cm and outer radius of $r_{\rm top} = 6.72 \times 10^{10}$cm, with $L = (r_{\rm top} - r_{\rm bot}) = 1.72 \times 10^{10}$cm the thickness of the spherical shell. Evaluated at mid-depth are the Rayleigh number ${\rm Ra} = (-\partial\rho/\partial S)({\rm d}\bar{S}/{\rm d}r)gL^4/\rho\nu\kappa$, the Taylor number ${\rm Ta} = 4\Omega_0^2L^4/\nu^2$, the rms Reynolds number ${\rm Re} = v_{\rm rms}L/\nu$ and fluctuating Reynolds number ${\rm Re}' = v'_{\rm rms}L/\nu$, the magnetic Reynolds number ${\rm Rm} = v_{\rm rms}L/\eta$ and fluctuating magnetic Reynolds number ${\rm Rm}' = v'_{\rm rms}L/\eta$, the Rossby number ${\rm Ro} = \omega/2\Omega_0$, and the convective Rossby number ${\rm Roc} = ({\rm Ra}/{\rm Ta}\,{\rm Pr})^{1/2}$. Here the fluctuating velocity v' has the axisymmetric component removed: $v' = v - \langle v\rangle$, with angle brackets denoting an average in longitude. For all simulations, the Prandtl number ${\rm Pr} = \nu/\kappa$ is 0.25 and the magnetic Prandtl number ${\rm Pm} = \nu/\eta$ is 0.5. The viscous and magnetic diffusivity, ν and η, are quoted at mid-depth (in units of 10^{12} cm^{2}s^{-1}). The rotation rate Ω_0 of each reference frame is in multiples of the solar rate $\Omega_\odot = 2.6 \times 10^{-6}$ rad s^{-1} or 414 nHz. The viscous time scale at mid-depth $\tau_\nu = L^2/\nu$ is 3640 days for case D5 and the resistive time scale is 1820 days. Rotation periods at three and five times the solar rate are in turn 9.3 days and 5.6 days.

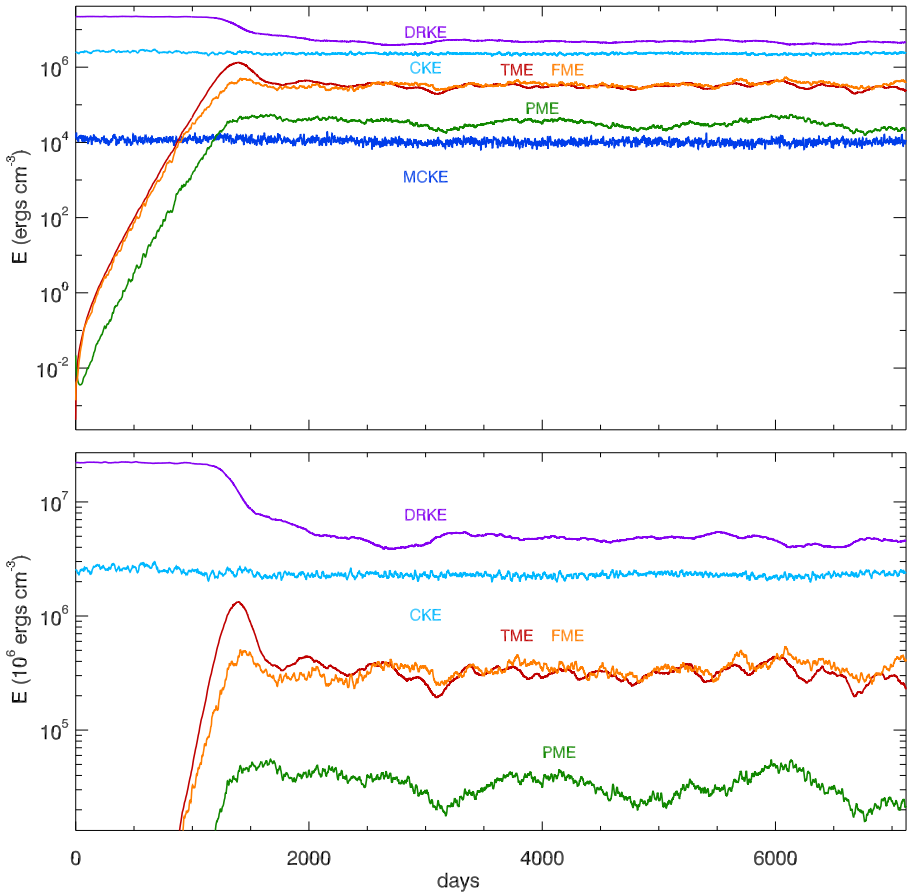

FIGURE 2.5 — Evolution of kinetic and magnetic energies in dynamo case D3. (*a*) Volume-averaged kinetic energy densities of differential rotation (DRKE), convection (CKE) and meridional circulations (MCKE) shown in logarithmic plot. Magnetic energy densities in fluctuating magnetic fields (FME), mean toroidal fields (TME) and mean poloidal fields (PME) are shown growing from an initial seed field. The dynamo saturates after roughly 1700 days. After saturation, DRKE has changed substantially but CKE and MCKE are largely unaffected. (*b*) Zoom in logarithmic plot of evolving kinetic and magnetic energies, emphasizing their behavior after saturation. Time is counted from day 0, when the last adjustments were made to parameters controlling the simulation (i.e. Ω_0, η, etc.).

reach sufficiently high magnetic Reynolds numbers to drive sustained dynamo action. In the simulations of Brun et al. (2004) only the simulations with Pm > 2.5 and $\mathrm{Rm}' \gtrsim 300$ achieved sustained dynamo action, where Rm' is the fluctuating magnetic Reynolds number. We are here able to use a lower magnetic Prandtl number for three reasons. Firstly, more rapid rotation tends to stabilize convection and lower values of ν and η are required to drive the convection. Once convective motions begin however they become quite vigorous and the fluctuating velocities saturate at values comparable to our solar cases. Thus the Reynolds numbers achieved are fairly large and we can achieve modestly high magnetic Reynolds numbers even at low Pm. Secondly, the differential rotation becomes substantially stronger with both more rapid rotation Ω_0 and with lower diffusivities ν and η. This global-scale flow is an important ingredient and reservoir of energy for these dynamos, and the increase in its amplitude means that low Pm dynamos can still achieve large magnetic Reynolds numbers based on this zonal flow. Thirdly, the critical magnetic Reynolds number for dynamo action likely decreases with increasing kinetic helicity (e.g., Leorat et al. 1981). Helicity generally increases with rotation rate (e.g., Käpylä et al. 2009), so the rapidly rotating flows considered here achieve dynamo action at somewhat lower Rm than the models of Brun et al. (2004), which rotated at the solar rate.

Case D3, which builds persistent wreaths of magnetism, is presented in Chapter 5. Case D5 at five times the solar rate has time-dependent wreaths that flip global-scale polarity and is presented in Chapter 6. An analysis of terms contributing to building and destroying the persistent magnetic fields is carried out for case D3 in Chapter 7. A variety of other dynamo cases, some at higher turbulence levels and rotation rates, will be in turn discussed in Chapter 8.

Chapter 3

Convection in Rapidly Rotating Younger Suns

We begin our exploration of convection and dynamo action in rapidly rotating suns with a series of hydrodynamic simulations which sample rotation rates between $1-10\,\Omega_\odot$. These correspond to cases G1-G10 in Table 2.2. In these systems, we explore how the patterns of convection are modified by more rapid rotation. We study the resulting differential rotation and meridional circulation and their scaling with rotation rate. In Chapter 4 we examine how novel modulated patterns of convection arise in the most rapidly rotating simulations.

These two chapters are based on work published in Brown et al. (2008)[1] and are largely a restatement of that paper. As the primary author of this paper, I conducted the simulations presented here, performed the analysis and wrote the text. My co-authors provided advice and guidance throughout the process, helping frame the questions which form the core of the study. Preliminary versions of these results have been presented in Brown et al. (2004), Brown et al. (2006), Brown et al. (2007a), and Brown et al. (2007d).

3.1 Early Results of Modulated Convection

In our early simulations of rapidly rotating suns we found that strongly localized states of convection emerged with more rapid rotation (Brown et al. 2004). A selection

[1] Brown, B. P., Browning, M. K., Brun, A. S., Miesch, M. S., & Toomre, J., 2008, "Rapidly Rotating Suns and Active Nests of Convection", *ApJ*, 689, 1354–1372.

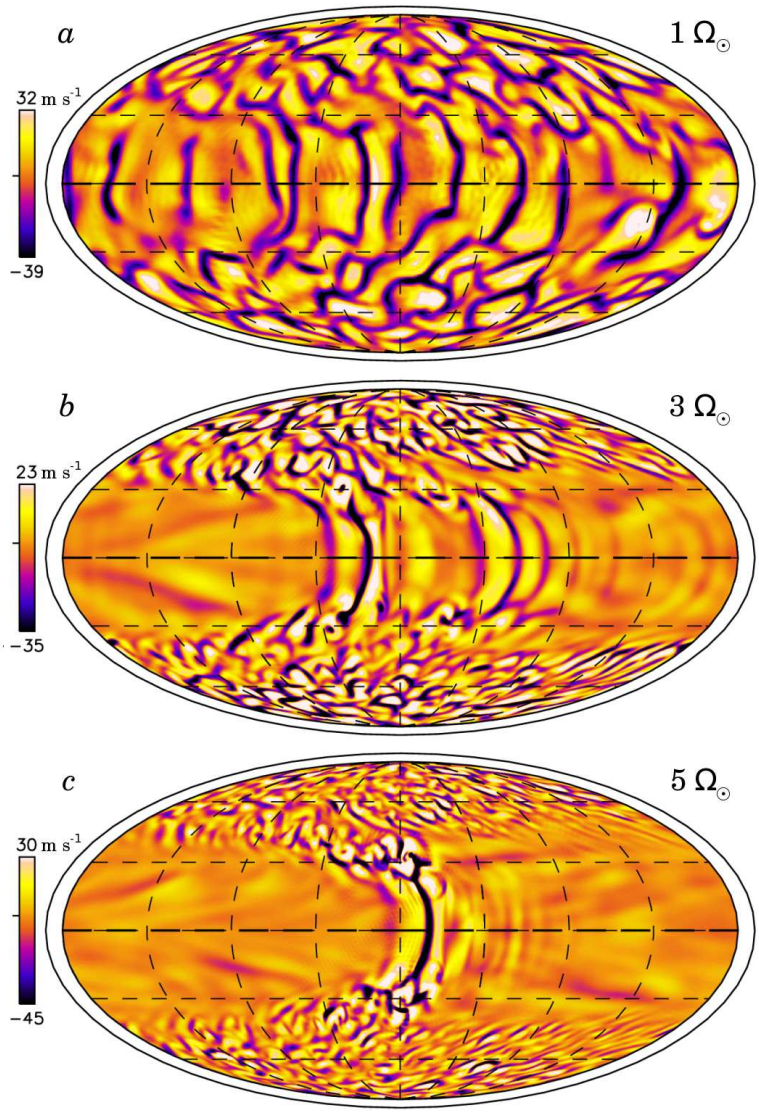

FIGURE 3.1 — Convective patterns in mildly turbulent simulations. Cases shown are rotating at (*a*) one, (*b*) three and (*c*) five times the solar rate. Shown as snapshots are radial velocities near top of layer in global Mollweide projection, with upflows light and downflows dark (scaling indicated by accompanying colorbars). Poles are at top and bottom, and the equatorial region appears at middle, with equator indicated by bold dashed line. Thin dashed lines denote circles of constant latitude or longitude, and the thin surrounding line indicates the location of the stellar surface at $R_\odot$. A striking pattern of convection localized into nests near the equator emerges as the rotation rate increases.

of these simulations in Figure 3.1 present snapshots of radial velocity near the top of the domain in global Mollweide projection, showing the entire spherical surface with minimal distortion. With more rapid rotation, a prominent longitudinal modulation appears in the patterns of equatorial convection. At the higher rotation rates the equatorial convection is confined to one or two nests, with streaming zonal flow filling the regions outside these nests of convection. These nests can persist for intervals spanning many hundreds of rotation periods, often with little change. Two nest states sometimes evolve into single nest states as one nest overtakes another.

The simulations shown in Figure 3.1 are less turbulent than the cases presented in the rest of this chapter, each possessing Reynolds numbers that are about three-fold smaller near the surface than in our new simulations. In these early models, a large portion of the energy transport in the upper convection zone was carried by unresolved scales of motion. This parametrized SGS flux, represented by κ_0, dominated transport in the upper 30% of the convection zone, leading to weaker enthalpy transport and weaker resolved convection there. This parametrized flux acts as a volume cooling term that removes flux from the regions where it is dominant; the dynamics were influenced by the presence of this cooling layer. The cases presented in detail in this chapter have a narrower unresolved flux layer, confined now to the upper 10% of the convection zone, and consequently much more vigorous convection is realized throughout the domain. In these more turbulent cases, the phenomena of localized nests of convection is realized at somewhat higher rotation rates.

3.2 Convective Patterns and Evolution with Rotation

The variation of convective patterns with increasing rotation rate Ω_0 in our more rapidly rotating suns is illustrated in Figure 3.2. Snapshots of the radial velocity near the top of the domain ($0.95R_\odot$) are shown in Mollweide projection for four cases: G1, G3, G5 and G10. The convection patterns are complex and time dependent, with

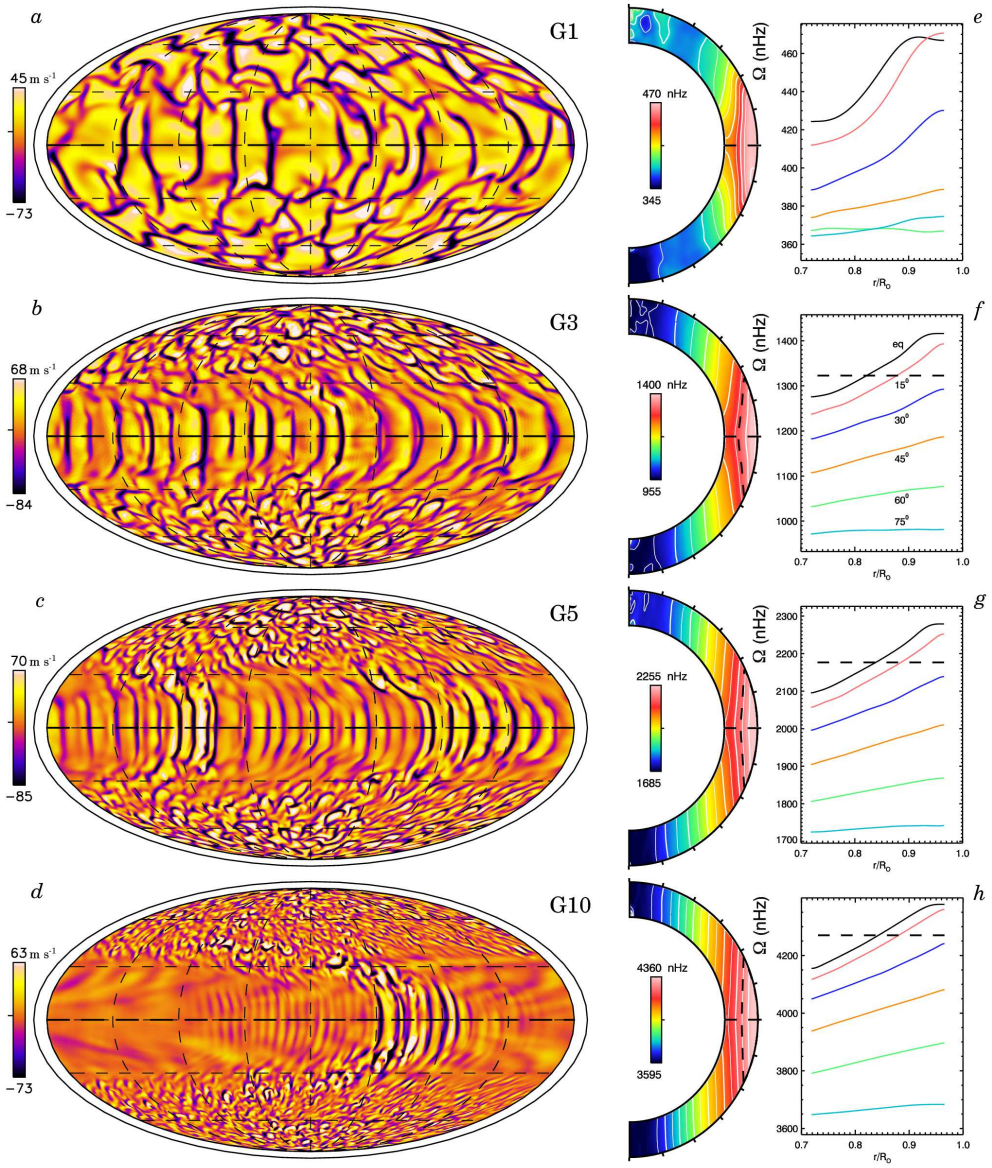

FIGURE 3.2 — Convective patterns in primary hydrodynamic cases. Shown are radial velocity patterns in Mollweide projection at $0.95R_\odot$ (left) and differential rotation profiles (middle, right) with increasing rotation rate in (a, e) for case G1, (b, f) for G3, (c, g) for G5, and (d, h) for G10. At higher rotation rates the horizontal scale of convective cells shrinks at all latitudes and cells are more strongly aligned with the rotation axis. A striking pattern of modulated convection emerges at low latitudes with faster rotation, consisting of spatially modulated or patchy convection. These active nests of convection are propagating structures which persist for long periods of time. At middle are profiles of mean angular velocity Ω with radius and latitude. These differential rotation profiles all involve fast equators (prograde relative to the frame rate Ω_0, indicated by tickmark on scale) and a monotonic decrease of Ω as the poles are approached. At right are radial cuts of the angular velocity at selected latitudes, as labeled. The dark dashed contour denotes the constant propagation rate of the nests where discernible.

asymmetries between the upflows and downflows owing to the density stratification. Thus narrow, fast downflow lanes are surrounded by broad, relatively weak upflows.

There is a clear difference in both the scale and structure of convection at high and low latitudes. In the equatorial regions (roughly $\pm 30^\circ$ in latitude), the downflows organize into large structures (loosely called banana cells) aligned with the rotation axis, thus extending in the north-south direction. At high rotation rates this tendency for alignment becomes pronounced, largely in the spirit of the Taylor-Proudman theorem, and the downflow network exhibits little of the east-west branching visible in case G1. These downflow lanes propagate in a prograde sense relative to the bulk rotation rate and do so more rapidly than the differential rotation which they themselves establish. The nests of convection, when they appear at the higher rotation rates, propagate at an intermediate rate as denoted by the heavy dashed contours in Figure $3.2f-h$. We defer discussion of the nature of these nests of convection to Chapter 4. Individual convective cells persist for about 10 to 30 days.

In the higher latitude regions, the convection cells are more isotropic and the downflow network organizes on smaller scales. Convection in these regions is vigorous and complex, with upflows and their downflow networks in a constant dance. The convective cells have a cusped appearance, with downflows leading upflows as both propagate in a retrograde fashion (most apparent in Figs $3.2b, c$). Strong vortical plumes form in the interstices of the downflow network at both high and low latitudes. In the polar regions above the middle of the convection zone, the sense of vorticity in these downflow plumes is generally cyclonic: counterclockwise in the northern hemisphere and clockwise in the southern. As they descend through the mid-layer their vorticity changes and they become largely anti-cyclonic. In contrast, the polar upflows are anti-cyclonic at all depths.

The latitudinal variation of convection patterns can be in part understood by considering a cylinder tangent to the base of the convection zone and aligned with the rotation axis. Within our geometry, this tangent cylinder intersects the outer boundary at about $\pm 42^{\circ}$ of latitude. It is well known that in a rotating convective shell the flow dynamics are different inside and outside of the tangent cylinder, owing to differences in the connectivity of the flows, the influence of the Coriolis forces and distance from the rotation axis (e.g., Busse 1970). These differences become more evident as the rotation rate, and hence the rotational constraints on the convection, increases. With more rapid rotation the longitudinal extent of the convective cells becomes progressively smaller. Linear theory, in the Boussinesq approximation, predicts that the wavenumber of the most unstable mode scales with rotation as $m \propto \mathrm{Ta}^{1/6} \propto \Omega_0^{1/3} \nu^{-1/3}$ (e.g., Chandrasekhar 1961; Dormy et al. 2004) for polar and equatorial convection. This effect is found in anelastic systems as well (Glatzmaier & Gilman 1981) and in our simulations is evident at both high and low latitudes.

Shown at right in Figures $3.2e-h$ are the profiles of differential rotation (as angular velocity Ω) realized in these simulations. These $\Omega(r, \theta)$ profiles are azimuthally and temporally averaged over a period of roughly 200 days. All of our more rapidly rotating stars exhibit solar-like differential rotation profiles, with prograde (fast) equators and retrograde (slow) poles. Contours of constant angular velocity are aligned nearly on cylinders, influenced by the Taylor-Proudman theorem, though recent simulations of solar convection suggest that this is sensitive to the treatment of the bottom thermal boundary condition (Miesch et al. 2006). As first shown in mean-field models by Rempel (2005) and then in global-scale convection models by Miesch et al. (2006), introducing a weak latitudinal gradient of entropy at the base of the convection zone, consistent with a thermal wind balance in a tachocline of shear, can serve to rotate the Ω contours toward the more radial alignment deduced from helioseismology without significantly changing either the overall Ω contrast with latitude or the convective patterns. We

expect similar behavior here, as briefly explored by Ballot et al. (2007) in younger suns with deeper convection zones, but have not explored this issue in detail at the higher rotation rates. More rapidly rotating suns may very well also possess tachoclines, but at this stage there is no observational evidence of this. Thus we have simplified these simulations by imposing a constant entropy at the bottom boundary. Our contours of Ω in Figure 3.2 show some differences between the northern and southern hemispheres, particularly at higher latitudes, and these differences decrease with more rapid rotation. The patterns of convection are not simply symmetric about the equator, and thus the accompanying mean zonal flows can be expected to show some variations between the two hemispheres. Also shown are radial cuts of Ω at six fixed latitudes that make evident the angular velocity contrasts with radius and latitude achieved in these simulations. The absolute contrast in latitude and radius clearly grows with rotation rate, and will be discussed in §3.5.

A most striking result of our simulations is the emergence of persistent, spatially modulated convection in the equatorial regions at high rotation rates. At these low latitudes, convection becomes modulated in longitude and forms distinct active nests where the convective vigor is enhanced compared to the regions outside. The amplitude of the convective motions and enthalpy transport is larger within these nests, and indeed at the highest rotation rates, convection in the equatorial band is confined entirely to the nests. These nests of convection propagate at a velocity distinct from either the zonal flow of differential rotation or that of the individual cells of convection and persist for very long periods of time (more than 5000 days in case G5). The nature of these active nests of spatially localized convection will be explored in detail in Chapter 4.

Weak modulation in longitude is already evident at low rotation rates. When long time series are considered, we have positively identified nests of convection in all simulations rotating at $\Omega_0 \gtrsim 3\ \Omega_\odot$. As the rotation rate increases, the modulation level gradually increases; at the highest rotation rates ($\gtrsim 7\ \Omega_\odot$) the equatorial convection is

almost solely confined to the nests. The convection realized in case G10 (Fig. 3.2*d*) is marked by this extreme modulation, with strong upflows and downflows inside the nest and very little convection in the surrounding regions. These most rapidly rotating cases maintain a strong differential rotation profile, even though the equatorial convection occupies only a narrow interval in longitude. The regions outside the nest are filled with fast streaming zonal flows consistent with the differential rotation.

3.2.1 Radial Connectivity of Convection

The nests of enhanced convection span the convection zone and propagate everywhere at a constant prograde angular velocity relative to the bulk rotation rate of the star. A contour corresponding to this characteristic propagation rate is overplotted on the differential rotation profiles in Figures 3.2$f-h$ for cases G3, G5 and G10. As is evident from these profiles, the angular velocity associated with the differential rotation exceeds that of the propagation rate of the nests near the surface and is slower than that near the base of the convection zone. The nests of convection therefore live within an environment of substantial zonal shear with radius, as is quantified for case G5 in Figure 3.3. Here the shearing zonal velocity of differential rotation is plotted in latitude at six radial depths. At all depths there is substantial zonal flow through the nests of convection.

Other studies of solar convection with ASH show that strong downflow lanes extend throughout the entire depth of the domain (Miesch et al. 2000; Brun & Toomre 2002; Miesch et al. 2008). In our more rapidly rotating stars, this connectivity with depth changes markedly, as is illustrated for case G5 in Figure 3.4 showing radial velocities throughout the convection zone. In these rapidly rotating suns, the strong variation of mean zonal flow with radius in the equatorial regions prevents all but the strongest downflows from spanning the convection zone. Within the nest of enhanced convection the plumes are able to traverse the convection zone. Yet in the quieter regions outside,

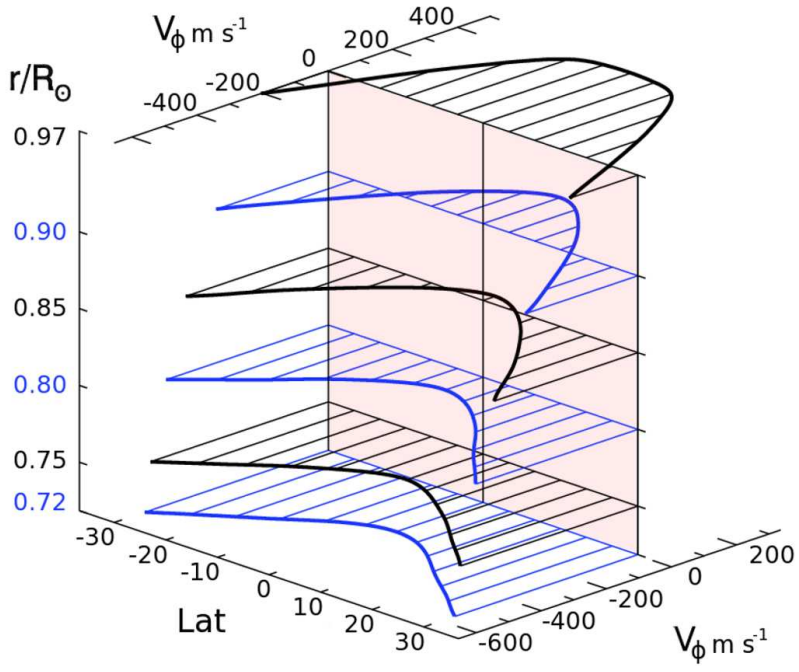

FIGURE 3.3 — Profile of $\langle v_\phi \rangle$ in case G5. The variation of mean zonal velocity $\langle v_\phi \rangle$ with latitude for case G5 is sampled at six radial cuts as labeled and shown here relative to the uniform propagation rate of the nests of convection. The nests experience a strong prograde zonal flow (positive) near the top of layer and a prominent retrograde flow within the lower half.

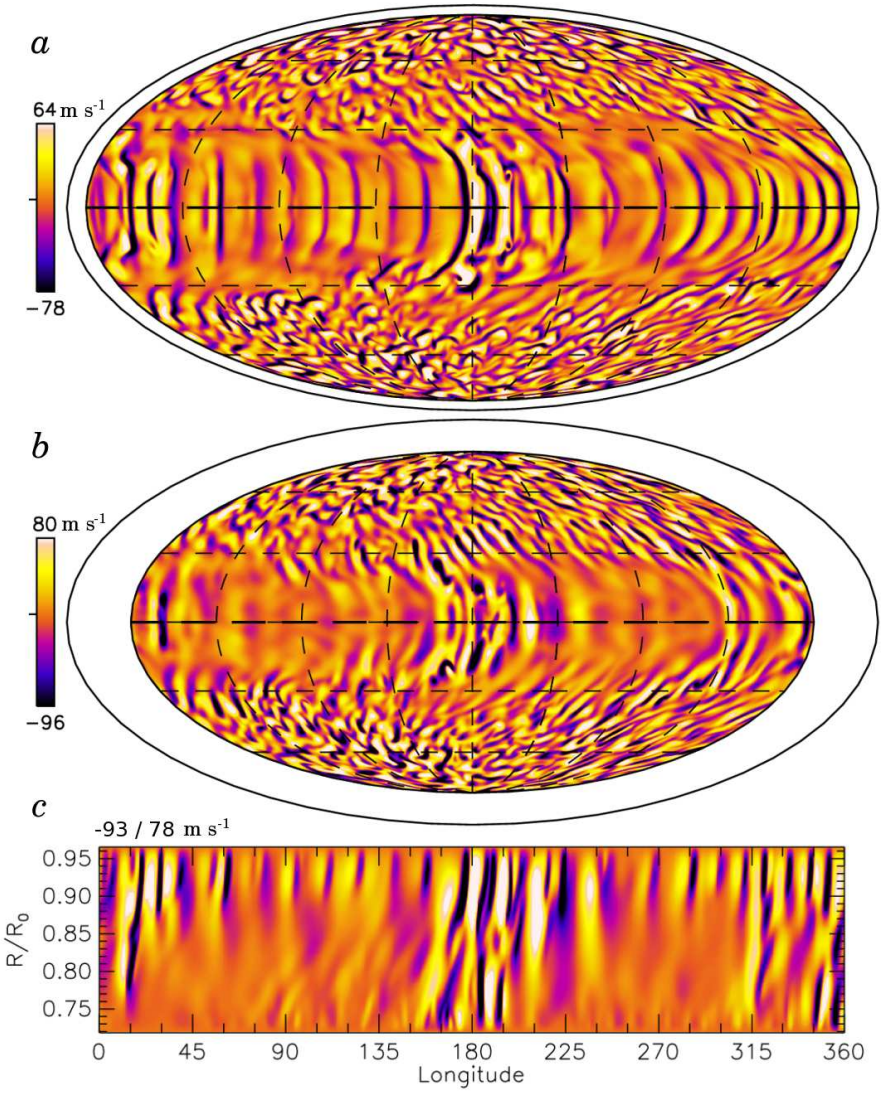

FIGURE 3.4 — Connectivity of radial velocity with depth in case G5. Shown at the same instant in Mollweide view are v_r (a) near top of domain ($0.95R_\odot$), (b) at mid depth ($0.85R_\odot$), and in (c) for an equatorial cut in longitude over full depth range. Strong plumes span the convection zone in the equatorial regions only within the nest of enhanced convection. The weaker cellular flows outside the nests are confined by shear to the upper reaches.

the weaker downflow plumes are truncated by shear before reaching the middle of the convection zone. It is evident (Fig 3.4*c*) that the amplitude of convective motions is pronounced at all depths within the nest of active convection.

The downflowing plumes are influenced by the strong radial shear and some break into multiple cells with radius even before the full blown nests of localized convection emerge, as is evident already in our simulation rotating at twice the solar rate (case G2). When the downflow networks only span a portion of the convection zone and experience a limited range of the full density stratification, the importance of compressible effects decreases. This has important consequences for the energetics of the simulations, particularly the radial kinetic energy flux, as will be addressed in §3.7. In contrast, the downflowing plumes in the polar regions experience much less shear from either the differential rotation or the relatively weak meridional circulations and continue to span the entire convection zone depth.

3.2.2 Thermal Structuring

In these rapidly rotating suns, the turbulent alignment of convection with the rotation axis leads to a net latitudinal transport of enthalpy, yielding a prominent latitudinal gradient of temperature. The resulting thermal structuring in case G5 is shown in Figure 3.5, presenting both the mean temperature profile and representative temperature fluctuations in a snapshot near the surface. In the latter, individual convection cells are associated with small fluctuations with amplitudes of a few K. Downflows are generally cool while upflows are relatively warmer. The enhanced enthalpy transport within the active nests of convection appears as positive temperature fluctuations in the equatorial region.

Evident at high latitudes (Fig. 3.5*c*) are broad spatial structures (in addition to small-scale convection) which appear in the temperature fluctuations and are not readily visible in the maps of radial velocity (see Fig. 3.4 at same instant). These

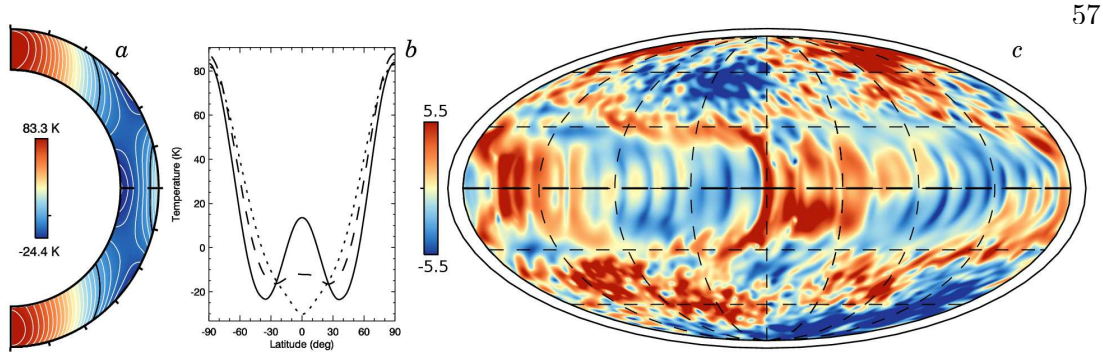

FIGURE 3.5 — Temperature structures within case G5. Mean latitudinal variations in temperature are shown relative to their spherical average $\bar{T}$ in (a) as contours with radius and latitude and (b) as cuts at fixed radii at the top (solid, $0.96R_\odot$), middle (dashed, $0.84R_\odot$) and bottom (dotted, $0.72R_\odot$) of the domain. (c) Temperature fluctuations in a snapshot near top of domain ($0.95R_\odot$) relative to the mean structure in (a).

structures are long lived and appear to be a separate phenomena from the nests of convection. The polar patterns propagate in a retrograde sense more rapidly than the differential rotation in which they are embedded, and though streaming wakes from the active nests print weakly into the polar regions, the polar patterns and nests appear to be distinct phenomena. The large-scale polar patterns are not evident in the slowly rotating cases (G1 and G2); in the most rapidly rotating cases this modulation attains a more complicated form than the two-lobed structure shown here.

The zonally-averaged thermal structure (Fig. 3.5a, b) is quite smooth and is characterized by warm poles and a cool equator, with yet cooler mid-latitudes. In contrast, the mean entropy increases monotonically from equator to pole, due to effects of pressure. All of the more rapidly rotating cases have similar latitudinal thermal profiles, though the temperature difference between equator and pole increases with more rapid rotation, as will be discussed further in §3.3. In case G5, the latitudinal pole to equator temperature contrast is approximately 100 K throughout the convection zone. These latitudinal variations remain small at all rotation rates in comparison to the spherically symmetric background $\bar{T}$, which ranges from 2.7×10^5 K near the surface to 2.2×10^6 K near the bottom of the convection zone (as shown in Fig. 2.1).

3.3 Thermal Wind Balance

Rapidly rotating systems are constrained by the Taylor-Proudman theorem to have minimal variations in flow dynamics along the direction of the rotation axis. In stratified flows, gradients in density and pressure contribute to baroclinic terms in the vorticity equations (Pedlosky 1982; Zahn 1992) which maintain flows that can break the Taylor-Proudman constraint. In our rapidly rotating suns, convective plumes tilt toward the rotation axis as rotation effects increase. This results in latitudinal as well as radial transport of enthalpy and builds a latitudinal gradient of temperature and entropy. Such gradients arise naturally in a rotating convective system even with uniform thermal boundary conditions. For a nearly adiabatic stratified, rotating, non-magnetized fluid it can be shown that in the limit of small Rossby number and negligible viscous effects the zonal component of the vorticity equations reduces to the well known thermal wind balance (e.g., Brun & Toomre 2002; Miesch et al. 2006):

$$\frac{\partial \widehat{v_\phi}}{\partial z} = \frac{g}{2C_P r \Omega_0} \frac{\partial \widehat{S}}{\partial \theta}, \tag{3.1}$$

where z is directed along the rotation axis and a hat denotes an average in longitude and time. We have further assumed that the turbulent pressure is negligible.

From equation (3.1) it is clear that departures from rotation constant on cylinders (as observed in the solar interior by helioseismology) can be maintained by a latitudinal gradient of entropy. The left and right hand sides of equation (3.1) are shown for case G5 in Figure 3.6. In the bulk of the convection zone, the differential rotation profiles realized in these more rapidly rotating suns are substantially in thermal wind balance. Significant departures arise near the inner and outer boundaries (Fig. 3.6*c*) where Reynolds stresses and boundary conditions play a dominant role, as was found in earlier simulations of solar convection (Brun & Toomre 2002).

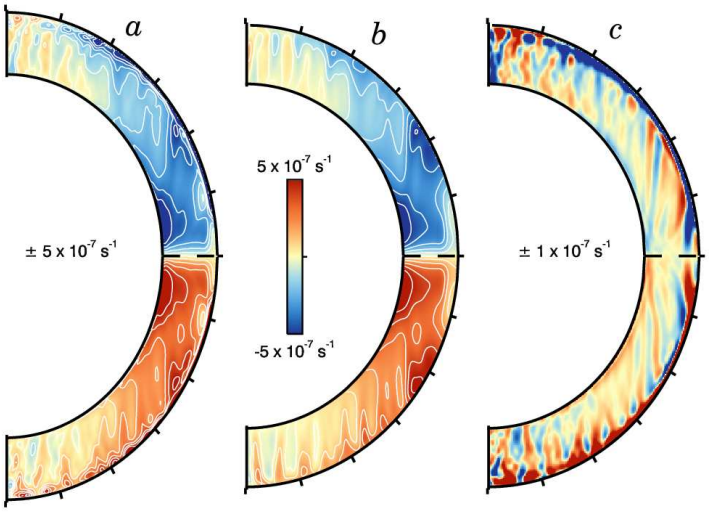

FIGURE 3.6 — Thermal wind balance achieved in case G5. (a) Gradients of $\widehat{v_\phi}$ along the rotation axis, $\partial\widehat{v_\phi}/\partial z$, ($b$) the scaled latitudinal entropy gradient from the right-hand side of eq. (3.1), and (c) their difference, with contours in the latter rescaled to show the departures near the boundaries. The bulk of the convection zone is in thermal wind balance, but substantial departures arise near the top and bottom of the domain where Reynolds stresses dominate.

Another striking property of the thermal wind balance is that increasing Ω_0 leads to more cylindrical profiles of $\widehat{v_\phi}$ unless $\partial\widehat{S}/\partial\theta$ also adjusts with the rotation rate. In our more rapidly rotating suns we find that the latitudinal gradients of temperature and entropy increase with more rapid rotation. The growth of $\Delta\widehat{S}$ (difference between the surface value of $\widehat{S}$ at say 60° and the equator) with increasing rotation rate Ω_0 is shown in Figure 3.7. The latitudinal structure of entropy is always monotonic in these simulations, with lower entropy at the equator and higher entropy at the poles. Convection in these more rapidly rotating systems establishes stronger latitudinal gradients of entropy, but not enough in these simulations to maintain the Ω profiles unchanged.

Accompanying the growth of $\Delta\widehat{S}$ is a growth in the latitudinal temperature contrast, as shown by the maximum temperature contrast in latitude near the stellar surface in Figure 3.7. Typically, the maximal contrast occurs between the poles and latitudes of ±40°, as seen in Figure 3.5 for case G5 with a contrast of about 100 K. In the

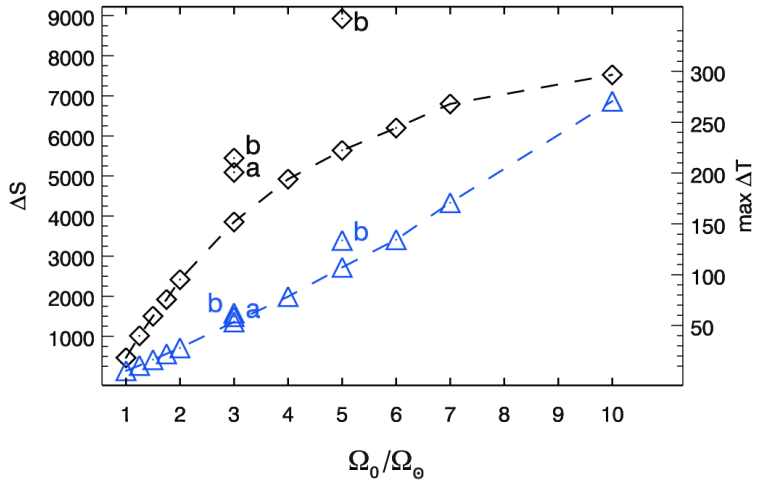

FIGURE 3.7 — Scaling of $\Delta\widehat{S}$ and maximal latitudinal temperature contrast with Ω_0. The latitudinal contrast of entropy $\Delta\widehat{S}$ (plotted as diamonds) is measured between equator and high latitudes at $0.96R_\odot$. It increases with more rapid rotation. The more turbulent cases (G3a, G3b and G5b as labeled) have larger entropy contrasts, in keeping with their generally stronger differential rotation. Blue triangles indicate the maximum temperature contrast in latitude at the upper boundary in each simulation.

rapidly rotating simulations, the primary flux balance in latitude is between thermal eddy diffusion $\kappa\bar{\rho}\bar{T}\langle\partial S/\partial\theta\rangle$ and convective enthalpy transport $C_p\bar{\rho}\langle v'_\theta T'\rangle$. Here convective transport moves warm material to the poles as the downflows align more strongly with the rotation axis while eddy diffusion works to erode the gradient. The meridional circulations appear to play a relatively minor role in maintaining the overall latitudinal entropy contrast.

3.4 Angular Momentum Redistribution

In these simulations of stellar convection, complex couplings between rotation and convection build the profiles of differential rotation and meridional circulation. With stress-free boundary conditions at the top and bottom of the shell there are no net torques and thus the total angular momentum is conserved. Couplings between rotation and convection lead to a global-scale redistribution of angular momentum, resulting in

the sustained flows of both differential rotation and meridional circulation. To assess the transport of angular momentum in these systems we follow the approach of Miesch et al. (2008), examining the average radial and latitudinal angular momentum transport as detailed in their equations (10)-(12) (see also Brun & Toomre 2002; Miesch 2005). The angular momentum fluxes from Reynolds stresses (RS), meridional circulations (MS) and viscous diffusion (VD) are

$$\boldsymbol{F}^{\mathrm{RS}} = \bar{\rho} r \sin\theta \left(\langle v_r' v_\phi' \rangle \hat{\boldsymbol{r}} + \langle v_\theta' v_\phi' \rangle \hat{\boldsymbol{\theta}} \right), \tag{3.2}$$

$$\boldsymbol{F}^{\mathrm{MC}} = \bar{\rho} \mathcal{L} \left(\langle v_r \rangle \hat{\boldsymbol{r}} + \langle v_\theta \rangle \hat{\boldsymbol{\theta}} \right), \tag{3.3}$$

$$\boldsymbol{F}^{\mathrm{VD}} = -\bar{\rho} \nu r^2 \sin^2\theta \nabla \Omega, \tag{3.4}$$

where

$$\mathcal{L} = r \sin\theta \left(\Omega_0 r \sin\theta + \langle v_\phi \rangle \right) \tag{3.5}$$

is the specific angular momentum.

The total radial and latitudinal fluxes of angular momentum are shown for case G1 and G5 in Figure 3.8. Here we have integrated in co-latitude and radius respectively to deduce the net fluxes through shells at various radii and through cones at various latitudes (c.f., Miesch 2005). The three major contributions arise from Reynolds stresses, meridional circulations and viscous terms. Velocity correlations lead to net angular momentum transport by Reynolds stresses as convective structures develop organized tilts and align partially with the axis of rotation (e.g., Brummell et al. 1998; Brun & Toomre 2002; Miesch et al. 2008). This alignment is particularly prominent in the fast downflow lanes, and becomes stronger as rotation increases.

Turning first to our solar case (G1, Fig. 3.8a, b), we see that in radius the meridional circulations and Reynolds stresses play similar and nearly equal roles in transporting angular momentum outward. The viscous flux meanwhile is negative and transports angular momentum inward, in keeping with the positive radial gradient of the differential rotation profile (eq. 3.4), and the total flux in radius is nearly zero. The transport

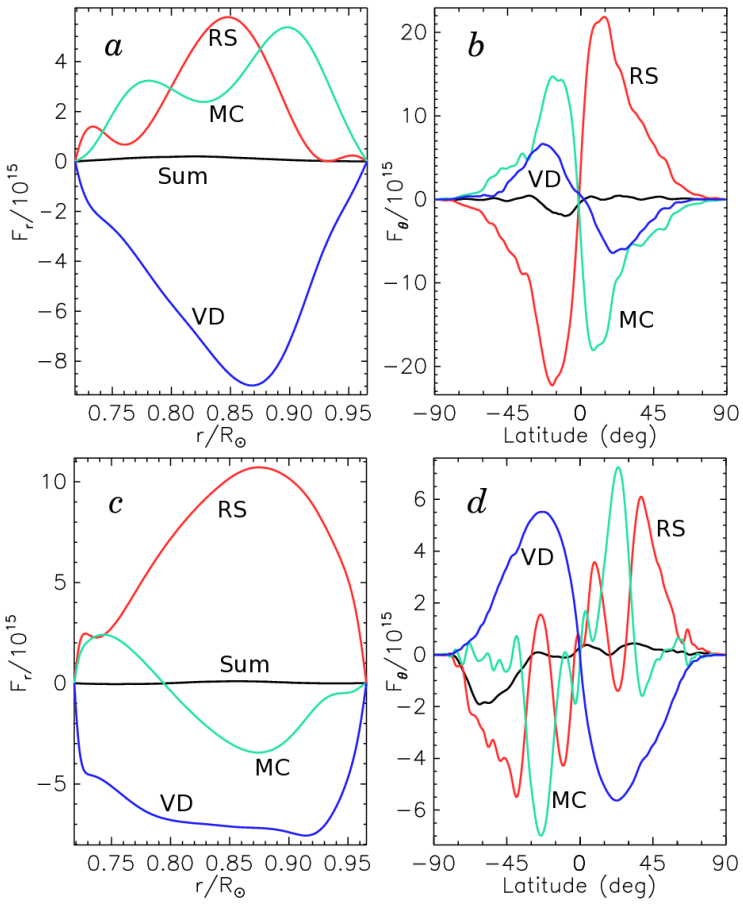

FIGURE 3.8 — Angular momentum fluxes in radius and latitude for cases G1 and G5. Shown are time averages of the integrated radial (F_r) and latitudinal (F_θ) angular momentum flux for case G1 (a, b) and case G5 (c, d). Contributions arise from Reynolds stresses (RS), meridional circulations (MC) and viscous diffusion (VD). Their total is also shown (Sum). Transport by viscous diffusion remains comparable in all cases, while the transport by Reynolds stresses and meridional circulations changes markedly with more rapid rotation.

in latitude is somewhat different. Here meridional circulations combine with viscous fluxes to transport angular momentum away from the equator and toward the poles (i.e., positive in the southern hemisphere and negative in the northern hemisphere). This tendency is opposed by Reynolds stresses, which continuously accelerate the equatorial regions and dynamically maintain the angular velocity contrast $\Delta\Omega$ in latitude.

The transport of angular momentum in our more rapidly rotating cases are all similar in form and are well represented by case G5 (Fig. 3.8*c*, *d*). In these more rapidly rotating stars, the radial balance is dominantly between the Reynolds stresses transporting angular momentum outward and viscous terms transporting it inward. The viscous transport is similar in magnitude to that of case G1, though the radial boundary layers are now much narrower. The transport by Reynolds stresses is nearly twice as large, and this likely arises from the strong alignment of convective structures in both polar and equatorial regions. In these stars the weaker meridional circulations become relatively minor and disorganized players in the radial flux balance, moving angular momentum outward in some regions of the shell and inward in others. This opposing behavior between the upper and lower convection zone arises from the meridional circulations breaking into multiple cells in radius.

The balances achieved in the latitudinal transport in case G5 (Fig. 3.8*d*) are more complex. As the rotation rate has increased, the total viscous transport has remained nearly constant, with the significantly stronger gradients of angular velocity in the differential rotation profiles offset by the lower turbulent diffusivities dictated by our path through parameter space. That these two opposing actions should conspire to produce a nearly constant profile of viscous angular momentum transport is striking and not intuitive. This is particularly apparent when we examine the two other terms in the flux balance. The meridional circulations have reversed their role from our solar-like case G1 and now work with the Reynolds stresses to accelerate the equator and spin down the polar regions. The reduced contribution of the meridional circulations

to the total balance arises as the flows become both weaker and multi-celled in radius and latitude. The smaller transport by Reynolds stresses appears to result from the destruction by radial shear of some of the downflow plumes.

3.5 Differential Rotation and Scaling with Rotation

In analyzing our simulation results, it is the differential rotation established by the convection that may yield the most direct contact with observations. Stellar observations across the HR diagram indicate that differential rotation is a common feature in many stars, particularly stars of spectral class F and later. In the sun, differential rotation has been measured throughout the bulk of the convection zone (as reviewed by Thompson et al. 2003), but at present for more distant stars only the surface differential rotation can be inferred. A variety of observational techniques have been employed, ranging from photometric variability studies (e.g., Donahue et al. 1996; Walker et al. 2007), Doppler imaging techniques (e.g., Donati et al. 2003) and Fourier transform methods (e.g., Reiners & Schmitt 2003). Typically, these observations seek to measure the amount of angular velocity contrast at the stellar surface, denoted as $\Delta\Omega_*$, though what is being measured may be somewhat uncertain. Variations in $\Delta\Omega_*$ have been found with both rotation rate and spectral type, however these quantities are correlated and in observations to date it is difficult to disentangle their possible separate effects (Reiners 2006).

Different techniques measure fundamentally different tracers of surface differential rotation, either following variability of Ca emission (photometric), darkening from inferred starspot presence (photometric and Doppler imaging) or rotational broadening of absorption lines of unspotted stars (Fourier transform methods). Each technique also is most applicable in only a limited region of stellar parameter space. As such, overlapping surveys are in short supply. Generally, most observations indicate that the relative shear, $\Delta\Omega_*/\Omega_*$, depends on the stellar rotation rate Ω_* as a power law, though

different surveys find different scalings for the differential rotation, expressed as

$$\frac{\Delta\Omega_*}{\Omega_*} \propto \Omega_*^n \tag{3.6}$$

(e.g., $n = -0.3 \pm 0.1$ in Donahue et al. 1996 and $n = -0.34 \pm 0.26$ in Reiners & Schmitt 2003, but $n = -0.85 \pm 0.10$ in Barnes et al. 2005). Whereas some global models of convection in more rapidly rotating stars have been conducted (e.g., Rüdiger et al. 1998; Küker & Stix 2001; Küker & Rüdiger 2005a,b), these have been largely carried out in 2-D under the simplifying assumptions of mean-field theory.

The amount of latitudinal shear observed at the surface $\Delta\Omega$ is an important quantity both for interpreting stellar observations and for many dynamo theories. Here we define $\Delta\Omega$ more specifically as the difference in angular velocity between the equator and say at 60° latitude, namely

$$\Delta\Omega = \Omega_{\rm eq} - \Omega_{60} \propto \Omega_0^m. \tag{3.7}$$

Going to higher latitudes yields comparable behavior. As shown in Figure 3.9, we find that $\Delta\Omega$ increases with rotation rate in our simulations, with $m = 0.3$ in the most rapidly rotating simulations. The radial shear also increases with more rapid rotation, and at the equator the difference between the mean angular velocity at top and bottom of the shell scales as $m = 0.4$ for the rapid rotators. Because $m < 1$, the relative shear $\Delta\Omega/\Omega_{\rm eq}$ decreases with rotation rate Ω_0 for the rapid rotators, in nearly a power law fashion for the path through parameter space explored here. The scaling exponent from Equation (3.6) exhibited by these cases is $n = -0.6$, but this may be influenced by our choice in the scaling of diffusivities with rotation. We are encouraged that our more turbulent cases G3b and G5b, with the same diffusivities at different rotation rates, exhibit similar behavior. Our choice of low Prandtl number also has an effect on this scaling (see Ballot et al. 2007). Additionally, different treatments of the SGS unresolved flux, which has the most effect in the upper 10% of the convection zone, can

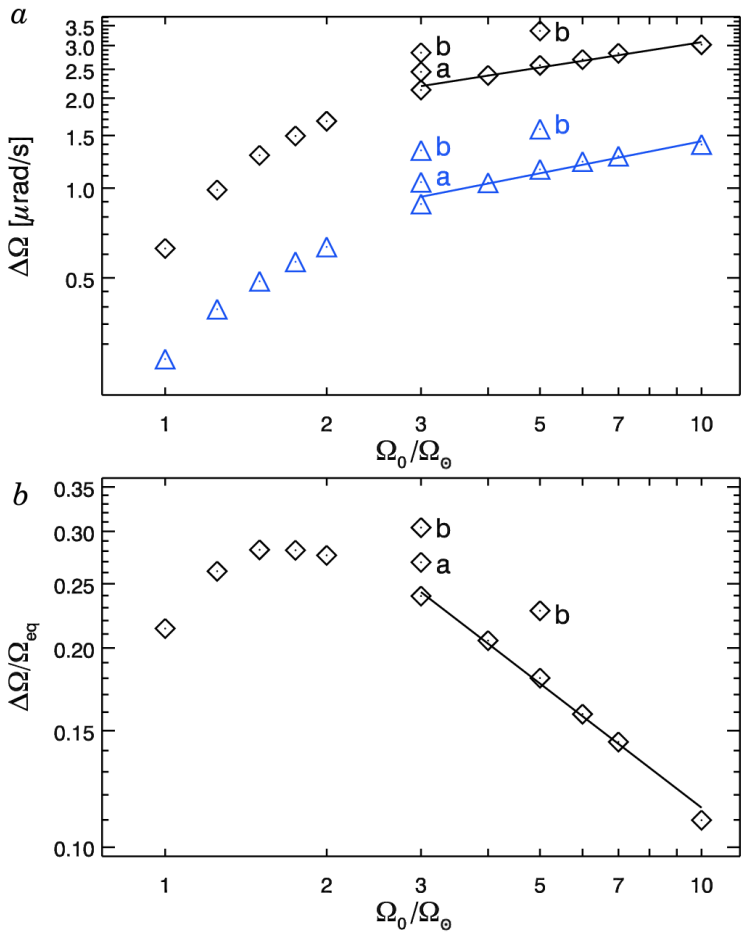

FIGURE 3.9 — Scaling of $\Delta\Omega$ and $\Delta\Omega/\Omega_{\rm eq}$ with Ω_0. (*a*) Angular velocity contrast $\Delta\Omega$ in latitude between equator and 60° (diamonds) and in radius across the shell at the equator (blue triangles). The more rapidly rotating cases appear to follow a power law, which for the latitudinal contrast is $m = 0.3$ and for the radial contrast is $m = 0.4$ (as in eq. 5.1). (*b*) Relative latitudinal angular velocity contrast $\Delta\Omega/\Omega_{\rm eq}$, with the shown power law having $n = -0.6$ (as in eq. 3.6). The scaling may vary with the path in parameter space, as suggested by cases G3a, G3b and G5b.

alter the particular scaling law. The early simulations presented in Brown et al. (2004) and shown in Figure 3.1, which had a much thicker unresolved flux layer, had a scaling of $n = -0.8$ in the rapid rotation limit. We have found that normalizing $\Delta\Omega$ by Ω_0 rather than $\Omega_{\rm eq}$ leads to a systematic offset for n of about -0.05 in the inferred scaling law.

3.6 Meridional Circulations and Scaling with Rotation

The meridional circulations realized within our simulations are of significance since they can variously transport heat, angular momentum and even magnetic fields between the equator and the poles, though the latter are not included in the present simulations. Our time and longitude-averaged meridional circulation patterns are shown in Figure 3.10 for cases G1, G5 and G10, depicted as streamlines of mass flux Ψ,

$$r\sin\theta\langle\bar{\rho}v_r\rangle = -\frac{1}{r}\frac{\partial\Psi}{\partial\theta} \quad \text{and} \quad r\sin\theta\langle\bar{\rho}v_\theta\rangle = \frac{\partial\Psi}{\partial r} \tag{3.8}$$

and averaged here over a period of at least 150 days.

In our more rapidly rotating cases the meridional circulations have broken into several cells strongly aligned with the rotation axis (Fig. 3.10b, c), particularly in the equatorial regions. Weak connections between the equatorial and polar regions persist at the highest rotation rates studied, with organized flows along the tangent cylinder. These internal flows weaken with more rapid rotation. The meridional circulations are complex and time dependent, with large fluctuations around the statistically-steady states shown here, involving variations comparable to or larger than the mean values themselves. The circulations are driven by small imbalances between relatively large forces and their nature is subtle. The variation of the meridional flows near the surface ($0.96R_\odot$) with rotation rate is shown in Figure 3.10d. The amplitude of the flows decreases substantially with more rapid rotation. Peak velocities drop from 22 $\mathrm{m\,s^{-1}}$ in case G1 to 14 $\mathrm{m\,s^{-1}}$ in G5 and about 7 $\mathrm{m\,s^{-1}}$ in G10.

The total energy contained in these meridional circulations decreases quickly with more rapid rotation, as shown in Figure 3.11. This drop in energy is independent of the detailed structure of the convection, showing no change in behavior at the transition to spatially modulated convection. In contrast to the energy contained in convection (CKE) and differential rotation (DRKE), the energy in the meridional circulations (MCKE) is much less sensitive to the level of turbulence in any particular simulation, as

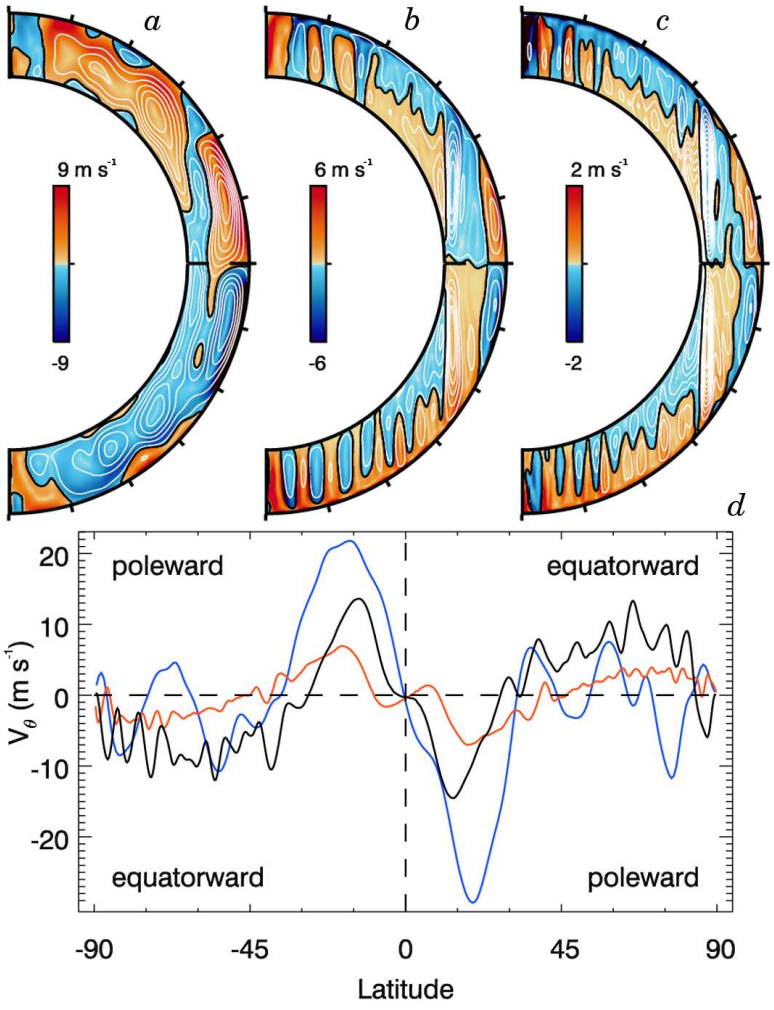

FIGURE 3.10 — Changes in structure of meridional circulations with faster rotation. Shown are profiles of time and azimuthally averaged meridional circulations with latitude and radius for (a) case G1, (b) case G5 and (c) case G10 with streamlines of mass flux Ψ overlaid. Colors indicate the sense (red counter-clockwise, blue clockwise) and magnitude of the meridional velocity $\langle \boldsymbol{v_m} \rangle = \langle v_r \rangle \hat{\boldsymbol{r}} + \langle v_\theta \rangle \hat{\boldsymbol{\theta}}$. With more rapid rotation the meridional circulation cells align strongly with the rotation axis and weaken in amplitude. (d) Amplitude of the mean latitudinal component v_θ at the top of the simulation for case G1 (blue), G5 (black), and G10 (red), with regions of poleward and equatorward flow denoted.

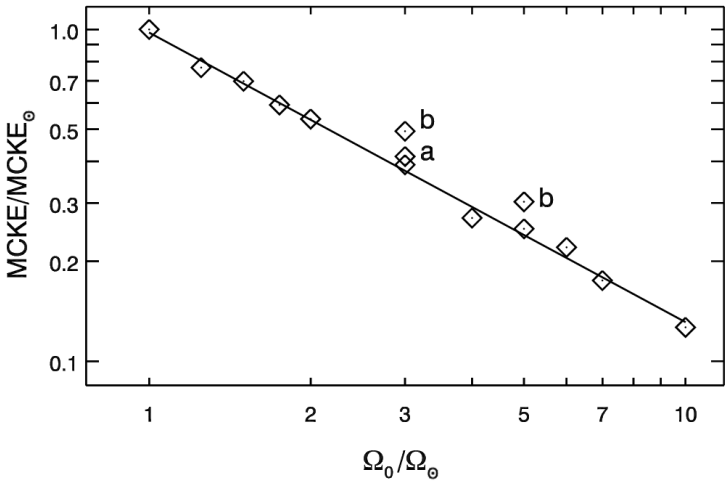

FIGURE 3.11 — Scaling of kinetic energy of meridional circulations (MCKE) with Ω_0. The MCKE is normalized by that energy in case G1 at the solar rate (2.5×10^4 ergs cm^{-3}). The kinetic energy of these circulations decreases with rotation rate; a power law scaling of $\Omega_0^{-0.9}$ is shown for reference.

indicated by cases G3, G3a and G3b (detailed in Table 3.1). The meridional circulations remain important to the global-scale dynamics as their gradual redistribution of angular momentum contributes to the large angular velocity gradients in latitude. Yet they are inefficient at transporting heat out of the star and at redistributing thermal material to maintain the latitudinal gradients of temperature and entropy (which correspond to the thermal-wind component of the achieved differential rotation).

This finding is in striking contrast to the assumptions of many Babcock-Leighton dynamos, which often take the meridional velocity to scale as $v_m \propto \Omega$ or $v_m \propto \log \Omega$ (e.g., Charbonneau & Saar 2001; Dikpati et al. 2001). In these models faster meridional circulations lead to shorter dynamo cycles as surface flux is returned more rapidly to the tachocline. Currently, the observational data does not appear good enough to distinguish between the competing models and we will have to await better measurements of the scaling between cycle period and rotation rate and possible observations of the meridional circulations themselves (Rempel 2008). Existing 2-D mean-field models of

rapidly rotating suns (Küker & Stix 2001; Rüdiger et al. 1998; Küker & Rüdiger 2005a) also predict an increase of meridional circulation velocities with more rapid rotation. This is in contrast to their decrease in our simulations.

3.7 Energy Balances and Flux Transport

Convection is responsible for transporting the stellar flux emerging from the deep interior through the convection zone. In these simulations, the total luminosity $L(r)$ and its components are

$$F_e + F_k + F_r + F_u + F_\nu = \frac{L(r)}{4\pi r^2} = F_t \,, \tag{3.9}$$

with

$$F_e = c_p \bar{\rho} \overline{v_r T'}, \qquad F_k = \tfrac{1}{2} \bar{\rho} \overline{v_r v^2} \,, \tag{3.10}$$

$$F_r = -\kappa_r c_p \bar{\rho} \frac{\mathrm{d}\bar{T}}{\mathrm{d}r}, \qquad F_u = -\kappa_0 \bar{\rho} \bar{T} \frac{\mathrm{d}\bar{S}}{\mathrm{d}r}, \quad F_\nu = -\overline{\boldsymbol{v} \cdot \boldsymbol{\mathcal{D}}}\big|_r \,, \tag{3.11}$$

where F_e is the enthalpy transport by convective motions, F_k is the kinetic energy flux, F_r is the transport by radiation, F_u is the unresolved SGS heat flux for parametrized transport by scales of motion below the resolution of our simulation and F_ν is the SGS viscous flux. Figure 3.12 shows the flux balance with radius achieved in cases G1 and G5, averaged over horizontal surfaces and converted to relative luminosities. In the deepest layers the radiative flux becomes significant as the radiative conductivity steadily increases with depth. By construction this flux suffices to carry all of the imposed flux through the lower boundary, where the radial velocities and convective flux vanish. A similar role is played near the top of the convection zone by the sub-grid scale transport which yields F_u. The main role of F_u is to transport energy outward through the impenetrable upper boundary where the convective fluxes vanish and the remaining fluxes are small, thereby avoiding the building of strong superadiabatic radial gradients there.

The functional form of $\kappa_0(r)$ is chosen so that the entire stellar luminosity will be transported at the surface of the simulation by F_u. A subtlety of this treatment of the SGS flux lies in $\mathrm{d}\bar{S}/\mathrm{d}r$. In the more rapidly rotating simulations, we find that convection is less able to establish an adiabatic profile throughout the convection zone. Instead, much of the convection zone remains slightly superadiabatic ($\mathrm{d}\bar{S}/\mathrm{d}r < 0$). This property is also realized in local-domain simulations of rapidly rotating convection, where more rapid rotation leads to enhanced horizontal mixing through vortex interactions and a resulting decrease in enthalpy transport as vertical velocities and thermal perturbations become more decorrelated (Julien et al. 1996; Brummell et al. 1996). The change of $\mathrm{d}\bar{S}/\mathrm{d}r$ with rotation rate is shown in Figure 2.1*a* for four of our simulations. Fixing the amplitude and structure of $\kappa_0(r)$ across simulations leads F_u to influence a greater portion of the convection zone at more rapid rotation, as indicated by the slight growth of F_u in case G5. Though this effect becomes stronger as our simulations rotate more rapidly, at no point in these simulations does F_u transport more than 10% of the total luminosity at mid convection zone.

In all these simulations, the strong correlations between radial velocities and temperature fluctuations yield the enthalpy flux F_e, which dominates the energy transport at mid convection zone. Both warm upflows and cool downflows serve to transport flux out of the star, and the two carry comparable amounts of flux to one another in the rapidly rotating simulations. In going to the more rapidly rotating simulations, we find that the average convective enthalpy flux through the polar regions is greater than that through the equator. This is shown in Table 3.1. In case G1 (at the solar rate) slightly more flux is transported through the equator than the poles, but as the rotation rate increases significantly more flux is transported through the poles than the equator. This latitudinal variation becomes somewhat weaker in our more turbulent cases (G3a, G3b and G5b), but remains present. Interestingly, cases G7 and G10 follow similar trends in their equatorial enthalpy transport, despite the emergence of strong nests of convection

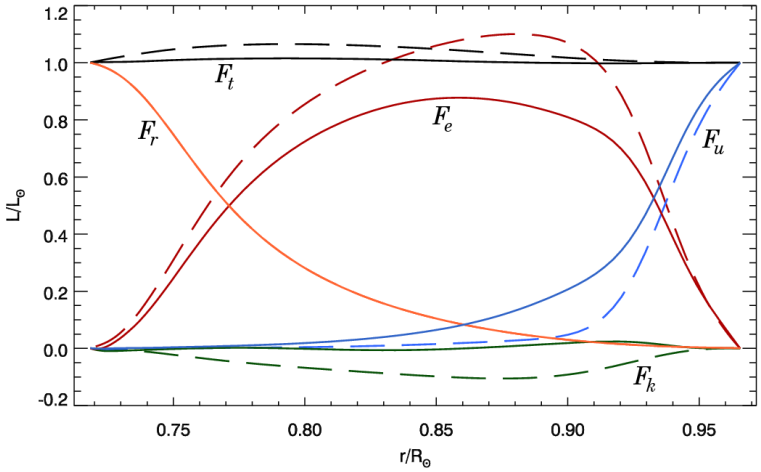

FIGURE 3.12 — Average radial energy fluxes in cases G1 and G5. Energy fluxes are shown with radius with case G1 (dashed) and G5 (solid) overlain for comparison. Shown are the radiative luminosity (F_r), convective enthalpy transport (F_e), unresolved flux (F_u), kinetic energy transport (F_k), and the total flux through the simulation (F_t), all normalized by $L_\odot/(4\pi r^2)$. Case G1 has a large positive convective enthalpy flux throughout the domain, with the excess in luminosity largely balanced by an inward flux of kinetic energy. At higher rotation rates (as in G5), the kinetic energy flux is nearly zero throughout the domain. In both cases F_ν is negligible and not shown.

at the equator and the suppression of convection in the rest of that region.

In case G1, convection transports slightly more enthalpy than the solar luminosity. This over luminosity is balanced by an inward transport of kinetic energy, which is primarily due to compressible effects and the transport of v_r^2 within strong downflows that span the convection zone and feel the full density stratification (Hurlburt et al. 1986). In the more rapidly rotating cases, the prominent differential rotation shears apart the convection cells. The downflows lose much of their coherence and only the strongest downflows within the nests of localized convection survive to span the full convection zone. Individual downflows thus feel less density stratification, and compressible effects become less important, leading to a balance in the transport of v_r^2 between the upflows and downflows. Instead, as shown in Table 3.1 the sense of F_k reverses in the equatorial regions, becoming dominated by the outward transport of v_ϕ^2. The polar regions remain largely unchanged and the total F_k across spherical surfaces is nearly zero.

Table 3.1. Flux Balances and Energies

Case	$F_{e,\mathrm{pole}}$[a]	$F_{e,\mathrm{eq}}$[a]	$F_{k,\mathrm{pole}}$[a]	$F_{k,\mathrm{eq}}$[a]	CKE[b]	DRKE[b]	MCKE[b]	ΔT_{max}[c]
G1	1.014	1.140	-0.118	-0.190	3.28	2.26	0.025	5.50
G2	1.300	0.684	-0.088	0.046	2.64	13.2	0.015	28.0
G3	1.349	0.628	-0.077	0.071	2.40	20.5	0.011	53.5
G4	1.327	0.631	-0.065	0.073	2.21	25.5	0.009	78.5
G5	1.329	0.625	-0.079	0.078	2.11	30.1	0.007	107
G7	1.298	0.581	-0.097	0.080	1.69	38.7	0.005	171
G10	1.236	0.623	-0.093	0.090	1.51	47.1	0.003	271
G3a	1.268	0.655	-0.071	0.068	2.73	27.7	0.012	58.7
G3b	1.101	0.780	-0.065	0.043	3.34	37.9	0.013	62.4
G5b	1.172	0.668	-0.047	0.081	2.44	57.4	0.008	134

[a]Average convective enthalpy (F_e) and kinetic energy (F_k) fluxes at mid-layer scaled by the solar flux, shown for polar (latitudes above $\pm 60^\circ$) and equatorial (from $\pm 30^\circ$) regions.

[b]Kinetic energy density relative to the rotating coordinate system, for convection (CKE), differential rotation (DRKE) and meridional circulations (MCKE), averaged over the full shell and over ~ 300 days; units are 10^6 erg cm^{-3}.

[c]Maximum temperature contrast at $0.96 R_\odot$ in K, typically occurring between pole and $\pm 40^\circ$

Volume-averaged energy densities for a selection of our simulations are shown in Table 3.1. At the solar rotation rate, convective kinetic energy (with kernel $\frac{1}{2}\bar{\rho}v'^2$ and labeled CKE) and the kinetic energy in the average differential rotation ($\frac{1}{2}\bar{\rho}\langle v_\phi\rangle^2$, DRKE) are comparable. As the rotation rate is increased, DRKE grows strongly and convective energy decreases slightly, leading DRKE to dominate the total energy budget. This is true even in our significantly more turbulent solutions. The energy in meridional circulations ($\frac{1}{2}\bar{\rho}(\langle v_r\rangle^2+\langle v_\theta\rangle^2)$, MCKE) is always small, and decreases in both magnitude and percentage of the total energy with more rapid rotation.

3.8 Conclusions

When stars like our sun are young they rotate much more rapidly than the present sun. In these stars rotation must strongly influence the convective motions and may lead to stronger global-scale dynamo action. In this chapter, we have explored the effects of more rapid rotation on global-scale convection in simulations of stars like our sun. The mean zonal flows of differential rotation become much stronger with more rapid rotation, scaling as $\Delta\Omega \propto \Omega_0^{0.3}$ or as $\Delta\Omega/\Omega_{\rm eq} \propto \Omega_0^{-0.6}$. In striking contrast, the meridional circulations become much weaker with more rapid rotation, and the energy contained in them drops approximately as $\Omega_0^{-0.9}$. Accompanying the growing differential rotation is a significant latitudinal temperature contrast, with amplitudes of 100 K or higher in the most rapidly rotating cases. The maximum temperature contrast near the surface occurs between the hot poles and the cool mid latitudes at about $\pm 40^\circ$. If this latitudinal temperature contrast prints through the vigorous convection at the stellar surface, it may appear as an observable latitudinal variation in intensity. The thermal contrast would presumably persist for long periods compared to stellar activity, offering a way to disentangle this intensity signature from that caused by spots of magnetism at the stellar poles.

These simulations are entirely hydrodynamic and this provides a major caveat to our findings on the scaling of differential rotation and latitudinal temperature contrast with rotation rate Ω_0. Prior MHD simulations of stellar convection have demonstrated that in some parameter regimes strong dynamo-generated magnetic fields can react back strongly on the differential rotation, acting to lessen angular velocity contrasts or largely eliminate them (e.g., Brun et al. 2005; Featherstone et al. 2007; Browning 2008). It is unclear whether the scaling trends identified here for differential rotation as a function of Ω_0 will survive in the presence of dynamo action and magnetic fields. Likewise, magnetic fields may lessen the strong temperature contrasts realized here, doing so through their feedback on the convective flows and energy transport. We expect that the weaker meridional circulations may be less affected by magnetic feedbacks, and thus the prediction that meridional circulations lessen in energy and amplitude with more rapid rotation may be of greater significance though harder to confirm observationally. Weaker meridional circulations in more rapidly rotating stars will have a strong impact on many theories of stellar dynamo action, including the Babcock-Leighton flux-transport model favored for solar-type stars. To answer such questions, we will turn in due course in Chapters 5-8 to MHD simulations that capture dynamo action in the bulk of the convection zone.

Chapter 4

Dynamics Within Confined Nests of Convection

The emergence of localized nests of convection at higher rotation rates is a striking feature that calls out for an explanation. In many ways, it is quite surprising that convection chooses to be confined to narrow intervals in longitude, but such states have also been realized in a number of other dynamical systems. Generally the appearance of nests is a challenge to explain in detail, yet the onset of spatially modulated states which are their precursor is better understood.

4.1 Spatially Localized Convection in Other Settings

The phenomena of spatially localized convection has a rich history, variously appearing in laboratory experiments and numerical simulations. Much interest in confined states of convection was motivated by the discovery of such states in binary fluid convection (e.g., Anderson & Behringer 1990; Kolodner & Glazier 1990; Niemela et al. 1990; Surko et al. 1991), where traveling waves of convection appear via subcritical Hopf bifurcations and near onset are seen to evolve into traveling patches of convection separated by regions of nearly quiescent fluid. From a theoretical perspective, these confined states near onset are accessible to weakly nonlinear theory and considerable progress has been made in understanding their nature (e.g., Riecke 1992; Barten et al. 1995; Batiste & Knobloch 2005; Batiste et al. 2006; Burke & Knobloch 2007). The confined states found in binary convection differ from our active nests of convection in several respects.

The most important is that in binary convection there is no net vertical transport of solute. The confined states instead pump solute horizontally and create regions of stable vertical stratification in the quiescent regions. A possibly related phenomena is that of localized states in magnetoconvection, as studied by Blanchflower (1999) and in 3-D by Blanchflower & Weiss (2002). Here single convective cells (called "convectons") formed in a region of initially uniform strong vertical magnetic field by a process of flux expulsion. Convection within the localized states was strong and was entirely suppressed in the surrounding medium. These convectons could contain several convective cells and were generally stationary, though some solutions exhibited time dependent behavior. Recently, progress has been made addressing these systems in approximate 2-D models (Dawes 2007).

Confined states are also realized in other doubly diffusive systems, as in theoretical studies of thermosolutal convection (Knobloch et al. 1986; Deane et al. 1987, 1988; Spina et al. 1998). In the latter studies a variety of traveling convective patches were found, and in these the convective transport of heat and solute was enhanced compared to that in the interpatch regions. In all cases the patches propagated in the same direction as the individual convective cells, though more slowly. Such behavior persisted for long periods of time. These localized states occurred well above the onset of convection, and convection continued in the interpatch regions. There may also be analogues in convection within the Earth's atmosphere, where deep convection in the tropics tends to be organized on global scales into regions of locally enhanced convection which propagate in a prograde sense. These organized convective structures are called the Madden-Julien Oscillation and appear to have their origin in the coupling of convective motions with equatorially trapped waves (perhaps Rossby or Kelvin waves; see review by Zhang 2005).

The spatially modulated states in our simulations of stellar convection exist at Rayleigh numbers far above the onset of convection. Spatially modulated states in this parameter regime have also been observed in geophysically motivated 3-D Boussi-

nesq simulations of convection within a thick, rotating spherical shell (Grote & Busse 2000; Busse 2002; Busse & Simitev 2005). In these studies, spatially localized states emerged at moderate Rayleigh numbers, involving an equilibrium between the shearing flow of differential rotation destroying convective eddies and the Reynolds stresses in the convection driving the differential rotation. These effects led to localized states where convection occupied a limited portion of the domain and the region outside the convective patch was filled with quiescent streaming flow and almost no radial motions. In the quiescent regions the thermal gradients become increasingly unstable until they are advected back into the patch where they help sustain the convective eddies. The patches in these geophysical simulations moved slowly retrograde and persisted up to Rayleigh numbers of about 10^6. Beyond this point the differential rotation became so strong that no sustained convection was possible. Instead the system began to behave as a relaxation oscillator, with short bursts of convection temporarily building a strong differential rotation which then sheared out the convective eddies. Convective transport remained suppressed until the shear of differential rotation decayed viscously, whereupon a new burst of convection would begin the process anew. In all cases with localized convection, significant oscillations were seen in the kinetic energies of both differential rotation and convection (Grote & Busse 2000).

Similar states have also been realized in anelastic simulations of stellar convection in spherical shells for a rotating younger sun with a much thicker convection zone (Ballot et al. 2006, 2007). The spatially modulated states found there appear in the equatorial convection for models with low Prandtl number (Pr = 0.25, as in the models of this paper). Localized states turn into bursty, vacillating convection at large Taylor numbers (Ta $\gtrsim 10^9$), much like those in Grote & Busse (2000). Localized states observed in thick convective shells (with typical aspect ratios $\chi = r_{\rm bot}/r_{\rm top} = 0.58$) differ in many important respects from the states we find in our relatively thin shells of convection ($\chi = 0.76$), most notably in their temporal stability, which we will next discuss.

4.2 Properties of the Active Nests

Our active nests of convection appear first as regions of mildly enhanced convective amplitude. As the rotation rate increases, convection in the equatorial regions gradually becomes more localized (as in Fig. 3.2) and eventually is present only within the active nest. In some of our systems we observe two nests or patches in longitude (such as case G5) and in some only a single nest (as in case G10). Generally, convection at the highest rotation rates possesses only a single nest, and for moderate rotation rates the system can alternate between two-nest states and single-nest states, suggesting that several attractors exist within the phase space.

To study the temporal evolution of our convective patterns in more detail, we employ time-longitude maps as shown in Figure 4.1. Here radial velocities are sampled at the equator for all longitudes, considering case G5 at three depths (near the top, middle and bottom of the convection zone) and doing so over an interval of 260 days (or about 45 rotation periods). In these maps, structures propagating in a prograde fashion relative to the frame of reference are tilted to the upper-right and patterns propagating in a retrograde sense tilt to the upper-left. To construct these maps we have chosen a frame of reference propagating in a prograde sense relative to the bulk rotation frame ($\Omega_0 = 1.3 \times 10^{-5}$ rad s^{-1} or 2070 nHz), with constant relative angular velocity 6.75×10^{-7} rad s^{-1} (107 nHz, for a total rotation rate of 1.052 Ω_0). This corresponds to the propagation rate of the modulated convection pattern, and thus the nests appear stationary in this frame. In the Ω_0 reference frame the nest takes about 108 days to complete one lap around the equator, thus for the time interval shown in Figure 4.1 the nests travel about 870° in longitude and completes about 2.4 circuits around the equator. The active nests of convection can persist for extremely long periods of time. The two nests visible in Figure 4.1 remain coherent for over 5000 days of simulated time.

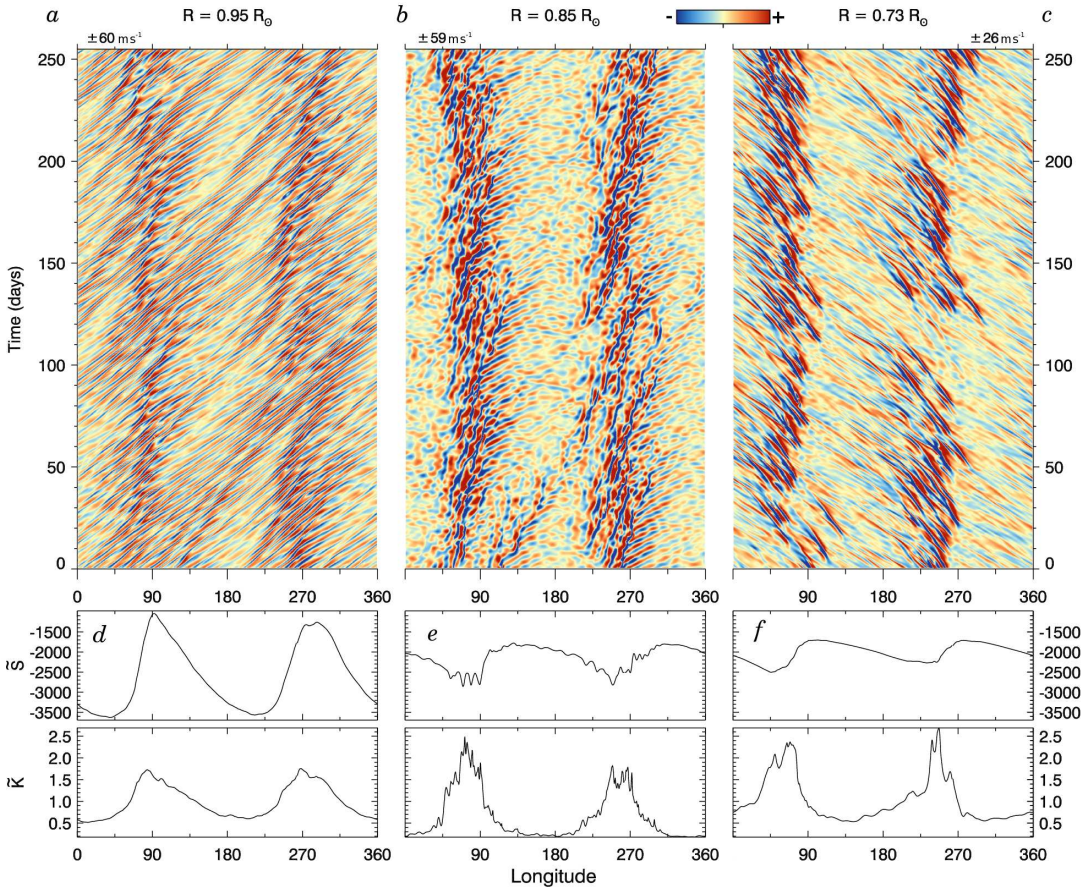

FIGURE 4.1 — Nests of convection in G5 shown in time-longitude maps at three depths. Radial velocity v_r is sampled (a) near top ($0.95\,R_\odot$), (b) middle ($0.85\,R_\odot$) and (c) bottom ($0.73\,R_\odot$) of layer. These samples are extracted at the equator, using a reference frame tracking the nests and starting from a mature state in the simulation. Two nests are visible, and individual convective cells appear as paired upflows and downflows, which propagate slightly faster than the mean zonal flow that they establish and thus pass through the nests. (d, e, f) Time averages with longitude of entropy fluctuations $\widetilde{S}$ and convective kinetic energy density $\widetilde{K}$ in these samples.

Individual convective upflows and downflows appear as streaked red and blue regions respectively. In the upper convection zone ($0.95R_\odot$), the convective cells propagate more rapidly than the nests of convection. Here they overtake the nests from behind (from smaller longitudes) and then slowly swim through at a reduced speed. Within the nests convective cells collide and interact, and the strongest survive to emerge from the front of the nest, where they speed up as they then propagate through the more quiescent region. When this occurs, typically a small wave train comprised of 2 to 3 upflow/downflow pairs escapes, and as they enter the quiescent regions these convective cells speed up to once again outpace the zonal flow. In the lower convection zone ($0.73R_\odot$), the nests propagate more rapidly than the convective cells, and the individual upflows and downflows appear as strong retrograde-directed streaks. Also visible in the lower convection zone are low-amplitude velocity structures of rapid retrograde propagation. They appear to be the weak equatorward extension of the large-scale (retrograde rotating) polar patterns evident in Figure 3.5. At mid-convection zone ($0.85R_\odot$), nearly all vertical flow is occurring within the nests of active convection, though the strongest cells outside the nest in the upper convection zone manage to weakly print down to this intermediate depth.

The typical angular velocities of the differential rotation, the individual convective cells and the active nests of convection are shown in Figure 4.2 for case G5 and detailed for several cases in Table 4.1. The nests of convection propagate at a constant angular velocity at all depths in the convection zone and over the entire range of latitudes ($\pm 30^\circ$) where they are present. In contrast, the angular velocity Ω of the differential rotation varies substantially with radius and latitude. At all depths, the individual convective cells propagate more rapidly than the zonal flow of differential rotation which they drive. Because the nests of convection propagate at an intermediate prograde rate, they experience a head-wind from the differential rotation in the deep convection zone and a tail-wind near the surface. Despite this strong radial shear, the nests remain coherent

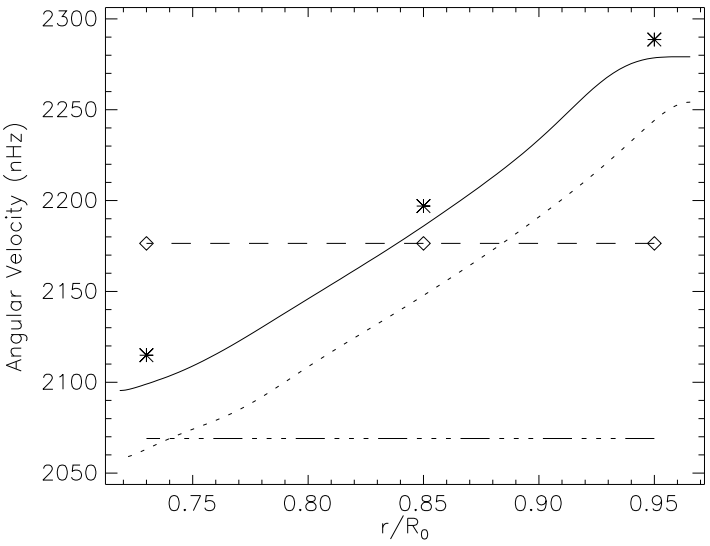

FIGURE 4.2 — Angular velocities of various structures with radius in case G5. The mean shearing zonal flow of differential rotation Ω is denoted for all depths at the equator (solid curve) and at $\pm 15°$ latitude (dotted). The propagation rate of the active nests (diamonds) is constant across the entire latitude and radial range where they appear ($\pm 30°$). The average velocity of individual convective cells at the equator (asterisks) is more rapid than the mean zonal flow they establish. Their propagation is faster than the nests near the top and slower near the bottom. The global rotation rate Ω_0 is 2070 nHz (marked).

across the entire convection zone for long periods compared with either the lifetime of individual convective cells (10-30 days), the rotation period of the star (5 days) or typical thermal and viscous diffusion times ($\tau_\kappa = 910$ days, $\tau_\nu = 3640$ days, both at mid-depth). The time for the differential rotation to lap the nests at the equator is about 112 days near the surface and 143 days at the bottom of the shell.

At the higher rotation rates, single stable nests of convection dominate the equatorial region. Time-longitude maps are shown in Figure 4.3 for the equatorial radial velocity at two depths in case G10, our most rapidly rotating simulation. Within the nest, convection remains vigorous, with the strongest downflow networks still spanning the entire depth of the convection zone. This nest again propagates in a prograde sense relative to Ω_0, with constant relative angular velocity 8.3×10^{-7} rad s^{-1} (132 nHz, for

Table 4.1. Angular Velocities of Various Structures

Case	Ω_0	$\Omega_{\rm nest}$	$\Omega_{\rm eq,top}$	$\Omega_{\rm eq,bot}$	$\Omega_{c,\rm top}$	$\Omega_{c,\rm bot}$
G1	2.60	—	0.341	0.060	0.535	0.180
G3	7.80	0.511	1.094	0.220	1.176	0.330
G5	13.00	0.675	1.319	0.197	1.381	0.288
G10	26.00	0.830	1.497	0.140	1.623	0.280
G3a	7.80	0.690	1.295	0.265	1.421	0.373
G3b	13.00	0.670	1.555	0.250	1.590	0.413
G5b	13.00	0.750	1.778	0.246	1.800	0.430

Note. — All angular velocities in μrad s^{-1} and, except for the frame rate Ω_0, are given relative to Ω_0. The differential rotation at the equator $\Omega_{\rm eq}$ is measured at $0.95R_\odot$ (**top**) and $0.73R_\odot$ (**bot**). The mean propagation rate of individual convective structures Ω_c is measured at the same depths in time-longitude maps of v_r and has a typical variance of ± 0.04 μrad s^{-1} .

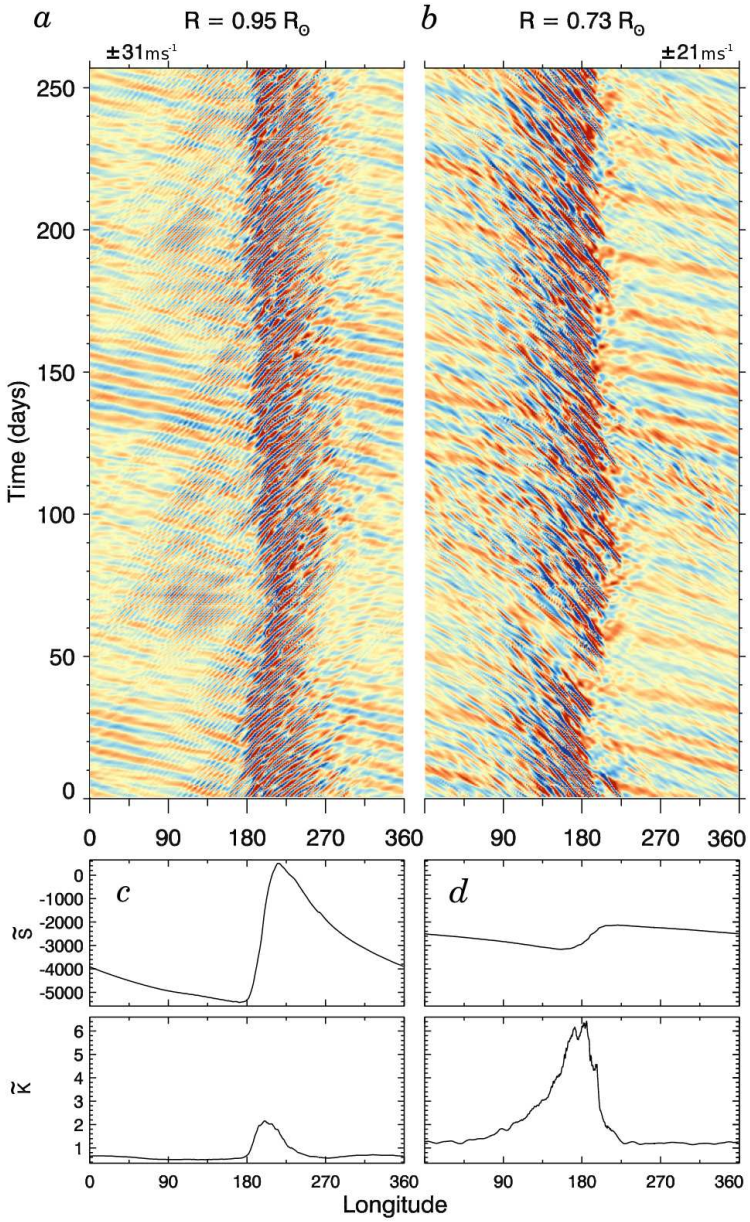

FIGURE 4.3 — Time-longitude map of single nest of convection in case G10. As in Fig. 4.1, radial velocity v_r is shown (a) near top and (b) near bottom of layer. Here a single nest is realized, with individual convective cells almost entirely confined to the nest, though they continue to propagate within it. (c, d) Time averages $\widetilde{S}$ and $\widetilde{K}$ constructed in the same reference frame.

a total rotation rate of 1.032 Ω_0). Over the interval shown the nest completes almost 3 circuits of the equator relative to the Ω_0 reference frame. Individual convective cells continue to swim through the nest, moving more rapidly near the surface and more slowly in the deep convection zone. The very strong radial shear prevents all but the strongest of downflows from spanning the full convection zone. In the region outside the nest, convection is strongly suppressed and the main features are the weak flows associated with the retrograde propagating polar pattern. In the upper convection zone, occasional weak convective disturbances appear upstream of the nest. As these fluctuations enter the nest they grow in amplitude.

Our nests of active convection may owe their existence to a competition between the shearing action of differential rotation acting on the individual convective eddies and Reynolds stresses within the convection helping to maintain the strong zonal flows. Unlike the systems studied by Grote & Busse (2000) and Ballot et al. (2007), our patchy convection is not accompanied by relaxation oscillation behavior or large exchanges between the kinetic energy in convection and in the differential rotation. Rather, our nests are not bursty in time and instead persist for long periods in quasi-steady states. This is true even for our most rapidly rotating case considered here (G10) and at much higher turbulent driving (G5b), though these simulations exist at Taylor numbers below the threshold suggested by Ballot et al. (2007) (Ta $\gtrsim 10^9$). Coupling between equatorially trapped waves and convection may also have a role, but the contribution of this coupling to spatial localization has been difficult to elucidate.

4.3 Detailed Structure of an Active Nest of Convection

We focus here on the structure of the nests so evident in Figures 4.1 and 4.3 for cases G5 and G10, but devote particular attention to the single nest realized in the latter as a representative case. The active nests extend throughout the depth of the convection zone. This is illustrated most clearly in Figure 4.4*a*, showing the vertical

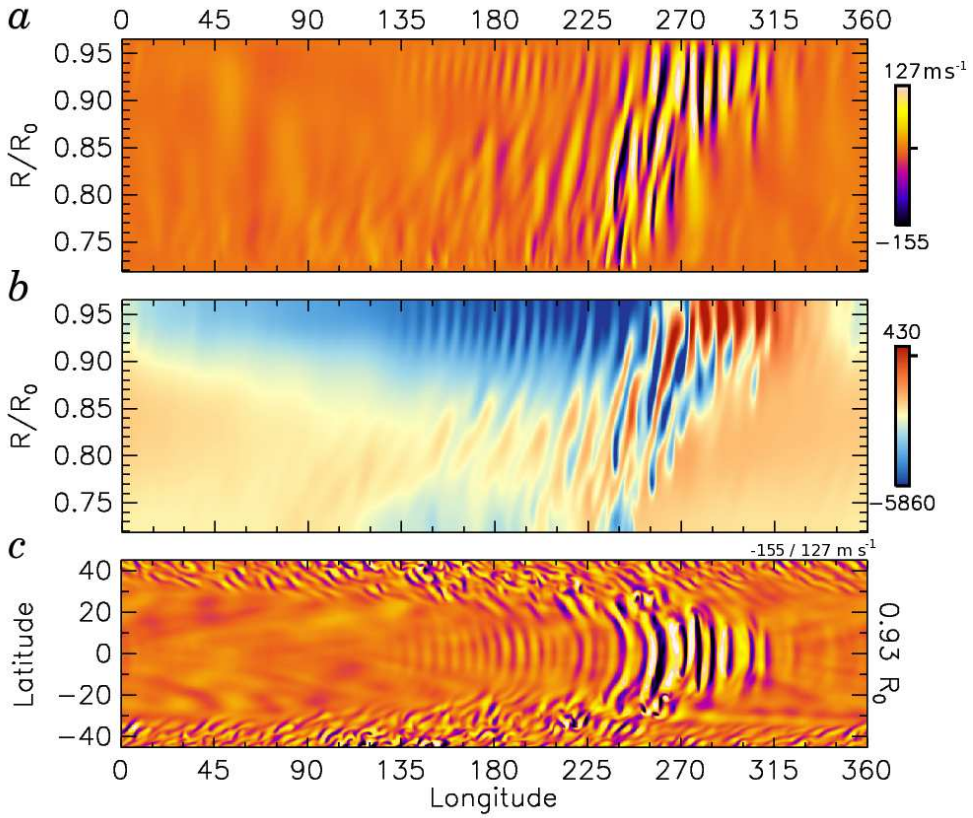

FIGURE 4.4 — Detailed structure of convective nest in case G10. This snapshot of nest structure is shown at relative day 221 of Fig. 4.3. (a) Radial velocities in an equatorial cut shown for all longitudes and radii. (b) Companion entropy fluctuations S about their spherical means $\bar{S}$ (in cgs units), with high entropy fluid in red tones. (c) Radial velocity in the equatorial region shown near the top of layer.

profile of radial velocities with longitude in a cut at the equator. Convection is broken into multiple cells, one set above $0.9R_\odot$ and another below $0.8R_\odot$. Only within the nest do strong downflows span the convection zone. The nest is embedded in a region of strong latitudinal and radial zonal shear (as shown by the tilted nature of its structure), yet the pattern propagates at a constant angular velocity at all depths and latitudes. At the surface and near the equator the nest propagates more slowly than the zonal wind, whereas at the base of the convection zone it propagates more rapidly. Individual convective structures swim still more rapidly and both enter and exit the region of enhanced convection. As such, the nest experiences a strong retrograde flow at the base and a strong prograde flow near the surface.

The thermal structure of the nests is revealed by their entropy fluctuations, as shown in Figure 4.4*b*. In the upper convection zone, the mean zonal flow advects low entropy fluid into the nests from the left side. This fluid is then swept away by intermittent downflows and replaced by higher entropy fluid from below. In the lower convection zone, higher entropy fluid is swept into the nest from the right and lower entropy exits to the left. At mid convection zone, regions outside the nest remain convectively unstable, but only weak radial motions are driven here.

The mean longitudinal structure of the nests can be assessed by forming temporal averages of various properties in a frame co-rotating with the nests of convection (these averages denoted by a tilde). This is done at the equator for entropy $\widetilde{S}$ and convective kinetic energy density $\widetilde{K}$ (with same form as CKE) for case G5 in Figure 4.1$d-f$ and for case G10 in Figure 4.3c,d. There are distinctive differences between the leading (to the right) and trailing (to the left) portions of the profiles, with $\widetilde{S}$ showing a gradual rise and steeper drop in going to decreasing longitudes (from right to left). The envelope of $\widetilde{S}$ is largely similar in form at the top and bottom of the convection zone. In contrast $\widetilde{K}$, which traces the fluctuating velocities of convection, changes form with depth, being skewed in the direction of the mean zonal flow. At the top of the convection zone this

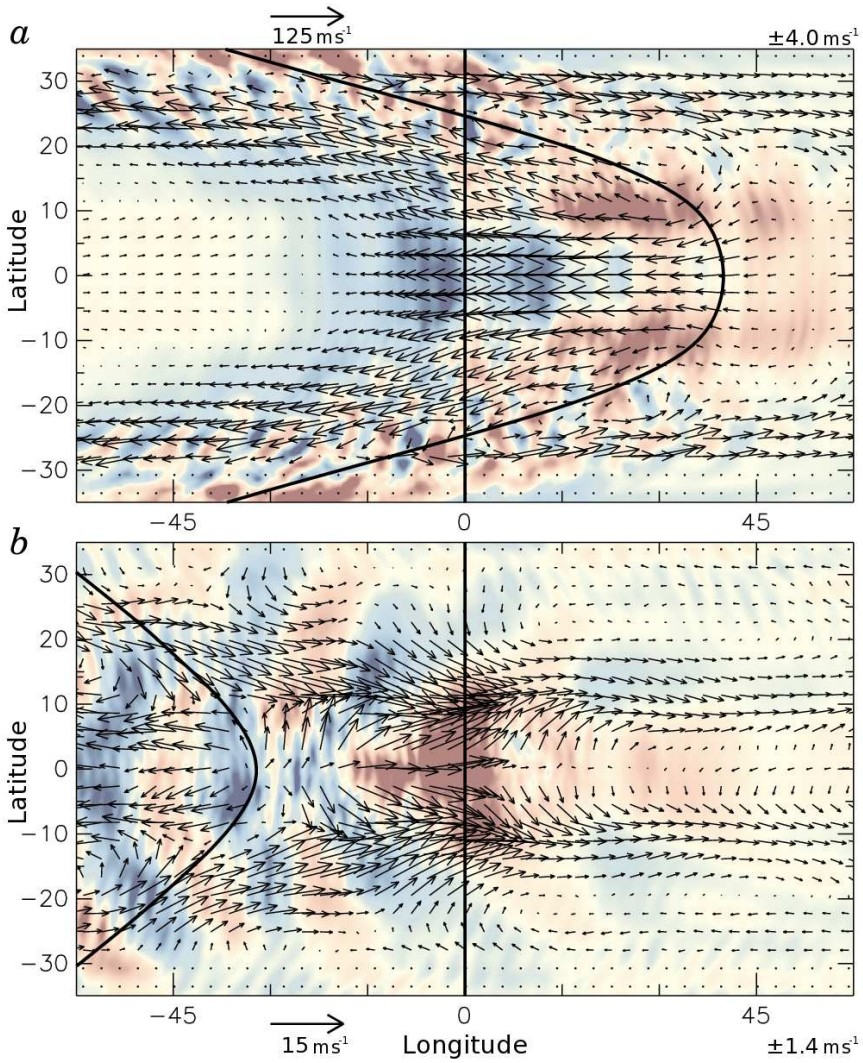

FIGURE 4.5 — Mean circulations associated with the nest in case G10. (a) Time averaged radial (colors) and horizontal flows (arrows) near the top and (b) near the bottom of the shell, in a reference frame tracking the nest. The strong zonal flow of differential rotation has been subtracted at each latitude and is shown by the solid curves (both scaled by 125 $\mathrm{m\,s^{-1}}$ arrow length, with zero velocity relative to the nest indicated by the vertical line). Within the nest strong eddy currents partially decelerate the flow, while outside the streaming mean zonal flow dominates.

sense of skew is toward the right, and at the bottom it is toward the left.

These nests must have gradual circulations associated with them, though these are a challenge to discern as they are much weaker than the strong mean zonal flows. We can get some sense of them by averaging the vertical and horizontal flows in the surroundings of a nest while tracking it over long time intervals. Shown in Figure 4.5 are the slow circulations associated with the nest in case G10 near the top and bottom of the convection zone. These flows have been averaged over a period of 615 days starting at the beginning of the interval shown in Figure 4.3. The flows suggest a systematic zonal circulation from fore to aft in the upper convection zone and toward higher latitudes and diverging from the nest at depth, though to achieve this we have subtracted the fast mean zonal flow which varies with latitude as shown. The mean upflows and downflows in the nest are quite weak, with amplitudes of a few $\mathrm{m\,s^{-1}}$, as compared with the convection which can have peak velocities of a few hundred $\mathrm{m\,s^{-1}}$. Test particles released in the flow would not simply circulate according to these mean circulations and would be instead swept along by the strong mean zonal flow and of course by the vigorous convection cells that propagate through the nest. Some test particles would encounter strong downflows and would be swept down through the nest to the bottom of the convection zone while others would likely be carried horizontally out the nest and remain at a similar depth. Yet Figure 4.5 indicates that a weak large-scale circulation is realized, and this may serve to slowly pump fluid through the system. These mean circulatory flows may also serve to inform analytic models of such nests of convection.

4.4 Conclusions

A striking feature of these simulations is the emergence of a pattern of strongly modulated convection in the equatorial regions. These nests of active convection are regions of enhanced convective vigor and transport which propagate at rates distinct from either the mean zonal flows of differential rotation or the individual convective cells. In the most rapidly rotating systems, such as case G10, convection at the equator is entirely dominated by motions inside the nest with only very weak radial motions present in the regions outside the nest. Though their impact on the convection is most obvious in the rapidly rotating limit, we find some evidence for weak modulation even in our more slowly rotating cases.

All of our simulations stop short of the turbulent stellar surface, and it is thus difficult to estimate how these nests of active convection may affect stellar observations in detail. The convective velocities associated with the nests are small compared to the nearly supersonic flows in stellar granulation, and in the Sun such global-scale convective structures have evaded direct detection despite intensive searches throughout the near-surface layers by helioseismology. The extremely localized nests found in our most rapidly rotating cases may however influence the thermal stratification and thus convective vigor in the near surface regions, as most of the flux at the equator is transported through a narrow range of longitudes. These nests may act as traveling hot spots with enhanced convection even in the surface layers where the higher emerging flux escapes the system.

These spatially localized states of convection may also have some bearing on the active longitudes of magnetic activity observed in the Sun, if the enhanced pummeling of the tachocline by the convection within the nest preferentially destabilizes magnetic structures within the tachocline that then rise to the surface. If they do survive in a magnetic environment, then their strongest signature is likely to emerge in magnetic

stars, where magnetic fields threading the bulk of the convection zone may be concentrated in the nests and mimic giant, propagating starspots which survive for very long epochs in time. If the nests lead to active longitudes of enhanced magnetic activity in rapidly rotating stars, we might expect these long-lived magnetic structures to propagate at a rate different from the stellar rotation rate as measured at the surface or from the stellar differential rotation.

We recognize that our simulations remain separated by many orders of magnitude from the parameter space of real stellar convection. As such, we must be cautious with our interpretations of the overall dynamics. However, we have found that these nests of convection are a robust feature over a range of parameters and that they are able to persist as entities for as long as we could pursue their modelling. Thus one should be prepared to consider the possibility of their presence also in real stellar convection zones, where they may appear as long-lived propagating features.

Our current family of dynamo simulations indicate that nests of convection can coexist with magnetism in portions of parameter space. We will explore this possibility in Chapter 8, but first we turn to a more general exploration of dynamo activity in these rapidly rotating suns.

Chapter 5

Global Dynamo that Builds Persistent Wreaths of Magnetism

Having explored the coupling of convection and rotation in our hydrodynamic simulations, it is now time to turn to the question of possible dynamo action in rapidly rotating suns. The hydrodynamical simulations showed us that the shearing flows of differential rotation generally grow in amplitude with more rapid rotation, possessing rapid equators and slower poles, while the meridional circulations weaken and break up into multiple cells in radius and latitude. More rapid rotation can also substantially modify the patterns of convection in a surprising fashion. With more rapid rotation, localized states begin to appear in which the convection at low latitudes is modulated in its strength with longitude. At the highest rotation rates, the convection can become confined to active nests which propagate at distinct rates and persist for long epochs.

Motivated by these discoveries, we turn here to explorations of the possible dynamo action achieved in solar-type stars rotating at three and five times the current solar rate. Magnetism leads to strong feedbacks on the flows, particularly modifying the differential rotation and its scaling with overall rotation rate Ω_0. The magnetic fields which form in these dynamos have prominent global-scale organization within the convection zone, in contrast to previous solar dynamo simulations (Brun et al. 2004; Browning et al. 2006). Quite strikingly, we find that coherent global magnetic structures arise naturally in the midst of the turbulent convection zones. These wreath-like structures are regions of strong longitudinal field B_ϕ organized loosely into tubes, with

fields wandering in and out of the surrounding convection. These wreaths of magnetism differ substantially from the idealized flux tubes supposed in many dynamo theories, though they may be related to coherent structures achieved in local simulations of dynamo action in shear flows (Cline et al. 2003; Vasil & Brummell 2008, 2009). Here we explore the nature of magnetic wreaths realized in our global simulations, and discuss their temporal behavior.

The contents of Chapters 5, 6 and 7 are based on work submitted for publication as Brown et al. (2009)[1] and are mainly a restatement of that paper under review. As the primary author of this paper, I conducted the simulations presented here, performed the analysis and wrote the text. My co-authors provided advice and guidance throughout the process, helping frame the questions which form the core of the study. Preliminary versions of these results have also been presented in Brown et al. (2007b), Brown et al. (2007c), Brown (2009a), and Brown (2009b).

We begin by turning to case D3 whose formulation is shown in Figure 2.5. This dynamo yields fairly persistent wreaths of magnetism in its two hemispheres, though these structures did wax and wane somewhat in strength once established. Examining the properties of this dynamo solution helps to provide a perspective for the greater variations realized in our more rapidly rotating case D5.

5.1 Patterns of Convection in Case D3

The complex and evolving convective structures in our dynamo cases are substantially similar to the patterns of convection found in our hydrodynamic simulations. Our dynamo solution rotating at three times the solar rate, case D3, is presented in Figure 5.1, along with its hydrodynamic progenitor, case H3. The radial velocities shown near the top of the simulated domain (Figs. 5.1a, e) have broad upflows and narrow

[1] Brown, B. P., Browning, M. K., Brun, A. S., Miesch, M. S., & Toomre, J., 2009, Persistent wreathes of magnetism in a rapidly rotating sun, *ApJ*, under review.

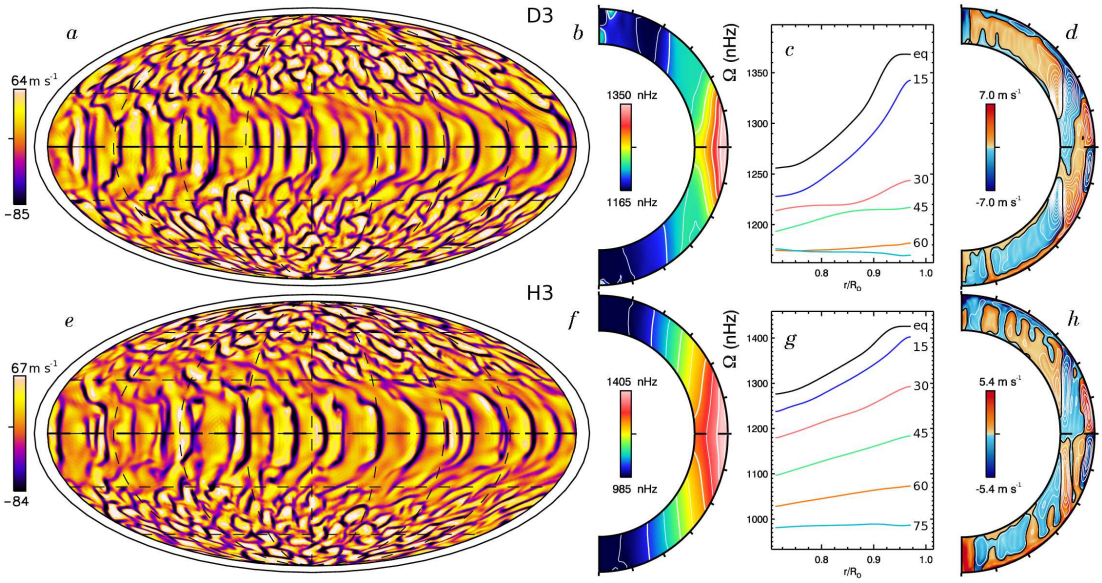

FIGURE 5.1 — Convective structures and mean flows in cases D3 and H3. (a) Radial velocity v_r in dynamo case D3, shown in global Mollweide projection at $0.95R_\odot$, with upflows light and downflows dark. Poles are at top and bottom and the equator is the thick dashed line. The stellar surface at $R_\odot$ is indicated by the thin surrounding line. (b) Profiles of mean angular velocity $\Omega(r,\theta)$, accompanied in (c) by radial cuts of Ω at selected latitudes. A strong differential rotation is established by the convection. (d) Profiles of meridional circulation, with sense of circulation indicated by color (red counter-clockwise, blue clockwise) and streamlines of mass flux overlaid. ($e-h$) Companion presentation of fields for hydrodynamic progenitor case H3. The patterns of radial velocity are very similar in both cases. The differential rotation is much stronger in the hydrodynamic case and the meridional circulations there are somewhat weaker, though their structure remains similar.

downflows as a consequence of the compressible motions. Near the equator the convection is aligned largely in the north-south direction, and these broad fronts sweep through the domain in a prograde fashion. The strongest downflows penetrate to the bottom of the convection zone; the weaker flows are partially truncated by the strong zonal flows of differential rotation. In the polar regions the convection is more isotropic and cyclonic. There the networks of downflow lanes surround upflows and both propagate in a retrograde fashion.

The convection establishes a prominent differential rotation profile by redistributing angular momentum and entropy, building gradients in latitude of angular velocity and temperature. Figures 5.1b, f show the mean angular velocity $\Omega(r, \theta)$ for cases D3 and H3, revealing a solar-like structure with a prograde (fast) equator and retrograde (slow) pole. This property is also realized for cases D5 and H5 with faster rotation. Figures 5.1c, g present in turn radial cuts of Ω at selected latitudes, which are useful as we consider the angular velocity patterns realized here with faster rotation. These $\Omega(r, \theta)$ profiles are averaged in azimuth (longitude) and time over a period of roughly 200 days. Contours of constant angular velocity are aligned nearly on cylinders, influenced by the Taylor-Proudman theorem.

As discussed in Chapter 1, helioseismology has revealed that in the Sun the contours of angular velocity are aligned almost on radial lines rather than on cylinders. The tilt of Ω contours in the Sun may be due in part to the thermal structure of the solar tachocline, as first found in the mean-field models of Rempel (2005) and then in 3-D simulations of global-scale convection by Miesch et al. (2006). In those computations, it was realized that introducing a weak latitudinal gradient of entropy at the base of the convection zone, consistent with a thermal wind balance in a tachocline of shear, can serve to tilt the Ω contours toward a more radial alignment without significantly changing either the overall Ω contrast with latitude or the convective patterns. We expect similar behavior here, but at present, observations of rapidly rotating stars only measure differential rotation at the surface and do not offer constraints on either the existence of tachoclines in young suns or the nature of their internal differential rotation profiles. As such, we have neglected the possible tachoclines of penetration and shear entirely in these models and instead adopt the simplification of imposing a constant radial entropy gradient at the bottom of the convection zone.

The differential rotation achieved is stronger in our hydrodynamic case H3 than in our dynamo case D3. This can be quantified by measurements of the latitudinal

angular velocity shear $\Delta\Omega_{\rm lat}$. Here, as in Chapter 3 we define $\Delta\Omega_{\rm lat}$ as the shear near the surface between the equator and a high latitude, say $\pm 60^\circ$

$$\Delta\Omega_{\rm lat} = \Omega_{\rm eq} - \Omega_{60}, \tag{5.1}$$

and the radial shear $\Delta\Omega_{\rm r}$ as the angular velocity shear between the surface and bottom of the convection zone near the equator

$$\Delta\Omega_{\rm r} = \Omega_{0.97R_\odot} - \Omega_{0.72R_\odot}. \tag{5.2}$$

We further define the relative shear as $\Delta\Omega_{\rm lat}/\Omega_{\rm eq}$. In both definitions, we average the measurements of $\Delta\Omega$ in the northern and southern hemispheres, as the rotation profile is often slightly asymmetric about the equator. Case H3 achieves an absolute contrast $\Delta\Omega_{\rm lat}$ of 2.22 μ rad s^{-1} (352 nHz) and a relative contrast of 0.247. The strong global-scale magnetic fields realized in the dynamo case D3 serve to diminish the differential rotation. As such, this case achieves an absolute contrast $\Delta\Omega_{\rm lat}$ of only 1.17 μ rad s^{-1} (186 nHz) and a relative contrast of 0.136. This results from both a slowing of the equatorial rotation rate and an increase in the rotation rate in the polar regions. These results are quoted in Table 5.1, along with related measurements for our five solar dynamo case D5 and hydrodynamic cases H3 and H5. It is interesting to note that in both dynamo cases the amount of latitudinal and radial shear is almost the same, whereas in the hydrodynamic simulations the more rapidly rotating case H5 has larger angular velocity contrasts than the slower case H3.

The meridional circulations realized in the dynamo case D3 are very similar to those found in its hydrodynamic progenitor (case H3). As illustrated in Figures 1d, h, the circulations are multi-celled in radius and latitude. The cells are strongly aligned with the rotation axis, though some flows along the inner and outer boundaries cross the tangent cylinder and serve to couple the polar regions to the equatorial convection. Flows of meridional circulation are slightly stronger in the dynamo cases than in the purely hydrodynamic cases, and these flows weaken with more rapid rotation.

Table 5.1. Near-surface $\Delta\Omega$ in Cases at 3 and 5 $\Omega_\odot$

Case	$\Delta\Omega_{\rm lat}$	$\Delta\Omega_{\rm r}$	$\Delta\Omega_{\rm lat}/\Omega_{\rm eq}$	Epoch
D3	1.17	0.71	0.136	6460-6920
$D5^{\rm avg}$	1.14	0.71	0.083	3500-5700
$D5^{\rm min}$	0.91	0.39	0.067	3702
$D5^{\rm max}$	1.43	0.98	0.102	4060
H3	2.22	0.94	0.246	-
H5	2.77	1.31	0.192	-

Note. — Angular velocity shear in units of μrad s^{-1}, with $\Delta\Omega_{\rm lat}$ and $\Delta\Omega_{\rm lat}/\Omega_{\rm eq}$ measured near the surface ($0.97R_\odot$) and $\Delta\Omega_{\rm r}$ measured across the full shell at the equator. For the dynamo cases, these measurements are taken over the indicated range of days. In oscillating case D5, these measurements are averaged over a long epoch (avg), and are also taken at two instants in time when the differential rotation is particularly strong (max) and when magnetic fields have suppressed this flow (min). The hydrodynamic cases are each averaged for roughly 300 days. Case D3 also shows slow variations in $\Delta\Omega_{\rm lat}$ over periods of about 2000 days.

5.2 Kinetic and Magnetic Energies

Convection in these rapidly rotating dynamos is responsible for building the differential rotation and the magnetic fields. In a volume averaged sense, the energy contained in the magnetic fields in case D3 is about 10% of the kinetic energy. About 35% of this kinetic energy is contained in the fluctuating convection (CKE) and about 65% in the differential rotation (DRKE), whereas the weaker meridional circulations contain only a small portion (MCKE). The magnetic energy is split between the contributions from fluctuating fields (FME), involving roughly 53% of the total magnetic energy, and the energy of the mean toroidal fields (TME) that are 43% of the total. The energy contained in the mean poloidal fields (PME) is only 4% of the total magnetic energy. These energies are quoted in Table 5.2 and are defined as

$$\begin{aligned}
\mathrm{CKE} &= \frac{1}{2}\bar{\rho}\Big[(v_r - \langle v_r \rangle)^2 + (v_\theta - \langle v_\theta \rangle)^2 + \\
&\qquad (v_\phi - \langle v_\phi \rangle)^2 \Big], && (5.3)\\
\mathrm{DRKE} &= \frac{1}{2}\bar{\rho}\langle v_\phi \rangle^2, && (5.4)\\
\mathrm{MCKE} &= \frac{1}{2}\bar{\rho}\Big(\langle v_r \rangle^2 + \langle v_\theta \rangle^2 \Big), && (5.5)\\
\mathrm{FME} &= \frac{1}{8\pi}\Big[(B_r - \langle B_r \rangle)^2 + (B_\theta - \langle B_\theta \rangle)^2 + \\
&\qquad (B_\phi - \langle B_\phi \rangle)^2 \Big], && (5.6)\\
\mathrm{TME} &= \frac{1}{8\pi}\langle B_\phi \rangle^2, && (5.7)\\
\mathrm{PME} &= \frac{1}{8\pi}\Big(\langle B_r \rangle^2 + \langle B_\theta \rangle^2 \Big). && (5.8)
\end{aligned}$$

where angle brackets denote an average in longitude.

These results are in contrast to our previous simulations of the solar dynamo, where the mean fields contained only about 2% of the magnetic energy and the fluctuating fields contained nearly 98% (Brun et al. 2004). In simulations of the solar dynamo that included a stable tachocline at the base of the convection zone (Browning et al. 2006), the energy of the mean fields in the tachocline can exceed the energy of the

Table 5.2. Energies in Cases at 3 and 5 $\Omega_\odot$

Case	CKE	DRKE	MCKE	FME	TME	PME
D3	2.31	4.35	0.010	0.36	0.29	0.029
$D5^{avg}$	1.85	4.46	0.006	0.55	0.43	0.048
$D5^{min}$	1.70	2.85	0.005	0.50	0.25	0.062
$D5^{max}$	1.85	7.52	0.007	0.39	0.65	0.042
H3	2.56	22.2	0.012	-	-	-
H5	2.27	34.3	0.008	-	-	-

Note. — Volume-averaged energy densities relative to the rotating coordinate system. Kinetic energies are shown for convection (CKE), differential rotation (DRKE) and meridional circulations (MCKE). Magnetic energies are shown for fluctuating magnetic fields (FME), mean toroidal fields (TME) and mean poloidal fields (PME). All energy densities are reported in units of $10^6 \mathrm{erg\,cm^{-3}}$ and are averaged over 1000 day periods except for time-varying case D5, where intervals are as in Table 5.1.

fluctuating fields there by about a factor of three, though the fluctuating fields still dominate the magnetic energy budget within the convection zone itself. Simulations of dynamo activity in the convecting cores of A-type stars (Brun et al. 2005) achieved similar results. There in the stable radiative zone the energies of the mean fields were able to exceed the energy contained in the fluctuating fields, but in the convecting core the fluctuating fields contained roughly 95% of the magnetic energy. Simulations of dynamo action in fully-convective M-stars do however show high levels of magnetic energy in the mean fields (Browning 2008). In those simulations the fluctuating fields still contain much of the magnetic energy, but the mean toroidal fields possess about 18% of the total throughout most of the stellar interior. In our rapidly rotating suns, the mean fields comprise a significant portion of the magnetic energy in the convection zone and are as important as the fluctuating fields.

Convection is similarly strong in all four rapidly rotating cases, and CKE is similar in magnitude. The differential rotation in the dynamo cases is much weaker than in the hydrodynamic progenitors and DRKE has decreased by about a factor of five. The magnetic fields and differential rotation in case D5 change in time, but the average energy contained in DRKE is nearly the same in both dynamo cases despite their very different rotation rates. This is in striking contrast to the behavior of the hydrodynamic cases, where DRKE is much larger in the more rapidly rotating case H5 than in case H3. Meridional circulations are comparably weak in all cases.

The amount of energy contained in the magnetic fields is different in these two dynamo cases, with energies generally stronger in case D5 than in case D3. In an average sense, all three magnetic energies are about 1.5 times greater in case D5 than in case D3. Case D5 shows substantial time variation, and at periods either FME or TME can become quite similar to those values realized in case D3. Meanwhile, PME is always stronger in D5 than in D3.

5.3 Wreaths of Magnetism

These dynamos produce striking magnetic structures in the midst of their turbulent convection zones. The magnetic field is organized into large banded, wreath-like structures positioned near the equator and spanning the depth of the convection zone. These wreaths are shown at two depths in the convection zone in Figure 5.2. The dominant component of the magnetic wreaths is the strong longitudinal field B_ϕ, with each wreath possessing its own polarity. The average strength of the longitudinal field at mid-convection zone is ± 7 kG and peak field strengths there reach roughly ± 26 kG. Threaded throughout the wreaths are weaker radial and latitudinal magnetic fields, which connect the two structures across the equator and also to the high-latitude regions.

These wreaths of magnetism survive despite being embedded in vigorous convective upflows and downflows. The convective flows leave their imprint on the magnetic structures, with individual downflow lanes entraining the magnetic field, advecting it away, and stretching it into B_r while leaving regions of locally reduced B_ϕ. The slower upflows carry stronger B_ϕ up from the depths. Where the magnetism is particularly strong the convective flows are disrupted. Meanwhile, where the convective flows are strongest, the longitudinal magnetic field is weakened and appears to vanish. In reality, the magnetic wreaths here are diving deeper below the mid-convection zone, apparently pumped down by the pummeling action of the strong downflows.

The deep structure of these wreaths is revealed by field line tracings throughout the volume, shown in Figure 5.3 for the same instant in time. The wreaths are topologically leaky structures, with magnetic field lines threading in and out of the surrounding convection. The wreaths are connected to the high-latitude (polar) convection, and on the poleward edges they show substantial winding from the highly vortical convection found there. This occurs in both the northern and southern hemispheres, as shown in

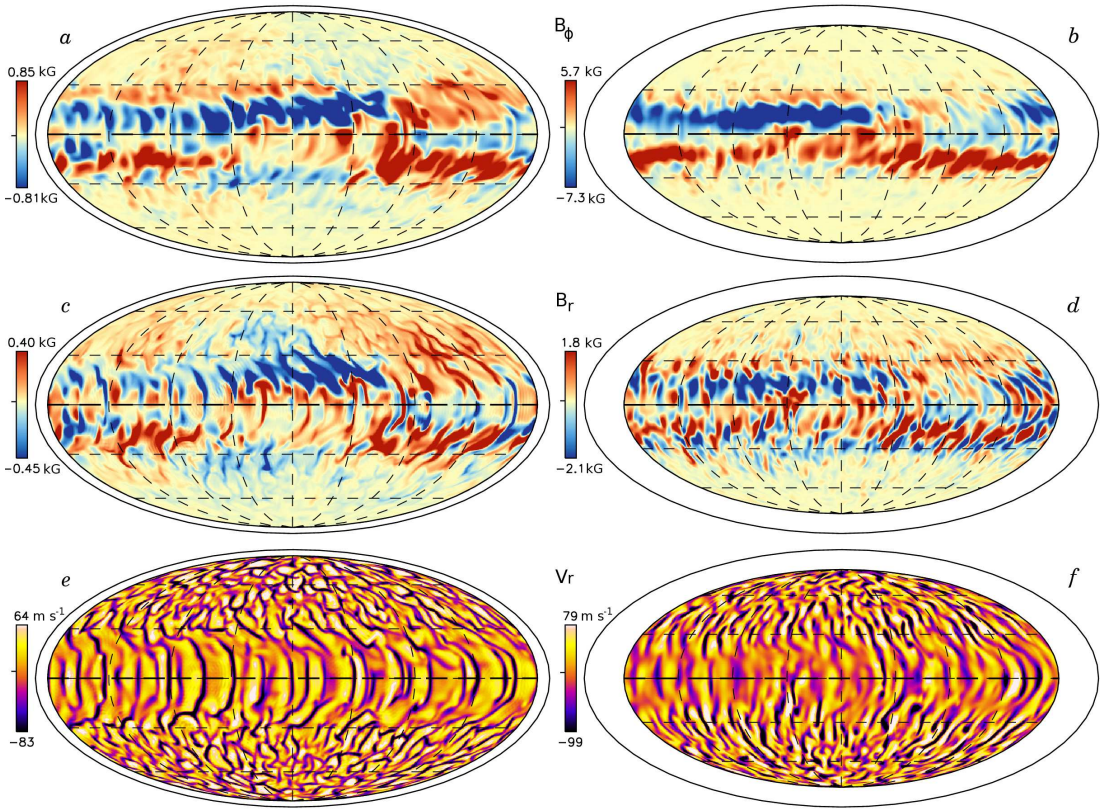

FIGURE 5.2 — Magnetic wreaths and convective flows sampled at the same instant in case D3. (a) Longitudinal magnetic field B_ϕ near the top of the shell $(0.95R_\odot)$ and (b) at mid-depth $(0.85R_\odot)$. Strong flux structures with opposite polarity lie above and below the equator and span the convection zone. (c, d) Weaker radial magnetic field B_r permeates and encircles each wreath. (e, f) Strong convective upflows and downflows shown by V_r pass through and around the wreaths. The regions of strong magnetism tend to disrupt the convective flows while the strongest downflows serve to pump the wreaths to greater depths.

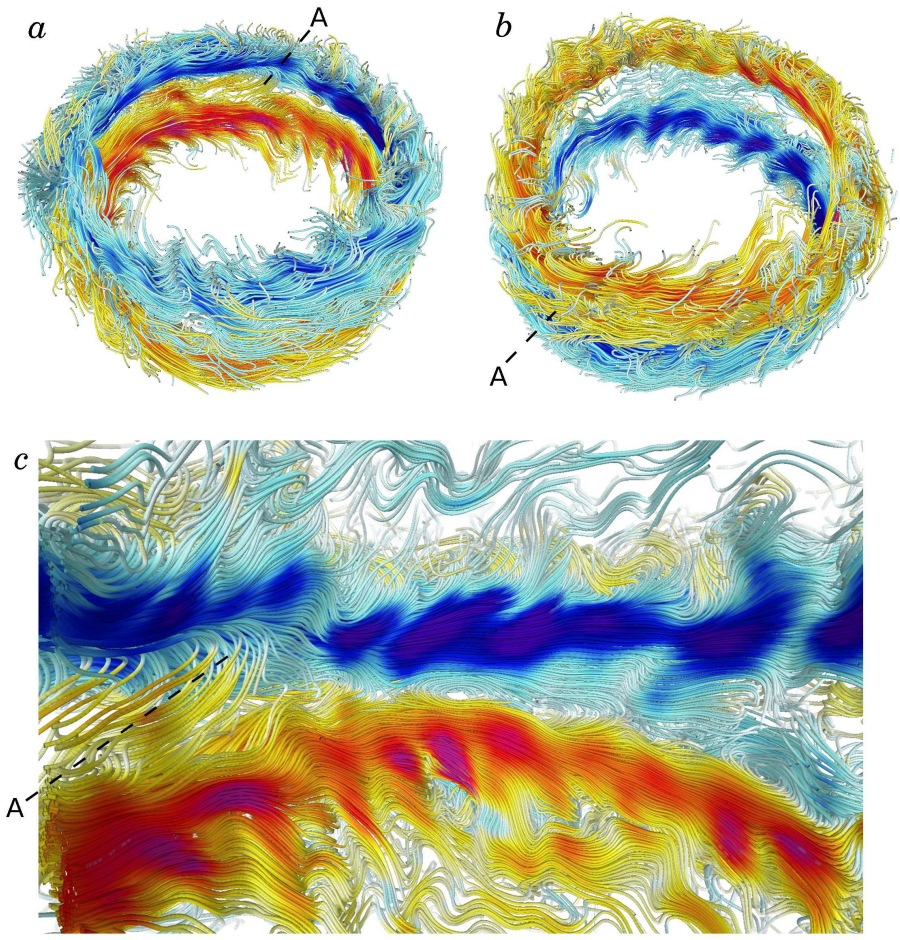

FIGURE 5.3 — Field line visualization of magnetic wreaths in case D3. (a) Snapshot of two wreaths in full volume at same instant as in Fig. 5.2. Lines trace the magnetic fields, color denoting the amplitude and polarity of the longitudinal field B_ϕ (red, positive; blue, negative). Magnetic field threads in and out of the wreaths, connecting the two opposite polarity structures across the equator (i.e., region A) and to the polar regions where the magnetic field is wound up by the cyclonic convection. (b) Same snapshot showing south polar region. (c) Zoom in on region A showing the complex interconnections across the equator between the two wreaths and to high latitudes. Convective flows create the distinctive waviness visible in all three images.

two views at the same instant (north, Fig. 5.3*a* and south, Fig. 5.3*b*). It is here that the global-scale poloidal field is being regenerated by the coupling of fluctuating velocities and fluctuating fields. Magnetic fields cross the equator, tying the two wreaths together at many locations (Fig. 5.3*c*). The strongest convective downflows leave their imprint on the wreaths as regions where the field lines are dragged down deeper into the convection zone, yielding a wavy appearance to the wreaths as a whole.

5.4 Wreaths Persist for Long Epochs

The wreaths of magnetism built in case D3 persist for long periods of time, with little change in strength and no reversals in global-scale polarity for as long as we have pursued these calculations. The long-term stability of the wreaths realized by the dynamo of case D3 is shown in Figure 5.4. Here the azimuthally-averaged longitudinal field $\langle B_\phi \rangle$ and colatitudinal field $\langle B_\theta \rangle$ are shown at mid-convection zone at a point after the dynamo has equilibrated and for a period of roughly 5000 days (i.e., several ohmic diffusion times). During this interval there is little change in either the amplitude or structure of the mean fields. This is despite the short overturn times of the convection (10-30 days) or the rotation period of the star ($\sim$ 9 days). The ohmic diffusion time at mid-convection zone is approximately 1300 days.

Though the mean (global-scale) fields are roughly steady in nature (Figs. 5.4*a*, *b*), the magnetic field interacts strongly with the convection on smaller scales. Several samples of longitudinal field B_ϕ are shown in full Mollweide projection at mid-convection zone (Fig. 5.4*c*). The magnetic fields are clearly reacting on short time scales to the convection but the wreaths maintain their coherence.

There are also some small but repeated variations in the global-scale magnetic fields. Visible in Figure 5.4*b* are events where propagating structures of $\langle B_\theta \rangle$ reach toward higher latitudes over periods of about 1000 days (i.e., from day 3700 to day 4500 and from day 5600 to day 6400). These are accompanied by slight variations

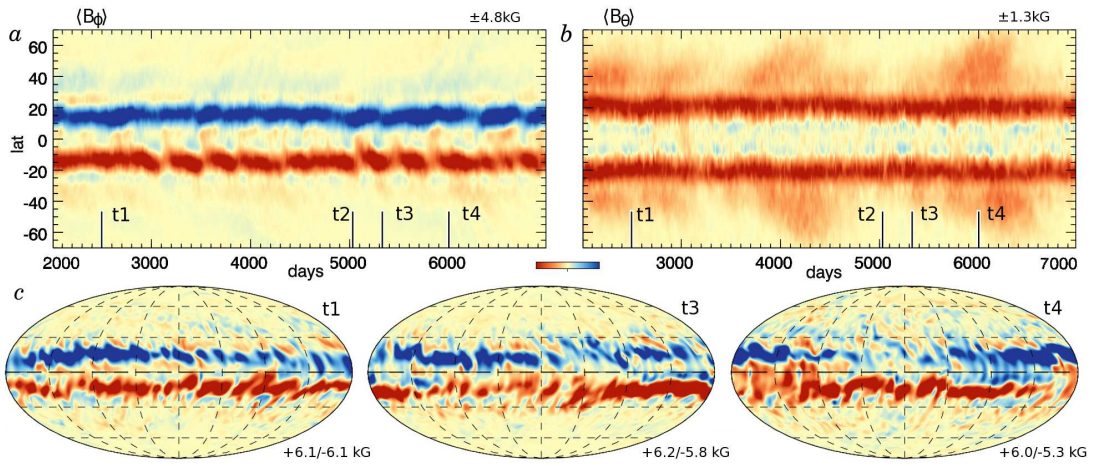

FIGURE 5.4 — Persistent wreaths of magnetism in case D3. (a) Time-latitude plots of azimuthally-averaged longitudinal field $\langle B_\phi \rangle$ at mid-convection zone ($0.85R_\odot$) in a view spanning latitudes from $\pm 70°$, with scaling values indicated. The two wreaths of opposite polarity persist for more than 4000 days. (b) Mean colatitudinal magnetic field $\langle B_\theta \rangle$ at mid-convection zone over same interval. (c) Snapshots of B_ϕ in Mollweide projection at mid-convection zone, shown for three times indicated in a, b. The wreaths maintain constant polarity over long time intervals, but still show variation as they interact with the convection. Time t2 corresponds to the snapshot in Fig. 5.2b.

in the volume-averaged magnetic energy densities and the comparable kinetic energy of the differential rotation. These variations are also visible in the differential rotation itself, as shown in Figure 5.5. The differential rotation is fairly stable, though some time variation is visible at high latitudes. This is better revealed (Fig. 5.5b) by subtracting the time-averaged profile of Ω at each latitude, revealing the temporal variations about this mean. In the polar regions above $\pm 40°$ latitude, speedup features move poleward over 500 day periods. These features track similar structures visible in the mean magnetic fields (Fig. 5.4b).

These evolving structures of magnetism and faster and slower differential rotation appear to be the first indications of behavior where the mean fields themselves begin to wax and wane substantially in strength. As the magnetic Reynolds number is increased, this time varying behavior becomes more prominent and can even result in organized changes in the global-scale polarity. Such behavior is evident in our case D5.

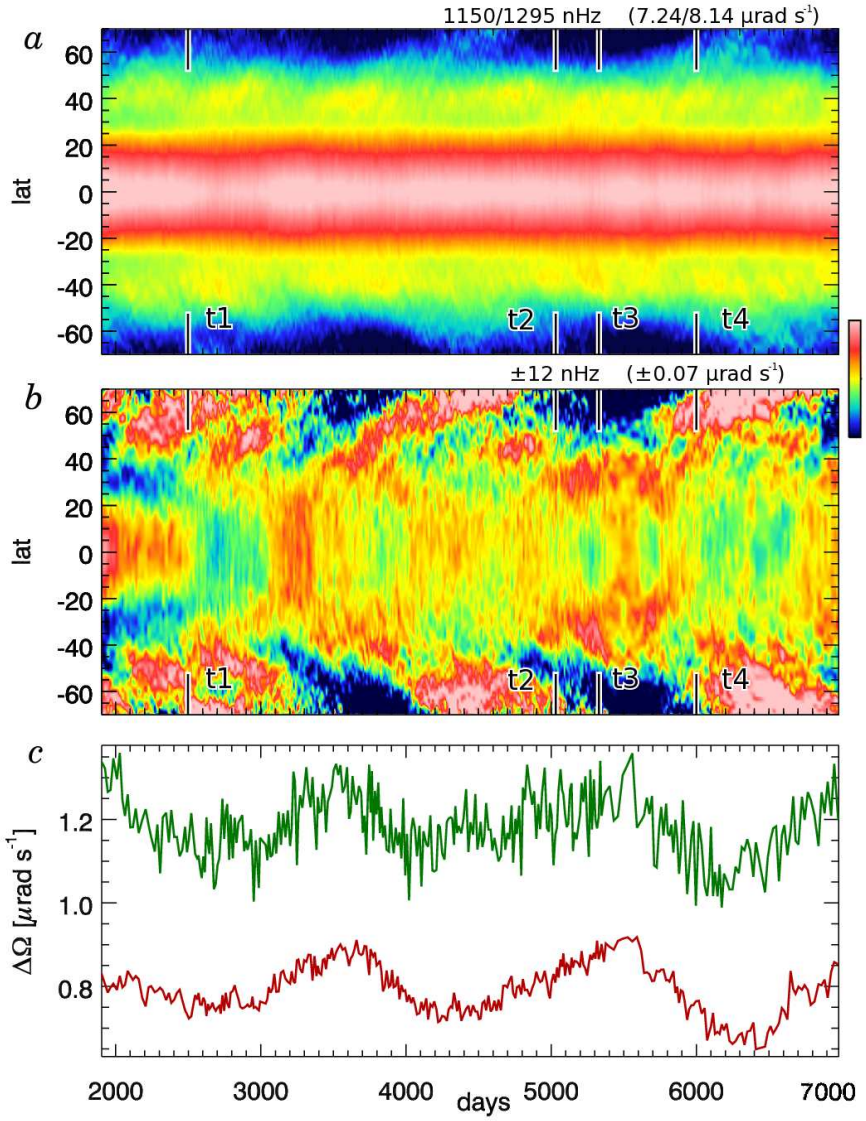

FIGURE 5.5 — Temporal variations of differential rotation in case D3. (a) Angular velocity Ω at mid-convection zone ($0.85R_\odot$), with ranges in both nHz and μrad s^{-1}. The equator is fast while the poles rotate more slowly. (b) Temporal variations are emphasized by subtracting the time-averaged profile of $\Omega(r,\theta)$, revealing speedup structures at high latitudes and pulses of fast and slow motion near the equator. These bands have average amplitudes of ± 20 m s^{-1} and peak amplitudes of about ± 60 m s^{-1}. (c) Angular velocity shear $\Delta\Omega_{\rm lat}$ (eq. 5.1) near the surface (upper curve, green) and at mid-convection zone (lower, red).

5.5 Conclusions

The ability for a dynamo to build wreaths of strong magnetic fields in the bulk of the convection zone has largely been a surprise, for it had generally been supposed that turbulent convection would disrupt such magnetic structures. To avoid these difficulties, many solar and stellar dynamo theories shift the burden of magnetic storage, amplification and organization to a tachocline of shear and penetration at the base of the convection zone where motions are more quiescent. In contrast, our simulations of rapidly rotating stars are able to achieve sustained global-scale dynamo action within the convection zone itself, with the magnetic structures both being built and able to survive while embedded deep within the turbulence. These dynamos are able to circumvent the Parker instability by means of turbulent Reynolds and Maxwell stresses that contribute to the mechanical force balance and prevent the wreaths from buoyantly escaping the convection zone. This striking behavior may be enabled by the stars rotating three to five times faster than the current Sun, which yields a strong differential rotation that is a key element in the dynamo behavior. It is quite interesting that in our dynamo cases the angular velocity contrast in latitude and radius is almost constant at differing rotation rates, whereas our hydrodynamic cases tend to have increasing $\Delta\Omega$ with more rapid rotation Ω_0.

As we have seen in this chapter, we have achieved some dynamo states that are persistent. Others flip the sense of their magnetic fields. In our case D3 the global-scale fields have small vacillations in their amplitudes, but the magnetic wreaths retain their identities for many thousands of days. This represents hundreds of rotation periods and several magnetic diffusion times, indicating that the dynamo has achieved a persistent equilibrium. As we will see next in Chapter 6, increasing the rotation rate yields more complex time dependence.

Chapter 6

Cyclic Dynamo Action Achieved at $5\,\Omega_\odot$

Our more rapidly rotating simulation, case D5 at five times the current solar rate, also builds strong wreaths of magnetism that span the convection zone. However, in this simulation the dynamo is not steady in time and instead goes through cycles of activity. During a cycle, the global-scale magnetic fields wax and wane in strength and at the lowest field strengths they can flip their polarity. We shall begin by looking at the general properties of the convective flows and their associated differential rotation and meridional circulation, and then turn to examining the nature of the magnetic fields and their time-varying behavior.

6.1 Patterns of Convection in Case D5

Figure 6.1*a* shows a snapshot of the patterns of convection realized in case D5 near the top of the domain. Much as in the radial velocity patterns shown for case D3 (Figs. 5.1*a*,5.2*e*), here with faster rotation we continue to have prominent north-south aligned cells in the lower latitudes and more isotropic patterns near the poles. There is some modulation with longitude in the equatorial roll amplitudes. The downflows are fast and narrow, while the upflows are broader and slower. The convection establishes a prominent differential rotation, with a fast equator and slow poles (Fig. 6.1*c*).

As in case D3, here too the convective downflow structures propagate more rapidly than the differential rotation in which they are embedded. In the equatorial band, these

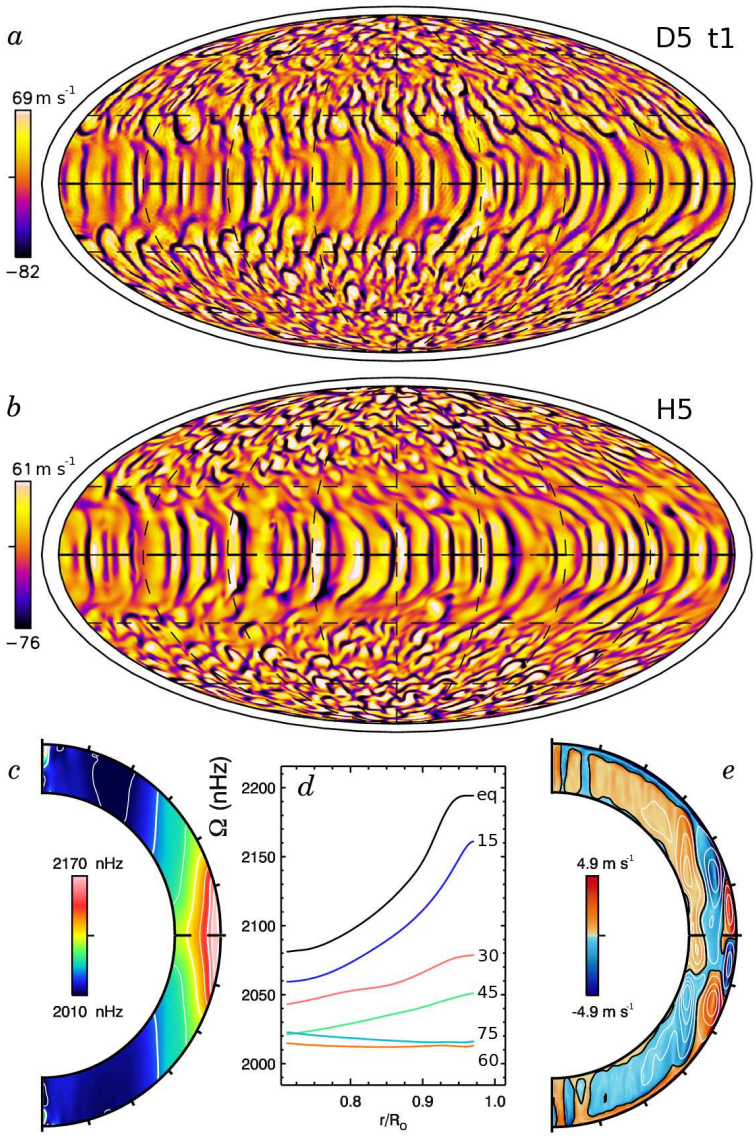

FIGURE 6.1 — Patterns of convection in case D5. This simulation is rotating at five times the solar rotation rate. (*a*) Radial velocity v_r in Mollweide projection at $0.95R_\odot$ for case D5. This snapshot samples day 3880 (time t1) when the magnetic fields are strong. (*b*) Companion hydrodynamic case H5, whose stronger differential rotation shears out convective structures in the mid-latitudes. (*c*) Profile of mean angular velocity $\Omega(r, \theta)$ for case D5, with (*d*) radial cuts of Ω at selected latitudes. (*e*) Meridional circulations for case D5, with magnitude and sense of circulation indicated by color (red counter-clockwise, blue clockwise) and streamlines of mass flux overlaid.

structures move in a prograde fashion and at high latitudes in the retrograde sense. In the polar regions, the radial velocity patterns have a somewhat cuspy appearance, with the strongest downflows appearing to favor the westward and lower-latitude side of each convective cell. This may be a consequence of the strong retrograde differential rotation in those regions.

The convective structures are quite similar to those realized in the hydrodynamic case H5 (Fig. 6.1*b*), though there are some noticeable differences, particularly at the mid latitudes (around $\pm 30^\circ$). In the hydrodynamic case there is little radial flow in these regions, as the strong differential rotation shears out the convective cells. This region is equatorward of the tangent cylinder, an imaginary boundary tangent to the base of the convection zone and aligned with the rotation axis. For rotating convective shells, it has generally been found that the dynamics are different inside and outside the tangent cylinder, due to differences in connectivity and rotational constraint in these two regions (e.g., Busse 1970). The tangent cylinder in our geometry intersects with the stellar surface at roughly $\pm 42^\circ$ of latitude. In our compressible simulations, we generally find that the convective patterns in the equatorial regions are bounded by a conic surface rather than the tangent cylinder (Brown et al. 2008). In case H5 the strong differential rotation serves to disrupt the convection at the mid-latitudes. In contrast, in the dynamo case D5 the differential rotation is substantially weaker in both radial and latitudinal angular velocity contrasts (Table 5.1). As is evident in Figure 6.1*a*, the convective cells fill in this region quite completely.

The time-averaged angular velocity profile $\Omega(r, \theta)$ is shown for case D5 in Figures 6.1*c*, *d*. The latitudinal angular velocity contrast $\Delta\Omega_{\rm lat}$ and radial contrast $\Delta\Omega_r$ in this case is remarkably similar in amplitude to that realized in case D3 (Table 5.1), even though the basic rotation rate Ω_0 is substantially faster. This is in marked contrast to our hydrodynamic companion cases where faster rotation leads to greater angular velocity contrasts. The accompanying meridional circulation patterns for case D5 (Fig. 6.1*e*)

appear to have three major cells of circulation in each hemisphere. These flows are weaker than in case D3. They are very similar to the circulations found in case H5.

6.2 Oscillations in Energies and Changes of Polarity

The dynamo action realized by the convection in case D5 exhibits significant changes in time. This time-varying behavior is readily visible as oscillations of the volume-averaged kinetic and magnetic energy densities, as shown in Figure 6.2*a* at a time long after the dynamo has saturated and reached equilibration. Here the kinetic energy of differential rotation (DRKE) undergoes factor of five changes on periods of 500-1000 days. As DRKE decreases the magnetic energies increase. Moving in concert are the mean toroidal (TME) and mean poloidal (PME) magnetic energies. The mean poloidal fields appear to lag slightly behind the mean toroidal fields as they both change in strength. The fluctuating magnetic energies (FME) track the largest rises in the mean fields but decouple during many of the deepest dips. In contrast, the variations in convective kinetic energies (CKE) show little organized behavior in time, and appear to change substantially only when the differential rotation is highly suppressed during the period from day 7500 to day 8300. The energy contained in the meridional circulations (MCKE) is weaker and not shown. Though it varies somewhat in time, there is not a clear relation to the changes in magnetic energies.

Magnetic energies in case D5 can rise to be a substantial fraction of the kinetic energies. Averaged over the nearly 16000 days shown here, the magnetic energies are about 17% of the kinetic energies. During individual oscillations the magnetic energies can range from a few percent of the kinetic energies to levels as high as 50%. The kinetic energy is largely in the fluctuating convection and differential rotation, with CKE fairly constant and ranging from 15-60% of the total kinetic energy as DRKE grows and subsides, itself contributing between 40 to 85% of the kinetic energy. The magnetic energies are largely split between the mean toroidal fields and the fluctuating fields, with

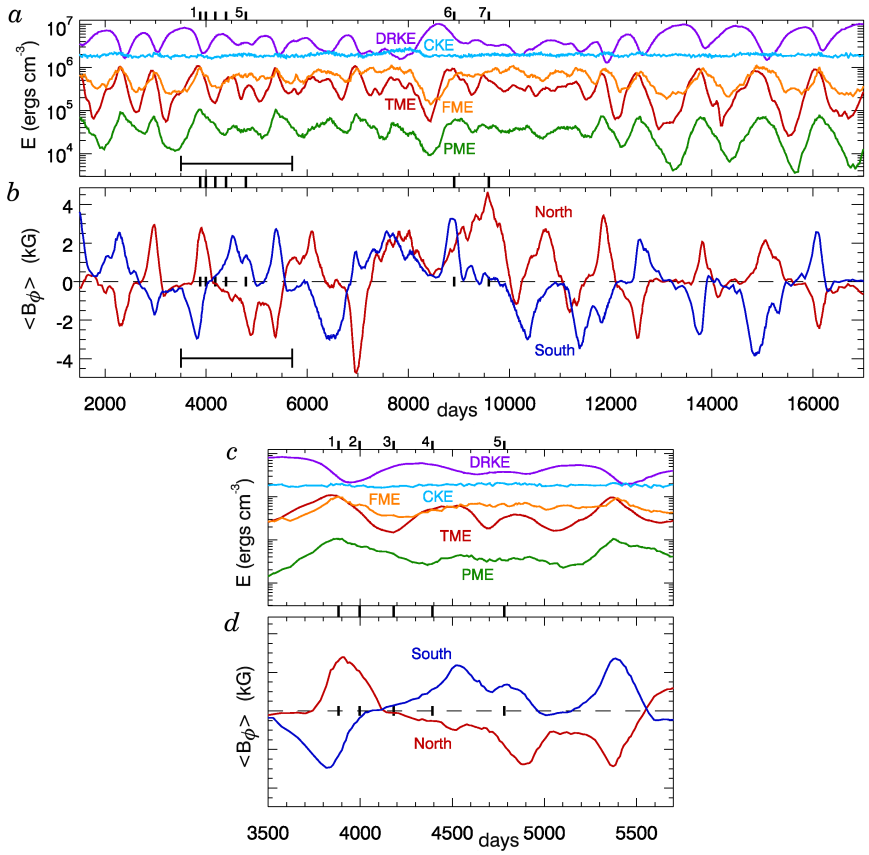

FIGURE 6.2 — Complex time evolution in case D5 with flips in polarity of magnetic wreaths. (a) Volume-averaged energy densities for kinetic energy of convection (CKE), differential rotation (DRKE) and for magnetic energy in fluctuating fields (FME), in mean toroidal fields (TME) and in mean poloidal fields (PME) as labeled. Oscillations on roughly 500-1000 day periods are visible in the magnetic energies and in DRKE, though CKE stays nearly constant. (b) Mean toroidal field $\langle B_\phi \rangle$ averaged over entire northern and southern hemispheres (labeled) at mid-convection zone ($0.85R_\odot$). Early in the simulation, opposite polarities dominate each hemisphere. Several reversals occur, along with several extreme excursions which do not flip the polarity of the global-scale field. During the interval from roughly day 7700 to 10200, the dynamo falls into peculiar single polarity states, with one polarity dominating both hemispheres. Bracketed interval from day 3500 to 5700 spans one full polarity reversal; (c) shows volume-averaged energy densities during this period, and (d) the mean toroidal field with same vertical axis scales as in (a, b). Thick labeled tick marks above a, c indicate time samples used in later images.

TME containing about 35% of the magnetic energy on average, FME containing about 61% and PME containing 4%. The roles of these energy reservoirs change somewhat through each oscillation. At any one time, between 10 and 60% of the magnetic energy is in TME while FME contains between 30 and 85% of the total. Meanwhile, PME can comprise as little as 1% or as much as 10% of the total. Generally, PME is about 12% of TME, but because PME lags the changes in TME slightly, there are periods of time when PME is almost 40% of TME.

The global-scale magnetic fields can reverse their polarities during some of the oscillations in magnetic energies. This is evident in Figure 6.2*b* showing averages at mid-convection zone of the longitudinal magnetic field $\langle B_\phi \rangle$ over the northern and southern hemispheres. Reversals in field polarity occur periodically, with typical time scales of roughly 1500 days. These reversals appear to happen shortly after peak magnetic energies are achieved, but do not occur every time magnetic energies undergo a full oscillation. Rather, it appears that several failed reversals occur where the magnetic energies drop and the average fields decline in strength, only to return with the same polarity a few hundred days later, for each successful polarity reversal.

We focus in the following discussion on one such reversal, shown in closeup in Figures 6.2*c*, *d* and spanning the interval of time between days 3500 and 5700. Two reversals occur during this interval, with the global polarities flipping into a new state at roughly day 4100 and then changing back again at about day 5500. Detailed measurements of kinetic and magnetic energies during this interval are shown in Table 5.2.

6.3 Global-Scale Magnetic Reversals

The nature of the global-scale magnetic fields during the reversal spanning days 3500-5700 are presented in detail in Figure 6.3. Several samples of longitudinal magnetic field B_ϕ are shown at mid-convection zone spanning this time period. The timing of these samples is indicated in Figure 6.2 by numeric labels and likewise in Figure 6.3*a*

which shows azimuthally-averaged $\langle B_\phi \rangle$ in a time-latitude map that spans the reversal.

Before a reversal, the magnetic wreaths of case D5 are very similar in appearance to the wreaths realized in case D3. They are dominated by the azimuthally-averaged component of B_ϕ, while also showing small-scale variations where convective plumes distort the fields (Fig. 6.3*b*). At mid-convection zone, typical longitudinal field strengths are of order ± 13 kG, while peak field strengths there can reach ± 40 kG. Meanwhile $\langle B_\phi \rangle$ is fairly anti-symmetric between the northern and southern hemispheres (Fig. 6.3*g*). Shortly before a reversal, the magnetic wreaths strengthen in amplitude and become more anti-symmetric about the equator.

They reach their peak values just before the polarity change at roughly day 4000 but then quickly begin to unravel, gaining significant structure on smaller scales (Fig. 6.3*c*). At the same time, prominent magnetic structures detach from the higher-latitude edges and begin migrating toward the polar regions. Meanwhile, $\langle B_\phi \rangle$ loses its anti-symmetry between the two hemispheres, with $\langle B_\phi \rangle$ in one hemisphere typically remaining stronger and more concentrated than in the other (Fig. 6.3*h*). The stronger hemisphere (here the northern) retains its polarity for about 100 days as the fields in the other hemisphere (here southern) weaken and reverse in polarity. At this point the new wreaths of the next cycle, with opposite polarity, are already faintly visible at the equator.

Within 100 days these new wreaths grow in strength and become comparable with the structures they replace, which are still visible at higher latitudes (Figs. 6.3*d*, *i*). The mean $\langle B_\phi \rangle$ begins to contribute significantly to the overall structure of the new wreaths, and soon the polarity reversal is completed. In the interval immediately after the reversal, small-scale fluctuations still contribute significantly to the overall structure of the wreaths, and B_ϕ has complicated structure at mid-convection zone. At this time, the peak magnetic field strengths are somewhat lower, at about ± 20 kG. As $\langle B_\phi \rangle$ becomes stronger, the wreaths return to an anti-symmetric state, with similar

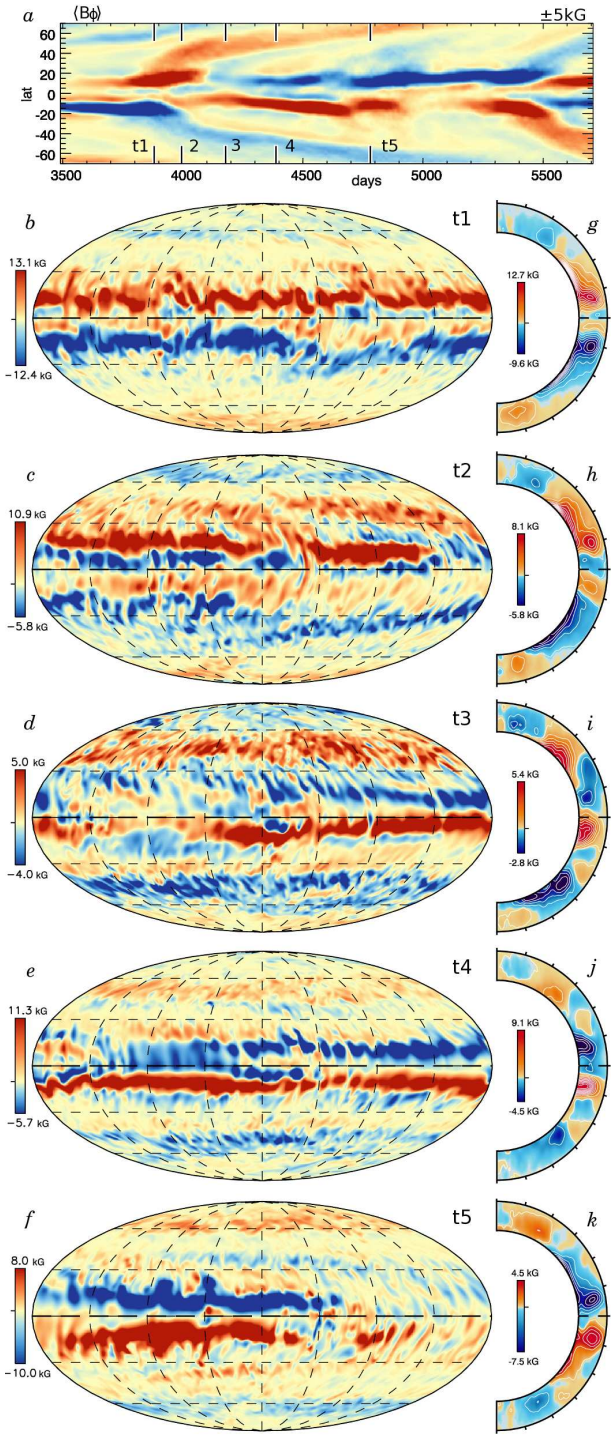

FIGURE 6.3 — Evolution of B_ϕ during a polarity reversal in case D5. (a) Time-latitude plot of $\langle B_\phi \rangle$ at mid-convection zone. $(b-f)$ Snapshots of B_ϕ in Mollweide projection at mid-convection zone $(0.85R_\odot)$ at times indicated by numbers in a. Between reversals the field is dominated by the mean component, but during reversals substantial fluctuations develop. $(g-k)$ Accompanying samples of azimuthally-averaged $\langle B_\phi \rangle$, showing structure of mean fields with radius and latitude at same instants in time.

amplitudes and structure in both the northern and southern hemispheres (Figs. 6.3e, j). They look much as they did before the reversal, though now with opposite polarities.

The wreaths from the previous cycle appear to move through the lower convection zone and toward higher latitudes. This can be seen variously in the time-latitude map at mid-convection zone (Fig. 6.3a), in the Mollweide snapshots (Figs. 6.3$c-e$), as well as in the samples of $\langle B_\phi \rangle$ (Figs. 6.3$h-j$). This poleward migration is likely due to hoop stresses within the magnetic wreaths and an associated poleward-slip instability (e.g., Spruit & van Ballegooijen 1982; Moreno-Insertis et al. 1992). Even at late times some signatures of the previous wreaths persist in the polar regions, and are still visible in Figures 6.3e, j at day 4390. They are much weaker in amplitude than the wreaths at the equator, but they persist until the wreaths from the next cycle move poleward and replace them. As they approach the polar regions, the old wreaths dissipate on both large and small scales, for the vortical polar convection shreds them apart and ohmic diffusion reconnects them with the relic wreaths of the previous cycle.

Though reversals occur on average once every 1500 days, substantial variations can occur on shorter time scales. Here at mid-cycle the mean longitudinal field $\langle B_\phi \rangle$ becomes quite weak as the wreaths become concentrated in smaller longitudinal intervals of the equatorial region (as in Figs. 6.3f, k at day 4780). At other times the mean longitudinal fields become quite asymmetric, with one hemisphere strong and one weak (i.e., during days 4900-5200) before regaining their anti-symmetric nature shortly prior to the next reversal.

6.4 Temporal Changes in Differential Rotation

The strong magnetic fields in case D5 suppress the global-scale flow of differential rotation. As the fields themselves vary in strength, the differential rotation responds in turn, becoming stronger as the fields weaken and then diminishing as the fields are amplified. These cycles of faster and slower differential rotation are visible in the traces

of DRKE shown in Figure 6.2*a*. We revisit here the interval explored in closer detail both in Figure 6.2*c* and in Figure 6.3, spanning days 3500 to 5700 of the simulation and one full polarity reversal.

The angular velocity Ω at mid-convection zone is shown for this period as a time-latitude map in Figure 6.4*a*. Here again the timing marks t1–t5 refer to the snapshots of B_ϕ shown in Figures 6.3$b-k$. In the equatorial regions, the differential rotation remains fast and prograde, but with some modulation in time. Prominent structures of speedup are visible propagating toward the poles at the high latitudes. These structures are much more evident when we subtract the time-averaged profile of Ω for this period at each latitude (Fig. 6.4*b*). They appear as strong, tilted fast (red) structures extending from roughly $\pm 30^\circ$ latitude poleward. In the northern hemisphere, three such structures are launched over this interval. In contrast, in the south only two such structures are evident. One is perhaps launched around day 4500 but does not survive or propagate. Comparing these features with the propagation of magnetic fields shown in Figure 6.3*a* over the same interval, we find that velocity speedup features are well correlated with the poleward migration of mean longitudinal magnetic field. The velocity features bear some resemblance to the poleward branch of torsional oscillations observed in the solar convection zone over the course of a solar magnetic activity cycle, though on a much shorter time scale here as befits the correspondingly shorter time between magnetic polarity reversals in these dynamo simulations.

These velocity features propagate toward the poles relatively slowly. In a period of roughly 500 days they travel about 40° in latitude, or a distance of about 410 Mm. Their propagation velocity is about 0.8 Mm day^{-1} or about 9 m s^{-1}. This is considerably slower than the fluctuating latitudinal flows associated with the convection which at this depth have peak speeds of ± 200 m s^{-1} during this time period. The meridional circulations have amplitudes of about ± 6 m s^{-1} here but do not have a latitudinal structure at all similar to the pattern propagation. The propagation speed of the speedup

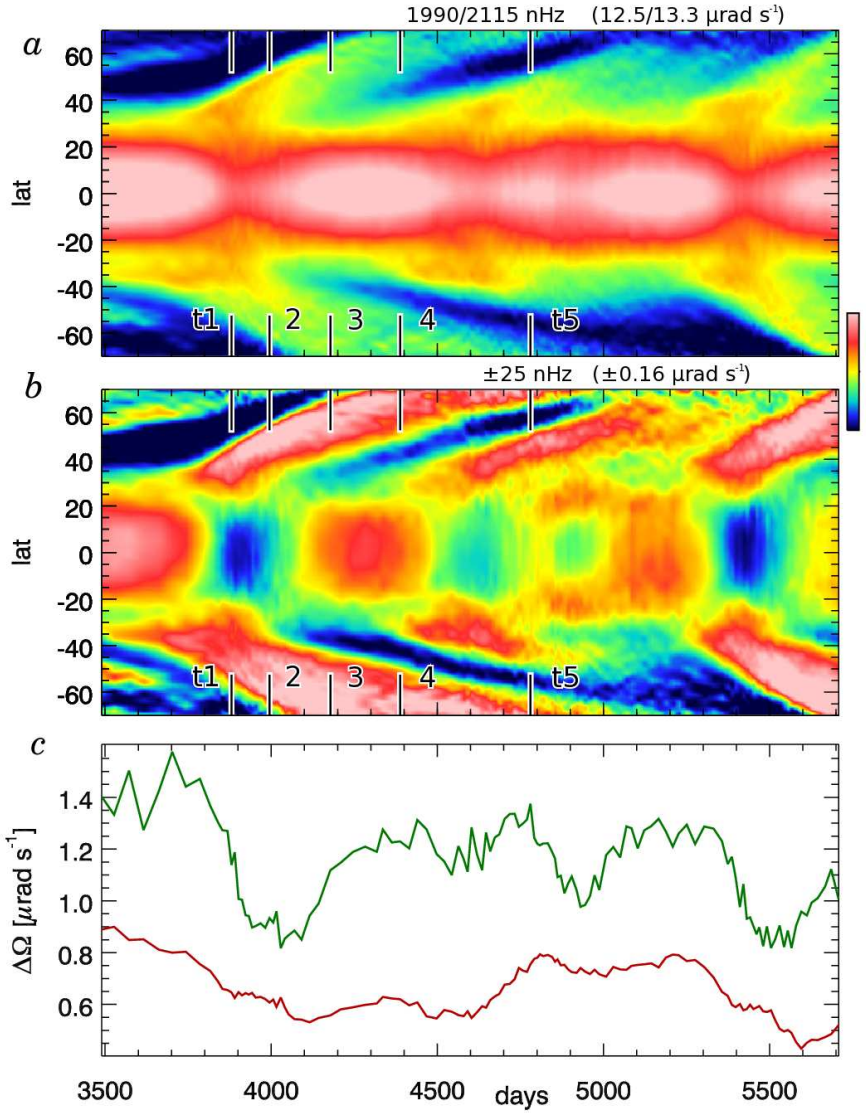

FIGURE 6.4 — Time-varying differential rotation in case D5. (a) Time-latitude map of angular velocity Ω at mid-convection zone ($0.85R_\odot$). There are substantial temporal variations at both the equator and high latitudes. (b) These are accentuated by subtracting the time-averaged profile of $\Omega(r,\theta)$ at each latitude. Visible are poleward propagating speedup structures at high latitudes and more uniform modulations near the equator. (c) Corresponding variations in $\Delta\Omega_{\rm lat}$ near the surface (upper curve, green) and at mid-convection zone (lower, red).

patterns is closer to the Alfvén velocity of the mean latitudinal magnetic fields, namely

$$v_{A,\theta} = \frac{\langle B_\theta \rangle}{\sqrt{4\pi\bar{\rho}}}. \tag{6.1}$$

At mid-convection zone the mean density is about 0.065 g cm^{-3} and $\langle B_\theta \rangle$ in the poleward propagating plumes ranges between roughly $\pm$1.5 kG, yielding Alfvén velocities of about $\pm$17 m s^{-1}. This poleward migration may also be due to a poleward-slip instability arising from the strong toroidal fields. In this scenario, if we neglect rotation and turbulent pumping in latitude (e.g., Moreno-Insertis et al. 1992; Jouve & Brun 2009), the propagation speed should be approximately the Alfvén velocity of the mean toroidal magnetic fields, or about $\pm$45 m s^{-1} based on a mid-convection zone B_ϕ of approximately $\pm$4 kG in the propagating features. If the poleward-slip instability is occurring, the velocity speedup features may result from conservation of angular momentum in the plasma that travels poleward with the wreaths. Rotation is likely to partially stabilize wreaths against poleward-slip (Moreno-Insertis et al. 1992), and this may help explain their slower poleward propagation. The leaky topology of the wreaths will allow plasma to escape these structures, and this may modify the rate of their poleward propagation. The weak propagating features seen in case D3 (Fig. 5.5) required nearly 700 days to propagate a similar distance in latitude. This difference may be due to the somewhat lower magnetic field strengths achieved in that dynamo.

With the expanded sensitivity of Figure 6.4*b*, we can see that the equatorial modulation appears as fast and slow pulses which span the latitude range of $\pm 20^\circ$. These variations are fairly uniform across this equatorial region. The velocity variations at the equator do not correspond with the equatorial propagating branch of torsional oscillations seen in the Sun (Thompson et al. 2003). In the Sun, the equatorial branch may arise from enhanced cooling in the magnetically active regions (e.g., Spruit 2003; Rempel 2006, 2007).

The temporal variations of the angular velocity contrast in latitude $\Delta\Omega_{\rm lat}$ is shown for this period in Figure 6.4*c*. At mid-convection zone (sampled by red line) the variations in $\Delta\Omega_{\rm lat}$ are modest, varying by roughly 15%. Near the surface (green line) $\Delta\Omega_{\rm lat}$ shows more substantial variations, with large contrasts when the fields are strong in the magnetic cycle (prior to t1) and smaller contrasts when the fields are in the process of reversing (t2, t3). These near-surface values of $\Delta\Omega_{\rm lat}$ are reported in Table 5.1, averaged over this entire period (avg) and at points in time when the contrast is large (max, at day 3702) and small (min, at day 4060).

6.5 Sampling Many Magnetic Cycles in Case D5

The variations of angular velocities over considerably longer intervals of time for case D5 are shown in Figures 6.5a, b. Here too we see the equatorial modulation over many magnetic cycles and the poleward propagating speedup bands. Asymmetries between the northern and southern hemisphere are evident at many times in different cycles. The latitudinal angular velocity contrasts shown in Figure 6.5*c* exhibit large variations. Successive magnetic cycles can have distinctly different angular velocity contrasts, and there are additional long-term modulations that span many magnetic cycles.

A sampling of the associated magnetic field behavior is shown in the time-latitude maps of $\langle B_\phi \rangle$ and $\langle B_\theta \rangle$ in Figures 6.6a, b. From day 1500 to 7300, four cycles occur in which wreaths of opposite polarity are achieved in each hemisphere. After this period, the dynamo explores unusual single-polarity states. Here either a single wreath is built (t7), or two wreaths of the same polarity (t6) occupy the two hemispheres. After day 10700 the dynamo emerges from this state and returns to building two wreaths of opposite polarity which flip in their sense an additional three times as the simulation continues.

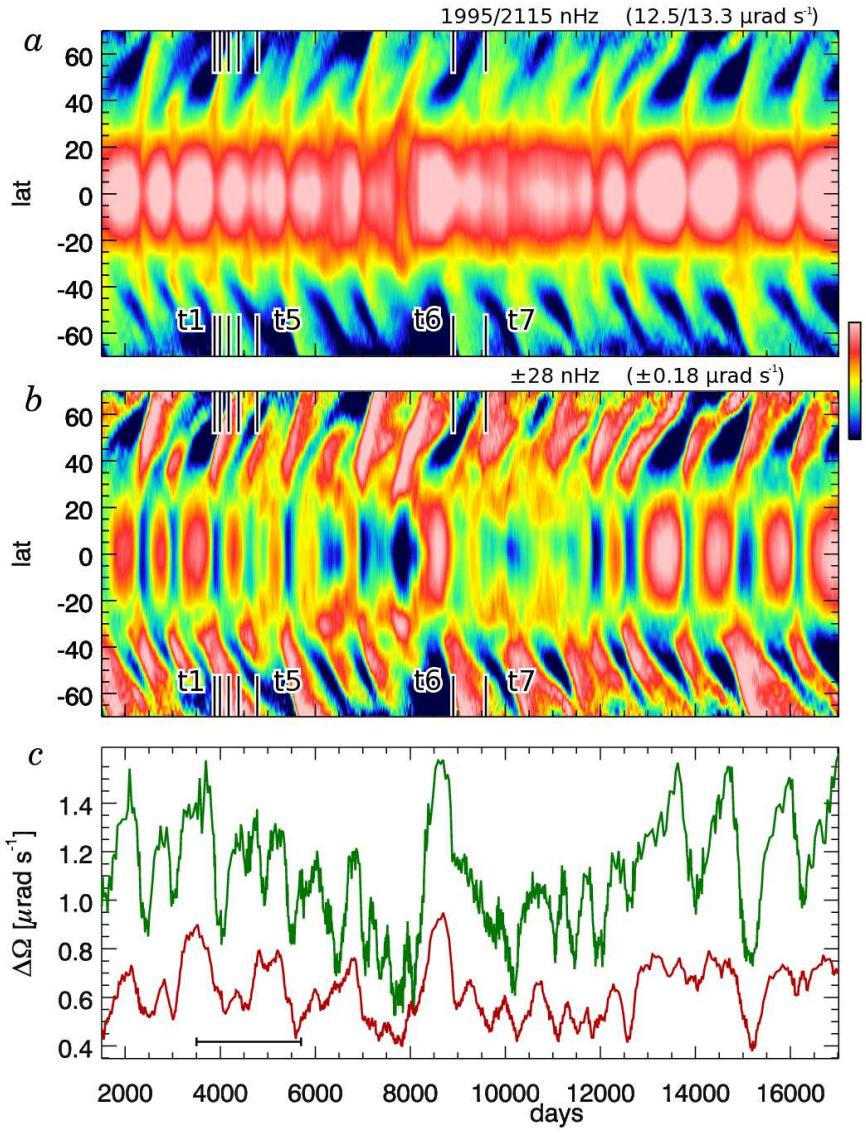

FIGURE 6.5 — Extended history of varying differential rotation in case D5. (a) Variations of $\Omega(r, \theta)$ at mid-convection zone. (b) Temporal variations are emphasized by subtracting the time-averaged profile of Ω. Poleward propagating speedup structures are visible in each magnetic oscillation. (c) Variations in $\Delta\Omega_{\rm lat}$ near the surface (upper curve, green) and at mid-convection zone (lower, red).

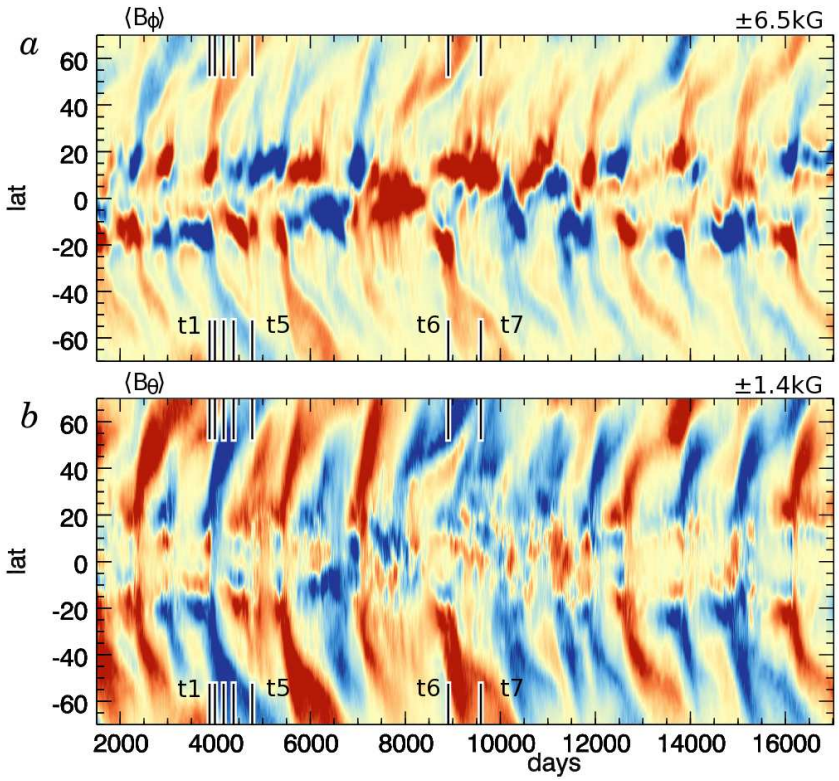

FIGURE 6.6 — Time-latitude plots of magnetic fields in case D5. Shown at mid-convection zone are (*a*) mean longitudinal field $\langle B_\phi \rangle$, and (*b*) mean colatitudinal field $\langle B_\theta \rangle$. Cycles of activity are visible, with fields changing polarity in the equatorial region. Also prominently visible are plumes of field reaching toward the polar regions in a manner recalling Fig. 5.4. The time samples used in Figs. 6.3 and 6.7 are indicated.

The poleward propagating magnetic features shown previously in Figures 6.3a are evident throughout this longer time sampling, now appearing as nearly vertical streaks in both $\langle B_\phi \rangle$ and $\langle B_\theta \rangle$. These features continue to correlate well with the velocity speedup features evident in Figure 6.5b.

6.6 Strange States and Wreaths of a Single Polarity

These oscillating dynamos occasionally wander into distinctly different states, and this occurs for case D5 around day 7300. Instead of the two nearly anti-symmetric wreaths of opposite polarity above and below the equator, the dynamo enters a state where the polarity in each hemisphere is the same, as shown in Figures 6.7a, b at day 8903. Here two wreaths of same polarity occupy the two hemispheres and persist for an interval of more than 500 days. The positive-polarity B_ϕ reaches average amplitudes of 18 kG while the negative polarity structures have average amplitudes around 3 kG. The azimuthally-averaged profiles of $\langle B_\phi \rangle$ emphasize that these wreaths span the convection zone and have the same polarity everywhere. During this interval of time, the mean poloidal field has changed from an odd-parity state, with strong contributions from the odd-ℓ components, to an even-parity state where the even-ℓ components are more prominent.

The dynamo can also achieve states where only a single wreath is built in the equatorial regions, as in Figures 6.7c, d at day 9590. Here a single strong wreath of positive polarity fills the northern hemisphere, with $\langle B_\phi \rangle$ reaching a peak amplitude of +18 kG. This unique structure persists for about 800 days before the dynamo flips polarity and builds a strong wreath of negative polarity. The predecessor of this new wreath can be seen in profiles of $\langle B_\phi \rangle$ where a much weaker structure of negative polarity is visible in the lower convection zone.

The strong magnetic fields realized in the single wreath states react back on the convective flows. This is evident in the accompanying snapshot of radial velocities

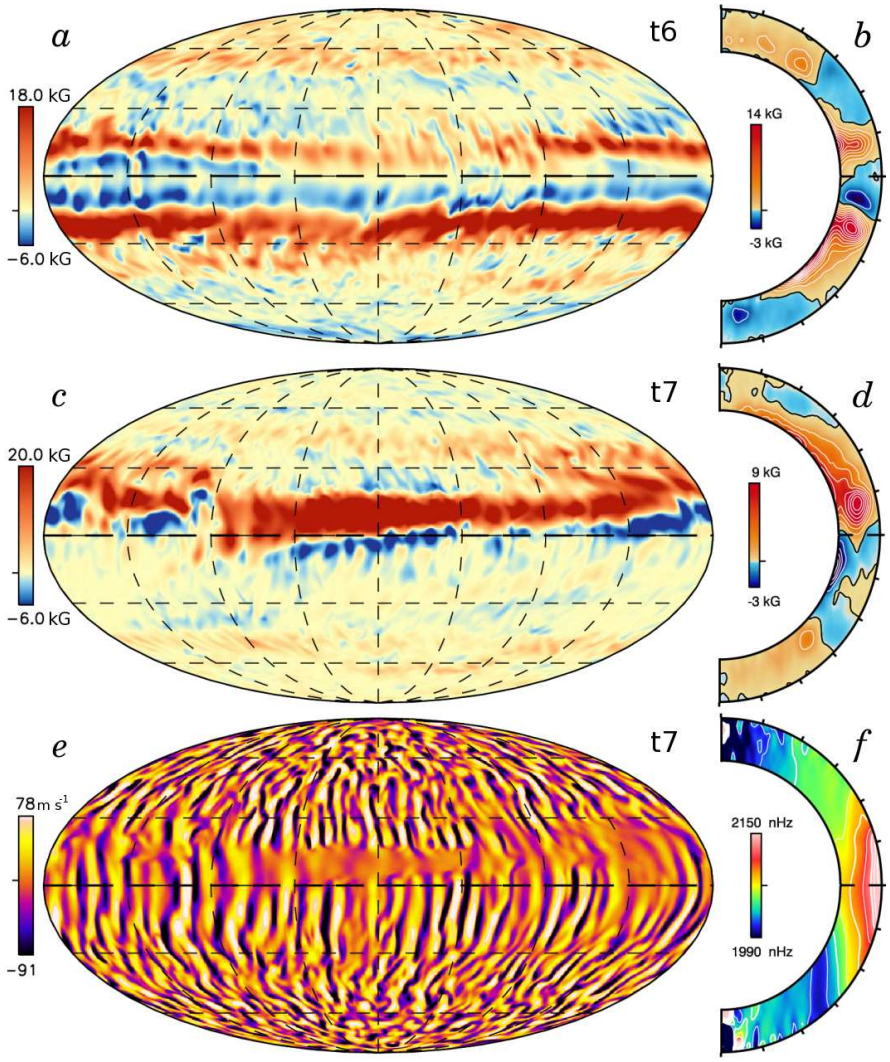

FIGURE 6.7 — Strange single-polarity states in case D5. (a) Snapshot of B_ϕ at mid-convection zone, showing two strong wreaths of the same polarity. (b) Instantaneous profile of $\langle B_\phi \rangle$ at same time. (c) Snapshot of B_ϕ at mid-convection zone at a time when a single wreath is formed. (d) Weaker negative polarity structures are visible in profile of $\langle B_\phi \rangle$ at same instant. (e) Accompanying snapshot of v_r at mid-convection zone, showing flows strongly affected by magnetism. (f) The instantaneous differential rotation, shown here as profile of $\Omega(r, \theta)$, is unaffected by the strong wreath.

at mid-convection zone (Fig. 6.7e). In a narrow band spanning $0 - 20^\circ$ latitude and coinciding with the strong tube, the upflows and downflows have been virtually erased. Fluctuations in v_ϕ and v_θ are also very small in this region, and the flow is dominated by the streaming flows of differential rotation. Within the wreath the total magnetic energy (ME) at mid-convection zone is locally about 10 to 100 times larger than the total kinetic energy (KE), while outside the wreath KE exceeds ME by factors of roughly 10 to 10^4 at this depth. We see similar restriction of the convective flows whenever the magnetic fields become this strong.

The differential rotation itself (Fig. 6.7f) is largely unaffected by the presence of the strong magnetic wreath. There is no clear signature of faster flow down the middle of the wreath. Likewise, there is no sign of the structure in profiles of the thermodynamic variables P, T, S, or ρ, with the mean profile instead dominated by latitudinal variations consistent with thermal wind balance.

6.7 Conclusions

In our case D5 the oscillations can become large, and may result in the global-scale fields repeatedly flipping their polarity. At times this dynamo appears to be cyclic but in other intervals it behaves more chaotically.

The transition to richer time dependence with increasing rotation rate in case D5 appears to arise from subtle changes and phasing relationships between the toroidal and poloidal magnetic production terms. These are difficult to assess, since the production terms themselves are complex in space and now vary in time as well. It is evident that the mean poloidal fields lag the changes in the mean toroidal fields, and there is clear migration of magnetic field to the higher latitudes during a reversal. This latitudinal migration may result from a polarward-slip instability, triggered by the stronger magnetic fields that are generated by this dynamo, and this migration may lead to the oscillations in field strength and polarity. The analysis of magnetic field production that we

have carried out for case D3 (Chapter 7) requires significant averaging of the turbulent correlations, accomplished there by time averaging, to obtain a coherent picture of the balances achieved. This has not yet been tractable for the oscillating solutions, as the generation terms change on shorter time scales than needed to obtain stable averages of the turbulent processes. It appears that the imbalances in the production and destruction of mean magnetic fields during cyclic behavior are modest, and currently we cannot pinpoint just which terms out of the large medley serve to drive the oscillations.

These dynamo oscillations are not special to case D5. Indeed, we have explored a broader class of oscillating dynamo solutions, which will be detailed in Chapter 8. Some of these solutions are realized by taking our more slowly rotating case D3 to higher levels of turbulence by reducing the eddy diffusivities, while others are achieved at even higher rotation rates. We find such global-scale oscillations and polarity reversals fascinating, since these appear to be the first self-consistent 3-D stellar dynamo simulations which achieve such temporally organized behavior in the bulk of the convection zone.

Accompanying the oscillations in global-scale magnetic field are changes in the differential rotation, and these signatures are the most likely to be found through stellar observations. The angular velocity contrast $\Delta\Omega_{\rm lat}$ between the equator and high latitudes can vary by 20% over periods of hundreds or thousands of days. The patterns of speedup which we find propagating toward the polar regions of these dynamos may have correspondence with the polar branch of the torsional oscillations which are observed in the Sun. The speedup features may arise from conservation of angular momentum in fluid which is partially trapped within the wreaths as they slip toward the poles. The leaky nature of our wreaths will modify this somewhat and that may explain why the wreaths are not stabilized by rotation (e.g., Moreno-Insertis et al. 1992).

In the next chapter, we return to our steady case D3 to examine how the magnetic fields are produced and maintained by the turbulent convection and global-scale flows against resistive dissipation.

Chapter 7

Analysis of Production terms in Dynamos with Sustained Wreaths

The magnetic wreaths formed in case D3 are dominated by strong mean longitudinal field components and show little variation in time. To understand the physical processes responsible for maintaining these magnetic wreaths, we examine the terms arising in the time- and azimuth-averaged induction equation for case D3. We derive diagnostic tools to evaluate the generation and transport of magnetic field in a magnetized and rotating turbulent convection zone. This derivation is in spherical coordinates, and is under the anelastic approximation.

7.1 Production of Axisymmetric Toroidal Field

We begin our analysis by exploring the maintenance of the mean toroidal field $\langle B_\phi \rangle$. Here it is helpful to break the induction term from equation (2.4) into contributions from shear, advection and compression. In the induction equation (2.4), the first term on the right hand side represents production of magnetic field while the second term represents its diffusion. We rewrite the production term to make the contributions of shear, advection and compressible effects more explicit as

$$\boldsymbol{\nabla} \times (\boldsymbol{v} \times \boldsymbol{B}) = (\boldsymbol{B} \cdot \boldsymbol{\nabla})\boldsymbol{v} - (\boldsymbol{v} \cdot \boldsymbol{\nabla})\boldsymbol{B} - \boldsymbol{B}(\boldsymbol{\nabla} \cdot \boldsymbol{v}). \tag{7.1}$$

Under the anelastic approximation the divergence of $\boldsymbol{v}$ can be expressed in terms of the logarithmic derivative of the mean density because

$$\boldsymbol{\nabla}\cdot(\bar{\rho}\boldsymbol{v}) = 0 = \bar{\rho}(\boldsymbol{\nabla}\cdot\boldsymbol{v}) + (\boldsymbol{v}\cdot\boldsymbol{\nabla})\bar{\rho},$$

and therefore

$$\boldsymbol{\nabla}\cdot\boldsymbol{v} = -v_r\frac{\partial}{\partial r}\ln\bar{\rho}. \tag{7.2}$$

The induction equation thus becomes

$$\frac{\partial \boldsymbol{B}}{\partial t} = \underbrace{(\boldsymbol{B}\cdot\boldsymbol{\nabla})\boldsymbol{v}}_{\text{shearing}} - \underbrace{(\boldsymbol{v}\cdot\boldsymbol{\nabla})\boldsymbol{B}}_{\text{advection}} + \underbrace{v_r\boldsymbol{B}\frac{\partial}{\partial r}\ln\bar{\rho}}_{\text{compression}} - \underbrace{\boldsymbol{\nabla}\times(\eta\boldsymbol{\nabla}\times\boldsymbol{B})}_{\text{diffusion}} \tag{7.3}$$

As labeled, the first term represents shearing of $\boldsymbol{B}$, the second term advection of $\boldsymbol{B}$, the third one compressible amplification of $\boldsymbol{B}$, and the last term ohmic diffusion.

To identify the processes contributing to the production of mean (axisymmetric) field, we separate our velocities and magnetic fields into mean and fluctuating components $\boldsymbol{v} = \langle\boldsymbol{v}\rangle + \boldsymbol{v}'$ and $\boldsymbol{B} = \langle\boldsymbol{B}\rangle + \boldsymbol{B}'$ where angle brackets denote an average in longitude. Thus $\langle\boldsymbol{v}'\rangle = \langle\boldsymbol{B}'\rangle = 0$ by definition. Expanding the production term of equation (7.3) we obtain the mean shearing term

$$\langle(\boldsymbol{B}\cdot\boldsymbol{\nabla})\boldsymbol{v}\rangle = (\langle\boldsymbol{B}\rangle\cdot\boldsymbol{\nabla})\langle\boldsymbol{v}\rangle + \langle(\boldsymbol{B}'\cdot\boldsymbol{\nabla})\boldsymbol{v}'\rangle, \tag{7.4}$$

the mean advection term

$$-\langle(\boldsymbol{v}\cdot\boldsymbol{\nabla})\boldsymbol{B}\rangle = -(\langle\boldsymbol{v}\rangle\cdot\boldsymbol{\nabla})\langle\boldsymbol{B}\rangle - \langle(\boldsymbol{v}'\cdot\boldsymbol{\nabla})\boldsymbol{B}'\rangle, \tag{7.5}$$

and the mean compressibility term

$$\langle v_r\boldsymbol{B}\frac{\partial}{\partial r}\ln\bar{\rho}\rangle = \left(\langle v_r\rangle\langle\boldsymbol{B}\rangle + \langle v_r'\boldsymbol{B}'\rangle\right)\frac{\partial}{\partial r}\ln\bar{\rho}. \tag{7.6}$$

In a similar fashion, the mean diffusion term becomes

$$-\langle\boldsymbol{\nabla}\times(\eta\boldsymbol{\nabla}\times\boldsymbol{B})\rangle = -\boldsymbol{\nabla}\times(\eta\boldsymbol{\nabla}\times\langle\boldsymbol{B}\rangle). \tag{7.7}$$

The axisymmetric component of the induction equation is written symbolically as:

$$\frac{\partial \langle \boldsymbol{B} \rangle}{\partial t} = P_{\rm MS} + P_{\rm FS} + P_{\rm MA} + P_{\rm FA} + P_{\rm MC} + P_{\rm FC} + P_{\rm MD} \tag{7.8}$$

With $P_{\rm MS}$ representing production of field by mean shear, $P_{\rm FS}$ production by fluctuating shear, $P_{\rm MA}$ advection by mean flows, $P_{\rm FA}$ advection by fluctuating flows, $P_{\rm MC}$ amplification arising from the compressibility of mean flows, $P_{\rm FC}$ amplification arising from fluctuating compressible motions, and $P_{\rm MD}$ ohmic diffusion of the mean fields. In turn, these terms are

$$\begin{aligned}
P_{\rm MS} &= (\langle \boldsymbol{B} \rangle \cdot \boldsymbol{\nabla}) \langle \boldsymbol{v} \rangle , & P_{\rm FS} &= \langle (\boldsymbol{B}' \cdot \boldsymbol{\nabla}) \boldsymbol{v}' \rangle , \\
P_{\rm MA} &= -(\langle \boldsymbol{v} \rangle \cdot \boldsymbol{\nabla}) \langle \boldsymbol{B} \rangle , & P_{\rm FA} &= -\langle (\boldsymbol{v}' \cdot \boldsymbol{\nabla}) \boldsymbol{B}' \rangle , \\
P_{\rm MC} &= (\langle v_r \rangle \langle \boldsymbol{B} \rangle) \frac{\partial}{\partial r} \ln \bar{\rho} , & P_{\rm FC} &= \left(\langle v_r' \boldsymbol{B}' \rangle \right) \frac{\partial}{\partial r} \ln \bar{\rho} , \\
P_{\rm MD} &= -\boldsymbol{\nabla} \times (\eta \boldsymbol{\nabla} \times \langle \boldsymbol{B} \rangle) .
\end{aligned} \tag{7.9}$$

We now expand each of these terms into their full representation in spherical coordinates.

$$\frac{\partial \langle B_\phi \rangle}{\partial t} = P_{\rm MS} + P_{\rm FS} + P_{\rm MA} + P_{\rm FA} + P_{\rm MC} + P_{\rm FC} + P_{\rm MD}$$

$$P_{\rm MS} = \left[\langle B_r \rangle \frac{\partial}{\partial r} + \frac{\langle B_\theta \rangle}{r} \frac{\partial}{\partial \theta} \right] \langle v_\phi \rangle + \frac{\langle B_\phi \rangle \langle v_r \rangle + \cot\theta \langle B_\phi \rangle \langle v_\theta \rangle}{r} \tag{7.10}$$

$$P_{\rm FS} = \left\langle \left[B_r' \frac{\partial}{\partial r} + \frac{B_\theta'}{r} \frac{\partial}{\partial \theta} + \frac{B_\phi'}{r \sin\theta} \frac{\partial}{\partial \phi} \right] v_\phi' \right\rangle + \frac{\langle B_\phi' v_r' \rangle + \cot\theta \langle B_\phi' v_\theta' \rangle}{r} \tag{7.11}$$

$$P_{\rm MA} = -\left[\langle v_r \rangle \frac{\partial}{\partial r} + \frac{\langle v_\theta \rangle}{r} \frac{\partial}{\partial \theta} \right] \langle B_\phi \rangle - \frac{\langle v_\phi \rangle \langle B_r \rangle + \cot\theta \langle v_\phi \rangle \langle B_\theta \rangle}{r} \tag{7.12}$$

$$P_{\rm FA} = -\left\langle \left[v_r' \frac{\partial}{\partial r} + \frac{v_\theta'}{r} \frac{\partial}{\partial \theta} + \frac{v_\phi'}{r \sin\theta} \frac{\partial}{\partial \phi} \right] B_\phi' \right\rangle - \frac{\langle v_\phi' B_r' \rangle + \cot\theta \langle v_\phi' B_\theta' \rangle}{r} \tag{7.13}$$

$$P_{\rm MC} = (\langle v_r \rangle \langle B_\phi \rangle) \frac{\partial}{\partial r} \ln \bar{\rho} , \qquad P_{\rm FC} = \left(\langle v_r' B_\phi' \rangle \right) \frac{\partial}{\partial r} \ln \bar{\rho} \tag{7.14}$$

$$P_{\rm MD} = \eta \nabla^2 \langle B_\phi \rangle - \frac{\eta \langle B_\phi \rangle}{r^2 \sin^2\theta} + \frac{d\eta}{dr} \left(\frac{1}{r} \frac{\partial (r \langle B_\phi \rangle)}{\partial r} \right) \tag{7.15}$$

7.2 Maintaining Wreaths of Toroidal Field

The evolution of the mean longitudinal (toroidal) field $\langle B_\phi \rangle$ is described symbolically in equation (7.8), with individual terms defined in equation (7.9). When we analyze these terms in case D3, we find that $\langle B_\phi \rangle$ is produced by the shear of differential rotation and is dissipated by a combination of turbulent induction and ohmic diffusion. This balance can be restated as

$$\frac{\partial \langle B_\phi \rangle}{\partial t} \approx P_{\rm MS} + (P_{\rm FS} + P_{\rm FA} + P_{\rm MD}) \approx 0\,, \tag{7.16}$$

with $P_{\rm MS}$ representing production by the mean shearing flow of differential rotation, $P_{\rm FS}$ by fluctuating shear, $P_{\rm FA}$ by fluctuating advection, and $P_{\rm MD}$ by mean ohmic diffusion. Those terms are in turn

$$P_{\rm MS} = \left(\langle \boldsymbol{B} \rangle \cdot \boldsymbol{\nabla}\right) \langle \boldsymbol{v} \rangle \big|_\phi, \tag{7.17}$$

$$P_{\rm FS} = \left\langle \left(\boldsymbol{B'} \cdot \boldsymbol{\nabla}\right) \boldsymbol{v'} \right\rangle \big|_\phi, \tag{7.18}$$

$$P_{\rm FA} = -\left\langle \left(\boldsymbol{v'} \cdot \boldsymbol{\nabla}\right) \boldsymbol{B'} \right\rangle \big|_\phi, \tag{7.19}$$

$$P_{\rm MD} = -\boldsymbol{\nabla} \times \eta \boldsymbol{\nabla} \times \langle \boldsymbol{B} \rangle \big|_\phi, \tag{7.20}$$

where brackets again indicate an azimuthal average and primes indicate fluctuating terms: $\boldsymbol{v'} = \boldsymbol{v} - \langle \boldsymbol{v} \rangle$. The detailed implementation of these terms is presented for our spherical geometry in equations (7.10-7.15). These terms are illustrated in Figure 7.1 for case D3, averaged over a 450 day interval from day 6450 to 6900.

The structure of $\langle B_\phi \rangle$ is shown in Figure 7.1*a*. The shearing flows of differential rotation $P_{\rm MS}$ (Fig. 7.1*b*) act almost everywhere to reinforce the mean toroidal field. Thus the polarity of this production term generally matches that of $\langle B_\phi \rangle$. This production is balanced by destruction of mean field arising from both turbulent induction and ohmic diffusion (sum shown in Fig. 7.1*c*). The individual profiles of $P_{\rm FS}$, $P_{\rm FA}$ and $P_{\rm MD}$ are presented in turn in Figures 7.1d, e, f. The terms from turbulent induction ($P_{\rm FS}$ and $P_{\rm FA}$) contribute to roughly half of the total balance, with the remainder carried by ohmic

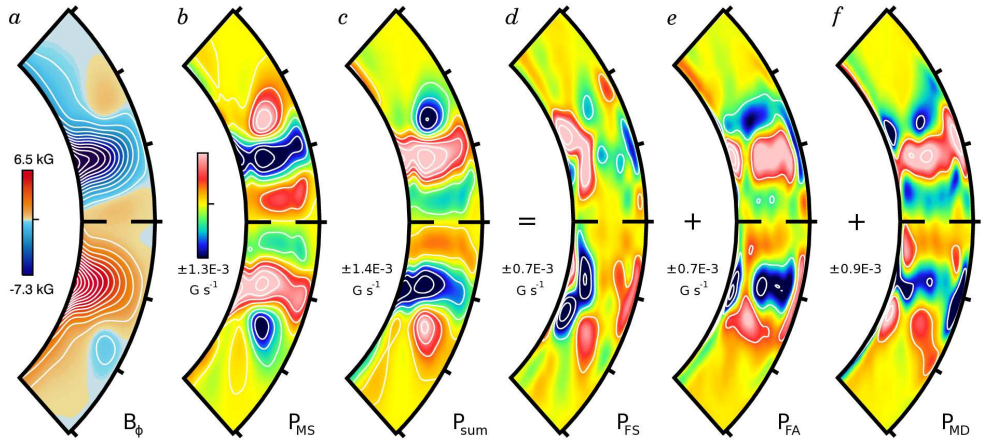

FIGURE 7.1 — Generation of $\langle B_\phi \rangle$ in case D3. The view is from $\pm 45^\circ$ latitude to emphasize the equatorial regions. (a) Mean toroidal field $\langle B_\phi \rangle$ with wreaths strongly evident. (b) Production by $P_{\rm MS}$ serves to build $\langle B_\phi \rangle$. This rate term generally matches the sense of $\langle B_\phi \rangle$, thus being negative (blue in colorbar, with ranges indicated) in the core of the northern wreath and positive (red) in that of the southern wreath. (c) Destruction of mean toroidal field is achieved by the sum of the two fluctuating (turbulent) induction terms and the ohmic diffusion ($P_{\rm FS} + P_{\rm FA} + P_{\rm MD}$). This sum clearly has opposite sense and similar magnitude to $P_{\rm MS}$. We break out these three destruction terms in the following panels. (d) Fluctuating (turbulent) shear $P_{\rm FS}$ is strongest near the high-latitude side of each wreath, and (e) fluctuating (turbulent) advection $P_{\rm FA}$ is strongest in the cores of the wreaths. The sum of these terms ($P_{\rm FS} + P_{\rm FA}$) is responsible for about half the destructive balance, with the remainder coming from (f) the mean ohmic diffusion $P_{\rm MD}$. Some differences arise in the boundary layers at top and bottom.

diffusion of the mean fields ($P_{\rm MD}$). In the core of the wreaths, removal of mean toroidal field is largely accomplished by fluctuating advection $P_{\rm FA}$ (Fig. 7.1e) and mean ohmic diffusion $P_{\rm MD}$ (Fig. 7.1f), with the latter also important near the upper boundary. Turbulent shear becomes strongest near the bottom of the convection zone and in the regions near the high-latitude side of each wreath. Thus $P_{\rm FS}$ (Fig. 7.1d) becomes the dominant member of the triad of terms seeking to diminish the mean toroidal field there. We find that the mean poloidal field is regenerated in roughly the same region.

In the analysis presented in Figure 7.1 we have neglected the advection of $\langle B_\phi \rangle$ by the meridional circulations (denoted by $P_{\rm MA}$), which we find plays a very small role in the overall balance. We have also neglected the amplification of $\langle B_\phi \rangle$ by compressibility

effects (namely, $P_{\rm MC}$ and $P_{\rm FC}$), though it does contribute slightly to reinforcing the underlying mean fields within the wreaths.

To summarize, the mean toroidal fields are built through an Ω-effect, where production by the mean shearing flow of differential rotation ($P_{\rm MS}$) builds the underlying $\langle B_\phi \rangle$. In the statistically steady state achieved, this production is balanced by a combination of turbulent induction ($P_{\rm FS} + P_{\rm FA}$) and ohmic diffusion of the mean fields ($P_{\rm MD}$).

7.3 Production of Axisymmetric Poloidal Field

When analyzing the production of the mean poloidal field, two contributions arise. One is for the mean radial field and one for the mean colatitudinal field. Evaluating the production of poloidal field in terms of the radial and colatitudinal field is a bit complex, and in practice the production of the mean poloidal vector potential is a more useful quantity. For clarity however, it is useful to first exhibit the production terms for radial and colatitudinal in a fashion similar to those evaluated for the mean toroidal field. With the same analysis approach, the induction equation for those two fields are in turn

$$\begin{aligned}
\frac{\partial \langle B_r \rangle}{\partial t} &= P_{\rm MS} + P_{\rm FS} + P_{\rm MA} + P_{\rm FA} + P_{\rm MC} + P_{\rm FC} + P_{\rm MD}\,, \\
P_{\rm MS} &= \left[\langle B_r \rangle \frac{\partial}{\partial r} + \frac{\langle B_\theta \rangle}{r} \frac{\partial}{\partial \theta} \right] \langle v_r \rangle - \frac{\langle B_\theta \rangle \langle v_\theta \rangle + \langle B_\phi \rangle \langle v_\phi \rangle}{r}\,, \qquad (7.21) \\
P_{\rm FS} &= \left\langle \left[B'_r \frac{\partial}{\partial r} + \frac{B'_\theta}{r} \frac{\partial}{\partial \theta} + \frac{B'_\phi}{r \sin\theta} \frac{\partial}{\partial \phi} \right] v'_r \right\rangle - \frac{\langle B'_\theta v'_\theta \rangle + \langle B'_\phi v'_\phi \rangle}{r}\,, \qquad (7.22) \\
P_{\rm MA} &= -\left[\langle v_r \rangle \frac{\partial}{\partial r} + \frac{\langle v_\theta \rangle}{r} \frac{\partial}{\partial \theta} \right] \langle B_r \rangle + \frac{\langle v_\theta \rangle \langle B_\theta \rangle + \langle v_\phi \rangle \langle B_\phi \rangle}{r}\,, \qquad (7.23) \\
P_{\rm FA} &= -\left\langle \left[v'_r \frac{\partial}{\partial r} + \frac{v'_\theta}{r} \frac{\partial}{\partial \theta} + \frac{v'_\phi}{r \sin\theta} \frac{\partial}{\partial \phi} \right] B'_r \right\rangle + \frac{\langle v'_\theta B'_\theta \rangle + \langle v'_\phi B'_\phi \rangle}{r}\,, \qquad (7.24) \\
P_{\rm MC} &= \left(\langle v_r \rangle \langle B_r \rangle \right) \frac{\partial}{\partial r} \ln \bar{\rho}\,, \qquad P_{\rm FC} = \left(\langle v'_r B'_r \rangle \right) \frac{\partial}{\partial r} \ln \bar{\rho}\,, \qquad (7.25) \\
P_{\rm MD} &= \eta \nabla^2 \langle B_r \rangle - 2\eta \frac{\langle B_r \rangle}{r^2} - \frac{2\eta}{r^2} \frac{\partial \langle B_\theta \rangle}{\partial \theta} - \frac{2\eta \cot\theta \langle B_\theta \rangle}{r^2}\,, \qquad (7.26)
\end{aligned}$$

and

$$\begin{aligned}
\frac{\partial\langle B_\theta\rangle}{\partial t} &= P_{\rm MS}+P_{\rm FS}+P_{\rm MA}+P_{\rm FA}+P_{\rm MC}+P_{\rm FC}+P_{\rm MD}\,,\\
P_{\rm MS} &= \left[\langle B_r\rangle\frac{\partial}{\partial r}+\frac{\langle B_\theta\rangle}{r}\frac{\partial}{\partial\theta}\right]\langle v_\theta\rangle+\frac{\langle B_\theta\rangle\langle v_r\rangle-\cot\theta\langle B_\phi\rangle\langle v_\phi\rangle}{r}\,, \qquad (7.27)\\
P_{\rm FS} &= \left\langle\left[B'_r\frac{\partial}{\partial r}+\frac{B'_\theta}{r}\frac{\partial}{\partial\theta}+\frac{B'_\phi}{r\sin\theta}\frac{\partial}{\partial\phi}\right]v'_\theta\right\rangle+\frac{\langle B'_\theta v'_r\rangle-\cot\theta\langle B'_\phi v'_\phi\rangle}{r}\,, \qquad (7.28)\\
P_{\rm MA} &= -\left[\langle v_r\rangle\frac{\partial}{\partial r}+\frac{\langle v_\theta\rangle}{r}\frac{\partial}{\partial\theta}\right]\langle B_\theta\rangle-\frac{\langle v_\theta\rangle\langle B_r\rangle-\cot\theta\langle v_\phi\rangle\langle B_\phi\rangle}{r}\,, \qquad (7.29)\\
P_{\rm FA} &= -\left\langle\left[v'_r\frac{\partial}{\partial r}+\frac{v'_\theta}{r}\frac{\partial}{\partial\theta}+\frac{v'_\phi}{r\sin\theta}\frac{\partial}{\partial\phi}\right]B'_\theta\right\rangle-\frac{\langle v'_\theta B'_r\rangle-\cot\theta\langle v'_\phi B'_\phi\rangle}{r}\,, \qquad (7.30)\\
P_{\rm MC} &= \left(\langle v_r\rangle\langle B_\theta\rangle\right)\frac{\partial}{\partial r}\ln\bar\rho\,, \qquad P_{\rm FC} = \left(\langle v'_r B'_\theta\rangle\right)\frac{\partial}{\partial r}\ln\bar\rho\,, \qquad (7.31)\\
P_{\rm MD} &= \eta\nabla^2\langle B_\theta\rangle+\frac{2\eta}{r^2}\frac{\partial\langle B_r\rangle}{\partial\theta}-\frac{\eta\langle B_\theta\rangle}{r^2\sin^2\theta}\\
&\quad+\frac{d\eta}{dr}\left(\frac{1}{r}\frac{\partial(r\langle B_\theta\rangle)}{\partial r}-\frac{1}{r}\frac{\partial\langle B_r\rangle}{\partial\theta}\right). \qquad (7.32)
\end{aligned}$$

In practice we use the above equations to diagnose and understand the local production of poloidal field, but will not show these terms explicitly.

Instead, we find that when analyzing the production of mean poloidal magnetic field, the balances achieved are somewhat clearer if we consider its vector potential rather than the two separate fields themselves. The mean poloidal field $\langle\boldsymbol{B}_{\rm pol}\rangle$ has a corresponding vector potential $\langle A_\phi\rangle$, where

$$\begin{aligned}
\langle\boldsymbol{B}_{\rm pol}\rangle &= \langle B_r\rangle\hat{\boldsymbol{r}}+\langle B_\theta\rangle\hat{\boldsymbol{\theta}}=\boldsymbol{\nabla}\times\langle\boldsymbol{A}\big|_\phi\rangle\\
&= \tfrac{1}{r\sin\theta}\tfrac{\partial}{\partial\theta}\langle A_\phi\sin\theta\rangle\,\hat{\boldsymbol{r}}-\tfrac{1}{r}\tfrac{\partial}{\partial r}\langle rA_\phi\rangle\,\hat{\boldsymbol{\theta}} \qquad (7.33)\\
&= \boldsymbol{\nabla}\times\left\langle A_\phi\hat{\boldsymbol{\phi}}\right\rangle.
\end{aligned}$$

The other components of the poloidal vector potential disappear, as terms involving $\partial/\partial\phi$ vanish in the azimuthally-averaged equations. Likewise, the ϕ-component of the possible gauge term $\boldsymbol{\nabla}\lambda$ is zero by virtue of axisymmetry. We recast the induction equation (eq. 2.4) in terms of the poloidal vector potential by uncurling the equation

once and obtain

$$\frac{\partial \langle \boldsymbol{A_\phi} \rangle}{\partial t} = \boldsymbol{v} \times \boldsymbol{B}\big|_\phi - \eta \boldsymbol{\nabla} \times \boldsymbol{B}\big|_\phi. \tag{7.34}$$

This can then be decomposed into mean and fluctuating contributions, and represented symbolically as

$$\frac{\partial \langle \boldsymbol{A_\phi} \rangle}{\partial t} = E_{\rm MI} + E_{\rm FI} + E_{\rm MD}, \tag{7.35}$$

with $E_{\rm MI}$ representing the electromotive forces (emf) arising from mean flows and mean fields, and related to their mean induction. Likewise, $E_{\rm FI}$ is the emf from fluctuating flows and fields and $E_{\rm MD}$ is the emf arising from mean diffusion. These are in turn

$$E_{\rm MI} = \langle \boldsymbol{v} \rangle \times \langle \boldsymbol{B} \rangle\big|_\phi = \langle v_r \rangle \langle B_\theta \rangle - \langle v_\theta \rangle \langle B_r \rangle, \tag{7.36}$$

$$E_{\rm FI} = \langle \boldsymbol{v'} \times \boldsymbol{B'} \rangle\big|_\phi = \langle v'_r B'_\theta \rangle - \langle v'_\theta B'_r \rangle, \tag{7.37}$$

$$E_{\rm MD} = -\eta \boldsymbol{\nabla} \times \langle \boldsymbol{B} \rangle\big|_\phi = -\eta \frac{1}{r} \left(\frac{\partial}{\partial r} \left(r \langle B_\theta \rangle \right) - \frac{\partial \langle B_r \rangle}{\partial \theta} \right). \tag{7.38}$$

7.4 Maintaining the Poloidal Field

The production of mean poloidal field is achieved through a slightly different balance, with turbulent induction producing poloidal field and ohmic diffusion acting to dissipate it. The mean flows play only a modest role in the overall balance.

In case D3 we find that the mean poloidal vector potential $\langle A_\phi \rangle$ is produced by the fluctuating (turbulent) emf and is dissipated by ohmic diffusion

$$\frac{\partial \langle A_\phi \rangle}{\partial t} \approx E_{\rm FI} + E_{\rm MD} \approx 0\,, \tag{7.39}$$

with $E_{\rm FI}$ the emf arising from fluctuating flows and fluctuating fields, and contributing to the mean induction. The $E_{\rm MD}$ is the emf arising from mean ohmic diffusion. These terms are

$$E_{\rm FI} = \langle \boldsymbol{v'} \times \boldsymbol{B'} \rangle\big|_\phi = \langle v'_r B'_\theta \rangle - \langle v'_\theta B'_r \rangle, \tag{7.40}$$

$$E_{\rm MD} = -\eta \boldsymbol{\nabla} \times \langle \boldsymbol{B} \rangle\big|_\phi. \tag{7.41}$$

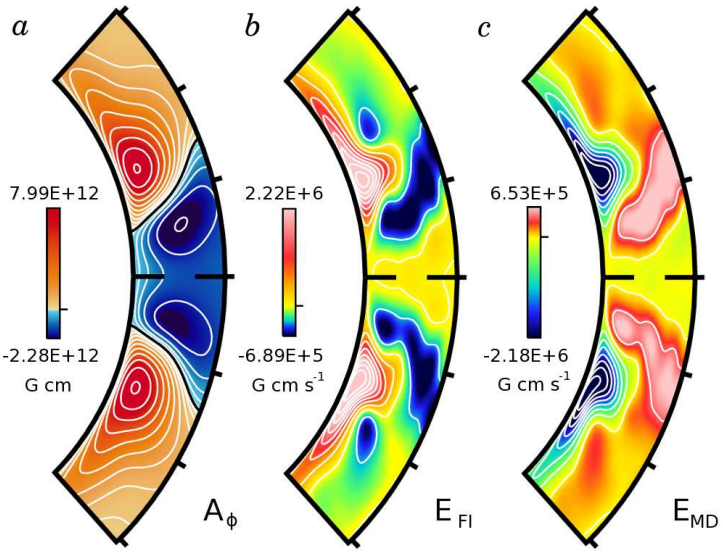

FIGURE 7.2 — Production of mean poloidal vector potential $\langle A_\phi \rangle$ in case D3. The view is restricted to $\pm 45^\circ$ latitude to emphasize the regions of production. (a) Mean poloidal vector potential $\langle A_\phi \rangle$, with sense denoted by color (red, clockwise; blue, counter-clockwise). (b) The fluctuating (turbulent) emf $E_{\rm FI}$ acts to build the vector potential. This term is strongest near the bottom of the convection zone and the poleward side of the wreaths. (c) Mean ohmic diffusion $E_{\rm MD}$ acts everywhere in opposition to $E_{\rm FI}$. The cores of the wreaths are positioned at roughly $\pm 15^\circ$ latitude (Fig. 7.1a).

The contribution arising from the omitted term $E_{\rm MI}$ (see eq. 7.36), related to the emf of mean flows and mean fields, is smaller than these first two by more than an order of magnitude. Additionally, $E_{\rm MI}$ has a complicated spatial structure which does not appear to act in a coherent fashion within the wreaths to either build or destroy mean poloidal field.

The mean vector potential $\langle A_\phi \rangle$ is shown in Figure 7.2a, with poloidal field lines represented by the overlying contours. The mean radial magnetic field $\langle B_r \rangle$ is about ± 1 kG in the cores of the wreaths, whereas the mean colatitudinal field $\langle B_\theta \rangle$ has an amplitude of roughly -2 kG (thus directed northward in both hemispheres), concentrated near the bottom of the convection zone.

The production of $\langle A_\phi \rangle$ by the fluctuating (turbulent) emf $E_{\rm FI}$ is shown in Figure 7.2*b*. Here too we average over the same 450 day interval. This term generally acts to reinforce the existing poloidal field, having the same sense as the underlying vector potential in most regions. It is strongest near the bottom of the convection zone and is concentrated at the poleward side of each wreath. This is similar, though not identical, to the structure of destruction of mean toroidal field by fluctuating shear $P_{\rm FS}$ (Fig. 7.1*d*). It suggests that mean toroidal field is here being converted into mean poloidal field by the fluctuating flows.

There are two terms that contribute to $E_{\rm FI}$, as shown in equation (7.40). Much of that fluctuating emf arises from correlations between fluctuating latitudinal flows and radial fields $\langle -v'_\theta B'_r \rangle$, which follows the structure of $E_{\rm FI}$ (Fig. 7.2*b*) closely. The contribution from fluctuating radial flows and colatitudinal fields $\langle v'_r B'_\theta \rangle$ is more complex in structure. Near $\pm 20^\circ$ latitude, this term reinforces $\langle -v'_\theta B'_r \rangle$, but acts against it at higher latitudes and thus diminishes the overall amplitude of $E_{\rm FI}$. The mean ohmic diffusion $E_{\rm MD}$ (Fig. 7.2*c*), almost entirely balances the production of $\langle A_\phi \rangle$ by $E_{\rm FI}$.

This shows that our mean poloidal magnetic field is maintained by the fluctuating (turbulent) emf and is destroyed by ohmic diffusion. In mean-field dynamo theory, this is often parametrized by an "α-effect." Now we turn to interpretations within that framework.

7.5 Exploring Mean-Field Interpretations

Many mean-field theories assert that the production of mean poloidal field is likely to arise from the fluctuating emf. This process is often approximated with an α-effect, where it is proposed that the sense and amplitude of the emf scales with the mean toroidal field

$$\langle \boldsymbol{v'} \times \boldsymbol{B'} \rangle = \alpha \langle \boldsymbol{B} \rangle, \tag{7.42}$$

where α can be either a simple scalar or may be related to the kinetic and magnetic (current) helicities. In isotropic (but not reflectionally symmetric), homogeneous, incompressible MHD turbulence

$$\alpha = \frac{\tau}{3}\left(\alpha_k + \alpha_m\right), \tag{7.43}$$

$$\alpha_k = -\boldsymbol{v'} \cdot \left(\boldsymbol{\nabla} \times \boldsymbol{v'}\right), \tag{7.44}$$

$$\alpha_m = \frac{1}{4\pi\rho}\boldsymbol{B'} \cdot \left(\boldsymbol{\nabla} \times \boldsymbol{B'}\right), \tag{7.45}$$

as discussed in Pouquet et al. (1976) and Brandenburg & Subramanian (2005). Here τ is the lifetime or correlation time of a typical turbulent eddy. In mean-field theory, these fluctuating helicities are typically not solved directly and are instead solved through auxiliary equations for the total magnetic helicity or are prescribed. Here we can directly measure our fluctuating helicities and examine whether they approximate our fluctuating emf.

To assess the possible role of an α-effect in our simulation, we show in Figures 7.3a, b the fluctuating kinetic and current helicities α_k and α_m realized in our case D3, averaged over the same 450 day analysis interval. To make an estimate of the α-effect, we approximate the correlation time τ by defining

$$\tau = \frac{H_P}{v'}, \tag{7.46}$$

where H_P is the local pressure scale height and v' is the local fluctuating rms velocity, which are functions of radius only. Estimated by this method, the turnover time τ has a smooth radial profile and is roughly 10 days near the bottom of the convection zone, 3 days at mid-convection zone, and slightly less near the upper boundary. If we use the fast peak upflow or downflow velocities instead of the rms velocities, our estimate of τ is about a factor of 4 smaller. Our mean-field α (eq. 7.43) is shown in Figure 7.3c. In the upper convection zone, this is dominated by the fluctuating kinetic helicity while the fluctuating magnetic (current) helicity becomes important at depth.

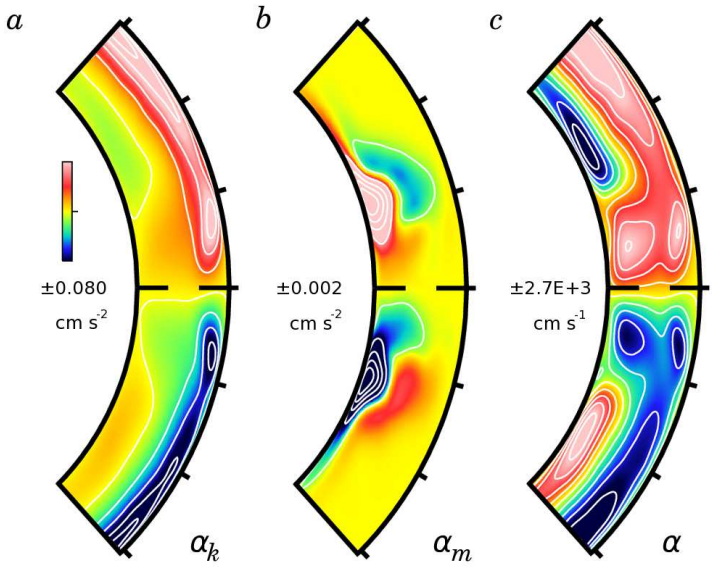

FIGURE 7.3 — Estimating the mean-field α-effect in case D3. (a) Fluctuating kinetic helicity α_k. (b) Fluctuating magnetic (current) helicity α_m. (c) Mean-field α, constructed by combining α_k and α_m with a turbulent correlation time τ.

We form a mean-field emf (right-hand side of eq. 7.42) by multiplying our derived α (Fig. 7.3c) with our $\langle B_\phi \rangle$ (Fig. 7.1a), and show this in Figure 7.4a. The turbulent emf $E_{\rm FI}$, which is the left-hand side of equation (7.42), can be measured in our simulations and is shown again in Figure 7.4b. Although there is some correspondence in the two patterns, there are significant differences. In particular, the mean-field emf has peak amplitudes in the cores of the wreaths (at $\pm 15^\circ$ latitude) and is negative there. In contrast, the actual fluctuating emf given by $E_{\rm FI}$ is positive and has its highest amplitude at the poleward side of the wreaths. Thus the mean-field emf predicts an incorrect balance in the generation terms and would yield a distinctly different mean poloidal magnetic field. To assess whether better agreement may be achieved with a latitude-averaged emf, we average the mean-field emf and $E_{\rm FI}$ separately over the northern and southern hemispheres and plot these quantities in Figure 7.4c. Though both have a similar positive sense near the base of the convection zone, the hemisphere-averaged $E_{\rm FI}$ becomes small above $0.8 R_\odot$ whereas the averaged mean-field emf $\alpha \langle B_\phi \rangle$ is large and negative there. Thus even the averaged emfs are not in accord.

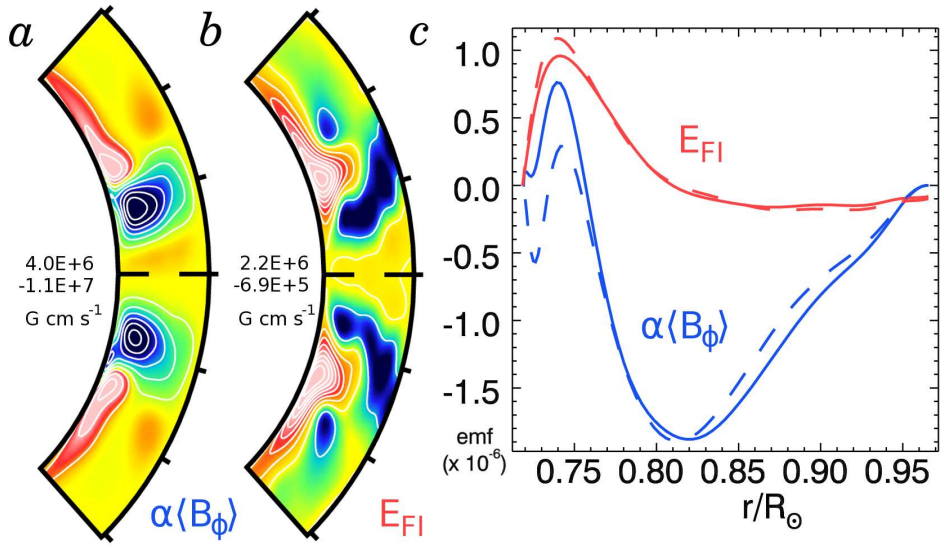

FIGURE 7.4 — Comparison of emfs in case D3. (*a*) Profile of proposed mean-field emf given by $\alpha\langle B_\phi\rangle$. (*b*) Actual turbulent emf $E_{\rm FI}$ measured in the dynamo. (*c*) Variation of hemisphere-averaged emfs with fractional radius. The mean-field approximated emf is shown in blue, and $E_{\rm FI}$ in red. The average over the northern hemisphere is shown solid, the southern is dashed.

In summary, it is evident that a simple scalar α-effect will predict the wrong sign for the fluctuating emf in the two hemispheres, as $\langle B_\phi\rangle$ is anti-symmetric across the equator while $\langle A_\phi\rangle$ is symmetric. An α-effect based on the kinetic helicity and magnetic helicity may capture some sense of the fluctuating emf, as those quantities are themselves anti-symmetric across the equator. Yet Figure 7.4 suggests that there are significant discrepancies between this particular approximation and our turbulent emf. In particular, this mean-field α-effect misses the offset between the generation regions for mean toroidal and mean poloidal field. This offset in latitude of the generation regions may be important for avoiding the α-quenching problems encountered in many mean-field theories. A more complex mean-field model, which takes spatial gradients of $\langle B_\phi\rangle$ into account, may do better. In particular, the $\boldsymbol{\Omega}\times\boldsymbol{J}$-effect (e.g., Moffatt & Proctor 1982; Rogachevskii & Kleeorin 2003) may be at work in these systems, and preliminary explorations indicate that this term matches the spatial structure of our

$E_{\rm FI}$ better than the above α-effect. A tensor representation of the α-effect may do much better, and test-field techniques could be employed to measure this quantity (e.g., Schrinner et al. 2005, and recently reviewed in Brandenburg 2009).

7.6 Production of Fluctuating (Non-Axisymmetric) Field

Left out of this analysis is the fluctuating component of the induction equation, which produces the small-scale but strong fluctuating magnetic fields. In case D3 these fields do not appear to be a dominant feature, but as will be seen in Chapter 8 the fluctuating fields become prominent in our more turbulent dynamo simulations. For completeness, we include their induction equation here. This can be derived by subtracting the mean induction equation (7.8) from the full induction equation, yielding the following equation for the fluctuating fields

$$\begin{aligned}\frac{\partial \boldsymbol{B'}}{\partial t} &= (\langle \boldsymbol{B} \rangle \cdot \boldsymbol{\nabla}) \boldsymbol{v'} + (\boldsymbol{B'} \cdot \boldsymbol{\nabla}) \langle \boldsymbol{v} \rangle + \boldsymbol{\mathcal{E}} \\ &\quad -(\langle \boldsymbol{v} \rangle \cdot \boldsymbol{\nabla}) \boldsymbol{B'} - (\boldsymbol{v'} \cdot \boldsymbol{\nabla}) \langle \boldsymbol{B} \rangle - \boldsymbol{\mathcal{F}} \\ &\quad +(\langle v_r \rangle \boldsymbol{B'} + v_r' \langle \boldsymbol{B} \rangle) \frac{\partial}{\partial r} \ln \bar{\rho} + \boldsymbol{\mathcal{G}} \\ &\quad -\boldsymbol{\nabla} \times (\eta \boldsymbol{\nabla} \times \langle \boldsymbol{B'} \rangle) \,, \end{aligned} \tag{7.47}$$

where the quantities $\boldsymbol{\mathcal{E}} = (\boldsymbol{B'} \cdot \boldsymbol{\nabla}) \boldsymbol{v'} - \langle (\boldsymbol{B'} \cdot \boldsymbol{\nabla}) \boldsymbol{v'} \rangle$, $\boldsymbol{\mathcal{F}} = (\boldsymbol{v'} \cdot \boldsymbol{\nabla}) \boldsymbol{B'} - \langle (\boldsymbol{v'} \cdot \boldsymbol{\nabla}) \boldsymbol{B'} \rangle$, and $\boldsymbol{\mathcal{G}} = (v_r' \boldsymbol{B'} - \langle v_r' \boldsymbol{B'} \rangle) \frac{\partial}{\partial r} \ln \bar{\rho}$, represent the difference between mixed stresses from which we subtract their axisymmetric mean. In the standard mean-field derivation, these quantities are siblings of the G-current involving the mean electromotive force $\langle \boldsymbol{v} \times \boldsymbol{B} \rangle$ and its 3-D equivalent $\boldsymbol{v} \times \boldsymbol{B}$ (i.e., the so called "pain in the neck" term, Moffatt 1978).

7.7 Conclusions

In our persistent case D3 we are able to analyze the generation and transport of mean magnetic field. We find that our dynamo action is of an $\alpha - \Omega$ nature, with the mean toroidal fields being generated by an Ω-effect from the mean shearing flow of

differential rotation. This generation is balanced by a combination of turbulent induction and ohmic diffusion. The mean poloidal fields are generated by an α-effect arising from couplings between the fluctuating flows and fluctuating fields, with this production largely balanced by the ohmic diffusion. This is unlike the toroidal balance, for here the mean flows play almost no role and the turbulent correlations are constructive rather than destructive. In assessing what a mean-field model might predict for the magnetic structures realized in case D3, we find that the isotropic, homogeneous α-effect based on kinetic and magnetic (current) helicities fails to capture the sense of our turbulent emf. In general, our $E_{\rm FI}$ is poorly represented by an $\alpha\langle B_\phi\rangle$ that is so determined.

The realization of global-scale magnetic structures in our simulations, and their great strength relative to the fluctuating fields, may in part be a consequence of the relatively modest degree of turbulence attained here. Whether such structures can be generated and sustained amidst the far more complex flows in actual stellar interiors is not yet clear. If such structures are indeed realized in stars, they may or may not survive to print through the highly turbulent convection occurring just below the stellar photosphere. If they do appear at the surface, some global-scale magnetic features may propagate toward the poles along with the bands of angular velocity speedup. There are some indications in stellar observations that global-scale toroidal magnetic fields may indeed become strong in rapidly rotating stars (Donati et al. 2006; Petit et al. 2008), though small-scale fields may still account for much of the magnetic energy near the surface (Reiners & Basri 2009). The global-scale poloidal fields may be more successful in surviving the passage through the turbulent surface convection. If they do, the stellar magnetic field will likely have significant non-dipole components. Thus the mean poloidal fields observed at the surface may give clues to the presence of large wreaths of magnetism that occupy the bulk of the convection zone.

Chapter 8

Menagerie of Wreath-Building Dynamos

In the preceding chapters we have extensively explored the characteristics of two dynamo solutions. Those simulations, cases D3 and D5 at three and five times the solar rotation rate, are part of a much larger family of simulations that we have conducted which explore the interplay between convection, rotation and magnetism in younger suns. In this chapter we present a sampling of simulations rotating from half the current solar rate to fifteen times the solar rate. This spans a range of ages for a star like the sun, from just a few million years after formation when its rotating quite rapidly to a few billion years older than the current age of the Sun, when our star will rotate more slowly. Rotation and age are inextricably linked, and there are likely to be significant changes in the stellar structure over these interval of several billion years, as the luminosity of the star gradually increases, helium settles into the core and the depth of the convection zone itself shifts. Here we have neglected those changes by retaining a stellar structure appropriate for the current Sun. We have instead explored only the effects of faster and slower rotation, to begin disentangling the varied physical effects present in real stellar observations. Future work should clearly include an exploration of the dual variation of rotation and structure with age, as in Ballot et al. (2007), but at present observed stellar ages remain highly imprecise which complicates such efforts.

The parameter space explored by the simulations is summarized in Tables 8.1-8.3. Table 8.1 details our successful dynamos at varying levels of turbulence conducted at a fixed magnetic Prandtl number Pm = 0.5 and fluid Prandtl number Pr = 0.25. One set of simulations (D3-D15) are conducted on the familiar parameter path with turbulent diffusivities scaling as

$$\nu, \kappa, \eta \propto (\Omega_0)^{-2/3} \ . \tag{8.1}$$

Other simulations (D3a, D3b, etc.) sample varying levels of turbulence at each rotation rate. At the lower rotation rates ($\Omega_0 \leq 1.5\,\Omega_\odot$), dynamo action was not realizable at Pm = 0.5 along this main branch of solutions, but is achieved for more turbulent simulations (D1.5a, D0.5a, etc.). Table 8.2 details an additional selection of simulations which were carried out at higher magnetic Prandtl numbers (Pm = 1 − 4) for various rotation rates. Lastly, a selection of failed dynamos are reported in Table 8.3, to help constrain the boundaries in parameter space for dynamo action in these simulations.

The parameter space explored by this family of dynamo solutions is illustrated in Figure 8.1. Here the primary input parameters of our dynamo simulations, the turbulent diffusivity η and the bulk rotation rate Ω_0, are shown for all of our convection zone dynamos. As detailed in the tables, triangles denote dynamos with Pm = 0.5 while diamonds denote high Pm dynamos. The failed dynamos are shown with blue crosses. As becomes immediately apparent, near the solar rotation rate there appears to be a deep dip in this parameter space where successful dynamos can occur, and such dynamos must be run at substantially lower diffusivities. A few dynamos are labeled with case names in Figure 8.1 for reference with the tables.

All dynamos shown in Figure 8.1 build large-scale magnetic wreaths in the bulk of their convection zone. The character of the wreaths changes somewhat across this parameter space. Generally, magnetic wreaths in the rapidly rotating simulations ($\Omega_0 \gtrsim 3\,\Omega_\odot$) fill the bulk of the convection zone, with substantial structure in both radius and

Table 8.1. Overview of Dynamos at Pm=0.5

Case	N_r, N_θ, N_ϕ	Ra	Ta	Re	Re′	Rm	Rm′	Ro	Roc	ν	η	$\Omega_0/\Omega_\odot$	Time-dependence
Dynamos on the $\eta \propto \Omega_0^{-2/3}$ path (denoted in Fig. 8.1 with black triangles)													
D3	$97 \times 256 \times 512$	3.28×10^5	1.22×10^7	173	104	86	52	0.374	0.315	1.32	2.64	3	S
D5	$97 \times 256 \times 512$	1.04×10^6	6.70×10^7	268	132	134	66	0.272	0.241	0.940	1.88	5	C
D10	$97 \times 512 \times 1024$	3.22×10^6	6.75×10^8	253	228	126	114	0.153	0.134	0.592	1.18	10	C
D15	$129 \times 512 \times 1024$	7.05×10^6	2.61×10^9	288	272	144	136	0.119	0.101	0.452	0.904	15	C
Dynamos at other turbulence levels (denoted with colored triangles)													
D0.5a	$145 \times 256 \times 512$	2.52×10^4	2.01×10^5	154	127	77	63	2.45	0.688	1.72	3.43	0.5	S
D0.5b	$145 \times 512 \times 1024$	1.43×10^4	8.03×10^5	395	347	197	173	3.29	0.779	0.859	1.72	0.5	O/C?
D1.5a	$97 \times 256 \times 512$	2.33×10^5	5.02×10^6	215	178	107	89	0.993	0.404	1.03	2.06	1	S
D1.5b	$257 \times 512 \times 1024$	7.24×10^5	2.01×10^7	483	414	241	207	1.54	0.371	0.515	1.03	1	O/C?
D3a	$97 \times 256 \times 512$	5.84×10^5	2.41×10^7	244	154	122	77	0.447	0.295	0.940	1.88	3	O/C
D3b	$143 \times 512 \times 1024$	1.11×10^6	6.08×10^7	343	273	171	136	0.566	0.257	0.592	1.18	3	C
D10 L	$97 \times 512 \times 1024$	2.15×10^6	2.68×10^8	331	110	165	55	0.131	0.177	0.940	1.88	10	C

Note. — Dynamo simulations at many different rotation rates. All simulations have inner radius $r_{\rm bot} = 5.0 \times 10^{10}$cm and outer radius of $r_{\rm top} = 6.72 \times 10^{10}$cm, with $L = (r_{\rm top} - r_{\rm bot}) = 1.72 \times 10^{10}$cm the thickness of the spherical shell. All quantities are the same as defined in Table 2.3. Briefly recapping, evaluated at mid-depth are the Rayleigh number Ra, the Taylor number Ta, the rms Reynolds number Re and fluctuating Reynolds number Re′, the magnetic Reynolds number Rm and fluctuating magnetic Reynolds number Rm′, the Rossby number Ro , and the convective Rossby number Roc. For all simulations, the Prandtl number $\mathrm{Pr} = \nu/\kappa$ is 0.25 and the magnetic Prandtl number $\mathrm{Pm} = \nu/\eta$ is 0.5. The viscous and magnetic diffusivity, ν and η, are quoted at mid-depth (in units of 10^{12} cm^{2}s^{-1}). The rotation rate Ω_0 of each reference frame is in multiples of the solar rate $\Omega_\odot = 2.6 \times 10^{-6}$ rad s^{-1} or 414 nHz. The viscous time scale at mid-depth $\tau_\nu = L^2/\nu$ is 3640 days for case D5 and the resistive time scale is 1820 days. Rotation periods at three and five times the solar rate are in turn 9.3 days and 5.6 days. The time-dependence of the dynamo is indicated, with dynamos that build persistent and steady wreaths labeled by **S**, dynamos where the energies oscillate significantly by **O**, and dynamos that achieve cycles of polarity reversal by **C**. These cases are denoted in Figure 8.1 with triangles.

Table 8.2. Dynamos at Higher Pm

Case	N_r, N_θ, N_ϕ	Ra	Ta	Re	Re$'$	Rm	Rm$'$	Ro	Roc	ν	η	Pm	$\Omega_0/\Omega_\odot$	Time-dependence
M3	$129 \times 512 \times 1024$	7.18×10^4	1.25×10^6	179	125	716	500	1.04	0.656	1.37	0.343	4	1	O/C?
M3-pcpf	$129 \times 512 \times 1024$	7.31×10^4	1.25×10^6	162	123	651	492	1.01	0.663	1.37	0.343	4	1	C
D1.25a-pm2	$145 \times 256 \times 512$	1.72×10^5	3.48×10^6	238	211	476	422	1.29	0.419	1.03	0.52	2	1.25	O?
D3-pm1	$145 \times 256 \times 512$	2.98×10^5	1.22×10^7	149	102	149	102	0.372	0.300	1.32	1.32	1	3	C
D3-pm2	$145 \times 512 \times 1024$	3.08×10^5	1.22×10^7	145	101	291	202	0.370	0.306	1.32	0.660	2	3	C
D3-pm4	$145 \times 512 \times 1024$	3.12×10^5	1.22×10^7	161	94	644	377	0.336	0.308	1.32	0.330	4	3	C?
D5-pm1	$97 \times 256 \times 512$	8.24×10^5	6.70×10^7	180	132	180	132	0.241	0.214	0.940	0.940	1	5	C

Note. — Parameters are defined in Table 8.1. The dynamos shown in this table are at relatively high magnetic Prandtl numbers, with $\mathrm{Pm} = 1 - 4$. These cases are denoted in Fig. 8.1 with diamonds. Case M3 was initially published in Brun et al. (2004) and has been continued here for comparison. Cases M3 and M3-pcpf are at Prandtl number $\mathrm{Pr} = 0.125$, rather than $\mathrm{Pr} = 0.25$ as in the other simulations of this thesis. Case D1.25a-pm2 has been run to help constrain the boundary of sustained dynamo action and has currently only evolved for 1000 days.

Table 8.3. Dynamos That Failed

Case	N_r, N_θ, N_ϕ	Ra	Ta	Re	Re$'$	Rm	Rm$'$	Ro	Roc	ν	η	Pm	$\Omega_0/\Omega_\odot$
D1a	$97 \times 256 \times 512$	5.67×10^4	8.03×10^5	138	118	69	59	1.22	0.494	1.72	3.43	0.5	1
D1a-pm1	$97 \times 256 \times 512$	5.66×10^4	8.03×10^5	140	118	140	118	1.22	0.493	1.72	1.72	1	1
D1a-pm2	$97 \times 512 \times 1024$	5.23×10^4	8.03×10^5	139	121	279	243	1.23	0.475	1.72	0.859	2	1
D1b	$97 \times 256 \times 512$	1.22×10^5	2.23×10^6	220	212	110	106	1.65	0.444	1.03	2.06	0.5	1
D1b-pm1	$97 \times 256 \times 512$	1.23×10^5	2.23×10^6	224	212	224	212	1.64	0.447	1.03	1.03	1	1
D1.25a	$145 \times 256 \times 512$	1.72×10^5	3.48×10^6	238	211	119	106	1.29	0.419	1.03	2.06	0.5	1.25
D1.25a-pm1	$145 \times 256 \times 512$	1.72×10^5	3.48×10^6	238	211	238	211	1.29	0.419	1.03	1.03	1	1.25
D1.5	$145 \times 256 \times 512$	8.73×10^4	1.21×10^6	137	74	68	37	0.682	0.516	2.10	4.19	0.5	1
D3 L	$97 \times 256 \times 512$	1.21×10^5	2.82×10^6	109	41	54	20	0.279	0.409	2.75	5.50	0.5	3

Note. — These simulations failed to attain substantial dynamo action. Some are marginal, with very low magnetic energies, but in most cases the magnetic energies decline exponentially. These cases are denoted in Fig. 8.1 with crosses and are labeled **F**.

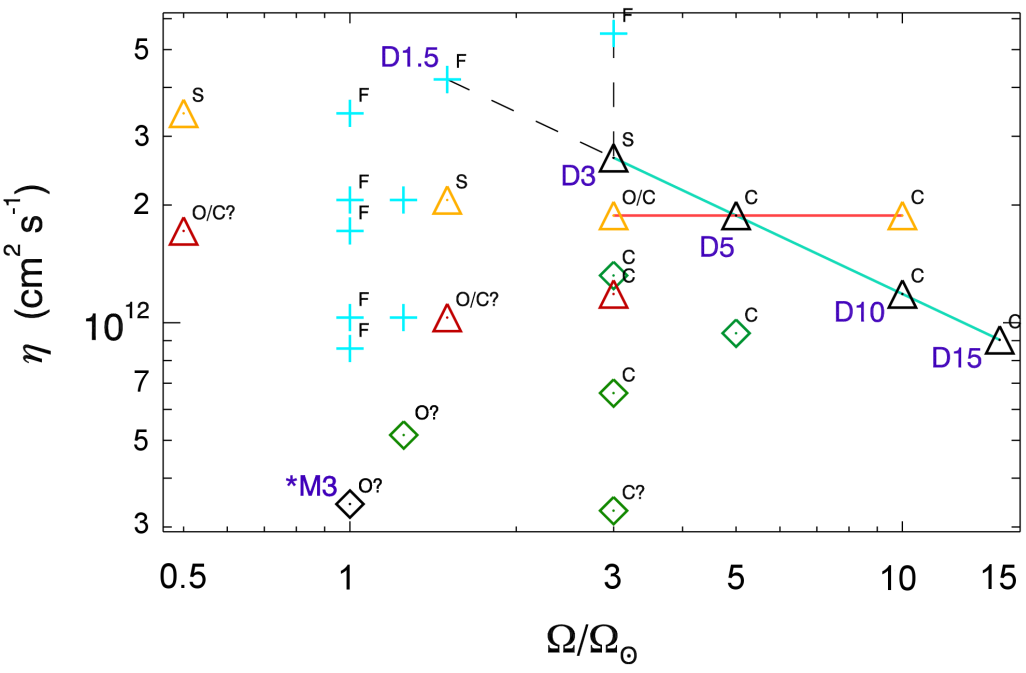

FIGURE 8.1 — Map of full dynamo $\eta - \Omega_0$ parameter space. These parameters are the eddy diffusivity η and bulk rotation rate Ω_0. Solutions at magnetic Prandtl number 0.5 are shown with triangles while cases at higher magnetic Prandtl numbers are shown with diamonds. Cases that build steady, persistent magnetic wreaths are labeled **S**, while those that undergo oscillations but rarely flip polarities are **O** and those that undergo many polarity reversals are **C**. Cases shown with blue crosses and labeled **F** are failed dynamos, where magnetic energies drop over long periods of time. Question marks indicate where the time-dependence remains uncertain. See Tables 8.1 (triangle symbols), 8.2 (diamonds) and 8.3 (crosses) for simulation details.

latitude, as seen previously in cases D3 and D5 (Chapters 5-7). The mean poloidal field is typically complex, with generally two different polarities in the polar and equatorial regions. These wreaths can also be single structures that cross the equator and primarily have a single polarity, as will be seen for the most rapidly rotating cases D10 and D15. In the more slowly rotating cases ($\Omega_0 \lesssim 1.5\,\Omega_\odot$), the wreaths become increasingly confined to the bottom of the convection zone, and while they retain their latitudinal extent, much of the prominent radial structure seen in the rapidly rotating cases disappears. At present it is unclear whether this is a matter of more effective turbulent pumping in those simulations, or changes in the differential rotation and the velocity shear available

for amplifying the magnetic fields. The mean poloidal field in these slower rotating simulations is often of a single polarity throughout the convection zone.

Many of the dynamos in Figure 8.1 exhibit temporal variations, with either oscillations in magnetic energies or cycles of activity where the polarity of the global-scale magnetic fields routinely changes. The labeling denotes the temporal characteristics of the dynamo solution, with steady solutions that do not oscillate noticeably indicated by **S**, solutions that oscillate frequently but rarely change their global-scale polarity by **O/C**, and solutions that routinely interchange polarities by **C**.

Overall, we have found three solutions that are steady in nature (cases D0.5a, D1.5a, and D3), and these generally appear to cluster near the boundary in parameter space between successful dynamos and failed dynamos that do not successfully regenerate their magnetic fields. Even these steady simulations evince small oscillations in their volume-averaged magnetic energy densities, as seen previously in case D3 (Chapter 5). As the magnetic Reynolds number increases, the flows and magnetic fields tend to become more time-dependent, with the dynamos showing either large oscillations in their magnetic energies or undergoing repeated global-scale magnetic polarity reversals.

We begin by returning to familiar ground, exploring with more extensive sampling the turbulent parameter space in a series of simulations rotating three times faster than the Sun. We first examine the onset of time-dependent behavior in simulations at three times the current solar rate.

8.1 Higher Levels of Turbulence at $3\,\Omega_\odot$ and $\mathrm{Pm} = 0.5$

In our simulations rotating at three times the solar rate, we have examined how our wreaths of magnetism change as we raise the overall level of turbulence. This is accomplished along one of two paths in parameter space. On the first path, we simultaneously decrease ν, κ and η, thus maintaining a fluid Prandtl number of 0.25 and magnetic Prandtl number of 0.5 as the diffusivities are decreased. This path corresponds

to dynamo cases D3, D3a and D3b. On this path the convection becomes more complex and turbulent and in hydrodynamic simulations would drive a substantially stronger differential rotation. Both the fluid Reynolds number and the magnetic Reynolds number increase in the successively more turbulent simulations. In these dynamo solutions we find that wreaths of magnetism persist but begin to undergo oscillations similar to those found in case D5 rotating at five times the solar rate.

Case D3a – The time-dependence of case D3a is shown in Figure 8.2. This simulation is somewhat more turbulent than case D3, with typical rms and fluctuating Reynolds numbers of 244 and 154 respectively, and rms and fluctuating magnetic Reynolds numbers of 122 and 77. Case D3a undergoes many oscillations in energy and mean field strength with a typical timescale of 500 days, as shown in the time traces of Figure 8.2a, b. Generally, the azimuthally averaged toroidal and poloidal fields are stable, retaining the same polarity through many such oscillations. Only very rarely (twice in the 16000 days shown here) do the global-scale fields flip in polarity. This is evident in time-latitude plots of $\langle B_\phi \rangle$ at mid-convection zone, shown in Figure 8.2c. Here we note that the large excursion in mean field strengths occurring between days 13000-14500 corresponds to a strong, single polarity state. As in case D5 during similar excursions, we find that during this interval of time the mean poloidal field has changed from an odd-parity state, with strong contributions from the odd-ℓ components, to an even-parity state where the even-ℓ components are more prominent. The dynamo exits this state at roughly day 14500 and appears to return to a more normal state, with two opposite polarity wreaths and a predominantly odd-parity poloidal field.

Throughout the history of this case, weak magnetic structures appear to propagate from the equatorial regions to both poles. As in case D5 (Chapter 6), these magnetic structures are associated with local bands of slightly faster differential rotation which also propagate toward the poles (Fig. 8.2d). These structures are observed with each oscillation, being launched from the equatorial regions roughly every 500 days.

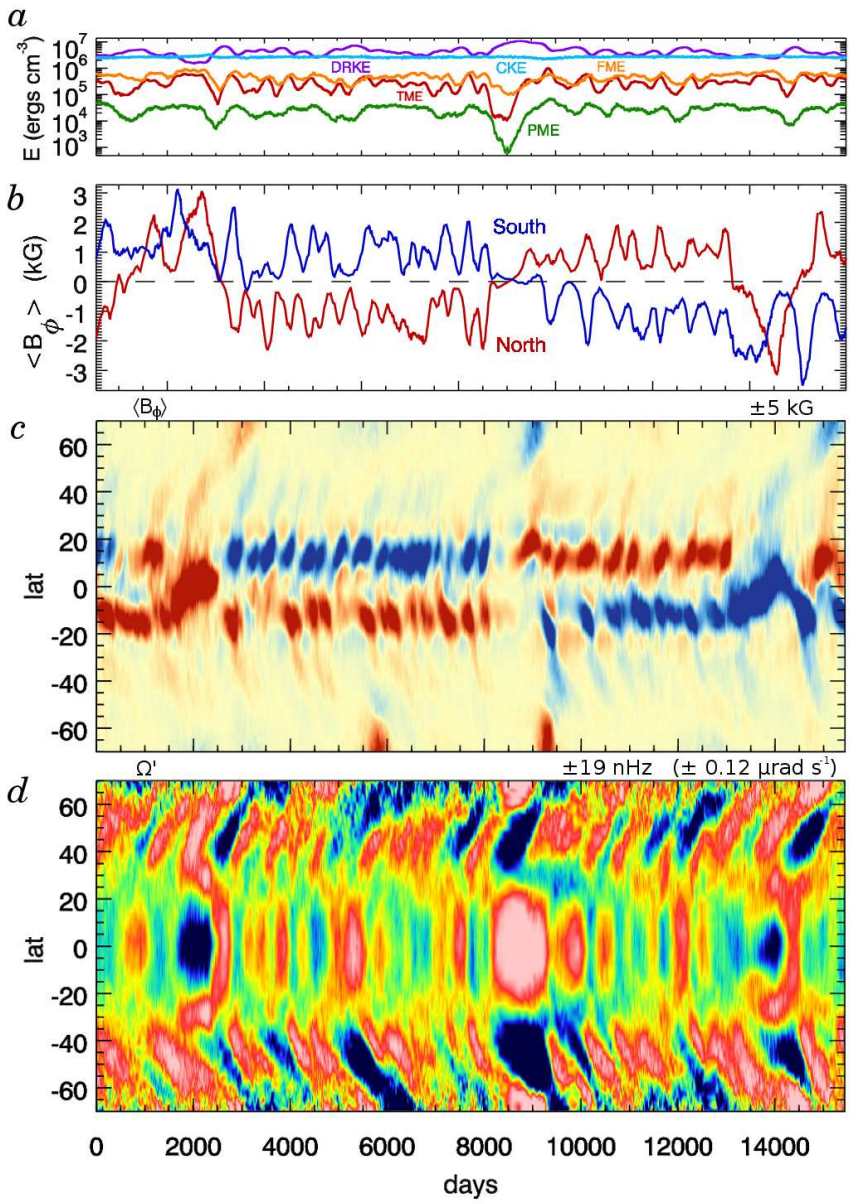

FIGURE 8.2 — Time-dependent behavior in the oscillating case D3a. (a) Volume-averaged kinetic and magnetic energies, showing DRKE, CKE, TME, PME and FME as labeled. Many small oscillations occur on roughly 500 day timescales, with a large excursion around day 9000. (b) Mean $\langle B_\phi \rangle$ averaged over northern and southern hemispheres at mid-convection zone. Despite the many oscillations, a global-scale polarity reversal occurs only once (near day 9000), with a second significant excursion between roughly days 13000-14500. (c) Time-latitude maps of $\langle B_\phi \rangle$ at mid-convection zone. During roughly days 13000-14500 a strange, single-polarity state emerges. (d) Time-latitude map of Ω' at mid-convection zone, with time average removed to emphasize the poleward propagating velocity structures.

At a few intervals in the simulation, very strong magnetic features appear near the poles (i.e. near days 5500-6000 and 9000-9500). At present it is unclear whether these are formed through local amplification of $\langle B_\phi \rangle$ by either the turbulence or the differential rotation, or if they represent a geometric amplification of magnetic field as particularly strong wreaths slip to the poles and are concentrated into a smaller volume there. These polar magnetic structures are associated with strong velocity structures.

The patterns of convection achieved in case D3a are shown in Figure 8.3. The convective cells are a little more complex than in case D3 (compare with Fig. 5.2) and the amplitude of the motions is 10% faster than in that case. The toroidal field in this more turbulent case is somewhat higher, with typical field strengths at mid-convection zone of almost ± 10 kG and peak field strengths of roughly ± 35 kG. In comparison, typical field strengths in case D3 were ± 7 kG with peak strengths of roughly ± 26 kG. This snapshot is taken at an instant when the mean toroidal fields are quite strong (TME is at a peak). As such, the magnetic wreaths are visibly dominated by the mean toroidal field $\langle B_\phi \rangle$ and their structure appears quite similar to those found in case D3. When the fields are weaker (say at day 12500 when TME and PME are at a minimum), the structure of the wreaths is very similar, though their typical field strengths at mid-convection zone are then only ± 5 kG, with peak field strengths of ± 20 kG. Thus at the times when $\langle B_\phi \rangle$ is weak, case D3a returns to a state very similar to case D3. When case D3a is in a single-polarity state, between days 13000-14500, the magnetic fields at mid-convection zone tend to be in a single wreath of negative polarity that wanders across the equator. Surrounding this structure is weaker positive polarity field.

The differential rotation in this case is similar to that realized in the less turbulent case D3. As shown in Figure 8.3*d*, the equator remains fast and prograde while the poles are filled with retrograde flow. There is substantial radial shear near the equator. The mean toroidal field associated with the wreaths of magnetism (Fig. 8.3*e*) is comparable in strength to the fields achieved in case D3, but the cores of the wreaths are located

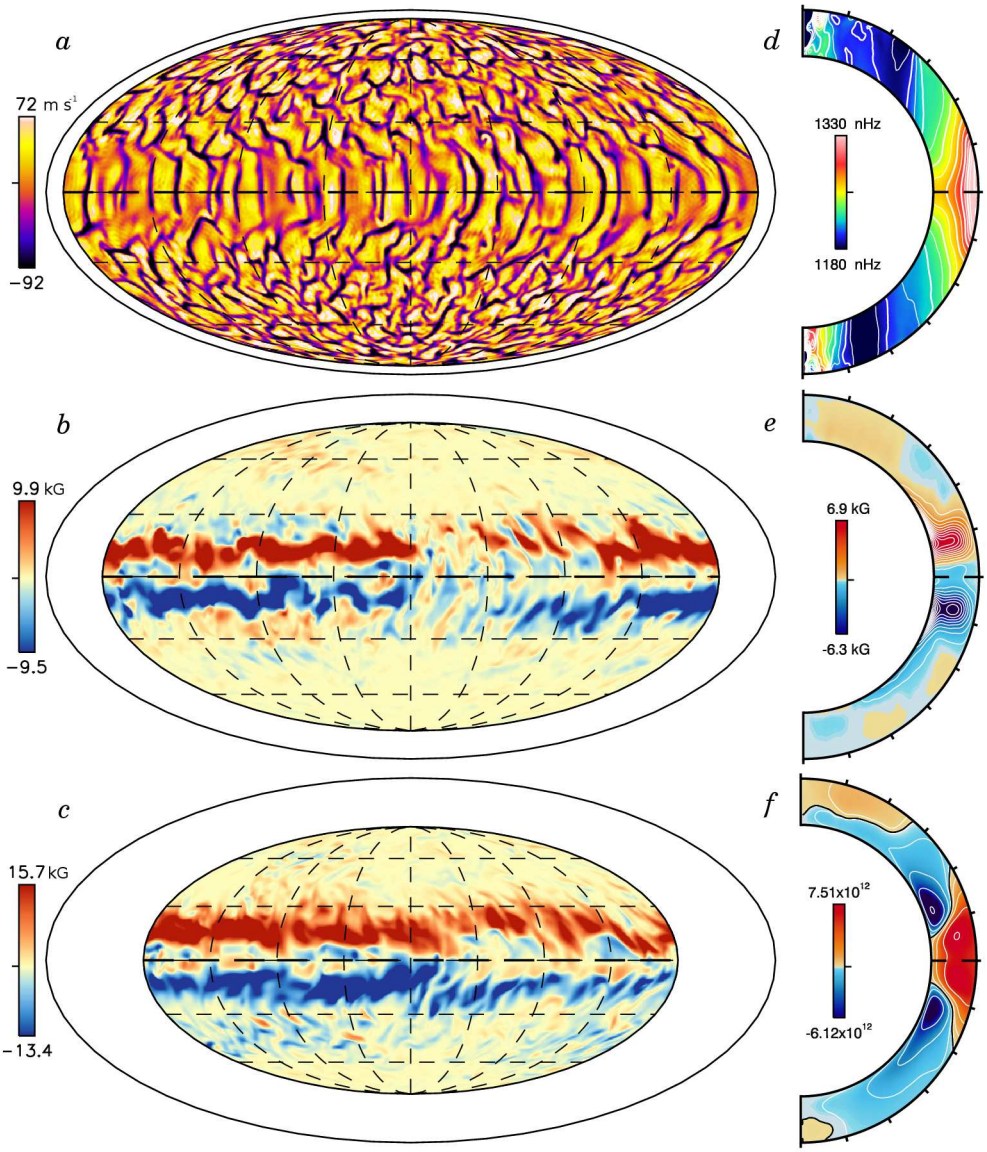

FIGURE 8.3 — Patterns of convection in case D3a. (a) Radial velocity v_r in Mollweide projection near the top of the shell ($0.95\,R_\odot$). (b) Toroidal magnetic field B_ϕ at mid-convection zone ($0.85\,R_\odot$) and (c) near the bottom of the convective shell ($0.73\,R_\odot$). These snapshots are shown at day 12200, a time when the mean magnetic fields are strong. Also shown are 100 day averaged profiles of (d) angular velocity Ω, with fast equator and slow poles, (e) mean toroidal field $\langle B_\phi \rangle$ and (f) mean poloidal vector potential $\langle A_\phi \rangle$ with contours representing the mean poloidal field lines.

slightly closer to the equator than in case D3 where they straddled $\pm 15^{\circ}$. The poloidal vector potential (Fig. 8.3*f*) is also similar in morphology, though now the equatorial region is comparable in strength to the poleward regions. In case D3, the vector potential near the equator was about a factor of three weaker than that found in this case above latitude $\pm 15^{\circ}$.

Case D3b – When the level of turbulence is increased further (case D3b, Fig. 8.4*a-d*), the global scale fields appear to flip far more frequently. This simulation is yet more turbulent, with typical rms and fluctuating Reynolds numbers of 343 and 273 respectively, and rms and fluctuating magnetic Reynolds numbers of 171 and 136. Though this simulation has not achieved nearly as much time evolution, with 3300 days of total evolution since the last adjustment of diffusivities, the global scale fields have already exchanged polarity at least once. We thus suspect that these oscillations are due to the higher magnetic Reynolds number achieved rather than being linked intrinsically to the higher rotation rate used in D5. At times, the magnetic wreaths survive for long intervals, with one pair existing from roughly day 1400 to day 2100. At other periods, strong wreaths are built in each hemisphere but only survive for short periods of time, disappearing within a few hundred days. This behavior holds true at deeper locations within the convection zone as well. After day 2700, wreath building occurs predominantly in only the southern hemisphere. As in the other simulations, prominent velocity structures are launched toward the polar regions. In the interval of simulated time, only a few such structures have appeared, with possibly two in the northern hemisphere and one in the southern.

The patterns of convection achieved in case D3b are shown in Figure 8.5. The radial velocity structures are more complex than in case D3a and average amplitudes of motion have increased a further 20% (or roughly 35% faster than the radial flows in case D3 at this depth). The toroidal fields have amplitudes very similar to those realized in case D3a, with typical strengths of ± 10 kG at mid-convection zone and peak ampli-

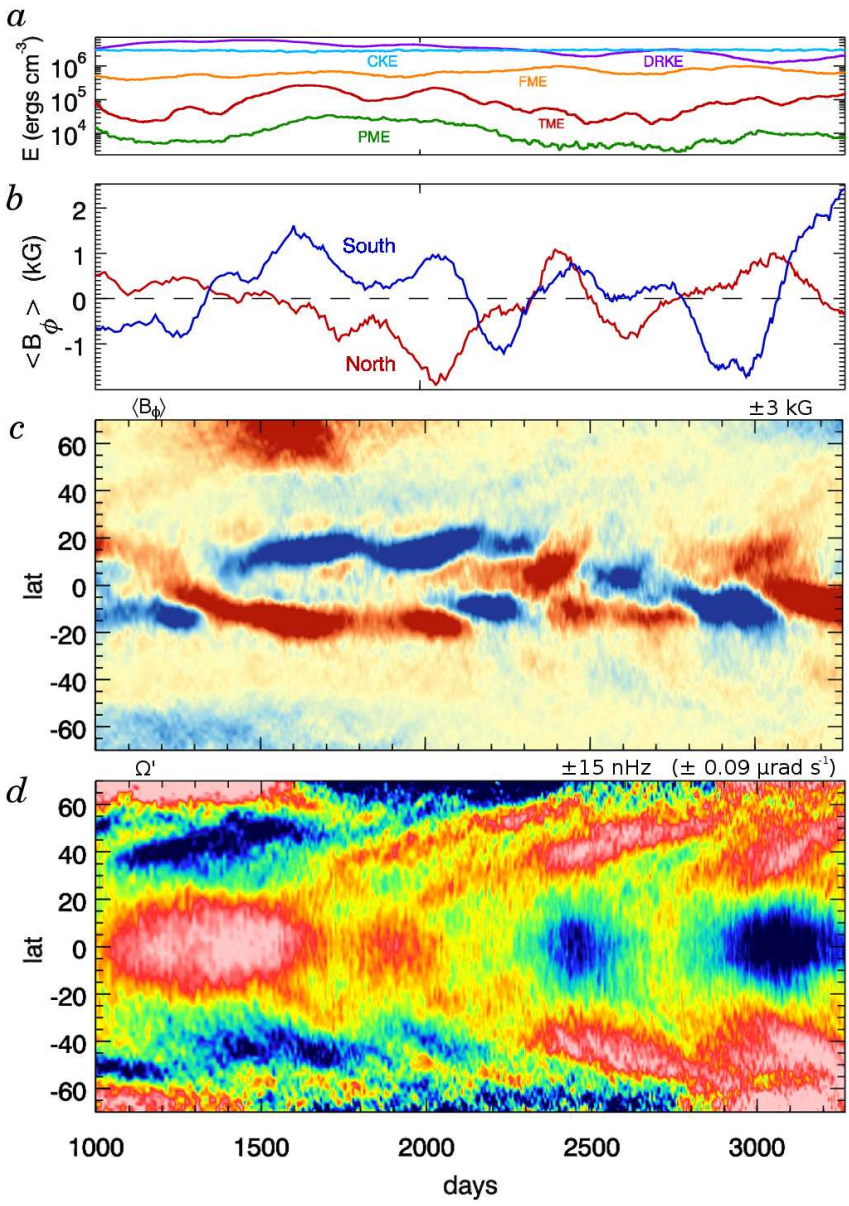

FIGURE 8.4 — Time-dependent behavior in the cyclic case D3b. (a) Volume-averaged kinetic and magnetic energies, and (b) mean $\langle B_\phi \rangle$ averaged over northern and southern hemispheres at mid-convection zone. Individual quantities are colored as in Fig. 8.4a, b. Though this simulation has evolved for only a short period, one polarity reversal has already occurred. (c) Time-latitude maps of $\langle B_\phi \rangle$ at mid-convection zone. The large structures visible at the poles near day 1500 appear to be part of the initial transient as the dynamo equilibrates and adjusts the profile of differential rotation. (d) Time-latitude map of Ω' at mid-convection zone, with time average removed to emphasize the poleward propagating velocity structures.

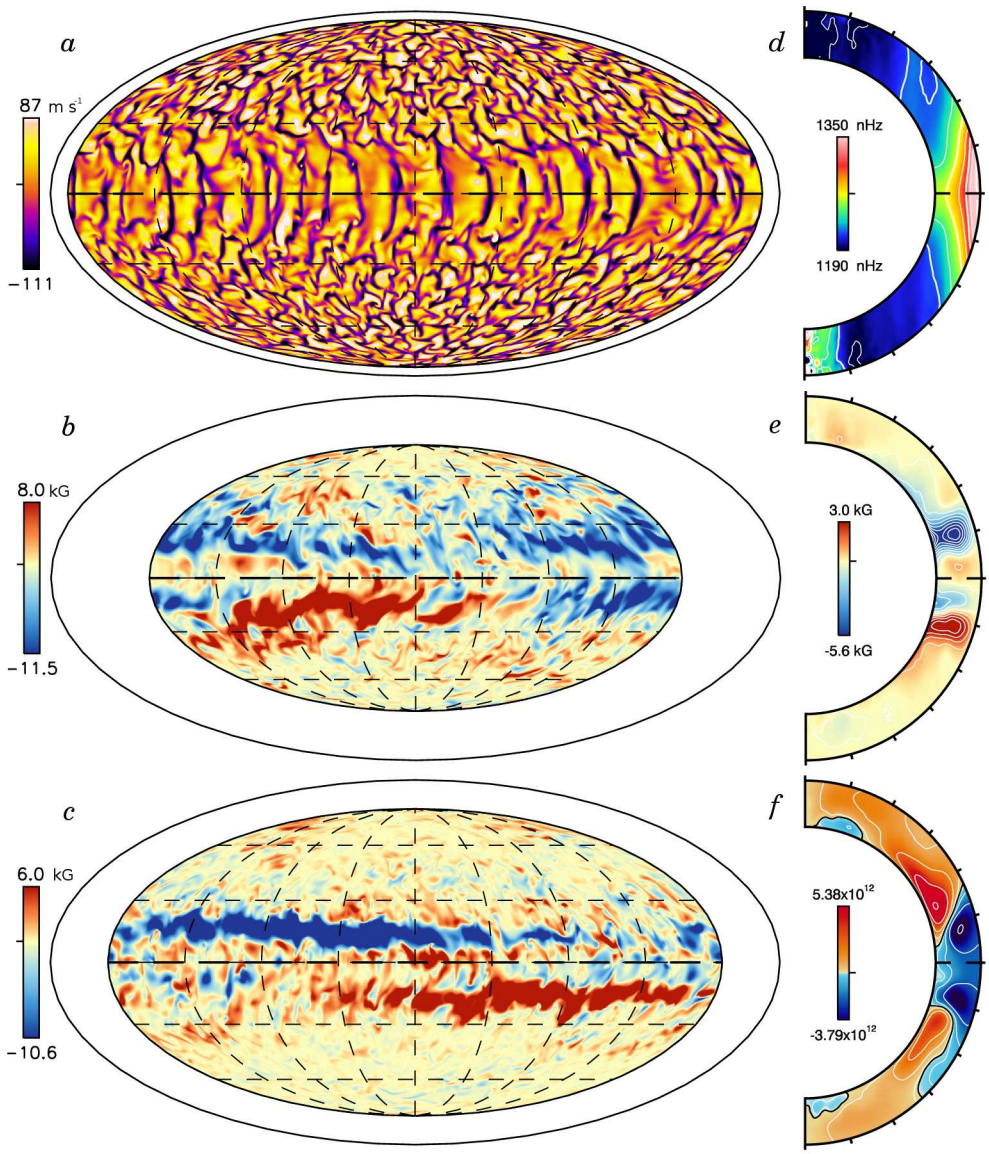

FIGURE 8.5 — Patterns of convection in case D3b. (a) Radial velocity v_r in Mollweide projection near the top of the shell ($0.95\,R_\odot$). (b) Toroidal magnetic field B_ϕ at mid-convection zone ($0.85\,R_\odot$) with two wreaths of opposite polarity. (c) Wreaths near the bottom of the convective shell (B_ϕ at $0.73\,R_\odot$). These snapshots are shown at day 2050, a time when the mean magnetic fields are strong. Also shown are 100 day averaged profiles of (d) Ω, (e) $\langle B_\phi \rangle$ and (f) $\langle A_\phi \rangle$.

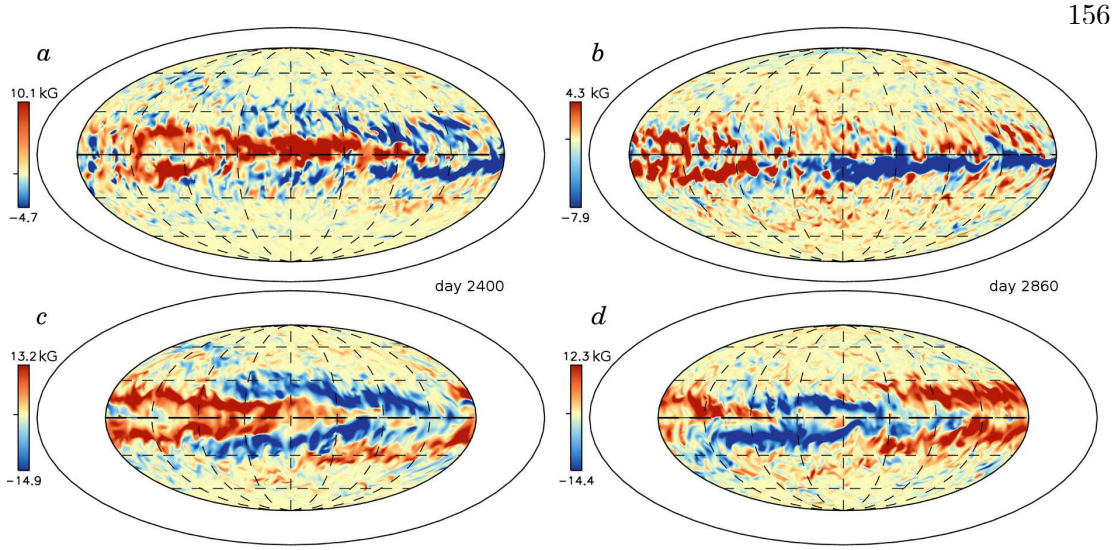

FIGURE 8.6 — B_ϕ achieving a more non-axisymmetric state in case D3b. (a) Mid-convection zone snapshot of B_ϕ at day 2400 and (b) at day 2860. At these times the wreaths have become highly non-axisymmetric structures. (c) Same fields near bottom of convection zone ($0.73\,R_\odot$) at day 2400 and (d) at day 2860.

tudes of ±35 kG. The toroidal fields at the poles are much stronger in case D3b than in the previous $3\,\Omega_\odot$ simulations, with fine-scale structure and typical field strengths of ±1.5 kG. In comparison, the polar B_ϕ of case D3a had amplitudes of ±1 kG, while those fields in case D3 rarely exceeded ±0.5 kG in amplitude. The profiles of differential rotation (Fig. 8.5d), mean toroidal magnetic field (Fig. 8.5e) and the mean poloidal vector potential (Fig. 8.5f) are all fairly similar to those found in case D3a.

The wreaths of magnetism in case D3b frequently attain strongly non-axisymmetric states. This is shown at two different times in Figure 8.6. At around day 2400 (Fig 8.6a), a region of reversed polarity appears in the midst of the southern hemisphere. This positive polarity B_ϕ replaces the preexisting negative wreath, and is more equatorially located than the previous wreaths (see Fig. 8.5b). The wreath in the northern hemisphere appears to peel apart and unwind toward the north pole. At this time the dynamo falls into a state where the southern hemisphere is generating magnetic wreaths, while the northern hemisphere is full of more complex structures, as near day 2900 (Fig. 8.6b).

Here $\langle B_\phi \rangle$ in the southern hemisphere is negative, but a positive polarity structure of substantial amplitude occupies roughly 25% of the domain in longitude. Near the bottom of the convection zone (Fig. 8.6*c*, *d*) the story is similar. There are distinct wreath-like structures in each hemisphere, but individual structures occupy only about 180° in longitude before being replaced by a structure with opposite polarity. As a result of this cancellation, $\langle B_\phi \rangle$ is very small in the lower convection zone. In case D3b the mean toroidal fields no longer dominate the structure of the wreaths, and these structures must be analyzed on local scales.

8.2 High Pm Dynamos at 3 $\Omega_\odot$

To further probe the nature and sensitivity of these dynamo solutions we explore a second path through parameter space where the magnetic Prandtl number is increased. Along this path, the viscous and thermal diffusivities ν and η are held constant while the magnetic diffusivity η is decreased, yielding larger magnetic Prandtl numbers and higher magnetic Reynolds numbers. This path corresponds to dynamo cases D3, D3-pm1, D3-pm2 and D3-pm4. These dynamo simulations begin occupying a similar region in parameter space as our previous dynamo simulations conducted at the solar rotation rate (e.g., Brun et al. 2004; Browning et al. 2006). Along this path, the magnetic Reynolds number increases while the fluid Reynolds number should remain approximately constant, only changing as the flows themselves respond to the magnetism that they generate. The convection retains a comparable level of complexity and the underlying driving of the differential rotation should be nearly constant.

Case D3-pm1 – At higher magnetic Prandtl numbers our dynamo simulations also begin to experience significant time dependence. This occurs already in our first case, case D3-pm1 with magnetic Prandtl number Pm = 1. The rms Reynolds number in this case is lower than in case D3, with a value of 149, owing to the weaker differential rotation realized in this simulation. The fluctuating Reynolds number is very similar

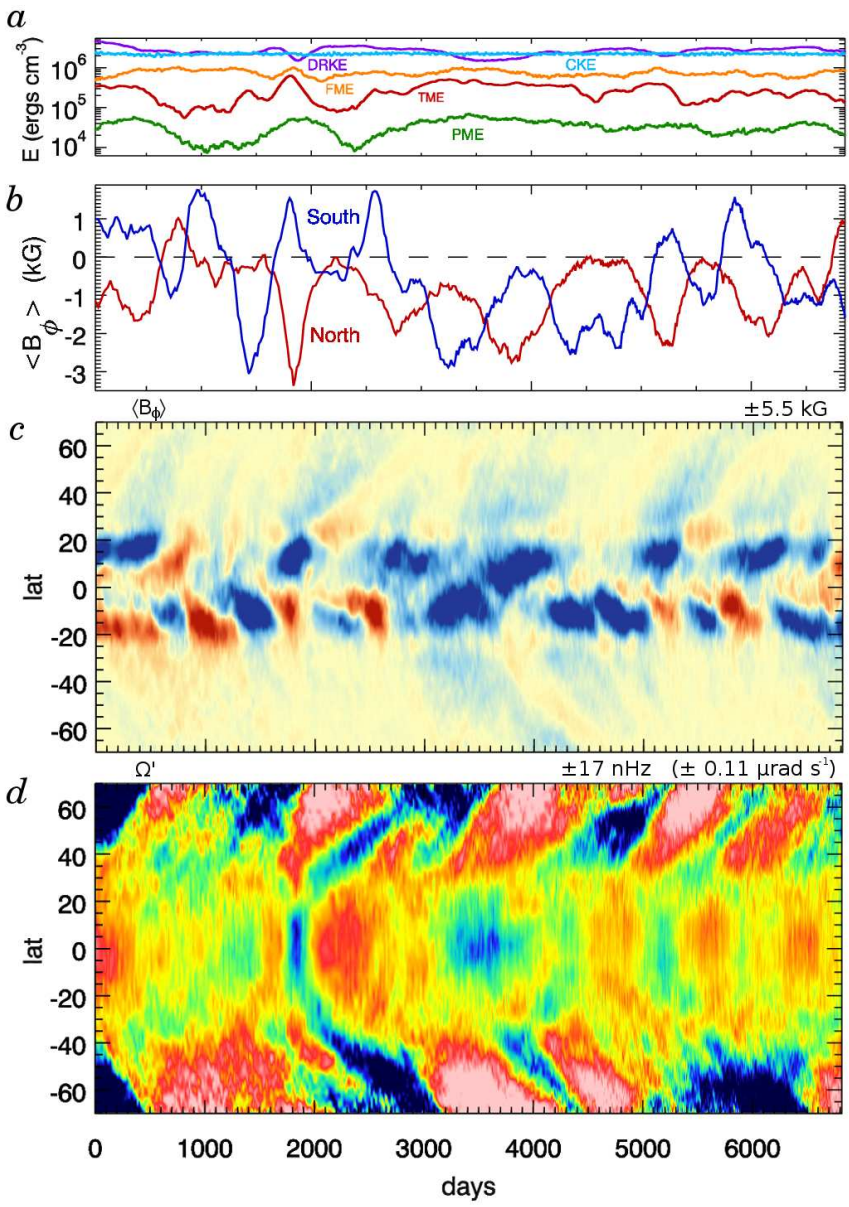

FIGURE 8.7 — Time-dependent behavior in cyclic case D3-pm1. (a) Volume-averaged kinetic and magnetic energies, and (b) mean $\langle B_\phi \rangle$ averaged over northern and southern hemispheres at mid-convection zone. (c) Time-latitude maps of $\langle B_\phi \rangle$ at mid-convection zone. (d) Time-latitude map of Ω' at mid-convection zone, with time average removed to emphasize the poleward propagating velocity structures.

with a value of 102, but the rms and fluctuating magnetic Reynolds numbers are higher than in that case, being 149 and 102 respectively.

The time history of case D3-pm1 is shown in Figure 8.7. At day 0 the values of η in case D3 were dropped by a factor of two. After about 500 days the steady wreaths from case D3 begin to break apart as new wreaths are generated near the equator. This is visible in time latitude maps of $\langle B_\phi \rangle$ (Fig. 8.7*c*) at mid-convection zone. The mean toroidal fields hunt between states with two wreaths of opposite polarity and states where one or two single polarity wreaths are built (i.e. days 3000-5000). When two wreaths are present the simulation appears to undergo frequent and rapid reversals, with typical timescales of only a few hundred days. Accompanying these reversals are strong angular velocity structures that propagate toward the polar regions (Fig. 8.7*d*).

Case D3-pm2 – Our next case on the high magnetic Prandtl number path is case D3-pm2, with Pm = 2. This case was initiated from case D3-pm1, and at roughly day 600 of that simulation the eddy diffusivity η was dropped by an additional factor of two, with ν and κ still the same as in case D3. In this simulation the rms and fluctuating Reynolds numbers are almost the same as in its progenitor (145 and 101 respectively), but the magnetic Reynolds numbers have increase by a factor of two to values of 291 and 202 for the rms and fluctuating quantities.

The time history for case D3-pm2 is shown in Figure 8.8. At first the wreaths from the previous dynamo persist, but after about 250 days they are replaced by different polarity structures and this dynamo diverges strongly from its progenitor. After about 1000 days the dynamo enters a state where almost all $\langle B_\phi \rangle$ is located in the northern hemisphere. The dynamo undergoes cycles in that hemisphere with the mean fields reversing on short timescales of a few hundred days. In the southern hemisphere the mean fields are weaker but are able to retain their average polarity and do not experience as many reversals. Angular velocity features launch toward the north pole frequently. These structures occasionally occur in the southern hemisphere, when the

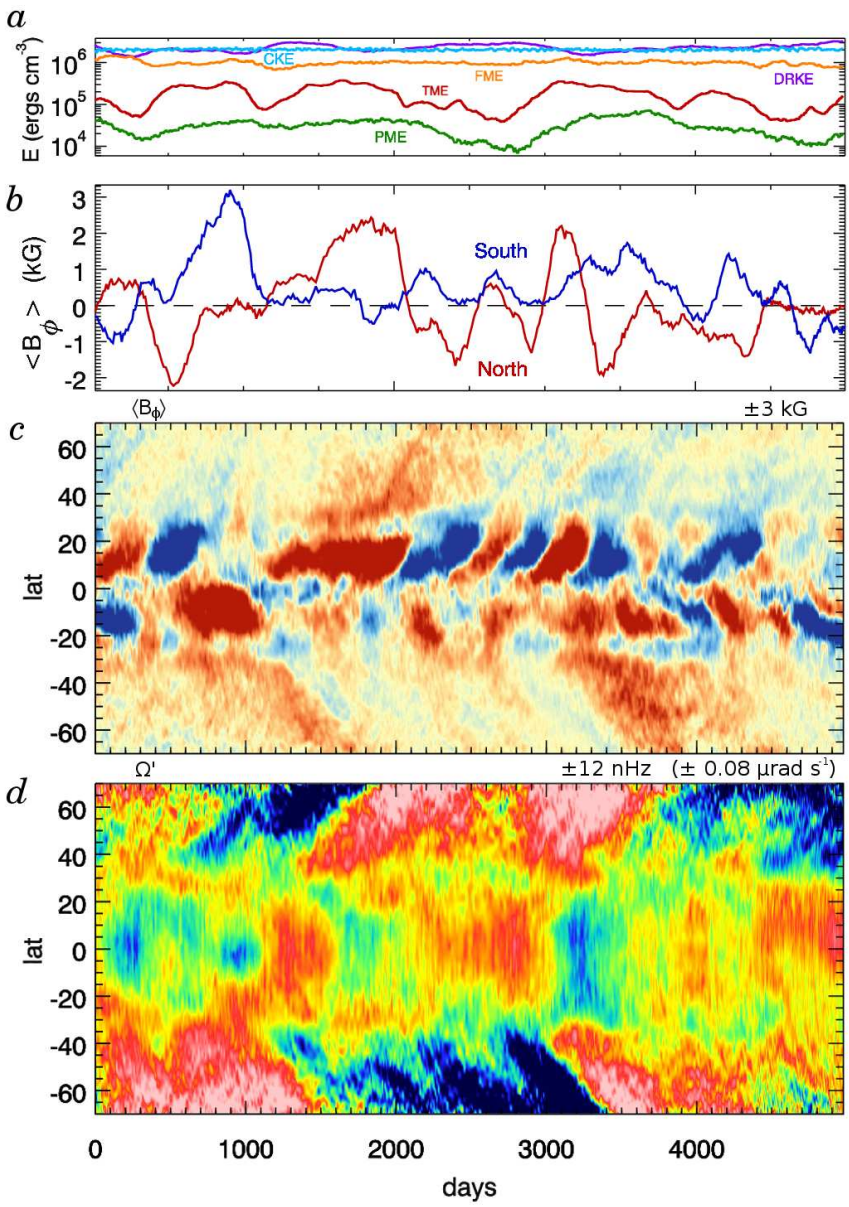

FIGURE 8.8 — Time-dependent behavior in cyclic case D3-pm2. (a) Volume-averaged kinetic and magnetic energies, and (b) mean $\langle B_\phi \rangle$ averaged over northern and southern hemispheres at mid-convection zone. (c) Time-latitude maps of $\langle B_\phi \rangle$ at mid-convection zone. (d) Time-latitude map of Ω' at mid-convection zone, with time average removed to emphasize the poleward propagating velocity structures.

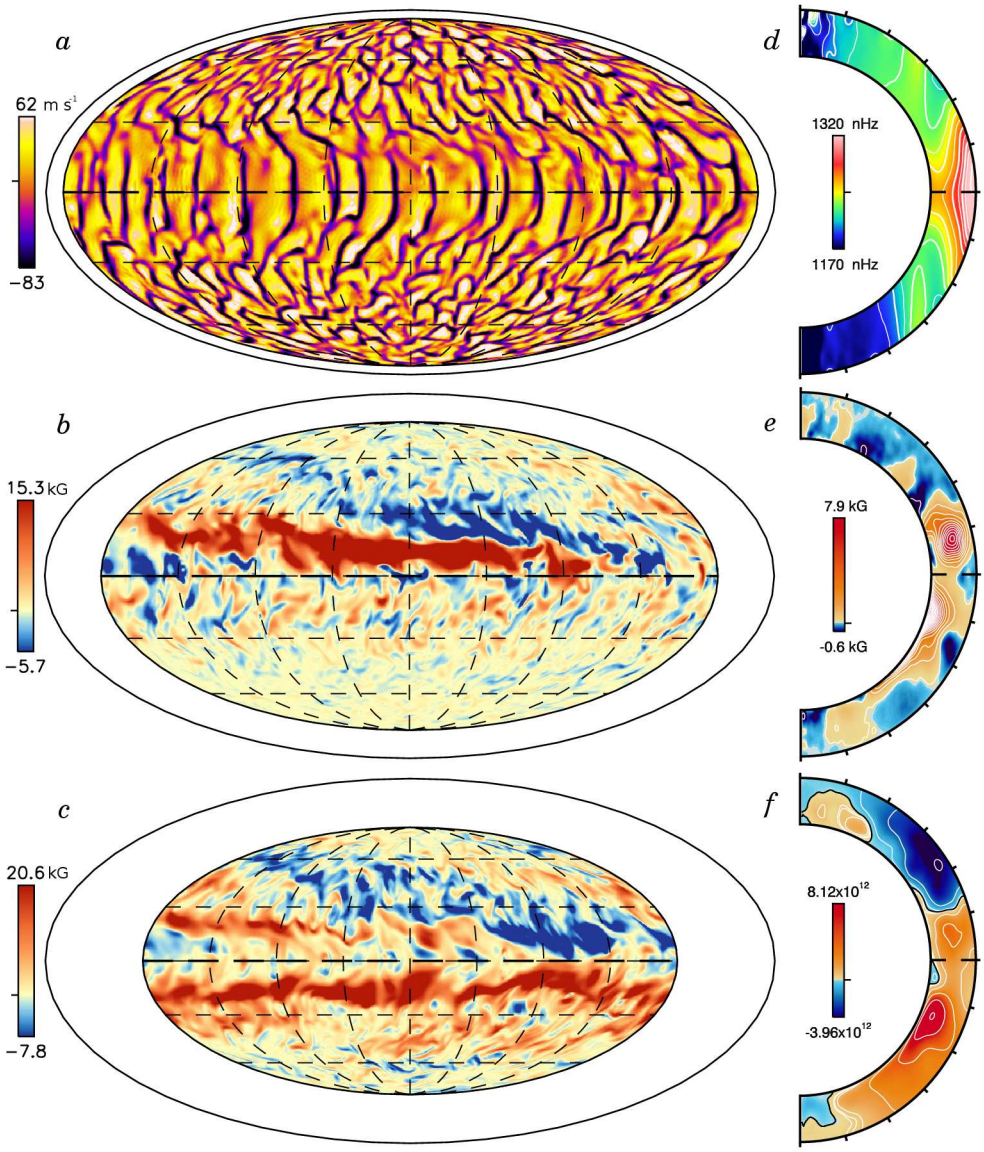

FIGURE 8.9 — Patterns of convection in case D3-pm2. (a) Radial velocity v_r in Mollweide projection near the top of the shell ($0.95\,R_\odot$). (b) Toroidal magnetic field B_ϕ at mid-convection zone ($0.85\,R_\odot$) with one strong wreath. (c) Two wreaths of same polarity are near the bottom of the convective shell (B_ϕ at $0.73\,R_\odot$). These snapshots are shown at day 3100, a time when the mean magnetic fields are strong in the northern hemisphere. Also shown are 100 day averaged profiles of (d) Ω, (e) $\langle B_\phi \rangle$ and (f) $\langle A_\phi \rangle$.

mean magnetic fields become particularly strong (i.e. days 3000-3800).

The patterns of convection in case D3-pm2 are shown in Figure 8.9. Near the surface, the convective cells are very similar to those found in our other simulations at three times the solar rate with velocities similar to those in case D3, rather than the faster flows found in cases D3a and D3b. The magnetic fields in this case are much stronger and show marked asymmetry, with strong fields occupying narrow ranges of longitude. At mid-convection zone, often a single strong wreath appears in the northern hemisphere. These states are similar to those realized occasionally in case D5, and as there, weaker opposite polarity field surrounds the single wreath. At greater depths, two wreaths of the same polarity occupy the two hemispheres. A profile of the mean differential rotation (angular velocity Ω) is shown averaged over a 100 day interval around the snapshots (Fig. 8.9*d*). Accompanying profiles show $\langle B_\phi \rangle$ and $\langle A_\phi \rangle$ averaged over the same interval (Fig. 8.9e, f). During this interval, the wreaths possess a substantially different mean poloidal field than in our previous simulations at three times the solar rate. Here the mean poloidal field is almost quadrupolar in nature.

Case D3-pm4 – Our highest magnetic Prandtl number case at three times the solar rate is case D3-pm4 with Pm = 4. This simulation is quite magnetically turbulent. The rms and fluctuating Reynolds numbers remain comparable to the other simulations on the high-Pm branch, with values of 161 and 94 respectively. The magnetic Reynolds numbers are much higher, with rms and fluctuating values of 644 and 377. The fluctuating magnetic Reynolds number is among the highest achieved in any of our rapidly rotating dynamo simulations and is comparable to those achieved in previous simulations of the solar dynamo (Brun et al. 2004; Browning et al. 2006). Despite this high level of magnetic turbulence, case D3-pm4 still builds significant magnetic wreaths within its convection zone.

The patterns of convection and the magnetic structures realized are shown in Figure 8.10 at a time shortly after the dynamo has equilibrated. Though the velocity patterns remain very similar, the magnetic fields have significantly more fine-scale structure. Though highly complex at mid-convection zone, the toroidal fields retain an overall polarity in each hemisphere (Fig. 8.10*b*). Near the bottom of the convection zone the wreaths again are marked by the strong mean fields (Fig. 8.10*c*, *e*). Indeed, the magnetic fields generated within these wreaths are among the strongest achieved in any of our rapidly rotating dynamos, with typical amplitudes of more than ± 20 kG in the fluctuating fields and peak amplitudes of ± 40 kG near the base of the convection zone. This simulation has only experienced about 1800 days of evolution and the timesteps are heavily limited by the Alfvénic CFL with typical limits near 30 seconds or less.

8.3 Resulting Differential Rotation

In our high magnetic Prandtl number branch of simulations, we find that the mean profile of differential rotation is somewhat different than in our Pm = 0.5 simulations. In these higher magnetic Prandtl number cases, the equator remains prograde with more retrograde poles, but the overall angular velocity contrast is significantly weaker. Measurements of the angular velocity contrast in latitude and in radius are shown for all of our dynamos at three times the solar rate in Table 8.4. These values are time-averaged over the indicated ranges of dates and these intervals typically span several magnetic oscillations or reversals. Case D3b is still undergoing some evolution in $\Delta\Omega$ at this time, as is case D3-pm4, which has seen approximately 1800 days of evolution and has uncertain time-dependence. The other cases are well equilibrated. Accompanying each measurement is an indication of the standard deviation of the angular velocity contrast in time, with case D3 showing little variation and the more turbulent cases showing substantially larger excursions.

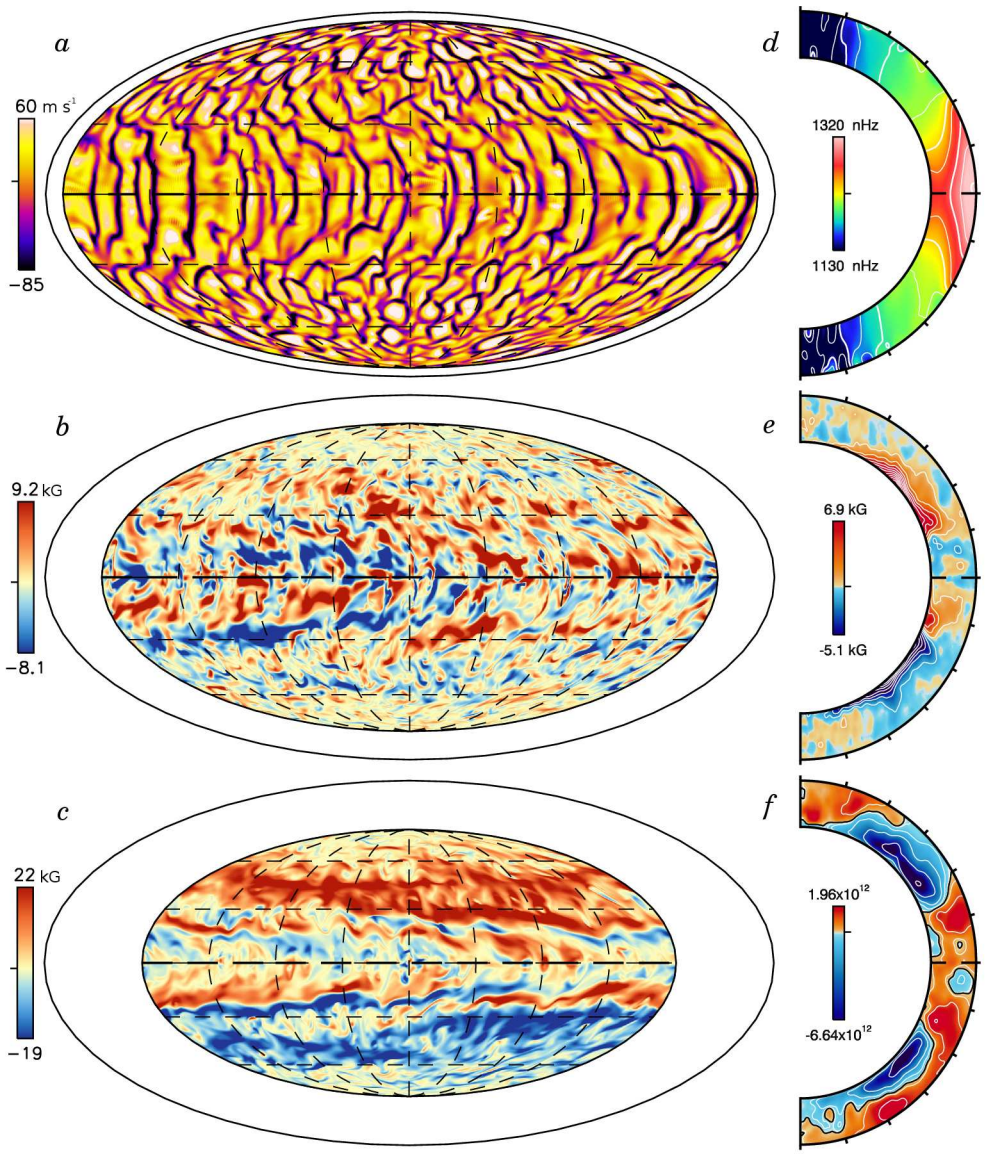

FIGURE 8.10 — Patterns of convection in case D3-pm4. (*a*) Radial velocity v_r in Mollweide projection near the top of the shell ($0.95\,R_\odot$). (*b*) Toroidal magnetic field B_ϕ at mid-convection zone ($0.85\,R_\odot$) with indistinct wreaths. (*c*) Two strong wreaths are at high latitudes near the bottom of the convective shell (B_ϕ at $0.73\,R_\odot$). These snapshots are shown at day 1830. The dynamo is still equilibrating at this time. Also shown are 20 day averaged profiles of (*d*) Ω, (*e*) $\langle B_\phi \rangle$ and (*f*) $\langle A_\phi \rangle$.

Table 8.4. Mean $\Delta\Omega$ in Dynamos at $3\,\Omega_\odot$

Case	$\Delta\Omega_{\rm lat}$		$\Delta\Omega_{\rm r}$	Epoch
	$0.97R_\odot$	$0.85R_\odot$	equator	days
D3	1.18 ± 0.05	0.79 ± 0.06	0.70 ± 0.02	2000 – 6980
D3a	1.11 ± 0.18	0.68 ± 0.10	0.71 ± 0.13	2000 – 15980
D3b	1.01 ± 0.17	0.56 ± 0.07	0.71 ± 0.14	1000 – 3120
D3-pm1	0.87 ± 0.10	0.53 ± 0.07	0.55 ± 0.06	1000 – 6850
D3-pm2	0.78 ± 0.08	0.48 ± 0.05	0.48 ± 0.06	1000 – 4730
D3-pm4	0.90 ± ?	0.74 ± ?	0.38 ± ?	1830 – 1850

Note. — Angular velocity shear in units of μrad s^{-1}, with $\Delta\Omega_{\rm lat}$ measured at two depths and $\Delta\Omega_{\rm r}$ measured across the full shell at the equator.

In the Pm = 0.5 branch of dynamos, the more turbulent dynamos still have a strong differential rotation. The latitudinal angular velocity contrast $\Delta\Omega_{\rm lat}$ in the upper convection zone decreases slightly as the diffusivities are dropped. At mid-convection zone the decrease is stronger. In contrast, the radial shear at the equator remains almost constant in this group of cases. The high magnetic Prandtl number dynamos have differential rotation profiles that become substantially weaker as η is decreased. In this family of solutions, both the latitudinal and radial shear are markedly smaller. In comparing to the Pm = 0.5 dynamos, case D3-pm1 and case D3b, with similar values of η throughout the convection zone, have similar latitudinal shear at mid-convection zone but different angular velocity contrasts in the upper convection zone and in radius.

8.4 Extreme Rotators: 10 and 15 $\Omega_\odot$ dynamos

Our most rapidly rotating dynamo simulations are currently at ten and fifteen times the current solar rotation rate. In a star like our Sun, such rapid rotation is likely only when the star is very young, shortly after reaching the main sequence. In these stars, we find that the dynamos can produce magnetic fields which are strong enough to largely quench the differential rotation. Despite this, cyclic oscillations and global-scale polarity reversals of the mean magnetic fields continue to occur.

In total, there are three simulations rotating in this regime. Two of these simulations are rotating at 10 $\Omega_\odot$, one with the same diffusivities used in case D5 (case D10L) and one with lower diffusivities in keeping with the scaling law of equation 8.1 (case D10). Our most rapidly rotating dynamo is case D15, at 15 $\Omega_\odot$. Here we will briefly examine the emergence of nests of convection in case D10L, and the suppression of differential rotation in case D15.

Case D10L – Only one of our most rapidly rotating cases retains a strong differential rotation. This is case D10L rotating at $10\,\Omega_\odot$ and with eddy diffusivities identical to those in both case D5 and case D3a. Typical rms and fluctuating Reynolds numbers in this simulation are 331 and 110 respectively, with rms and fluctuating magnetic Reynolds numbers of 165 and 55. The time history of case D10L is shown in Figure 8.11, covering 6000 days of the simulation after the initial seed magnetic fields are introduced. The magnetic energies grow quickly to near equipartition with the kinetic energies before they react back on the differential rotation and substantially suppress it.

Time-latitude maps of $\langle B_\phi \rangle$ and Ω reveal how this quenching occurs. Case D10L builds strong wreaths of magnetism which frequently propagate toward the polar regions (Fig. 8.11*c*). These poleward-slips of $\langle B_\phi \rangle$ are accompanied by substantial poleward propagating angular velocity structures, which transport quickly rotating material from the prograde equator to the retrograde poles. This is evident in the time-evolution of the latitudinal and radial angular velocity contrast $\Delta\Omega$ (Fig. 8.11*d*). During the initial transient, the latitudinal angular velocity contrast $\Delta\Omega_{\rm lat}$ is substantially reduced, dropping by a factor of about two in the upper convection zone and by nearly a factor of five at mid-convection zone. Convection rebuilds the differential rotation and by day 2300 nearly half the angular velocity contrast has been rebuilt. At this point however, strong magnetic wreaths are formed leading to another pulse of poleward propagating fields and flows. The radial angular velocity contrast $\Delta\Omega_r$ is less affected by the magnetism. It experiences temporal variations on similar timescales, but retains

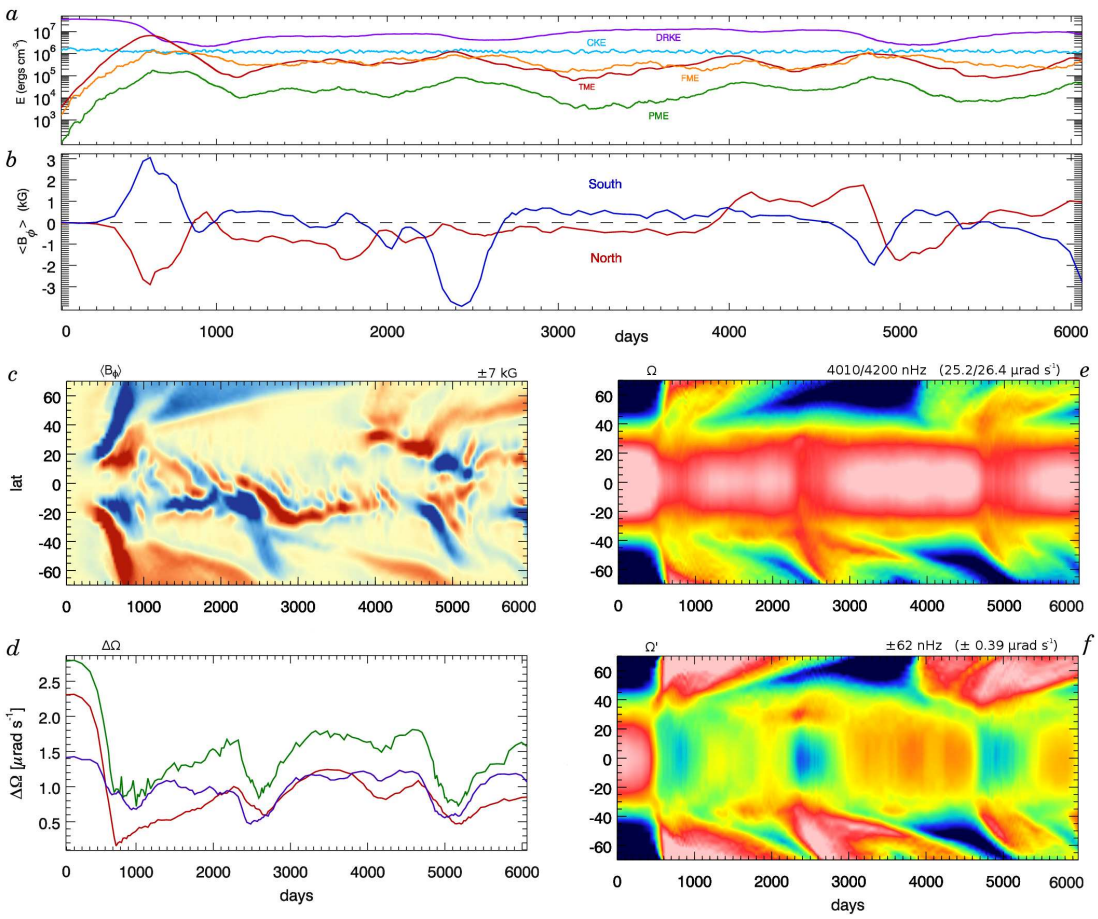

FIGURE 8.11 — Time-dependent behavior in case D10L. (a) Volume-averaged kinetic and magnetic energies, and (b) mean $\langle B_\phi \rangle$ averaged over northern and southern hemispheres at mid-convection zone. (c) Time-latitude maps of $\langle B_\phi \rangle$ at mid-convection zone. (d) Angular velocity contrast $\Delta\Omega$, with $\Delta\Omega_{\rm lat}$ measured near the surface (top line, green) and at mid-convection zone (bottom line, red) and with $\Delta\Omega_r$ measured across the shell at the equator (middle line, purple). (e) Time-latitude map of full angular velocity Ω at mid-convection zone, with fast equator and slow poles. (f) Map of Ω' with time average removed, emphasizing temporal variations. The initial transient slows the equator and speeds up the poles, reducing the overall differential rotation.

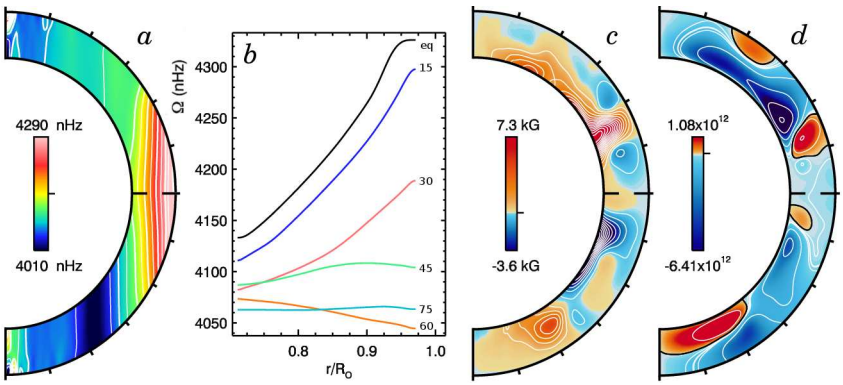

FIGURE 8.12 — Differential rotation and magnetism in case D10L. (*a*) Profile of angular velocity Ω averaged over an interval of about 100 days when the differential rotation is strong (days 4490-4600) accompanied by (*b*) radial cuts. (*c*) Two magnetic wreaths are present. (*d*) The poloidal vector potential $\langle A_\phi \rangle$ is complex and largely of a single polarity.

an average value similar to the hydrodynamic progenitor (visible at day 0).

The mean toroidal magnetic fields have a much more complex structure than in our three or five solar dynamos. Strong concentrations of $\langle B_\phi \rangle$ appear and disappear on short timescales near the equator while large wreaths occupy latitudes near $\pm 20°$. Those wreaths eventually slip toward the poles and are often replaced by wreaths of opposite polarity (i.e. the reversals that occur near day 2500 and day 4900). Though initially the dynamo builds quite symmetric wreaths, the wreaths which form after the initial transient are less symmetric and frequently are substantially stronger in one hemisphere and weaker in the other.

Time-averaged profiles in radius and latitude of the differential rotation and the magnetic fields are shown in Figure 8.12 at a time when the differential rotation is strong (days 4490-4600). The equatorial regions still possess a strong radial shear, and the profile and radial cuts are similar to cases D3 and D5. Two magnetic wreaths are formed, with a strong positive polarity in the northern hemisphere and a weaker wreath in the southern. Here the poloidal field is quite complex and is highly asymmetric with a major enhancement of $\langle A_\phi \rangle$ visible in the northern hemisphere. This is in marked

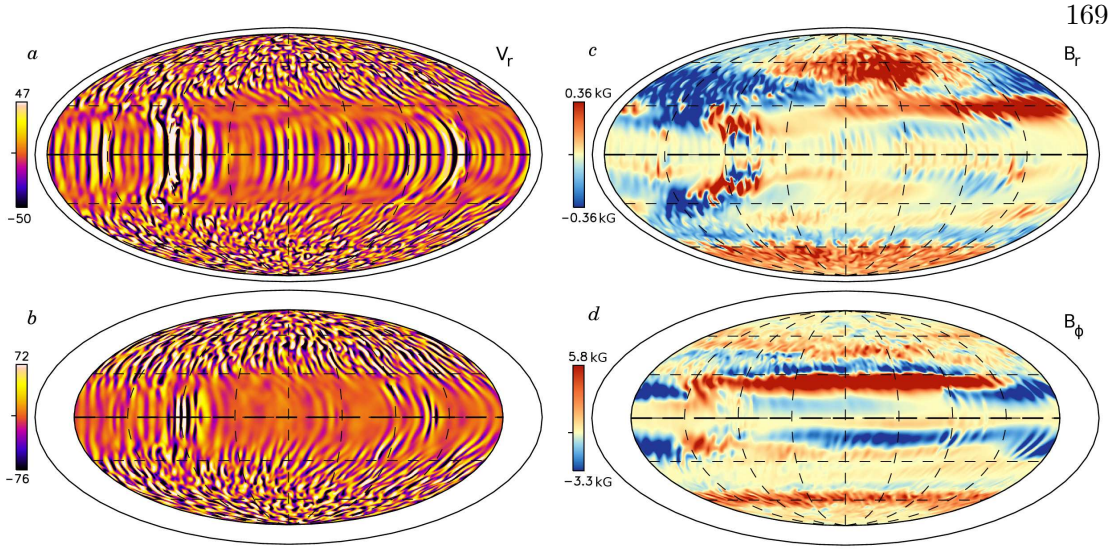

FIGURE 8.13 — Convective patterns in case D10L with nests of convection. Shown as snapshots in Mollweide projection are radial velocities v_r (a) near the surface ($0.95\,R_\odot$) and (b) at mid-convection zone ($0.85\,R_\odot$). Two active nests of convection are clearly visible. (c) Near the surface, the radial magnetic field B_r is concentrated in the stronger nest. (d) At mid-convection zone the active nests make an imprint on the magnetic wreaths. Also visible near the south pole are the remnants of the magnetic wreath from the previous cycle. These snapshots are of day 4490 at a period when the differential rotation is strong.

contrast to the poloidal fields achieved in our cases at three times the solar rate, which were dominated by low-ℓ structures with typically either largely octopolar (i.e. cases D3, D3a, D3b) or quadrupolar (i.e. case D3-pm2) topologies.

The patterns of convection in case D10L are unique among our rapidly rotating dynamos. The relatively strong differential rotation, combined with the rapid overall rotation, lead to strongly localized nests of convection in the equatorial regions. These nests are shown in Figure 8.13 at day 4490, when the differential rotation is strong. The localized convection once again is strongly visible in the radial velocity patterns throughout the convection zone (Fig. 8.13a, b). At this instant, two nests are visible, separated by almost 180° of longitude.

The nests have substantial magnetic signatures as well, particularly in the radial magnetic field near the surface (Fig. 8.13c). Here the stronger nest (at left) is accompanied by a significant enhancement of radial field. At mid-convection zone the nests also

Table 8.5. Mean $\Delta\Omega$ in Dynamos at 10 and 15 $\Omega_\odot$

Case	$\Delta\Omega_{\rm lat}$		$\Delta\Omega_{\rm r}$	Epoch
	$0.97R_\odot$	$0.85R_\odot$	equator	days
D10L	1.39 ± 0.27	0.83 ± 0.21	0.97 ± 0.19	1000 − 6060
D10	0.45 ± 0.08	0.22 ± 0.05	0.38 ± 0.10	2720 − 5000
D15	0.33 ± 0.07	0.12 ± 0.04	0.26 ± 0.08	1500 − 4500
D15	0.30 ± 0.04	0.10 ± 0.01	0.22 ± 0.03	2000 − 3500
D15	0.51 ± 0.01	0.17 ± 0.003	0.50 ± 0.02	3950 − 4100

Note. — Angular velocity shear in units of μrad s^{-1}, with $\Delta\Omega_{\rm lat}$ measured at two depths and $\Delta\Omega_{\rm r}$ measured across the full shell at the equator. These measurements are averaged over the indicated range of days. Dynamo case D15 suddenly amplifies its differential rotation for a period of time between days 3700-4300.

make an imprint on the toroidal field, locally stretching and shredding the wreaths. In the more quiescent regions between the nests, the wreaths are stronger and have less fine-scale structure (Fig. 8.13*d*).

In case D10L the active nests of convection are clearly visible and persist for many hundreds of days. The temporal variations in the differential rotation lead to periods when the nests are strong and the convection is highly confined in longitude, as well as other periods where the differential rotation and nests are weaker. Time-longitude maps reveal that on thousand day timescales the convection alternates between states with two or three active nests, spending a few hundred days in each state.

Cases D10 − Our other dynamo at ten times the solar rate is case D10, with diffusivities lower by slightly more than a factor of two compared to case D10L. This simulation is more turbulent, with rms and fluctuating Reynolds numbers of 253 and 228 and rms and fluctuating magnetic Reynolds numbers of 126 and 114 respectively. The small spread between the rms and fluctuating values is due to the differential rotation collapsing almost entirely.

The average angular velocity contrast achieved in these most rapidly rotating simulations is reported in Table 8.5. In case D10, the angular velocity contrast $\Delta\Omega$

and its temporal variations have both become much smaller than in case D10L. These quantities are measure over an interval of almost 2300 days. There is little angular velocity contrast in either radius or latitude.

Despite the small differential rotation, substantial toroidal magnetic fields are generated throughout the convection zone. Now however, the mean fields comprise a smaller proportion of the total magnetic energy while the fluctuating fields become more prominent. The fluctuations exist on large scales, and with substantial contributions from longitudinal wavenumbers m=1 or m=2. The structure of the magnetic fields remains wreath-like, though now more complex. The wreaths appear to still undergo cyclic variations in polarity.

Case D15 – In our most rapidly rotating dynamo, case D15, the differential rotation is even weaker. This dynamo is one of the more turbulent Pm = 0.5 dynamos, with a fluctuating Reynolds number of 272 and a fluctuating magnetic Reynolds number of 136. This case is thus comparable to case D3b. The hydrodynamic progenitor to this case had a very strong differential rotation, and its rms and fluctuating Reynolds numbers were 1670 and 293 respectively.

The time history of case D15 is shown in Figure 8.14. Starting from weak seed fields, the dynamo quickly builds strong magnetic wreaths whose energies on average reach equipartition with the convective flows. These fields quench the differential rotation, driving DRKE down into sub-equipartition with either the convection (CKE) or the fluctuating magnetism. Though the differential rotation is weak, the dynamo still undergoes substantial temporal variations and cycles of polarity change (Fig. 8.14*b*). Time-latitude maps reveal that, as in case D3-pm2, this cyclic wreath building activity is largely confined to the northern hemisphere (Fig. 8.14*c*). The wreaths that are achieved begin to slip toward the north pole almost immediately, and typically persist in the equatorial region for less than 500 days before beginning their poleward migration.

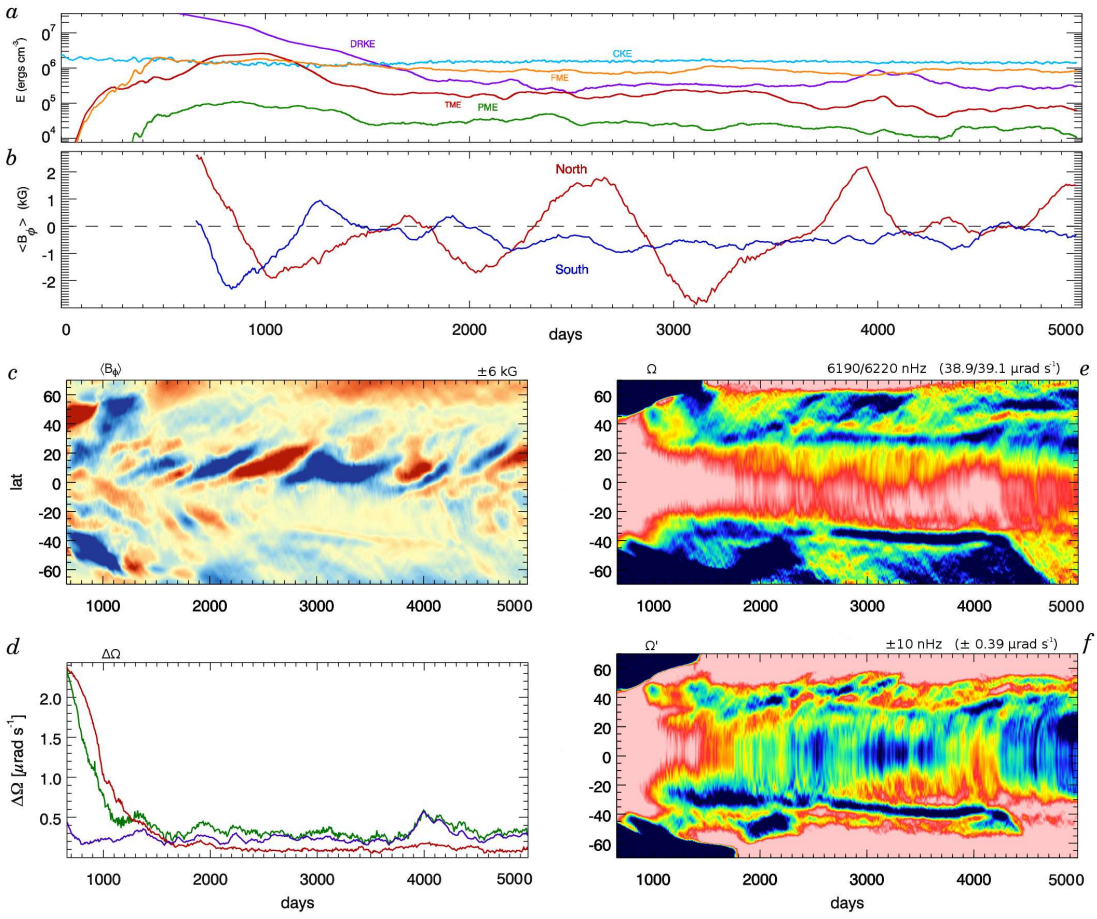

FIGURE 8.14 — Time-dependent behavior in case D15. (a) Volume-averaged kinetic and magnetic energies, and (b) mean $\langle B_\phi \rangle$ averaged over northern and southern hemispheres at mid-convection zone. The azimuthally averaged data exists from day 660 onwards. (c) Time-latitude maps of $\langle B_\phi \rangle$ at mid-convection zone. (d) Angular velocity contrast $\Delta\Omega$, with $\Delta\Omega_{\rm lat}$ measured near the surface (top line, green) and at mid-convection zone (bottom line, red) and with $\Delta\Omega_r$ measured across the shell at the equator (middle line, purple). The latitudinal differential rotation is highly suppressed after the dynamo equilibrates, but the radial shear at the equator is largely unaffected. (e) Time-latitude map of full angular velocity Ω at mid-convection zone. (f) Map of Ω' with time-average removed, emphasizing temporal variations. The initial transient slows the equator and speeds up the poles, reducing the overall differential rotation. In this dynamo, the poles actually become prograde, and retain that sense for long intervals.

The first magnetic wreaths that form were two strong wreaths of opposite polarity in the two hemispheres. These first magnetic wreaths slip to the poles and transport enough angular momentum from the prograde equator that above $\pm 70^\circ$ the polar regions change their sense of differential rotation from retrograde to prograde. Once prograde flows are established in the polar regions, they persist for the full 5000 simulated days shown here. The angular velocity contrasts become much weaker after the dynamo saturates and reduces the differential rotation. As in case D10L, the latitudinal contrast is affected more strongly by the magnetism than the radial shear, though $\Delta\Omega_r$ also decreases significantly (Fig. 8.14*d*). Dynamo case D15 has latitudinal and radial angular velocity contrasts which range from 0.3 to 0.5 μrad s^{-1} depending on the phase of the dynamo oscillations (see Table 8.5). During a brief period (days 3800 - 4500) the differential rotation in the upper convection zone becomes substantially stronger, with both the latitudinal and radial shear increasing by more than a factor of two. The mid-convection zone $\Delta\Omega$ shows almost no variation during this interval. Even at their peak levels (about day 400), the angular velocity contrasts in case D15 are dramatically weaker than the contrast achieved in the hydrodynamic progenitor, which had a near-surface $\Delta\Omega_{\rm lat}$ of 3.9 μrad s^{-1} and a radial shear $\Delta\Omega_r$ of 2 μrad s^{-1}.

The time-averaged profiles in radius and latitude of the differential rotation and the magnetic fields of case D15 are shown in Figure 8.15 at a time when the differential rotation is unusually strong (days 4000 - 4115). During this time interval, the radial shear in the equatorial regions remains substantial, but the mid-latitudes (30°-60°) have lost much of their contrast in radius or latitude. The polar regions above $\pm 75^\circ$ are spinning prograde at all depths. At other points in time, as indicated by the time trace of $\Delta\Omega_r$ in Figure 8.14*d*, the radial shear at the equator becomes much weaker, decreasing by more than a factor of two. In these states, the most visible features in the differential rotation profile are the prograde poles, which retain their strong angular velocity gradients at all times.

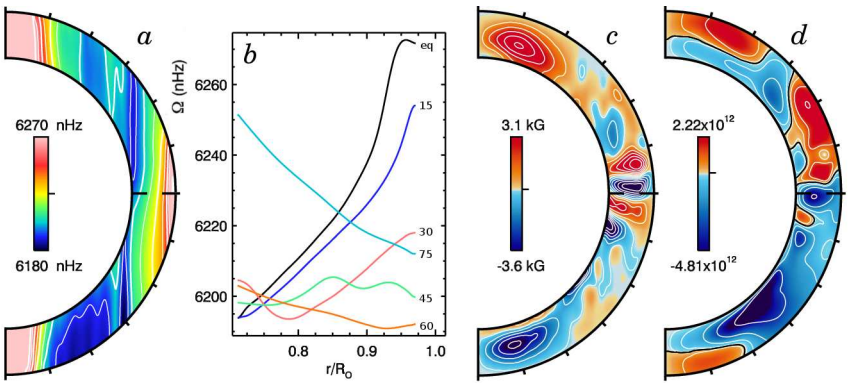

FIGURE 8.15 — Differential rotation and magnetism in case D15. (*a*) Profile of angular velocity Ω averaged over an interval of about 100 days when the differential rotation unusually strong (days 4000-4115) accompanied by (*b*) radial cuts. At other intervals, the equatorial shear disappears entirely. (*c*) Several narrow wreaths occupy the equatorial region, and two strong magnetic structures are visible at the poles. (*d*) As in case D10L, the poloidal vector potential $\langle A_\phi \rangle$ is quite complex.

The mean toroidal field in this case is substantially weaker than in many other simulations, with average amplitudes of roughly ± 3 kG during this interval (Fig. 8.15*c*). This decrease is due in part to the equatorial wreaths becoming substantially non-axisymmetric in structure. Strong wreaths are visible at the polar regions. At present it is unclear whether these wreaths are sustained by continual poleward transport of field by many generations of wreaths being built at the equator, or if they are locally built and maintained by the gradients in angular velocity near the poles. As in case D10L, the mean poloidal magnetic field has a complex structure, with a significant enhancement visible during this interval in the southern hemisphere.

The patterns of convection in case D15 are shown in Figure 8.16. The radial velocities show some modulation, but the strongly confined single nest of the hydrodynamic progenitor has disappeared as the differential rotation has collapsed. Time-longitude maps reveal that the modulation persists for more than a thousand days, and with the weak differential rotation, the pattern remains almost stationary relative to the rotating reference frame of the star. The strong magnetism disrupts the convective cells in some

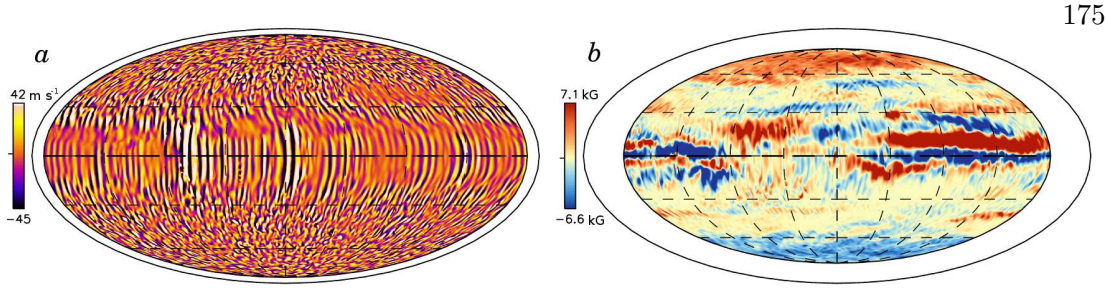

FIGURE 8.16 — Convective patterns in case D15. Shown in global Mollweide projection at day 4000 are (*a*) radial velocities v_r near the surface, with visible longitudinal modulation and (*b*) toroidal magnetic field B_ϕ at mid-convection zone, with highly asymmetric structures present throughout and strong structures near the poles. These snapshots are taken at day 4000, a time when the differential rotation is particularly strong.

regions, particularly at mid-convection zone. Shadows of these magnetic regions remain visible in the near-surface flows.

In case D15, wreaths of magnetism continue to pervade the convection zone. Now these structures have gained significant non-axisymmetric components which can span more than 90° of longitude. These structures retain a high level of organization but no longer encircle the entire convection zone. As a result of this, $\langle B_\phi \rangle$ has relatively low amplitudes while B_ϕ locally can still attain high values. In this snapshot, the peak amplitudes of B_ϕ at mid-convection zone are $\pm 38\,\mathrm{kG}$. This is comparable to the peak amplitudes achieved in case D3b.

8.5 Spinning Down to the Sun

We now return to the Sun, considering cases which rotate more slowly than three times the solar rate. In this regime, dynamo action is somewhat harder to excite. This is evident already in Figure 8.1 at $1.5\,\Omega_\odot$, with sustained dynamo action only appearing in the more turbulent cases (D1.5a, D1.5b). In these respective cases, persistent or temporally-varying wreaths are realized in the bulk of the convection zone.

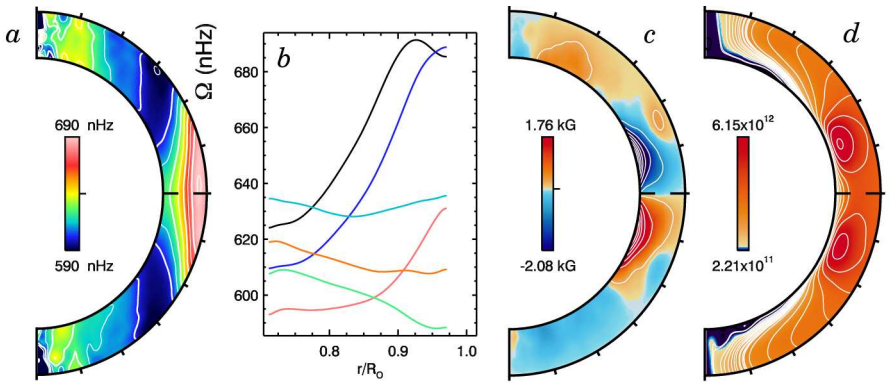

FIGURE 8.17 — Differential rotation and magnetism in case D1.5a. (*a*) Profile of angular velocity Ω averaged over an interval of about 100 days with (*b*) radial cuts. (*c*) Two wide wreaths occupy the equatorial region. (*d*) At these slower rotation rates, the poloidal vector potential $\langle A_\phi \rangle$ is much more dipolar.

Case D1.5a – Profiles of the differential rotation and magnetic wreaths generated in case D1.5a are shown in Figure 8.17. In this simulation, the differential rotation remains strong, with a fast equator and slow poles. The magnetic wreaths have lost some of the strong radial extent seen in the more rapidly rotating dynamos (e.g. case D3), and survive here near the bottom of the convection zone as structures which are highly extended in latitude. These wreaths persist with the same polarity for more than 5000 days after the dynamo equilibrates. The mean poloidal field is more dipolar in nature than those realized in the more rapidly rotating dynamos, and the equatorial region has the same polarity and sense as the polar regions.

The eddy diffusivity η must be reduced even further as the solar rotation rate is approached, and below $1.5\,\Omega_\odot$ we have shifted to high magnetic Prandtl numbers to excite dynamo action. Those simulations that achieve sustained dynamo action possess values of η which are comparable to our most turbulent rapidly rotating dynamos (e.g. cases M3 and D3-pm4 at similar values of η). This choice was necessary because in this range of rotation rates, decreasing ν and κ at fixed Prandtl number appears to lead to a decrease in the overall differential rotation that is achieved. This is in marked contrast to those simulations rotating faster than $1.5\,\Omega_\odot$, where decreasing ν and κ uniformly

leads to stronger differential rotation. A strong differential rotation greatly enhances dynamo action in these wreath-building dynamos. However, even the failed dynamos often initially create wreaths of magnetism. In these cases, dynamo action fails because the poloidal fields are not regenerated quickly enough. As the poloidal fields resistively decay away, the overall magnetic energies plummet with time.

8.6 The Mystery of Case M3

We turn now to case M3 rotating at the solar rotation rate. Case M3 was initially published in Brun et al. (2004). This simulation, at magnetic Prandtl number Pm = 4, generated strong fluctuating magnetic fields but produced only weak mean toroidal and poloidal fields, with little global-scale organization. There are no striking magnetic wreaths present in the simulation. The lack of wreaths is a mystery, as case M3 appears to lie well within the parameter space of wreath-building dynamos (Fig. 8.1). The differential rotation achieved in this case is somewhat weaker than that achieved in our rapidly rotating suns, but the high magnetic Prandtl number should still make the differential rotation highly effective at stretching and amplifying wreaths of magnetism.

Case M3 differs from the rapidly rotating dynamos in three characteristics, and one of these appears to be the answer to the missing wreaths. The first and most obvious difference is that case M3 rotates relatively slowly, at the solar rotation rate. If wreath-building is facilitated by more rapid rotation, than the slow rotation could explain the lack of wreaths in case M3. Fortunately, this does not appear to be the case. Even cases at $1.25\,\Omega_\odot$ build magnetic wreaths, as do simulations that rotate more slowly than the sun (i.e. case D0.5a). The second difference is that case M3 is at high magnetic Prandtl number and has very high fluctuating and rms magnetic Reynolds numbers at values of 716 and 500 respectively. If wreaths are shredded and destroyed in the presence of high magnetic Reynolds number flows, than the lack of wreaths in case M3 would raise serious questions for the rapidly rotating dynamos which are generally at lower magnetic

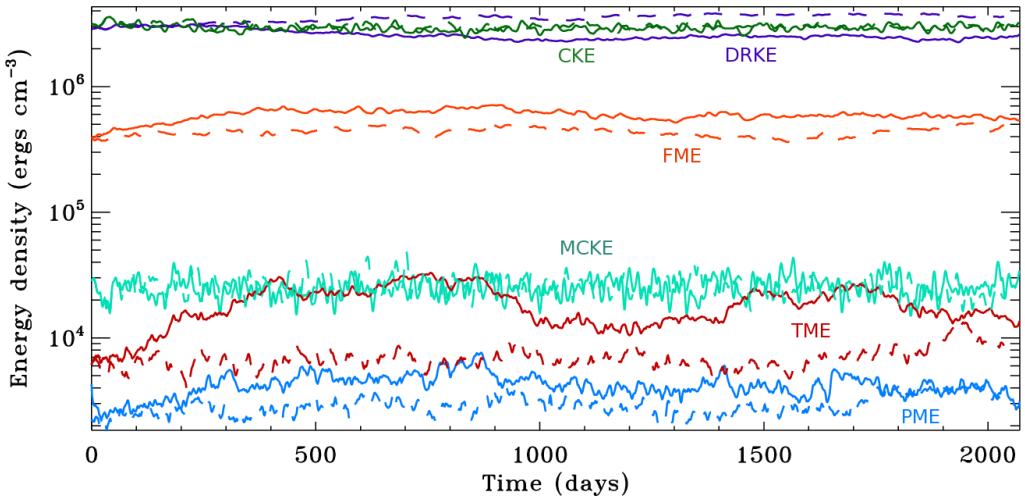

FIGURE 8.18 — Energy traces for cases M3 and M3-pcpf. Shown in overlaying volume-averaged energy traces are case M3-pcpf (solid) and the original case M3 (dashed), over the same interval in time. At day 0 the bottom boundary condition in case M3-pcpf was changed from potential field to perfect conductor. Shortly afterwards the energy contained in mean toroidal fields (TME) grows substantially.

Reynolds numbers. But magnetic wreaths appear to persist in our high Pm simulation case D3-pm4, with a similar fluctuating magnetic Reynolds number of 437.

The third and final significant difference between case M3 lies in the treatment of the bottom magnetic boundary condition. In case M3, the bottom boundary was taken to match onto a potential field solution, whereas in the rapidly rotating dynamos we have treated the bottom boundary as a perfect conductor. Perfectly conducting boundaries trap horizontal magnetic field, while potential field boundaries allow that field to exit the simulation. To test whether the treatment of boundary conditions affects the presence of magnetic wreaths, we have modified case M3 by changing the bottom boundary to a perfectly conducting medium. This new case, case M3-pcpf has a perfectly conducting bottom boundary and potential field top boundary, in the fashion of case D3 and all of our other rapidly rotating dynamos. No other changes were made between the two simulations. Cases M3 and M3-pcpf were continued in parallel, and their volume-averaged energies are shown over the same interval of time in Figure 8.18.

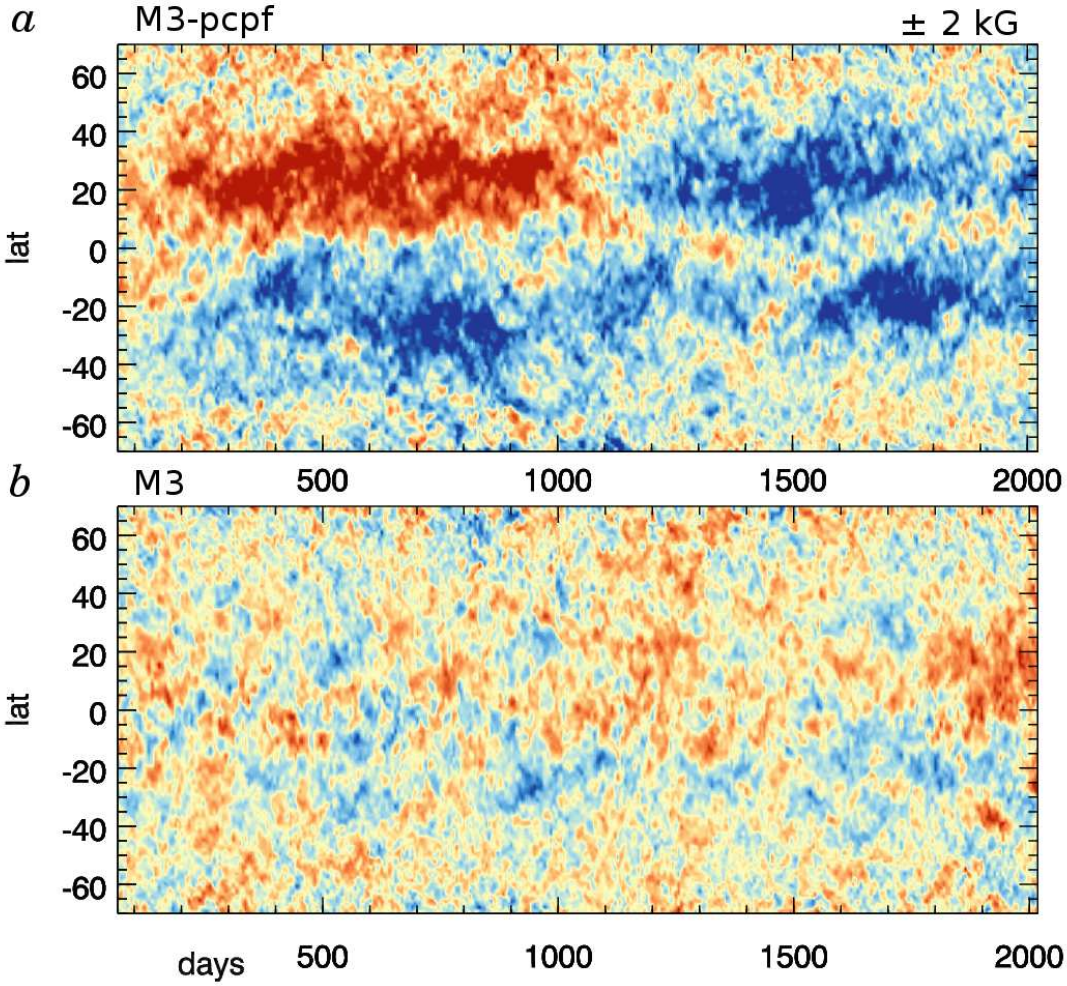

FIGURE 8.19 — Wreaths of magnetism in solar simulations. Shown are time-latitude maps of $\langle B_\phi \rangle$ at $0.75\,R_\odot$ for (a) case M3-pcpf and (b) case M3 over the same 2000 day interval of time. The bottom boundary conditions were changed in case M3-pcpf at day 0, and the two simulations quickly diverge. Case M3-pcpf builds strong wreaths of magnetism while case M3 has weaker and less organized mean fields. For both cases, the time-latitude maps are scaled from $\pm 2\,$kG.

The energy contained in the mean toroidal magnetic fields (TME) begins to grow almost immediately in case M3-pcpf after the change of boundary conditions. The fluctuating magnetic energies (FME) and the energy of the mean poloidal fields (PME) also grow relative to those of case M3. In response, the differential rotation is slightly reduced, the the convective kinetic energies (CKE) and the meridional circulations (MCKE) are basically unchanged.

Time-latitude maps of the mean toroidal field reveal that case M3-pcpf builds magnetic wreaths, while case M3 does not. Shown in Figure 8.19 are maps of $\langle B_\phi \rangle$ for both cases over the same 2000 day interval in time. Within 300 days, case M3-pcpf has built substantial magnetic wreaths with typical field strengths of $\pm 2\,\mathrm{kG}$ and peak mean toroidal fields of over $4\,\mathrm{kG}$. In contrast, case M3 builds weak and disorganized mean toroidal fields, with typical amplitudes of $\pm 1\,\mathrm{kG}$ and peak amplitudes of $\pm 2\,\mathrm{kG}$. Those fields are far less organized than the wreaths present in case M3-pcpf. The magnetic wreaths in case M3-pcpf undergo a partial polarity reversal around day 1000, with the toroidal fields in the northern hemisphere changing sign while those in the southern hemisphere retain their negative polarity. These time-latitude maps are made at a slightly deeper depth in the convection zone ($0.75\,R_\odot$) than the maps shown for the rapidly rotating cases. This is because the magnetic wreaths here are concentrated in the lower convection zone, as also seen case D1.5a.

The patterns of convection and magnetism in cases M3-pcpf and M3 are shown in Figures 8.20 and 8.21 respectively. The radial velocity structures are very similar in both cases, as are the profiles of mean differential rotation. The toroidal magnetic fields have fine structure throughout the convection zone, but those in case M3-pcpf also show organization on large scales at mid-convection zone and especially in the lower convection zone (Figs. 8.20b, c). In contrast, the toroidal fields in case M3 are comparably disorganized at all depths (Figs. 8.21b, c). Time-averaged profiles of $\langle B_\phi \rangle$ and the poloidal vector potential $\langle A_\phi \rangle$ show the wreaths of magnetism strongly in case M3-pcpf

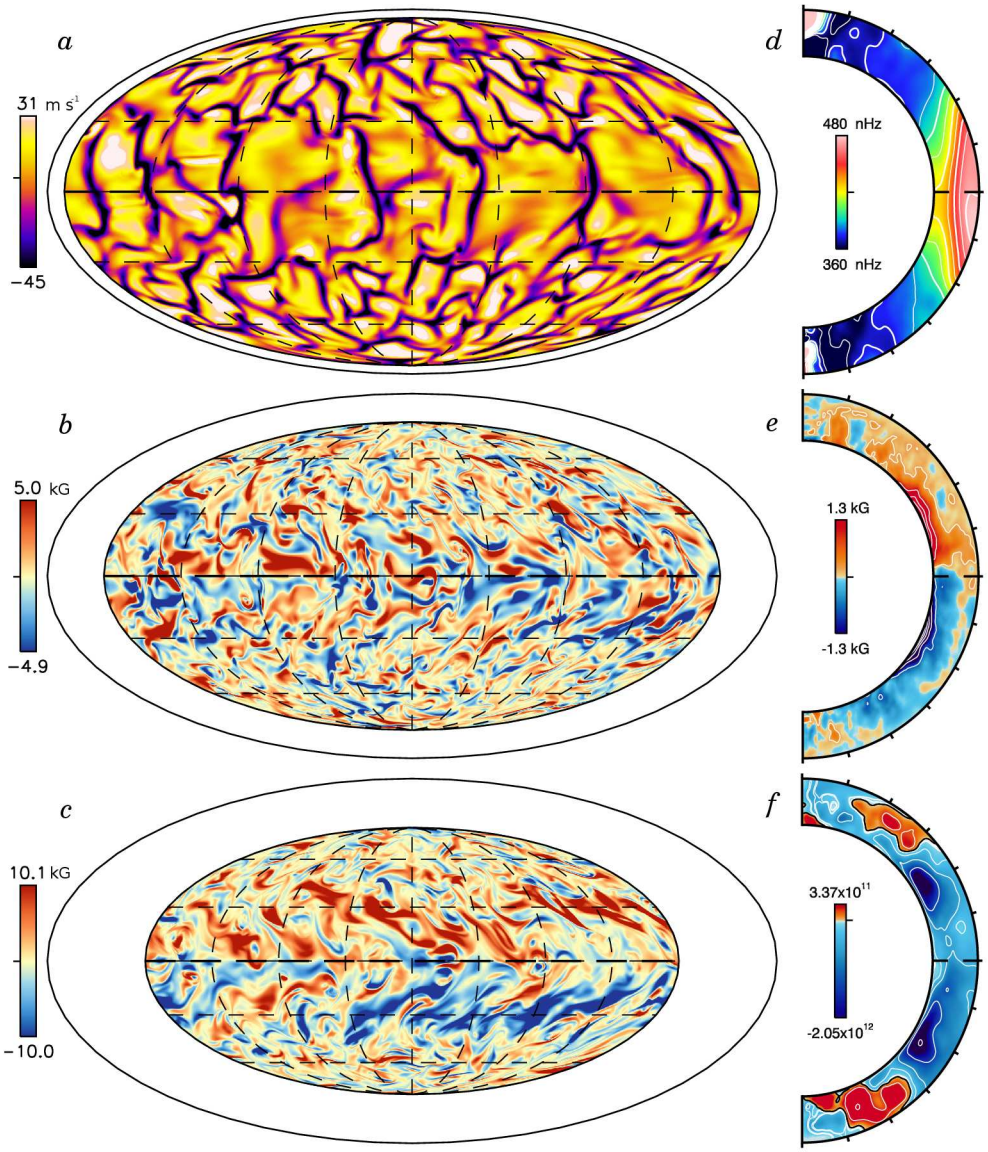

FIGURE 8.20 — Patterns of convection in case M3-pcpf. (a) Radial velocity v_r in Mollweide projection near the top of the shell ($0.95\,R_\odot$). (b) Toroidal magnetic field B_ϕ at mid-convection zone ($0.85\,R_\odot$) with weak wreath signatures. (c) The wreaths are significantly more evident are near the bottom of the convective shell (B_ϕ at $0.73\,R_\odot$). These snapshots are shown at day 700, a time when the mean magnetic fields are strong. Also shown are time-averaged profiles of (d) Ω, (e) $\langle B_\phi \rangle$ with wreaths of magnetism and (f) $\langle A_\phi \rangle$. These averages span the interval from days 700-800.

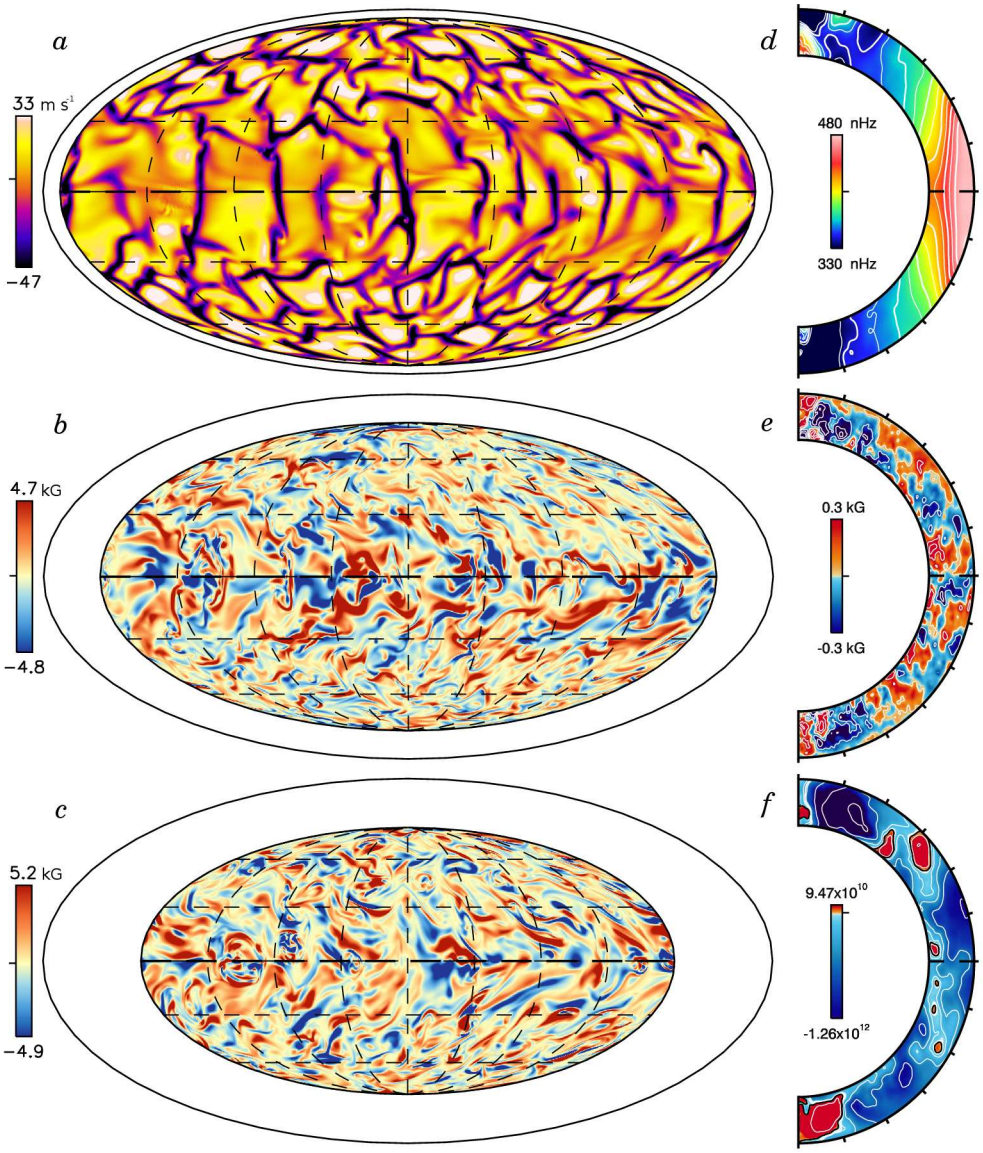

FIGURE 8.21 — Patterns of convection in case M3. (*a*) Radial velocity v_r in Mollweide projection near the top of the shell ($0.95\,R_\odot$). (*b*) Toroidal magnetic field B_ϕ at mid-convection zone ($0.85\,R_\odot$) with no wreaths present. (*c*) There are also no wreaths near the bottom of the convective shell, and the field amplitudes are comparable to those at mid-convection zone (B_ϕ at $0.73\,R_\odot$). These snapshots are shown at day 700. Also shown are time-averaged profiles of (*d*) Ω, (*e*) $\langle B_\phi \rangle$ with no wreaths and (*f*) $\langle A_\phi \rangle$ with disorganized mean poloidal fields. These averages span the interval from days 700-800.

(Figs. 8.20e, f). The mean poloidal field also shows more organization than those realized in case M3 and is somewhat stronger particularly near the bottom of the convection zone where the wreaths concentrate.

8.7 When the Sun is Old: Slowly Spinning Suns

While we have explored the likely effects of rapid rotation on convection and dynamo action in solar type stars, we have said little on the effects of slower rotation in these systems. As the Sun ages, its magnetized wind continues to carry angular momentum away from the star, slowing its rotation over billion year timescales. These older stars are relatively difficult to observe, often being in the halo of the galaxy. As such, they have received less observational attention. However, many other stars are effectively slow rotators. This is particularly true when we look at the rotational constraint of convection, measured by the Rossby number. Systems with very fast flows may act as slow rotators, even when their rotation periods are as short as the Sun's or several times shorter. The Sun is believed to have a Rossby number of nearly unity, straddling the regimes of the slow and fast rotators. To understand the solar differential rotation, we should understand the coupling of rotation and convection in the high Rossby number regime as well. Stars that have high luminosities and low average convection zone densities are likely to have extremely fast convective flows that are generally less constrained by the effects of rotation. We expect this behavior in main sequence F-type stars (Augustson et al. 2010) and also in the highly luminous red giant stars at the end of stellar life (Palacios & Brun 2007; Brun & Palacios 2009). Some simulations of convection in those systems are now underway.

We have conducted a limited exploration of the slow-rotation parameter space for solar-type stars. Our primary simulation in this regime is case D0.5a, rotating at $0.5\,\Omega_\odot$. This dynamo builds persistent wreaths of magnetism, though a more turbulent simulation at that rotation rate (case D0.5b) undergoes temporal oscillations and polar-

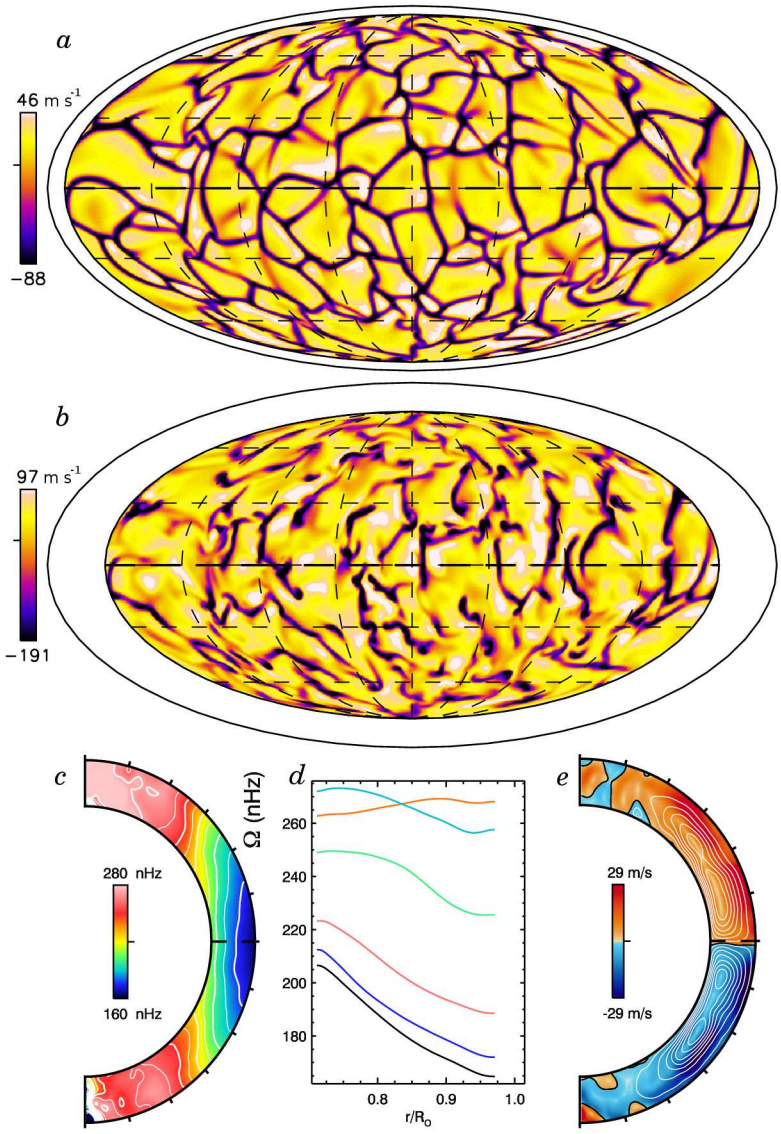

FIGURE 8.22 — Patterns of convection in case D0.5a. (*a*) Radial velocity v_r in Mollweide projection near the top of the shell ($0.95\,R_\odot$) and (*b*) at mid-convection zone ($0.85\,R_\odot$). (*c*) Time-averaged profile of angular velocity Ω with (*d*) accompanying radial cuts. The differential rotation has flipped in sense relative to the rapidly rotating simulations, here with a retrograde equator and prograde poles. There is still a substantial angular velocity contrast in latitude and radius. (*d*) Meridional circulations, with streamlines of mass flux overlain and sense of circulation indicated by color.

ity reversals. These successful dynamos have eddy diffusivities η which are much higher than those necessary for dynamo action in stars rotating near the solar rate. This is likely due to the relatively weak differential rotation in the Sun, as the slow rotators have substantial angular velocity contrasts. Now however, the differential rotation has changed in sense, with a retrograde equator and prograde poles.

The patterns of convection in case D0.5a are shown in Figure 8.22. The Rossby number in this case is high, with a value of 2.45, indicating that the rotation should only weakly influence the convective patterns. Despite this, a clear dichotomy exists between the equatorial convection, which retains a north/south alignment on average, and the polar convection which is more isotropic (Fig. 8.22*a*). In contrast to the rapidly rotating systems, where the downflows are shorn out in radius, here the downflows connect throughout the convection zone, with sheet-like structures near the equator and strong vortical plumes at higher latitudes (Fig. 8.22*b*). This leads to a substantial inward kinetic energy flux of almost $-0.5\,L_\odot$ at mid-convection zone, which is balanced by an outward enthalpy flux of nearly $1.5\,L_\odot$.

The differential rotation profile has flipped in sense from the rapidly rotating simulations. In the slowly rotating regime, anti-solar differential rotation appears to be a common feature, with retrograde equators and prograde poles (Fig. 8.22*c, d*). In case D0.5a, the latitudinal angular velocity contrast $\Delta\Omega_{\rm lat}$ near the surface is $-0.65\,\mu{\rm rad}s^{-1}$ and the radial shear $\Delta\Omega_r$ across the shell at the equator is $-0.26\,\mu{\rm rad}\,s^{-1}$. This is a substantial angular velocity contrast, with the latitudinal contrast being nearly 50% of the frame rotation rate. The meridional circulations in this simulation are much stronger and more organized than those found in the rapidly rotating simulations. Here, single-celled structures fill each hemisphere (Fig. 8.22*e*). At present, it is unclear where either the strong meridional circulations or the anti-solar differential rotation arise from. Strikingly, the thermal structure of the slowly rotating simulations retains an approximate sense of thermal wind balance, here with warm equators and cool poles.

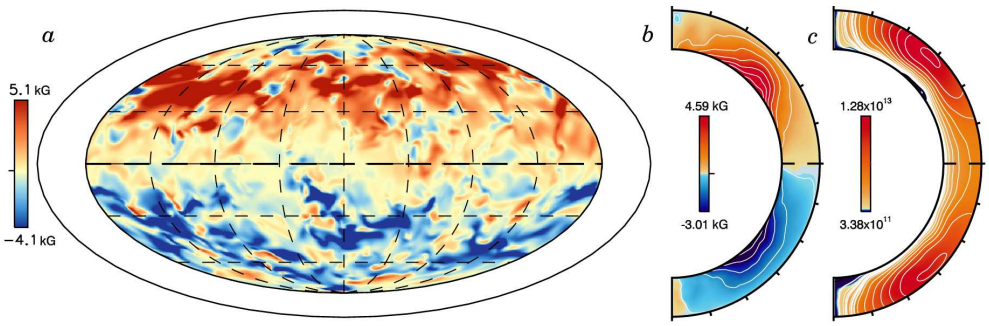

FIGURE 8.23 — Magnetic wreaths in case D0.5a. (a) Toroidal magnetic field B_ϕ at mid-convection zone, with wreaths visible in the high-latitude regions. (b) Time-averaged profiles of $\langle B_\phi \rangle$, with wreaths present throughout the convection zone and (c) of $\langle A_\phi \rangle$, with a single polarity of poloidal field.

The magnetic wreaths attained in this dynamo are shown in Figure 8.23. In case D0.5a, the wreaths are located in the region strong angular velocity contrast at high latitudes. These wreaths have complex structure at mid-convection zone, with substantial fluctuating fields, but the $\langle B_\phi \rangle$ is still visibly a major component (Fig. 8.23a). Profiles of $\langle B_\phi \rangle$ indicate that the wreaths extend throughout the convection zone (Fig. 8.23b). These magnetic structures extend mainly in latitude, with little radial structure, as also found in cases D1.5a and M3-pcpf. The accompanying mean poloidal field shown in Figure 8.23c is of a single polarity everywhere in the convection zone.

8.8 Conclusions

Wreaths of magnetism appear to be a ubiquitous feature in these dynamo simulations. These wreaths can be persistent for long intervals of time, with little change in their volume-averaged energies and polarities, or can show dramatic temporal oscillations including quasi-regular global-scale reversals of polarity. Both the toroidal and poloidal magnetic fields begin to show temporal variation as the level of turbulence is increased, with both magnetic fields waxing and waning in strength over periods of roughly 1000 days. The differential rotation grows in turn weaker and then stronger, being slowed by the strong magnetic fields or rebuilt by the convection.

During many of the temporal oscillations, remnant wreaths appear to slip toward the polar regions. These magnetic structures propagate to high latitudes over a period of roughly 500 days and are typically associated with bands of faster and slower rotating fluid that also propagate poleward at approximately the same rate. At present, it is unclear whether the global-scale polarity reversals are dependent on these cycles of wreath-amplification and poleward-slip. At least one simulation, case D3a, appears to undergo poleward-slip events without associated reversals of the global-scale polarities. However, when case D3a does flip its global polarities, it also launches substantial magnetic structures toward the polar regions.

Wreaths remain present in even the most turbulent simulations at all rotation rates (i.e. cases D3b, D1.5b, and D0.5b), and are also present in our high magnetic Prandtl number simulations (i.e. cases M3-pcpf and D3-pm4). At present, it is unclear whether the wreaths in the high magnetic Prandtl number regime differ substantially from those realized at low magnetic Prandtl numbers. When simulations with high magnetic Reynolds numbers at fixed rotation rate but differing Pm are compared, the fluctuating and mean fields appear comparable (i.e. cases D3b and D3-pm2) and temporal variation is achieved at similarly low levels of η.

Indeed, these dynamos generally appear to be more sensitive to the strength and structure of the differential rotation than the complexity or amplitude of the small-scale convection. The magnetic wreaths produced in dynamos at Pm = 0.5 with high levels of turbulence and very complex convective patterns, appear quite similar to the wreaths achieved in high Pm dynamos that have more laminar convective patterns. In the future, high Pm dynamos should be explored in the regions of parameter space near the onset of sustained dynamo action, to determine whether the critical magnetic Reynolds number scales with Pm and whether the fluctuating or rms magnetic Reynolds number is a better diagnostic for successful dynamo action. These simulations may additionally explore whether temporally varying behavior is linked to the small-scale

convection or the global-scale differential rotation. Without question it is also vital that more turbulent simulations be continued, to determine whether wreaths survive in substantially more turbulent regimes. The most turbulent dynamos considered here have fluctuating magnetic Reynolds numbers of just 500, which is far less than the values found in astrophysical regimes.

Our most rapidly rotating dynamos, at 10 and 15 $\Omega_\odot$, generate strong magnetic fields which significantly modify the differential rotation. The poleward propagating velocity features seen in our dynamos rotating at three times the solar rate (cases spanning from D3 to D3-pm4) here become strong enough to affect the underlying differential rotation when they ultimately reach the poles. In case D15, these structures appear to reverse the flows in the polar regions, flipping the differential rotation there from a retrograde sense to a prograde sense.

The modulated states found in hydrodynamic simulations (Chapters 3 and 4) remain present in regions of our dynamo parameter space, being most evident in case D10L which has rapid rotation, strong magnetic fields and a reasonably strong differential rotation. As the differential rotation weakens, the active nests become less distinct but remain evident when long intervals of time are examined in time-longitude maps.

Magnetic wreaths are now found in solar simulations as well as in rapidly rotating suns. Generally, as the rotation rate decreases, magnetic wreaths are confined to the lower portion of the convection zone and do not have the radial extent seen in case D3 and the other rapid rotators. In simulations at the solar rate, the mean toroidal fields have relatively small amplitudes, while the fluctuating fields remain strong. Despite this, the fluctuating fields are still organized on global-scales and wreaths are clearly evident.

These wreath-building dynamos are sensitive to the bottom magnetic boundary condition that is employed. In simulations at the solar rate, employing a potential field bottom boundary leads to dynamos without wreaths (case M3), while dynamos with

perfect conducting bottom boundaries build wreaths almost immediately (case M3-pcpf). Indeed, when we have attempted to run a version of our three solar dynamo case D3 with potential field bottom boundaries, we find that dynamo action is not sustained at the values of η employed in case D3. It appears that case M3 may be running a small-scale or fluctuating dynamo, which primarily relies on the turbulent correlations to generate magnetism, while case D3 runs a large-scale dynamo that relies primarily on the Ω-effect associated with the strong differential rotation. The success of case D3 as a dynamo is clearly enhanced when the bottom boundaries both allow horizontal magnetic fields near the boundary and prohibit their expulsion from the simulated domain.

At present, it is unclear how the poloidal fields are regenerated in the rapidly rotating suns. In particular, it is unknown whether this is a process arising from turbulent correlations on the smallest scales or from instabilities in the shearing flows of differential rotation. Case M3-pcpf may bridge the gap between these two regimes, possessing both a small-scale α-effect dominated dynamo and a large-scale Ω-effect dynamo operating in the same regions of the convection zone.

Wreath-building dynamos should be present in slowly rotating stars as well. These stars, which include both older suns and young but highly luminous main-sequence stars, are likely to possess an anti-solar differential rotation with a retrograde rotating equator and prograde pole. Here, wreaths appear at high latitudes, in the regions of strong angular velocity contrast. It is unclear whether the temporally varying behavior seen in some of the slowly spinning suns (i.e. case D0.5b) arises from the cycles of wreath-amplification, polarward slip and angular momentum transport that appear to operate in many of the rapidly rotating suns.

Chapter 9

Future Explorations and Wreath-building Dynamos with Tachoclines

In this thesis we have explored a variety of dynamo solutions in stars rotating more rapidly than the sun. Magnetic wreaths arise as a near ubiquitous feature of these simulations, irrespective of rotation rate or level of turbulence achieved. These simulations have at present included the convection zone only. In many solar dynamo theories, it is thought that the tachocline must play a major role. Clearly, a major thrust of future research must be the inclusion of this important internal boundary layer.

In studies of compressible convection that include regions of penetration at the bottom of the convection zone, organized magnetic fields are often efficiently pumped downwards and out of the convection zone (e.g., Tobias et al. 2001; Browning et al. 2006). Magnetic wreaths might be efficiently expelled from the convection zone by the compressible convection there. This could remove them from the region of amplification, as the poloidal field may not be regenerated within the tachocline by the same processes at work within the convection zone. This would likely cause magnetic wreaths to vanish entirely. Such a finding would cast serious doubt on the viability of magnetic wreaths in turbulent stellar convection zones.

We have begun explorations into whether magnetic wreaths survive in the presence of a tachocline in rapidly rotating suns. We find that the wreaths do survive, and indeed continue to fill the bulk of the convection zone, even as they become rooted within the tachocline. These wreaths still undergo temporal oscillations and cycles of

Table 9.1. Parameters of case T3

N_r, N_θ, N_ϕ	Ra	Ta	Re	Re′	Rm	Rm′	Ro	Roc	ν	η
$258 \times 256 \times 512$	$9.64{\times}10^5$	$1.39{\times}10^7$	184	129	92	64	0.481	0.333	1.37	2.75

Note. — Simulation parameters for case T3 rotating at $3\,\Omega_\odot$ and with a tachocline of shear. Parameters have same definition as in Table 8.1, with a deep inner radius of $r_{\rm bot} = 3.8 \times 10^{10}$cm and outer radius of $r_{\rm top} = 6.72 \times 10^{10}$cm. The base of convection zone is at $r_{\rm bcz} = 4.91 \times 10^{10}$cm or $0.705\,R_\odot$. Here we define $L = (r_{\rm top} - r_{\rm bcz}) = 1.81 \times 10^{10}$cm or $0.26\,R_\odot$.

polarity reversal. Preliminary results are reported on here for one simulation rotating at three times the solar rate, case T3, with similar input parameters to our wreath building case D3.

9.1 Capturing a Model Tachocline within ASH

The primary parameters of case T3 are reported in Table 9.1 and are similar to our cases D3 and D3a. Case T3 has a lower boundary at $r = 0.5\,R_\odot$ and an upper boundary at $0.965\,R_\odot$. There is thus an overall density contrast of 48 across the convection zone and 133 across the entire shell. This leads to somewhat lower values of ν, κ and η than in case D3, despite the two cases sharing the same values for eddy diffusivities at the top of the convection zone.

After thousands of days of evolution, this dynamo establishes a stable profile of $\mathrm{d}\bar{S}/\mathrm{d}r$, with the base of the convection zone where $\mathrm{d}\bar{S}/\mathrm{d}r$ crosses zero located at approximately $0.705\,R_\odot$. The fluctuating radial velocities extend somewhat deeper, and decrease from an average amplitude of $25\,\mathrm{m\,s^{-1}}$ to about $1\,\mathrm{m\,s^{-1}}$ by a depth of approximately $0.66\,R_\odot$. The fluctuating radial flows are much smaller below this depth. The peak downflows are moving at almost $-200\,\mathrm{m\,s^{-1}}$ at $0.705\,R_\odot$ but have slowed to roughly $-10\,\mathrm{m\,s^{-1}}$ when they reach $0.66\,R_\odot$.

To prevent the diffusive spread of the differential rotation profile from the convection zone into the stable radiative zone, we taper our eddy diffusivities with a smooth step function

$$\nu(r) = \nu_0 \left(\frac{\bar{\rho}_0}{\bar{\rho}(r)} \right)^{\alpha} \Phi(r) \,, \quad \kappa(r) = \kappa_0 \left(\frac{\bar{\rho}_0}{\bar{\rho}(r)} \right)^{\alpha} \Phi(r) \,, \quad \eta(r) = \eta_0 \left(\frac{\bar{\rho}_0}{\bar{\rho}(r)} \right)^{\alpha} \Phi(r) \,, \tag{9.1}$$

where $\alpha = -0.5$ as before, ν_0, κ_0 and η_0 are the values at the top of the convection zone and our taper with radius is given by

$$\Phi(r) = \frac{1}{2} \left(1 - \beta\right) \left(1 + \tanh \left(\frac{r - r_{\rm taper}}{\Delta_{\rm taper}} \right) \right) + \beta \,. \tag{9.2}$$

We recover our treatment of eddy diffusivities in the convection-zone dynamos when $\Phi = 1$ at all radii. In case T3 the taper function is centered at $r_{\rm taper} = 4.70 \times 10^{10}$ cm ($0.675\ R_\odot$) with width $\Delta_{\rm taper} = 5 \times 10^8$ cm ($0.007\ R_\odot$). The variable β controls the amplitude of the tapering function, which ranges from a value of one in the convection zone to β in the radiative interior. Here we set $\beta = 10^{-2}$ thus reducing our eddy diffusivities by two orders of magnitude in the stable radiative interior.

We expect that turbulent mixing and transport should generally be lower in the stable radiative zone than in the unstable convection zone, but these eddy diffusivities are still many orders of magnitude larger than the microscopic viscosities and diffusivities present in stellar interiors. Over long intervals of time, the differential rotation will still diffusively spread into the radiative interior. By tapering our eddy diffusivities by two orders of magnitude, we find that the differential rotation produced by convection remains well confined to the convection zone for more than 7000 days. It is likely that artificially lowering our viscosities is a more physically plausible approach to preventing "tachocline-creep" than other techniques employed in the past, which included mechanical forcing in the radiative zone and entropy forcing in the region of the tachocline to retain a comparably good structure of differential rotation (e.g., Browning et al. 2006).

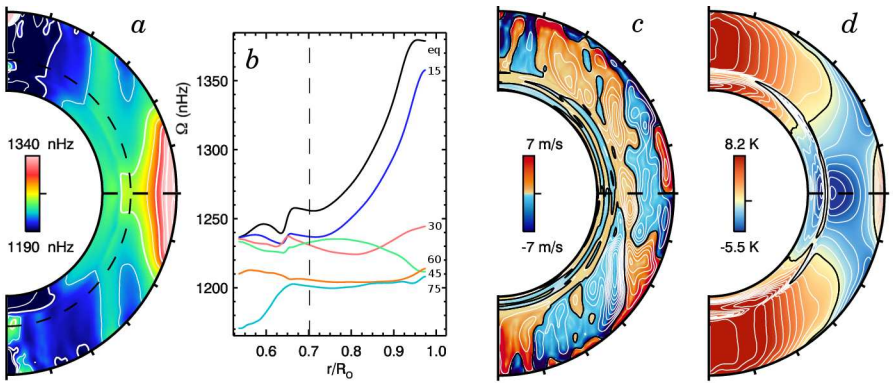

FIGURE 9.1 — Profiles of mean flows and temperature in dynamo case T3. These profiles are averaged over the interval from days 4050-4150 of dynamo case T3. The hydrodynamic progenitor ran for an additional 600 days previous to day 0. (*a*) Profile of differential rotation Ω with (*b*) accompanying radial cuts at selected latitudes as labeled. The bottom of the convection zone at $r_{\rm bcz} = 0.705\,R_\odot$ is marked on both with a dashed line. The equator is prograde, the poles are retrograde and the radiative interior is in nearly solid-body rotation between latitudes $\pm 45°$. (*c*) Meridional circulations with surface structure and amplitudes similar to those in case D3 but different at depth. (*d*) Profile of latitudinal temperature variations relative to the spherically symmetric average $\bar{T}$.

Time-averaged profiles of the differential rotation, meridional circulations and latitudinal temperature variations of case T3 are shown in Figure 9.1. After a total of more than 4500 days of evolution in both the hydrodynamic progenitor and then in case T3, the differential rotation remains well confined to the convection zone (Fig. 9.1*a*). Within the convection zone, there is a significant angular velocity contrast in latitude and radius, with a $\Delta\Omega_{\rm lat}$ near the surface of $1.04\,\mu{\rm rad}\,s^{-1}$ and a $\Delta\Omega_r$ across the convection zone at the equator of $0.89\,\mu{\rm rad}\,s^{-1}$. The latitudinal angular velocity contrast is similar to that achieved in dynamo case D3b, but the radial contrast is somewhat larger. Below the base of the convection zone, the location of the eddy diffusivity taper is visible as a slight contour in the profile of Ω (Fig. 9.1*a*) and as a small kink in the radial cuts of the same (Fig. 9.1*b*). In the radiative interior, a small latitudinal angular velocity contrast persists. This is especially prominent in the polar regions at latitudes above $\pm 60°$. Near the equator and up to latitudes of roughly $\pm 45°$ the radiative interior is almost in solid-body rotation.

The meridional circulations achieved in case T3 are shown in Figure 9.1*c*. In the upper convection zone, these circulations are similar to those found in case D3 (e.g., Fig. 5.1*d*). In the lower convection zone the flows penetrate into the tachocline and radiative interior. This largely removes the narrow return flow seen at the base of case D3 from the convection zone. The latitudinal temperature variations achieved in case T3 are shown in Figure 9.1*c*. As in the other rapidly rotating simulations, the convection builds a prominent gradient in latitude, with hot poles, cool mid-latitudes and a warm equator near the surface. The temperature gradients appear to have spread into the radiative interior, and the thermal wind associated with this likely helps maintain the small differential rotation that is present there. Temperature gradients will diffusively spread more easily than gradients in angular velocity, owing to the low Prandtl number of this simulation (as before, $\mathrm{Pr} = 0.25$). Lowering the value of β in the tapering function would likely further curtail this spreading, as would reducing ν and κ throughout the convection zone.

9.2 Magnetic Wreathes with a Tachocline

Case T3 continues to build large wreaths of magnetism that fill the bulk of its convection zone. The time history of this case is shown in Figure 9.2. As in many of our other rapidly rotating dynamos, wreaths appear at latitudes of roughly $\pm 20^\circ$ and undergo cycles of polarity change. In the 5800 days shown here, four polarity reversals occur in both hemispheres after the dynamo saturates at roughly day 1000. The wreaths are strong at mid-convection zone and stronger yet near the base of the convection zone (Figs. 9.2*c*, *d*). In both regions the wreaths have similar latitudinal structure. In the tachocline, the wreaths occupy a broader range of latitudes and remain strong (Fig. 9.2*e*). Time-radius maps at a fixed latitude of 20°, in the core of the magnetic wreaths, show that with each successive polarity reversal some field of the previous cycle migrates deeper into the radiative interior (Fig. 9.2*f*). At depths below $0.6\ R_\odot$

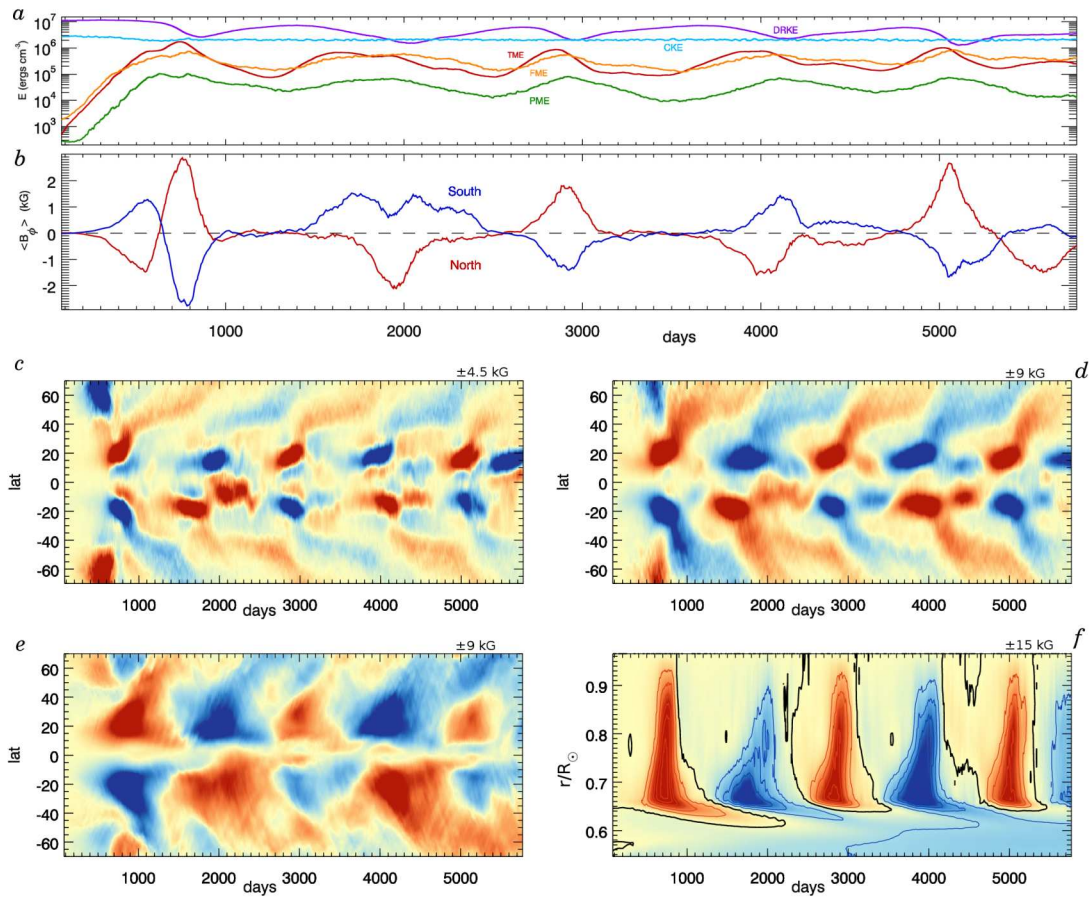

FIGURE 9.2 — Time-dependent behavior in case T3 with a model tachocline. (a) Volume-averaged kinetic and magnetic energies, and (b) mean $\langle B_\phi \rangle$ averaged over northern and southern hemispheres at mid-convection zone. (c) Time-latitude maps of $\langle B_\phi \rangle$ at mid-convection zone ($0.85\ R_\odot$) and (d) near the base of the convection zone ($0.7\ R_\odot$). Multiple cycles of wreath building occur in the roughly 5000 days after dynamo saturation. (e) The wreaths extend into the tachocline ($0.65\ R_\odot$), with somewhat broader structure. At greater depths single polarity wreaths persist for the entire simulated interval. (f) Time-radius map at a fixed latitude of 20°, in the core of the northern hemisphere wreaths. The black contour denotes the neutral line between successive wreaths.

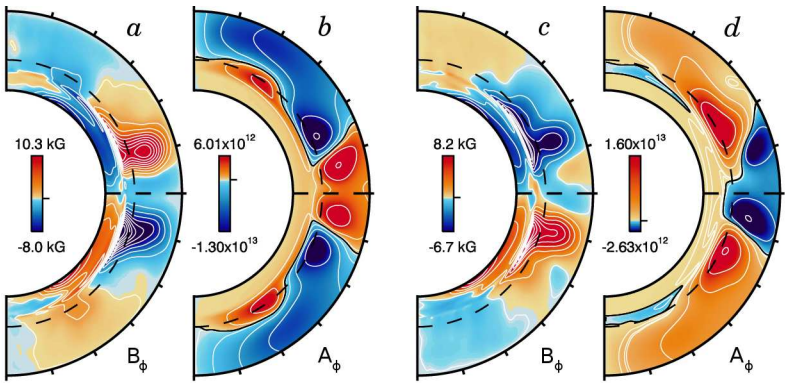

FIGURE 9.3 — Profiles of $\langle B_\phi \rangle$ and $\langle A_\phi \rangle$ in dynamo case T3. (a) Mean toroidal magnetic field $\langle B_\phi \rangle$ and (b) poloidal vector potential $\langle A_\phi \rangle$ averaged over days 4050-4150 at a time of peak mean fields. At this time, the wreaths and associated mean-poloidal field are out of phase with the magnetic field in the deep interior. (d) $\langle B_\phi \rangle$ and (e) $\langle A_\phi \rangle$ averaged over days 5000-5100 when the fields have flipped polarity and again reached peak amplitudes. At this time, the magnetic fields in the convection zone have the same polarity as those in the radiative interior. The bottom of the convection zone at $r_{\rm bcz} = 0.705\ R_\odot$ is indicated by the dashed semi-circle.

however a single polarity of wreathes are established and persist. During the 5800 days shown here, these deep magnetic structures slowly grow in strength. By the end of this interval, the mean toroidal fields have reached peak amplitudes of nearly ± 9 kG near the bottom boundary, with the strongest fields appearing near latitudes of $\pm 55°$. These deep fields may arise from turbulent transport and pumping within the convection zone and coupled down into the deep radiative interior. It seems more likely however that they result from stretching of the initial weak seed field by the differential rotation that has diffusively spread into the polar regions of the radiative interior, as the peak angular velocity contrast there occurs at the higher latitudes where the wreaths are located. Decreasing our tapering constant β to values of 10^{-3} or less should strongly decrease the diffusive spread of differential rotation and suppress the generation of these deep-seated wreaths.

Time-averaged profiles of the mean toroidal fields and poloidal vector potential are shown at two intervals in Figure 9.3. At both times the wreaths of magnetism are at

a point in the cycles of polarity reversal where the fields have attained peak amplitudes. The mean magnetic fields associated with the wreaths extend into the tachocline down to roughly where the eddy diffusivities taper in amplitude. This depth also roughly coincides with the depth at which the fastest downflows have their motion substantially braked by the stable stratification.

The mean fields produced in the convection zone undergo cycles of polarity reversal, while those deep in the radiative interior always retain the same polarity. During the first cycle shown in Figure 9.3, spanning days 4050-4150, the mean magnetic fields in the convection zone have opposite polarity from the fields in the radiative interior (Figs. 9.3a, b). After the fields flip in polarity and regrow in amplitude, they match the polarity of the radiative interior fields (days 5050-5150; Figs. 9.3c, d). At present, it is unclear whether the dynamo behaves substantially differently when the convection either matches or opposes the fields in the radiative interior. Convective patterns and the global-scale flows of differential rotation and meridional circulation are very similar during both of the intervals examined here.

These simulations of dynamo action in the presence of a tachocline are very promising. Wreaths of magnetism continue to fill the bulk of the convection zone and undergo cycles of polarity reversal. These polarity reversals occur on similar timescales to those found in the convection-zone dynamos studied in Chapters 6 and 8. The polarity reversals in real stars generally have slightly longer periods than those found here, and in the Sun magnetic polarity reversals occur on a time scale of roughly 11 years, or about 4000 days.

Our dynamo with a tachocline shows promise, but the model could be improved significantly. The background structure used within case T3 is shown in Figure 9.4. At present, our thermodynamic variables are in decent agreement with the solar structure model (a CESAM model based on work in Brun et al. 2002) throughout the bulk of the convection zone. In the stably-stratified radiative interior, ASH diverges from the

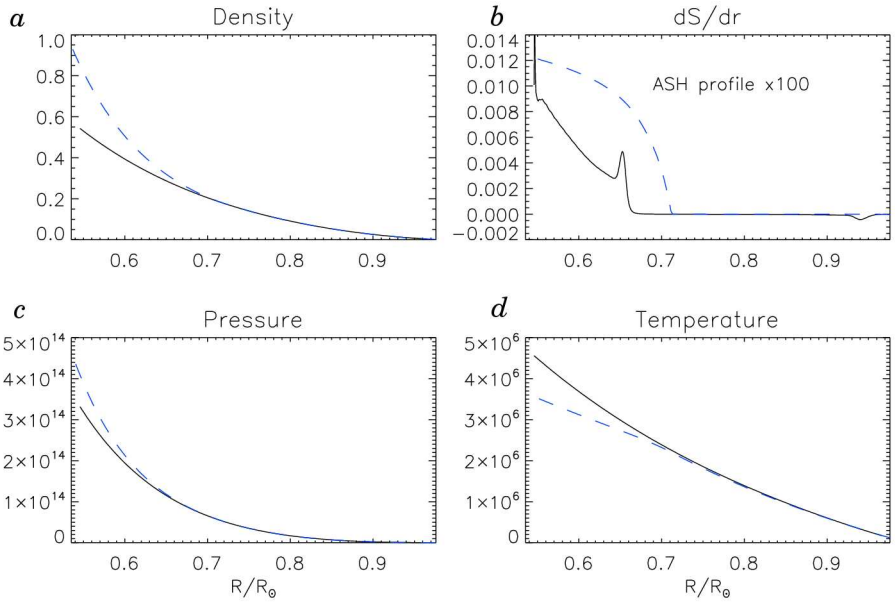

FIGURE 9.4 — Stellar structure of case T3. Shown are spherically symmetric profiles of thermodynamic variables (*a*) $\bar{\rho}$, (*b*) $\mathrm{d}\bar{S}/\mathrm{d}r$, (*c*) $\bar{P}$ and (*d*) $\bar{T}$. The adopted structure in ASH is shown with a black, solid line and the CESAM solar structure model is shown with a blue, dashed line (from Brun et al. 2002). The ASH entropy gradient shown in (*b*) has been multiplied by a factor of 100 to make it visible. The ASH structure and solar model are in good agreement within the convection zone, but diverge in the radiative interior.

model. This is particularly due to the low values of $\mathrm{d}\bar{S}/\mathrm{d}r$ used in ASH within the radiative interior. There, the values of the entropy gradient are more than two orders of magnitude smaller than those in the solar model. Additionally, the profile of $\mathrm{d}\bar{S}/\mathrm{d}r$ used in case T3 has developed kinks in the radiative zone (near radii $0.65\,R_\odot$ and $0.55\,R_\odot$) and grows in amplitude too slowly as the radius decreases. This leads to a softer tachocline than that likely present in real stars, which allows radial motions to penetrate too deeply into the radiative interior. Additionally, $\bar{T}$ is too large in the interior, while $\bar{\rho}$ and $\bar{P}$ are too small. Lastly, the $\mathrm{d}\bar{S}/\mathrm{d}r$ profile used in ASH is generally too large in amplitude in the upper convection zone, especially near $r = 0.95\,R_\odot$, as was also seen in the structure of our convection-zone models (see Figure 2.3).

New models are in progress which are appear likely to achieve both the steep gradient of $\mathrm{d}\bar{S}/\mathrm{d}r$ in the tachocline and the profile near the upper surface seen in 1-D solar structure models. Exploring how 3-D effects adjust the stratification of the tachocline will further require methods that accelerate the thermal relaxation of that layer. Such methods are in active development (Featherstone et al. 2010). Without an accelerated relaxation scheme, the thermal structure of the tachocline cannot be correctly captured in ASH. This problem arises due to the long timescales required for adjustment of the tachocline, which likely requires several million years. In comparison, we have evolved case T3 for roughly 16 simulated years. A case with a realistic stable region will likely have its timesteps strongly constrained by the high-frequency gravity waves propagating there. With the real solar stratification, we expect timesteps of roughly 200 seconds. This will be an issue for hydrodynamic simulations but is unlikely to significantly affect the dynamo simulations, as the Alfvénic CFL near the surface applies a more stringent limit.

These simulations of dynamo action in the presence of a tachocline are computationally demanding. To achieve the 5800 days of dynamo evolution in case T3 required over 6 million iterations of evolution, with typical timesteps of 80 seconds each. Running on a special allocation on the Kraken-XT4 at NICS, this tachocline simulation has required nearly 750000 cpu hours, running continuously on 512 processors there. Simulations that include tachoclines must however form the core of future explorations into wreath-building dynamos.

9.3 Perspective on Rapidly Rotating Suns

Our explorations of rapidly rotating suns have taken us into interesting territory and have ultimately raised fascinating questions about the solar dynamo. In hydrodynamic simulations, we found that generally the global-scale flow of differential rotation becomes considerably stronger as the rotation rate is increased. In the rapidly rotating systems we have studied, achieving greater levels of turbulence at fixed rotation rate leads to even stronger angular velocity contrasts in both radius and latitude. In our dynamo studies we find that the magnetism becomes so strong that it substantially suppresses the angular velocity contrast of differential rotation. Relative to similar hydrodynamic simulations, the angular velocity contrast in latitude and radius of the equilibrated dynamo solution can be reduced by more than a factor of two (i.e. cases H5 and D5). This effect becomes more pronounced as the rotation rate increases. In the most rapidly rotating dynamos (i.e. cases D10 and D15) the differential rotation can be wiped out almost entirely in the equatorial regions. These results may be in reasonable agreement with observations of differential rotation, where some disagreement remains between different groups using different observational techniques. Generally however, observations indicate that differential rotation either grows with faster rotation or perhaps remains nearly constant.

In contrast, the meridional circulations become substantially weaker as the rotation rate increases, their volume-averaged energies falling almost inversely with rotation rate. These flows, which in the Sun may be comprised of single cells in each hemisphere, break apart into multiple cells in both radius and latitude. The meridional circulations are less dependent on the level of turbulence attained, at least in the parameter space studied here. Additionally, these circulations are largely unchanged in either amplitude or spatial structure in the dynamo solutions.

The weakening of meridional circulations with faster rotation raises profound questions for stellar dynamo theory. In the case of the Sun, current theories of flux-transport dynamos, including the Babcock-Leighton dynamo, rely on the slow meridional circulations to return flux to the tachocline. It is the circulation time of that flow which largely sets the timescale of cyclic dynamo variations.

In the Sun the eleven-year activity cycle is close to estimated turnover times for the meridional circulations, based on the observed flow at the surface and mass-conservation arguments. In rapidly rotating stars, measurements of either cycle period or meridional circulation amplitude are quite difficult; the former because of the long time scales involved (decades), and the later because of the small amplitude of the meridional circulations relative to either flows associated with surface convection or the fast differential rotation. Observations seem to indicate that there may be a weak correlation between cycle period and rotation rate, with more rapidly rotating stars having slightly shorter periods then the Sun (Saar & Brandenburg 1999). This is in disagreement with the meridional circulations found in our rapidly rotating simulations, which in a flux-transport framework would likely lead to significantly longer dynamo cycles. Recent flux-transport dynamo models are beginning to explore how such variations in meridional circulation amplitude and 2-D structure may affect the operation of the dynamo (e.g., Jouve et al. 2009).

In many of the rapidly rotating suns, the strong differential rotation shears convective cells out in radius. This can lead to changes in the radial transport of energy. In particular, the inwards transport of kinetic energy is strongly reduced in these simulations. In some regimes, striking patterns of convection modulated in longitude arise. As the rotation rate increases, convection in the hydrodynamic models can become entirely confined to active nests with more quiescent streaming flow inbetween. These active nests persist for thousands of days and propagate at an angular velocity which is constant at all depths of the convection zone. This angular velocity typically matches that

of the differential rotation near mid-convection zone. As such, the active nests experience strong shear from the differential rotation, with a relative tailwind in the upper convection zone and a headwind in the lower convection zone. These nests reappear in nearly the same form in one of our MHD dynamo simulations (case D10L). In other dynamo simulations they appear to be weakly present, becoming somewhat more evident when the differential rotation is stronger. In stellar observations, such structures may lead to the presence of magnetic features at the surface which propagate at rates distinct from either the surface differential rotation or the overall rotation of the star.

Our dynamo simulations consistently build striking global-scale magnetic structures in the bulk of the convection zone. These structures are more topologically complex than ideal flux tubes, whose magnetic fields are confined within bounded surfaces. The magnetic wreaths which are self-consistently built in these rapidly rotating dynamos have more open topologies, with field wandering throughout the convection zone, reconnecting across the equator and being wound up in the vortical flows at high latitudes.

Some of these dynamos build persistent wreaths that survive relatively unchanged in the midst of the convection zone for thousands of days. As the magnetic Reynolds number increases, the wreaths become time-dependent, undergoing large oscillations in magnetic energy. These oscillations can lead to global-scale polarity reversals, with the mean toroidal and mean poloidal fields changing sign quasi-regularly. Associated with these oscillations or reversals are poleward propagating magnetic structures. These may be wreaths that become strong enough to undergo a poleward-slip instability where magnetic tension pulls the wreaths toward smaller cylindrical radii. Accompanying these magnetic features are local regions of more quickly rotating fluid. These angular velocity structures can cause changes in the overall differential rotation. They may bear some resemblance to the polar branch of torsional oscillations observed in the Sun.

Even the more slowly rotating simulations form wreaths of magnetism, including simulations at the solar rate and slower. These wreaths tend to be more concentrated in

the lower convection zone and less evident at mid-convection zone. Such structures may be pumped out of the convection zone when a tachocline of shear and penetration is included at the lower boundary. In our preliminary explorations however, we find that when a convection zone dynamo is coupled with a model tachocline, magnetic wreaths still form and fill the bulk of the convection zone. The wreaths realized in case T3 undergo similar polarity reversals to those found in other simulations at three times the solar rate. Case T3 has a very soft stable stratification, and this likely underestimates the amount of magnetism which is able to remain within the convection zone. This may change however at higher levels of turbulence if very strong downflows are able to overcome the shearing tendencies of the differential rotation and survive to efficiently pump the wreaths downward.

Wreaths have not been found in previous solar simulations in part due to the difference in lower magnetic boundary conditions employed. The wreath-building dynamos appear to work far more efficiently when the lower boundaries permit horizontal field and prevent that field from escaping the convection zone. It is reassuring that including a more realistic lower boundary for the convection zone by including a tachocline of penetration and shear leads to qualitatively and quantitatively similar behavior to the convection zone dynamos with perfectly conducting bottom boundaries. Namely, in case T3 wreaths of magnetism form, span the convection zone, reach similar amplitudes at mid-convection zone to other $3\Omega_\odot$ dynamos, and undergo cyclic polarity reversals on a similar timescale (roughly 1000 days). Simulations of the solar dynamo which include a tachocline of penetration appear to yield very similar results, though there the wreaths are confined almost entirely to the tachocline (Browning et al. 2006). It is unclear at present whether the magnetic structures in that dynamo arise locally within the shear of the tachocline or are produced in the convection zone and pumped downward. In case T3 however, the wreaths are clearly formed in the convection zone itself.

9.4 The Road Ahead

The rapidly rotating dynamos have opened a rich realm for further exploration. At present, we have followed one cut through turbulent parameter space with limited additional sampling at interesting rotation rates. The exploration of these stars is by no means complete. Here briefly are future projects which should be pursued. Some of these are underway presently or will be in the near future; others remain more speculative. A number of the projects will require significant computation, but several would involve deeper analysis of the rich dataset already produced in this research.

- **How are poloidal fields regenerated in wreath-building dynamos?** The mean poloidal magnetic fields are regenerated on the poleward edge of the magnetic wreaths. Here, field-line tracings in case D3 reveal fields that are partly wound up in the vortical polar convection. Larger-scale variations are also clearly evident. It is unclear at present which scale contributes to the regeneration of mean poloidal fields. This question should be answerable with the current set of simulations, by comparing features common to the three dynamos that build persistent wreaths (cases D0.5, D1.5a and D3).

- **What is the origin of cyclic reversals, and what sets their timescale?** In many of our dynamos, quasi-regular temporal oscillations are observed in the magnetic energies and the amplitudes of the mean toroidal and poloidal field. In many cases these are linked with global-scale reversals of polarity. It is unclear why organized time-dependent behavior occurs when the magnetic Reynolds number increases. Global-scale polarity reversals appear to occur even in those cases where the differential rotation is highly suppressed (i.e. case D15). These reversals may originate in changes to the magnetic production terms, but elucidating their variation has proven complex. The reversals that occur in these rapidly rotating suns typically span intervals of about 1000 days. In the Sun,

such reversals take roughly eleven years or about 4000 days. In other solar-like stars the timescales for reversal are comparable, though perhaps slightly decreasing in the more rapidly rotating suns. Understanding the origin of the organized polarity reversals, and why they are consistently shorter in these simulations than in real stellar dynamos, must be a high priority of future research.

- **Do mean-field theories reproduce wreath-building dynamos?** In our preliminary analysis of a simple mean-field model, we find that the EMF predicted by a simple α-effect fails to reproduce the 3-D EMF measured in our case D3. At present, it is unclear whether a more sophisticated approach will yield better agreement. Test-field methods and further expansions of the mean-field EMF should be carefully explored, to both understand how the 3-D dynamos are operating and to help improve stellar mean-field models. This analysis should be extended to the time-dependent cases, including to the initial dynamo growth phases.

- **Do wreath-building dynamos survive at high Reynolds numbers?** Our present simulations still have relatively low magnetic Reynolds numbers. As Rm' is increased, wreathes become more complex in spatial and temporal structure and are generally stronger in the lower convection zone than at mid-convection zone. At present, it is unclear whether such structures survive under highly turbulent conditions, in which a small-scale convective dynamo is active in addition to the global-scale wreath building dynamo. Case M3-pcpf and case D3-pm4 may be beginning to explore this coupled regime, but simulations should be carried out with fluctuating magnetic Reynolds numbers $\mathrm{Rm}' \sim 1000$ or higher to ensure strong dynamo action everywhere in the convection zone.

- **Are high-Pm dynamos different from low-Pm dynamos?** We have conducted a limited exploration on the effects of Pm on the magnetic wreaths and generally find that it is the value of η rather than Pm that defines the temporal variations and spatial structure of the wreathes. However, in these rapidly rotating dynamos the differential rotation itself changes as ν and κ are varied. This complicates exploration of the boundaries in parameter space variously for sustained dynamo action, temporally varying magnetism, cyclic polarity reversals or quenching of differential rotation. At certain special rotation rates however, clustering around $1.5\,\Omega_\odot$ in these simulations, the differential rotation appears to be less sensitive to variation of ν or κ. More extensive simulations should be carried out at $1.5\,\Omega_\odot$, exploring how varying Pm affects the wreaths when other factors, including the angular velocity contrast in latitude and radius, are approximately constant.

- **Why do high Rossby numbers lead to anti-solar differential rotation?** As we have taken our rapidly rotating suns back to the solar rate and then explored more slowly rotating stars, we have found that the differential rotation profile often flips in sense and becomes anti-solar, with fast, prograde poles and a slow, retrograde equator. This phenomena is however not confined to the older suns alone. Indeed, at the solar rotation rate, dropping ν and κ to the levels necessary to achieve dynamo action at $\mathrm{Pm} = 0.5$ causes the differential rotation to collapse entirely, or even flip sense and become anti-solar. The cause of this is as yet unknown, but appears to be related to the convection shifting from the low Rossby number regime that the rapid rotators inhabit to a high Rossby number regime. At rotation rates above approximately $1.5\,\Omega_\odot$, the differential rotation is solar in sense and becomes more strongly so as the diffusivities are dropped. At rotation rates below about $1.5\,\Omega_\odot$, the differential rotation becomes weaker

as ν and κ decrease. When conditions become sufficiently turbulent, the sense of differential rotation becomes anti-solar and this inverted profile of angular velocity is further enhanced as the diffusivities drop. The strength and sense of differential rotation appears to correlate reasonably well with the Rossby number of the convection, but the reason for this correlation is unknown. The Rossby number of the flows may in turn be related to the stratification we have adopted in our simulations. Promising work is underway on new models which better match the helioseismically determined solar stratification, but further work must be done on the sensitivity of the differential rotation profile, in the Sun and in other stars, to relatively small changes in the eddy diffusivities.

- **Do active nests of convection survive under more realistic conditions?** We still find strongly localized active nests of convection in one of our dynamo simulations (case D10L). It is unclear at present why they largely vanish as the differential rotation is quenched by strong magnetism. Weak localized structures remain and persist for thousands of days, but these structures are highly obscured by small-scale convection which emerges as the radial angular velocity shear decreases. We do not at present have a theory for the emergence or persistence of such modulated states. These structures appear to be hydrodynamic in nature, and they seem to survive under some magnetohydrodynamic conditions. Further work should be done on the theoretical side to understand where active nests arise from. Simulations should be undertaken that further constrain the dependence of active nests of convection on rotation, on the angular velocity shear of differential rotation, and on the hydrodynamic parameters of the simulations. Simulations should also be pursued which include tachoclines at the base of the convection zone, to determine whether active nests survive under conditions that are more similar to those found within stellar convection zones.

- **What is the origin of the rotation-activity relationship?** These simulations have not answered the questions posed by the observed correlation between rotation and stellar magnetic activity. It is unclear whether the observed correlation stems from dynamos that operate more efficiently with faster rotation and produce more magnetism, or from subtle changes in the emergence of magnetism at the stellar surface which are unrelated to changes in the global-scale dynamo itself. New observations are beginning to trace the multiple correlations between magnetic activity, differential rotation and overall rotation in stars (e.g., Saar 2008). These indicate that in the rising portion of the rotation-activity relationship the differential rotation is also growing, and in this regime there is a clear relation between magnetic activity and the amplitude of surface differential rotation. In the saturation regime however, this relationship breaks down and now magnetic activity appears to be uncorrelated with the amplitude of differential rotation. This is striking. Our simulations are beginning to explore multiple regimes, some where the differential rotation and magnetism coexist and some where the magnetism persists at similar amplitudes but the differential rotation is almost entirely quenched.

- **Do stars with deep convection zones operate wreathy dynamos?** Observations of fully convective M-dwarf stars, with masses below 0.35 $M_{\odot}$, indicate that these stars still have strong magnetic activity at their surfaces. These stars do not have stably-stratified radiative interiors and thus also should not have internal boundary layers such as tachoclines at the base of their convection zones. Additionally, K-type stars have much deeper convection zones than the Sun, and tachoclines in those stars are buried under more than 50% of the star in radius. It seems highly unlikely that the traditional interface model of stellar dynamos could be successfully operating in such stars. Instead, these stars

may run dynamos in the bulk of their convection zones, and those dynamos may be wreath-building dynamos. Convection and dynamo action in stars with deep convection zones should be explored. Changes in stellar luminosity at lower masses will additionally drive generally slower convective flows with correspondingly lower Rossby numbers. Simulations of these stars may help disentangle how convection, rotation and magnetism couple in stellar interiors.

- **Are tachoclines important?** These wreath-building dynamos are able to organize substantial global-scale magnetic fields in the bulk of their convection zones. They generally do so without resorting to tachoclines of penetration and shear for the storage and organization of such fields. Wreaths persist in the presence of tachoclines and, in the very limited explorations to date, are largely unmodified by the presence of this internal boundary layer. What role then do tachoclines play in stellar dynamos? These complex shear layers must contribute in some fashion to the operation of the global-scale dynamos but their role remains mysterious. If wreath-building dynamos continue to thrive under more realistic conditions, it seems likely that fully-convective stars and those with deep convection zones can still produce substantial global-scale magnetic fields. Simulations of these stars should be undertaken, to learn how these stellar dynamos are similar to and differ from the operation of the solar dynamo.

9.5 Final Reflections

In this thesis we have explored how stellar convection and magnetism built by dynamo action are affected by rotation. In rapidly rotating stars, the global-scale flows of differential rotation become stronger while the meridional circulations appear to become much weaker. The patterns of convection can achieve novel modulated states, and in some cases the equatorial convection is entirely confined to narrow active nests of convection with more quiescent flow in between. The rapidly rotating stars have strong dynamos that can build global-scale, wreath-like magnetic structures in the bulk of the convection zone. These wreaths can persist for thousands of days, or can become time-dependent with global-scale magnetic polarity reversals occurring quasi-regularly. Wreaths of magnetism can appear in solar simulations as well, and are also present in slowly spinning stars.

These projects sample only a small portion of the rich dynamics that arise from the coupling of convection, rotation, and magnetism in stellar interiors. Ultimately, they strive to better answer fundamental questions about stellar magnetism: Where are global-scale stellar magnetic fields built and organized, why is there a correlation between magnetic activity and stellar rotation rate, and what role does the tachocline play in a stellar dynamo?

Bibliography

Abbett, W. P., Fisher, G. H., Fan, Y., & Bercik, D. J. 2004, The dynamic evolution of twisted magnetic flux tubes in a three-dimensional convecting flow. II. Turbulent pumping and the cohesion of Ω-loops, ApJ, 612, 557–575

Anderson, K. E. & Behringer, R. P. 1990, Long time scales in traveling wave convection patterns, Physics Letters A, 145, 323–328

Augustson, K., Brown, B. P., Brun, A. S., & Toomre, J. 2010, Global-scale convection and dynamo action in F-type stars, ApJ, in preparation

Baliunas, S., Sokoloff, D., & Soon, W. 1996, Magnetic field and rotation in lower main-sequence stars: An empirical time-dependent magnetic Bode's relation?, ApJ, 457, L99–L102

Ballot, J., Brun, A. S., & Turck-Chièze, S. 2006, On the possible existence of localised vacillating convection state in rapidly rotating young solar-like stars, in ESA SP, Vol. 624, Proceedings of SOHO 18/GONG 2006/HELAS I, Beyond the spherical Sun, 108.1–108.5

Ballot, J., Brun, A. S., & Turck-Chièze, S. 2007, Simulations of turbulent convection in rotating young solarlike stars: Differential rotation and meridional circulation, ApJ, 669, 1190–1208

Barnes, J. R., Cameron, A. C., Donati, J.-F., James, D. J., Marsden, S. C., & Petit, P. 2005, The dependence of differential rotation on temperature and rotation, MNRAS, 357, L1–L5

Barnes, S. A. 2003, On the rotational evolution of solar- and late-type stars, its magnetic origins, and the possibility of stellar gyrochronology, ApJ, 586, 464–479

Barten, W., Lücke, M., Kamps, M., & Schmitz, R. 1995, Convection in binary fluid mixtures. II. Localized traveling waves, Phys. Rev. E, 51, 5662–5680

Batiste, O. & Knobloch, E. 2005, Simulations of localized states of stationary convection in^{3}He-^{4}He mixtures, Phys Rev Lett, 95, 244501.1–244501.4

Batiste, O., Knobloch, E., Alonso, A., & Mercader, I. 2006, Spatially localized binary-fluid convection, J. Fluid Mech., 560, 149–158

Blanchflower, S. 1999, Magnetohydrodynamic convectons, Phys Lett A, 261, 74–81

Blanchflower, S. & Weiss, N. 2002, Three-dimensional magnetohydrodynamic convectons, Phys Lett A, 294, 297–303

Brandenburg, A. 2009, Advances in theory and simulations of large-scale dynamos, Space Science Reviews, 144, 87–104

Brandenburg, A. & Subramanian, K. 2005, Astrophysical magnetic fields and nonlinear dynamo theory, Phys. Rep., 417, 1–4

Brown, B. 2009a, Global-scale stellar dynamos and wreathes of magnetism in rapidly rotating suns without tachoclines, in Bulletin of the American Astronomical Society, Vol. 41, 292

Brown, B. 2009b, Wreathes of magnetism built by dynamos without tachoclines, in AAS/Solar Physics Division Meeting, Vol. 40, #04.07

Brown, B., Browning, M., Brun, A., & Toomre, J. 2006, Localized nests of convection in rapidly rotating suns, in Bulletin of the American Astronomical Society, Vol. 38, 258

Brown, B., Browning, M. K., Brun, A. S., Miesch, M. S., & Toomre, J. 2007a, Rapid rotation and nests of convection in solar-like stars, in Bulletin of the American Astronomical Society, Vol. 38, 117

Brown, B., Brun, A. S., Miesch, M. S., & Toomre, J. 2007b, Strong global dynamo action in a younger sun, in Bulletin of the American Astronomical Society, Vol. 38, 130

Brown, B. P., Browning, M. K., Brun, A. S., Miesch, M. S., Nelson, N. J., & Toomre, J. 2007c, Strong dynamo action in rapidly rotating suns, in American Institute of Physics Conference Series, Vol. 948, 271–278

Brown, B. P., Browning, M. K., Brun, A. S., Miesch, M. S., & Toomre, J. 2007d, Rapid rotation, active nests of convection and global-scale flows in solar-like stars, Astron. Nachr., 328, 1002–1005

—. 2008, Rapidly rotating suns and active nests of convection, ApJ, 689, 1354–1372

—. 2009, Persistent wreathes of magnetism in a rapidly rotating sun, ApJ, submitted

Brown, B. P., Browning, M. K., Brun, A. S., & Toomre, J. 2004, Differential rotation when the Sun spun faster, in ESA SP, Vol. 559, Proceedings of the SOHO 14 / GONG 2004 Workshop, Helio- and Asteroseismology: Towards a Golden Future, ed. D. Danesy, 341–344

Browning, M. K. 2008, Simulations of dynamo action in fully convective stars, ApJ, 676, 1262–1280

Browning, M. K., Brun, A. S., & Toomre, J. 2004, Simulations of core convection in rotating A-type stars: Differential rotation and overshooting, ApJ, 601, 512–529

Browning, M. K., Miesch, M. S., Brun, A. S., & Toomre, J. 2006, Dynamo action in the solar convection zone and tachocline: Pumping and organization of toroidal fields, ApJ, 648, L157–L160

Brummell, N. H., Hurlburt, N. E., & Toomre, J. 1996, Turbulent compressible convection with rotation. I. Flow structure and evolution, ApJ, 473, 494–513

—. 1998, Turbulent compressible convection with rotation. II. Mean flows and differential rotation, ApJ, 493, 955–969

Brun, A. S., Antia, H. M., Chitre, S. M., & Zahn, J.-P. 2002, Seismic tests for solar models with tachocline mixing, A&A, 391, 725–739

Brun, A. S., Browning, M. K., & Toomre, J. 2005, Simulations of core convection in rotating A-type stars: Magnetic dynamo action, ApJ, 629, 461–481

Brun, A. S., Miesch, M. S., & Toomre, J. 2004, Global-scale turbulent convection and magnetic dynamo action in the solar envelope, ApJ, 614, 1073–1098

Brun, A. S. & Palacios, A. 2009, Numerical simulations of a rotating red giant star. I. Three-dimensional models of turbulent convection and associated mean flows, ApJ, 702, 1078–1097

Brun, A. S. & Toomre, J. 2002, Turbulent convection under the influence of rotation: Sustaining a strong differential rotation, ApJ, 570, 865–885

Burke, J. & Knobloch, E. 2007, Snakes and ladders: Localized states in the Swift-Hohenberg equation, Phys Lett A, 360, 681–688

Busse, F. H. 1970, Thermal instabilities in rapidly rotating systems., J. Fluid Mech., 44, 441–460

—. 2002, Convective flows in rapidly rotating spheres and their dynamo action, Physics of Fluids, 14, 1301–1314

Busse, F. H. & Simitev, R. 2005, Dynamos driven by convection in rotating spherical shells, Astron. Nachr., 326, 231–240

Chabrier, G. & Küker, M. 2006, Large-scale α^2-dynamo in low-mass stars and brown dwarfs, A&A, 446, 1027–1037

Chandrasekhar, S. 1961, Hydrodynamic and hydromagnetic stability (International Series of Monographs on Physics, Oxford: Clarendon, 1961)

Charbonneau, P. 2005, Dynamo models of the solar cycle, Living Reviews in Solar Physics, 2, 2:1–83

Charbonneau, P. & MacGregor, K. B. 1997, Solar interface dynamos. II. Linear, kinematic models in spherical geometry, ApJ, 486, 502–520

Charbonneau, P. & Saar, S. H. 2001, Stellar dynamos: A modeling perspective, in Astronomical Society of the Pacific Conference Series, Vol. 248, Magnetic Fields Across the Hertzsprung-Russell Diagram, ed. G. Mathys, S. K. Solanki, & D. T. Wickramasinghe, 189–198

Cline, K. S. 2003, PhD thesis, University of Colorado, Boulder

Cline, K. S., Brummell, N. H., & Cattaneo, F. 2003, On the formation of magnetic structures by the combined action of velocity shear and magnetic buoyancy, ApJ, 588, 630–644

Clune, T. L., Elliott, J. R., Glatzmaier, G. A., Miesch, M. S., & Toomre, J. 1999, Computational aspects of a code to study rotating turbulent convection in spherical shells, Parallel Computing, 25, 361–380

Clyne, J., Mininni, P., Norton, A., & Rast, M. 2007, Interactive desktop analysis of high resolution simulations: application to turbulent plume dynamics and current sheet formation, New Journal of Physics, 9, 301–+

Dawes, J. H. P. 2007, Localized convection cells in the presence of a vertical magnetic field, J. Fluid Mech., 570, 385–406

Deane, A. E., Toomre, J., & Knobloch, E. 1987, Traveling waves and chaos in thermosolutal convection, Phys. Rev. A, 36, 2862–2869

—. 1988, Traveling waves in large-aspect-ratio thermosolutal convection, Phys. Rev. A, 37, 1817–1820

Delfosse, X., Forveille, T., Perrier, C., & Mayor, M. 1998, Rotation and chromospheric activity in field M dwarfs, A&A, 331, 581–595

Dikpati, M., Saar, S. H., Brummell, N., & Charbonneau, P. 2001, Magnetic cycles and activity in FGK stars in the framework of Babcock-Leighton dynamos, in Astronomical Society of the Pacific Conference Series, Vol. 248, Magnetic Fields Across the Hertzsprung-Russell Diagram, ed. G. Mathys, S. K. Solanki, & D. T. Wickramasinghe, 235–238

Donahue, R. A., Saar, S. H., & Baliunas, S. L. 1996, A relationship between mean rotation period in lower main-sequence stars and its observed range, ApJ, 466, 384–391

Donati, J.-F., Cameron, A. C., Semel, M., Hussain, G. A. J., Petit, P., Carter, B. D., Marsden, S. C., Mengel, M., López Ariste, A., Jeffers, S. V., & Rees, D. E. 2003, Dynamo processes and activity cycles of the active stars AB Doradus, LQ Hydrae and HR 1099, MNRAS, 345, 1145–1186

Donati, J.-F., Forveille, T., Cameron, A. C., Barnes, J. R., Delfosse, X., Jardine, M. M., & Valenti, J. A. 2006, The large-scale axisymmetric magnetic topology of a very-low-mass fully convective star, Science, 311, 633–635

Dormy, E., Soward, A. M., Jones, C. A., Jault, D., & Cardin, P. 2004, The onset of thermal convection in rotating spherical shells, J. Fluid Mech., 501, 43–70

Fan, Y., Abbett, W. P., & Fisher, G. H. 2003, The dynamic evolution of twisted magnetic flux tubes in a three-dimensional convecting flow. I. Uniformly buoyant horizontal tubes, ApJ, 582, 1206–1219

Featherstone, N., Browning, M. K., Brun, A. S., & Toomre, J. 2007, Dynamo action in the presence of an imposed magnetic field, Astron. Nachr., 328, 1126–1129

Featherstone, N., Miesch, M. S., Brun, A. S., & Toomre, J. 2010, A better model of the solar tachocline, ApJ, in preparation

Featherstone, N. A., Browning, M. K., Brun, A. S., & Toomre, J. 2009, Effects of fossil magnetic fields on convective core dynamos in A-type stars, ApJ, 328, 1126–1129

Gilman, P. A. 1975, Linear simulations of boussinesq convection in a deep rotating spherical shell, J. Atmos. Sci., 32, 1331–1352

—. 1977, Nonlinear dynamics of Boussinesq convection in a deep rotating spherical shell. I., Geophys. Astrophys. Fluid Dyn., 8, 93–135

—. 1979, Model calculations concerning rotation at high solar latitudes and the depth of the solar convection zone, ApJ, 231, 284–292

Gilman, P. A. & Glatzmaier, G. A. 1981, Compressible convection in a rotating spherical shell. I. Anelastic equations. II. A linear anelastic model. III. Analytic model for compressible vorticity waves, ApJS, 45, 335–388

Glatzmaier, G. A. & Gilman, P. A. 1981, Compressible convection in a rotating spherical shell. II. A linear anelastic model, ApJS, 45, 351–380

Grote, E. & Busse, F. H. 2000, Dynamics of convection and dynamos in rotating spherical fluid shells, Fluid Dyn. Res., 28, 349–368

Hathaway, D. H. 2009, solar Physics Group, NASA Marshall Space Flight Center. http://solarscience.msfc.nasa.gov/SunspotCycle.shtml (accessed July 30, 2009)

Hawley, S. L., Gizis, J. E., & Reid, I. N. 1996, The Palomar/MSU nearby star spectroscopic survey. II. The southern M dwarfs and investigation of magnetic activity, AJ, 112, 2799–2827

Hurlburt, N. E., Toomre, J., & Massaguer, J. M. 1986, Nonlinear compressible convection penetrating into stable layers and producing internal gravity waves, ApJ, 311, 563–577

Jackson, J. D. 1998, Classical Electrodynamics, 3rd Edition (John Wiley & Sons, 1999. 808 p.)

James, D. J., Jardine, M. M., Jeffries, R. D., Randich, S., Collier Cameron, A., & Ferreira, M. 2000, X-ray emission from nearby M-dwarfs: the super-saturation phenomenon, MNRAS, 318, 1217–1226

Jouve, L., Brown, B. P., & Brun, A. S. 2009, Exploring the Prot vs Pcyc relation with flux transport dynamo models of solar-type stars, A&A, submitted

Jouve, L. & Brun, A. S. 2009, Three-dimensional nonlinear evolution of a magnetic flux tube in a spherical shell: Influence of turbulent convection and associated mean flows, ApJ, 701, 1300–1322

Julien, K., Legg, S., McWilliams, J., & Werne, J. 1996, Rapidly rotating turbulent Rayleigh-Benard convection, J. Fluid Mech., 322, 243–273

Käpylä, P. J., Korpi, M. J., & Brandenburg, A. 2009, Large-scale dynamos in rigidly rotating turbulent convection, ApJ, 697, 1153–1163

Knobloch, E., Moore, D. R., Toomre, J., & Weiss, N. O. 1986, Transitions to chaos in two-dimensional double-diffusive convection, J. Fluid Mech., 166, 409–448

Knobloch, E., Rosner, R., & Weiss, N. O. 1981, Magnetic fields in late-type stars, MNRAS, 197, 45P–49P

Kolodner, P. & Glazier, J. A. 1990, Interaction of localized pulses of traveling-wave convection with propagating disturbances, Phys. Rev. A, 42, 7504–7506

Küker, M. & Rüdiger, G. 1999, Magnetic field generation in weak-line T Tauri stars: an alpha (2) -dynamo, A&A, 346, 922–928

—. 2005a, Differential rotation of main sequence F stars, A&A, 433, 1023–1030

—. 2005b, Differential rotation on the lower main sequence, Astron. Nachr., 326, 265–268

Küker, M. & Stix, M. 2001, Differential rotation of the present and the pre-main-sequence Sun, A&A, 366, 668–675

Leorat, J., Pouquet, A., & Frisch, U. 1981, Fully developed MHD turbulence near critical magnetic Reynolds number, J. Fluid Mech., 104, 419–443

MacGregor, K. B. & Brenner, M. 1991, Rotational evolution of solar-type stars. I. Main-sequence evolution, ApJ, 376, 204–213

Matt, S. & Pudritz, R. E. 2008, Accretion-powered stellar winds. II. Numerical solutions for stellar wind torques, ApJ, 678, 1109–1118

Miesch, M. S. 1998, PhD thesis, University of Colorado, Boulder

—. 2005, Large-scale dynamics of the convection zone and tachocline, Living Reviews in Solar Physics, 2, 1:1–139

Miesch, M. S., Brun, A. S., DeRosa, M. L., & Toomre, J. 2008, Structure and evolution of giant cells in global models of solar convection, ApJ, 673, 557–575

Miesch, M. S., Brun, A. S., & Toomre, J. 2006, Solar differential rotation influenced by latitudinal entropy variations in the tachocline, ApJ, 641, 618–625

Miesch, M. S., Elliott, J. R., Toomre, J., Clune, T. L., Glatzmaier, G. A., & Gilman, P. A. 2000, Three-dimensional spherical simulations of solar convection. I. Differential rotation and pattern evolution achieved with laminar and turbulent states, ApJ, 532, 593–615

Moffatt, H. K. 1978, Magnetic field generation in electrically conducting fluids (Cambridge, England, Cambridge University Press, 1978. 353 p.)

Moffatt, H. K. & Proctor, M. R. E. 1982, The role of the helicity spectrum function in turbulent dynamo theory, Geophys. Astrophys. Fluid Dyn., 21, 265–283

Mohanty, S. & Basri, G. 2003, Rotation and activity in Mid-M to L field dwarfs, ApJ, 583, 451–472

Moreno-Insertis, F., Schuessler, M., & Ferriz-Mas, A. 1992, Storage of magnetic flux tubes in a convective overshoot region, A&A, 264, 686–700

Morin, J., Donati, J.-F., Petit, P., Delfosse, X., Forveille, T., Albert, L., Aurière, M., Cabanac, R., Dintrans, B., Fares, R., Gastine, T., Jardine, M. M., Lignières, F., Paletou, F., Ramirez Velez, J. C., & Théado, S. 2008, Large-scale magnetic topologies of mid M dwarfs, MNRAS, 390, 567–581

Niemela, J. J., Ahlers, G., & Cannell, D. S. 1990, Localized traveling-wave states in binary-fluid convection, Phys. Rev. Lett., 64, 1365–1368

Noyes, R. W., Hartmann, L. W., Baliunas, S. L., Duncan, D. K., & Vaughan, A. H. 1984, Rotation, convection, and magnetic activity in lower main-sequence stars, ApJ, 279, 763–777

Ossendrijver, M. 2003, The solar dynamo, A&A Rev., 11, 287–367

Palacios, A. & Brun, A. S. 2007, Simulation of turbulent convection in a slowly rotating red giant star, Astron. Nachr., 328, 1114–+

Parker, E. N. 1975, The generation of magnetic fields in astrophysical bodies. X. Magnetic buoyancy and the solar dynamo, ApJ, 198, 205–209

—. 1993, A solar dynamo surface wave at the interface between convection and nonuniform rotation, ApJ, 408, 707–719

Patten, B. M. & Simon, T. 1996, The evolution of rotation and activity in young open clusters: IC 2391, ApJS, 106, 489–531

Pedlosky, J. 1982, Geophysical fluid dynamics (New York and Berlin, Springer-Verlag, 1982. 636 p.)

Petit, P., Dintrans, B., Solanki, S. K., Donati, J.-F., Aurière, M., Lignières, F., Morin, J., Paletou, F., Ramirez Velez, J., Catala, C., & Fares, R. 2008, Toroidal versus poloidal magnetic fields in Sun-like stars: a rotation threshold, MNRAS, 388, 80–88

Pizzo, V., Schwenn, R., Marsch, E., Rosenbauer, H., Muehlhaeuser, K.-H., & Neubauer, F. M. 1983, Determination of the solar wind angular momentum flux from the HELIOS data - an observational test of the Weber and Davis theory, ApJ, 271, 335–354

Pizzolato, N., Maggio, A., Micela, G., Sciortino, S., & Ventura, P. 2003, The stellar activity-rotation relationship revisited: Dependence of saturated and non-saturated X-ray emission regimes on stellar mass for late-type dwarfs, A&A, 397, 147–157

Pouquet, A., Frisch, U., & Leorat, J. 1976, Strong MHD helical turbulence and the nonlinear dynamo effect, J. Fluid Mech., 77, 321–354

Reiners, A. 2006, Rotation- and temperature-dependence of stellar latitudinal differential rotation, A&A, 446, 267–277

Reiners, A. & Basri, G. 2007, The first direct measurements of surface magnetic fields on very low mass stars, ApJ, 656, 1121–1135

—. 2008, Chromospheric activity, rotation, and rotational braking in M and L dwarfs, ApJ, 684, 1390–1403

—. 2009, On the magnetic topology of partially and fully convective stars, A&A, 496, 787–790

Reiners, A., Basri, G., & Browning, M. 2009, Evidence for magnetic flux saturation in rapidly rotating M stars, ApJ, 692, 538–545

Reiners, A. & Schmitt, J. H. M. M. 2003, Rotation and differential rotation in field F- and G-type stars, A&A, 398, 647–661

Rempel, M. 2005, Solar differential rotation and meridional flow: The role of a subadiabatic tachocline for the Taylor-Proudman balance, ApJ, 622, 1320–1332

—. 2006, Flux-transport dynamos with Lorentz force feedback on differential rotation and meridional flow: Saturation mechanism and torsional oscillations, ApJ, 647, 662–675

—. 2007, Origin of solar torsional oscillations, ApJ, 655, 651–659

Rempel, M. 2008, Solar and stellar activity cycles, in J. Phys. Conf. Ser., Vol. 118, Proceedings of the Second HELAS International Conference: Helioseismology, Asteroseismology and MHD connections, ed. L. Gizon & M. Roth, Journal of Physics Conference Series (IoP), 012032.1–012032.10

Riecke, H. 1992, Self-trapping of traveling-wave pulses in binary mixture convection, Phys. Rev. Lett., 68, 301–304

Rogachevskii, I. & Kleeorin, N. 2003, Electromotive force and large-scale magnetic dynamo in a turbulent flow with a mean shear, Phys. Rev. E, 68, 036301–1 – 036301–12

Rüdiger, G., von Rekowski, B., Donahue, R. A., & Baliunas, S. L. 1998, Differential rotation and meridional flow for fast-rotating solar-type stars, ApJ, 494, 691–699

Saar, S. H. 1996, Recent magnetic fields measurements of stellar magnetic fields, in IAU Symposium, Vol. 176, Stellar Surface Structure, ed. K. G. Strassmeier & J. L. Linsky, 237–244

Saar, S. H. 2001, Recent measurements of (and inferences about) magnetic fields on K and M stars (CD-ROM Directory: contribs/saar1), in ASP Conference Series, Vol. 223, 11th Cambridge Workshop on Cool Stars, Stellar Systems and the Sun, ed. R. J. Garcia Lopez, R. Rebolo, & M. R. Zapaterio Osorio, 292–299

Saar, S. H. 2008, The activity cycles and surface differential rotation of single dwarfs, in Proceedings of SOHO 21/GONG 2008, Solar-stellar dynamos as revealed by helio- and asteroseismology, submitted

Saar, S. H. & Brandenburg, A. 1999, Time evolution of the magnetic activity cycle period. II. Results for an expanded stellar sample, ApJ, 524, 295–310

Schrinner, M., Rädler, K.-H., Schmitt, D., Rheinhardt, M., & Christensen, U. 2005, Mean-field view on rotating magnetoconvection and a geodynamo model, Astron. Nachr., 326, 245–249

Skumanich, A. 1972, Time scales for Ca II emission decay, rotational braking, and lithium depletion, ApJ, 171, 565–567

Spina, A., Toomre, J., & Knobloch, E. 1998, Confined states in large-aspect-ratio thermosolutal convection, Phys. Rev. E, 57, 524–545

Spruit, H. C. 2003, Origin of the torsional oscillation pattern of solar rotation, Sol. Phys., 213, 1–21

Spruit, H. C. & van Ballegooijen, A. A. 1982, Stability of toroidal flux tubes in stars, A&A, 106, 58–66

Steenbeck, M., Krause, F., & Rädler, K. H. 1966, A calculation of the mean electromotive force in an electrically conducting fluid in turbulent motion under the influence of coriolis forces, Z. Naturforsch. Teil A, 21, 369–376

Surko, C. M., Ohlsen, D. R., Yamamoto, S. Y., & Kolodner, P. 1991, Confined states of traveling-wave convection, Phys. Rev. A, 43, 7101–7104

Thompson, M. J. 2009, personal communication

Thompson, M. J., Christensen-Dalsgaard, J., Miesch, M. S., & Toomre, J. 2003, The internal rotation of the sun, ARA&A, 41, 599–643

Tobias, S. M., Brummell, N. H., Clune, T. L., & Toomre, J. 2001, Transport and storage of magnetic field by overshooting turbulent compressible convection, ApJ, 549, 1183–1203

Vasil, G. M. & Brummell, N. H. 2008, Magnetic buoyancy instabilities of a shear-generated magnetic layer, ApJ, 686, 709–730

—. 2009, Constraints on the magnetic buoyancy instabilities of a shear-generated magnetic layer, ApJ, 690, 783–794

Walker, G. A. H., Croll, B., Kuschnig, R., Walker, A., Rucinski, S. M., Matthews, J. M., Guenther, D. B., Moffat, A. F. J., Sasselov, D., & Weiss, W. W. 2007, The differential rotation of κ^1 Ceti as observed by MOST, ApJ, 659, 1611–1622

Weber, E. J. & Davis, L. J. 1967, The angular momentum of the solar wind, ApJ, 148, 217–227

West, A. A., Bochanski, J. J., Hawley, S. L., Cruz, K. L., Covey, K. R., Silvestri, N. M., Reid, I. N., & Liebert, J. 2006, Using the galactic dynamics of M7 dwarfs to infer the evolution of their magnetic activity, AJ, 132, 2507–2512

West, A. A., Hawley, S. L., Bochanski, J. J., Covey, K. R., Reid, I. N., Dhital, S., Hilton, E. J., & Masuda, M. 2008, Constraining the age-activity relation for cool stars: the sloan digital sky survey data release 5 low-mass star spectroscopic sample, AJ, 135, 785–795

West, A. A., Hawley, S. L., Walkowicz, L. M., Covey, K. R., Silvestri, N. M., Raymond, S. N., Harris, H. C., Munn, J. A., McGehee, P. M., Ivezić, Ž., & Brinkmann, J. 2004, Spectroscopic properties of cool stars in the sloan digital sky survey: An analysis of magnetic activity and a search for subdwarfs, AJ, 128, 426–436

Zahn, J.-P. 1992, Circulation and turbulence in rotating stars, A&A, 265, 115–132

Zhang, C. 2005, Madden-Julian Oscillation, Reviews of Geophysics, 43, G2003